Dissertation
submitted to the
Combined Faculties for the Natural Sciences and for Mathematics
of the Ruperto-Carola University of Heidelberg, Germany
for the degree of
Doctor of Natural Sciences

put forward by
Dipl.-Phys. Peter Lübcke
born in Bielefeld

Date of oral examination: 07.05.2014

Optical remote sensing measurements of bromine and sulphur emissions: Investigating their potential as tracers of volcanic activity

Referees: Prof. Dr. Ulrich Platt
Prof. Dr. Thomas Wagner

Abstract

The optical remote sensing of volcanic gas emissions has become an established field in recent decades. The total amount of gas emissions (quantified by measuring the SO_2 emission rate) as well as the composition of gases, can help researchers to understand volcanic systems. This knowledge is needed to improve forecasts of volcanic eruptions. For this thesis, volcanic gas emissions were investigated with two different techniques on different time scales. First, high time-resolution (order of 1 s) 2D-SO_2 column density images measured by an SO_2 camera were used to quantify SO_2 emission rates at Popocatépetl, Mexico, and Stromboli, Italy. The frequency of the flux was investigated with a wavelet analysis. It was verified that calibrating the SO_2 camera with help of a DOAS system leads to more robust results than using calibration cells, especially for a volcanic plume containing ash or aerosols. Second, spectra from the scanning DOAS network NOVAC (with a time resolution of $\approx 5-15$ minutes) were evaluated for BrO/SO_2 ratios. It was shown that data from NOVAC actually has sufficient quality to evaluate spectra for BrO. An automatic evaluation algorithm was developed and used to create a four-year time series (2009 – 2013) of BrO/SO_2 ratios at Nevado del Ruiz, Colombia. The BrO/SO_2 ratio showed variations that are closely correlated to the level of volcanic activity indicating its usefulness as an additional volcanological parameter. Several possibilities for further improving data quality were investigated. This included temperature effects on the DOAS retrieval, the influence of radiative transfer and problems arising from reference spectra contaminated with SO_2.

Zusammenfassung

Die optische Fernerkundung von Vulkangasen hat sich in den letzten Jahrzehnten etabliert. Damit wird die emittierte Gasmenge (zumeist von SO_2) sowie die chemische Zusammensetzung der Gase bestimmt. Dieses Wissen hilft, Vulkane besser zu verstehen und wird benötigt, um Vulkanausbrüche besser vorherzusagen. In dieser Arbeit wurden Vulkanemissionen mit zwei Methoden auf unterschiedlichen Zeitskalen untersucht. Mit einer SO_2 Kamera wurden, zeitlich hochaufgelöst ($\approx 1\,s$), die Emissionsraten von SO_2 am Popocatépetl, Mexiko, und am Stromboli, Italien bestimmt. Aus diesen Messungen wurde der Frequenzgehalt durch eine Wavelet-Analyse ermittelt. Es wurde gezeigt, dass die Kalibration mit Hilfe eines Spektrographens zu robusteren Ergebnissen führt als Kalibration mit Küvetten, besonders in Fällen, in denen die Vulkanfahne Aerosole oder Asche enthält. Desweiteren wurden aus Spektren des NOVAC Netzwerks (mit einer Zeitauflösung von 5 – 15 Minuten) die Säulendichten von BrO und SO_2 bestimmt. Insbesondere wurde gezeigt, dass die Qualität der Daten überhaupt für die BrO Auswertung ausreicht. Darauf aufbauend wurde ein Algorithmus für die automatische Auswertung der Spektren entwickelt und auf den vier Jahre (2009 – 2013) umfassendenden Datensatz vom Nevado del Ruiz, Kolumbien angewendet. Die Zeitreihe des BrO/SO_2 Verhältnisses korreliert mit der vulkanischen Aktivität, was für dessen Nutzen als vulkanologischer Parameter spricht. Zusätzlich wurden verschiedene Möglichkeiten, die Qualität der Daten weiter zu verbessern untersucht, wie z.B. Einflüsse der Temperatur auf die DOAS Auswertung, Einflüsse des Strahlungstransports sowie Probleme aufgrund von mit SO_2 kontaminierten Referenzspektren.

Contents

parts of this thesis have been published in:

- Lübcke, P., Bobrowski, N., Illing, S., Kern, C., Alvarez Nieves, J. M., Vogel, L., Zielcke, J., Delgado Granados, H., and Platt, U.: On the absolute calibration of SO_2 cameras, *Atmos. Meas. Tech.*, **6**, 677-696, doi:10.5194/amt-6-677-2013, 2013.
- Lübcke, P., Bobrowski, N., Arellano, S., Galle, B., Garzón, G., Vogel, L., and Platt, U.: BrO/SO_2 molar ratios from scanning DOAS measurements in the NOVAC network, *Solid Earth Discuss.*, **5**, 1845-1870, doi:10.5194/sed-5-1845-2013, in discussion, 2013.

...and the public need to know when and where eruptions will occur... These questions are much easier to ask than to answer.

R.S.J. Sparks

1 Introduction

Volcanoes have always influenced mankind in both, positive and negative ways. Gases released by volcanoes can lead to an increase in Earth's albedo and thus cause globally decreasing temperatures (see Chapter 2 and Robock, 2000). This might seem advantageous in the face of global warming, but drops in temperature can promote diseases and lead to significant crop losses. As far back as the 18^{th} century, Benjamin Franklin (Franklin, 1784) linked the unusually cold winter of 1783/84 to an eruption of Laki, Iceland. Just a few years later, in 1815, one of the largest eruptions (magma volume estimates vary between 100 – 1000 km^3 according to Stothers, 1984) in recent history happened at Tambora, Indonesia, causing 88,000 direct casualties (Stothers, 1984) and leading to the infamous "year without summer". The term "year without summer" arises from the exceptionally cold summer of 1816 that chilled North America and large parts of Europe. Europe experienced 1 – 2°C cooler average summer temperatures that year than during the rest of the decade (Oppenheimer, 2003b), which was already the coldest decade on the northern hemisphere since at least 1400 (Briffa et al., 1998). It is now suspected that the low summer temperatures caused epidemics in Europe and the loss of primary crops in parts of North America.

On the other hand, volcanoes can also be a positive influence and in some cases have even served as a source of life. Several volcanic island groups such as the Canary Islands or Hawaii are of volcanic origin and provide a place to live. Many volcanoes have a positive impact on the economy due to their relevance as tourist sites and in some countries as important sources of geothermal energy. Fertile soils and mineral deposits in the vicinity of volcanoes led humans to settle close to volcanoes at many places worldwide. People residing close to volcanoes live in potential danger of volcanic eruptions. Volcanic eruptions can be deadly

and can also cause significant economic losses. For instance, Mexico City, with almost 20 million inhabitants in its metropolitan area, is located only 70 km north east of Popocatépetl, which is still active today. Mexico City is mentioned here not only because of its size but also because Popocatépetl was one of the field sites at which data used in this dissertation were collected. But numerous other cities and small villages have been built close to volcanoes as well. Two examples in Europe are Vesuvius and Campi Flegrei in Italy, which are located close to the city of Naples. Barberi and Carapezza (1996) estimated that even a moderate eruption (with a magma volume of only $4 \times 10^{-2}\,\mathrm{km}^3$) poses a risk for a portion of the roughly 1 million inhabitants of Naples. There are some obvious dangers associated with the hot, dense material that is erupted from the volcano or with the toxic gases that are released, but indirect hazards like earthquakes or tsunamis caused by volcanic eruptions can endanger humans as well (Chester et al., 2000).

Furthermore, volcanic eruptions pose a risk for aircraft flying through volcanic ash plumes, as the eruption of Eyjafjallajökull in April 2010 recently showed again. Disturbances in air traffic due to volcanic clouds led to an estimated financial loss of 2.5 billion € (Zehner, 2010). Tilling and Lipman (1993) estimated that a total of 500 million people would be endangered by volcano hazards in 2000. Even more incidents are likely in the future due to the fact that the number of active volcanoes per year remains fairly constant while the population on Earth and the amount of air traffic increase exponentially (Tilling, 2008).

Considering the increasing risk from volcanic eruptions, the need to understand volcanic systems and to monitor their activity is obvious. However, this is a difficult task as "volcanoes are complex systems and many different processes control their behaviour" (Sparks, 2003a). There are some examples of successful monitoring of active volcanoes, like the 1980 eruption of Mt. St. Helens in the United States or the 1991 eruption of Mt. Pinatubo in the Philippines (Tilling, 2008). Despite being one of the largest eruptions in the 20$^{\mathrm{th}}$ century (magma volume $>5\,\mathrm{km}^3$) and occurring in a populated area, only roughly 800 casualties were caused by the eruption of Mt. Pinatuo (Tilling and Lipman, 1993). On the other hand, the 1985 eruption of Nevado del Ruiz in Colombia, which is the subject of a large part of this thesis, presents a particularly tragic example of the catastrophic events that can follow a volcanic eruption. Despite not being an extraordinarily large eruption (erupted magma volume of only $5 \times 10^{-3}\,\mathrm{km}^3$, Voight, 1990) the aftermath of the Nevado del Ruiz eruption caused almost 25,000 casualties. After almost one year of precursory activity and a minor eruption on 11 September 1985, Nevado del Ruiz erupted again on 13 November 1985. This eruption caused pyroclastic flows and surges which caused the glaciers on top of Nevado del Ruiz to melt. Water from the melting glaciers ultimately resulted in lahars[1] flowing down the mountain. Two hours after the eruption,

[1] A lahar is a debris or mud flow.

several lahars buried the town of Armero, which lies in a distance of almost 50 km north east of Nevado del Ruiz. Almost 22,000 people an amount which accounts for approximately 75% of the total population, were killed by mud flows. Voight (1990) stated that "Science accurately foresaw the hazards but was insufficiently precise to render reliable warning of the crucial event at the last possible minute." The tragedy of Armero is that while scientists were aware that the eruption had happened, there was insufficient monitoring and thus a "credibility gap" that prevented authorities from forcing a decision to evacuate the town of Armero.

The tragic example of Armero shows how important it is to monitor volcanoes in an attempt to forecast eruptions as accurately as possible. One crucial point in monitoring is that it has to be performed continuously. A baseline is needed for the behaviour of the different observables in order to to draw the correct conclusions from different measurement techniques at a volcano (Tilling, 2008). Several different techniques exist for monitoring volcanoes. These include seismicity, deformation measurements and the monitoring of volcanic gas emissions. All these techniques have quite a long history of being used to monitor volcanoes, but seismicity and deformation measurements have been used longer than gas measurements (Scarpa and Gasparini, 1996). Gorshkov (1971) writes of his first attempts to locate the depth of a magma chamber by measuring seismic waves in 1956 (the original manuscript Gorshkov, 1956, is only available in Russian and was therefore not used as a source here). Around the same time period, Mogi (1958) published his model, which describes the deformation of a volcano in response to pressure changes in the magma chamber. For a long time, monitoring of volcanic gases was done by in-situ sampling (e.g. Giggenbach, 1996), which has some obvious drawbacks due to the hazardous situations involved in obtaining gas samples. In 1957, Noguchi and Kamiya (1963) used alkaline traps at Mt. Asama, Japan, to measure the gas composition (CO_2, HCl, S) and suggested that variations of the gas composition from volcanoes could help predict volcanic eruptions. In recent decades, gas geochemistry has also become an established tool for monitoring volcanoes.

The remote sensing of volcanic gas emissions is, however, still a relatively new field when compared with in-situ methods. The first remote sensing instrument at volcanoes was the correlation spectrometer (COSPEC, Moffat and Millan, 1971; Stoiber et al., 1983), which is able to measure SO_2 emission rates using scattered solar radiation as a light source. In the 1990s the Fourier Transform InfraRed spectroscopy (FTIR) was first applied to measure the ratio between HCl and SO_2 (e.g. Francis et al., 1995; Mori et al., 1993). While FTIR is able to measure many volcanic trace gases, instruments are expensive and the evaluation and set-up of instruments in the field is rather complicated.

One big step forward came with the first measurements of volcanic gases using Differential Optical Absorption Spectroscopy (DOAS, e.g. Platt and Stutz, 2008) by Edner et al. (1994) at Etna, Italy. The simple and robust DOAS technique is

able to measure several volcanic trace gas species using scattered solar radiation in the UV as a light source. The availability of inexpensive, small and lightweight spectrometers (Galle et al., 2003) helped spread DOAS in the volcanological community. These days, DOAS is, besides FTIR, the most commonly used technique for the remote sensing of volcanic gases. Bobrowski et al. (2003) were able to detect bromine in volcanic plumes using DOAS, changing the commonly held view that volcanic emissions only had minimal influence on atmospheric chemistry. Another big success was the Network for Observation of Volcanic Activity and Atmospheric Change (NOVAC, Galle et al., 2010), an EU funded project. During the NOVAC project, scanning DOAS systems were installed at 26 volcanoes worldwide with the goal to automatically measure volcanic SO_2 emission rates. This network is still to this day the only global network to measure volcanic gas emissions.

Another relatively new technique for measuring volcanic SO_2 emission rates is the SO_2 camera (e.g. Bluth et al., 2007; Kern et al., 2010b; Mori and Burton, 2006). The SO_2 camera allows for the measurement of SO_2 emission rates with a high time resolution of approximately 1 Hz, which makes it possible to investigate volcanic degassing on unprecedented time scales.

This thesis covers measurements of volcanic gas emissions with two different techniques and on different time scales. SO_2 cameras were used to perform high time-resolution measurements at Popocatépetl, Mexico, and Stromboli, Italy. Furthermore, spectroscopic data recorded by the scanning DOAS instruments from NOVAC at Nevado del Ruiz, Colombia, were evaluated in order to obtain BrO/SO_2 ratios. The NOVAC data has a significantly lower time resolution (one scan roughly every 5 – 15 minutes) but covers almost four years of continuous measurements.

Both, variations of the SO_2 emission rate and variations of the ratios of the different trace gases can be used to gain additional insight into processes occurring at depth. This concept will be explained in more detail in Chapter 2, which provides a short overview about volcanoes and the processes happening inside them. The influences of SO_2 and BrO on the atmosphere and the climate will also briefly be discussed.

Chapter 3 covers basic physical concepts needed to understand the remote sensing of volcanic gases in the atmosphere and explains the applied measurement techniques (DOAS, SO_2 camera). Chapter 4 covers the SO_2 camera measurements. In this chapter, the accurate calibration of SO_2 cameras and the influence of ash and aerosol on the calibration are discussed in detail. One possible application of SO_2 camera measurements in volcanology, the wavelet analysis, is shown. This technique can be used to find frequencies in the SO_2 emission rates and their time dependency.

The second large part of this thesis, the evaluation of NOVAC data starts in Chapter 5 by explaining the retrieval of BrO/SO_2 ratios at Nevado del Ruiz. A four-year time series (2009 – 2013) was created that covers a period of interesting

volcanic activity at Nevado del Ruiz.

The following chapters (Chapters 6 and 7) each discuss possible error sources in the evaluation of NOVAC data and show possible ways to further improve the data set. Chapter 6 in particular discusses the influences of radiative transfer on the retrieved BrO/SO_2 ratios. This includes the influence of the distance between the instrument and the volcanic plume as well as meteorological clouds. Because the instruments in the NOVAC network are not thermally stabilised, Chapter 7 is dedicating to discussing the effects of variations in the instrument's temperature on the DOAS retrieval. Chapter 8 introduces a DOAS retrieval that uses a high-resolution solar atlas as a reference spectrum. This technique allows the absolute determination of SO_2 columns and thus can prevent erroneous results at times when the instruments are completely surrounded by volcanic gases.

The dissertation wraps up in Chapter 9 with conclusions and an outlook towards how the methods applied in this thesis can be further developed.

2

Volcanoes and volcanic gas emissions

volcano, n.: 1. Physical Geogr. A hill, mountain, or other feature, typically conical in form, that is built up of solidified lava and rock debris and has a crater or vent through which, in periods of activity, molten rock (lava), rock fragments, steam, and gas are emitted from within the planet's crust

Oxford English Dictionary (2013)

This chapter starts with a brief introduction to the reasons for volcanism and explains the different types of volcanism. Its purpose is to provide an overview of the complex processes happening during the long journey from the mantle and crust inside the Earth to the point at which the gases can be measured in the atmosphere.

From melting rock and the magma degassing to the chemistry happening in the atmosphere, there are numerous processes influencing the amounts of gas and composition that are ultimately measured. The basics of volcanism described in Section 2.1 mainly follow the textbooks by Schmincke (2003), Francis and Oppenheimer (2004) and Frisch and Meschede (2013). The basic concepts of volatile degassing from the magma and which processes influence the chemical composition of the gases will be explained in Section 2.2. The chemistry of sulphur and bromine after their release into the atmosphere as well as the implications of volcanic degassing on the atmosphere and the Earth's climate will be discussed in Section 2.3. The introductory chapter will conclude in Section 2.4 with examples of the usefulness of volcanic gas emission measurements. An outlook will be given as to how measurements of the SO_2 emission rate and the chemical composition can be used to gain knowledge about volcanic systems and especially how they can help to improve the accuracy of volcanic eruption forecasts.

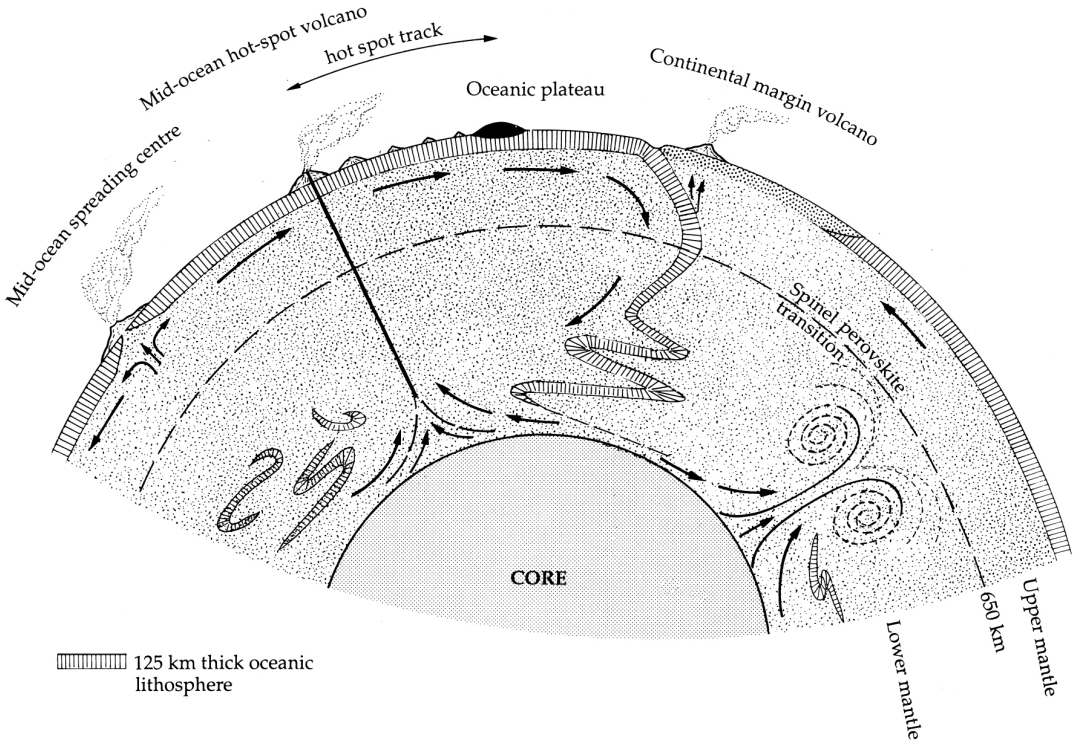

Figure 2.1.: Plate tectonics and their influence on volcanism. Diverging (mid-ocean spreading centre or mid-ocean ridge) and converging (subduction zone volcanoes, also called continental margin volcanoes) plates cause volcanism. Also shown are hot-spot volcanoes, which are caused not by plate movement but by hot material rising directly from the outer Earth's core. Reproduced from Francis and Oppenheimer (2004) with kind permission of Oxford University Press.

2.1 Volcanism

Volcanoes are the manifestation of large amounts of thermal energy inside Earth. A simplified depiction of the structure of Earth can be seen in Figure 2.1. Heat from the earth's core is to a large extent caused by decay of long-lived radioactive isotopes but also remaining from potential energy released by an increasing gravitational pressure during the formation of Earth. A small part might be caused by the impact of cosmic matter that collided with the Earth over the 4.5 billion years since the Earth's formation. A fraction the kinetic energy from these impacts is still stored in the core to this day (Francis and Oppenheimer, 2004).

The transfer of heat from the Earth's core towards the surface can occur in different ways: conduction (which is not of importance in the context of volcanology), convection or mantle plume volcanism. Convection in the lower and upper mantle leads to movement of the oceanic and continental plates (also called lithosphere). At the margins of the lithospheric plates, increased volcanic activity occurs. In the case of constructive margins (i.e., new crust is formed) this

phenomenon is called mid-ocean ridge volcanism for oceanic plates or continental rift zone volcanism for continental plates. In the case of destructive plate margins (i.e., the plate or slab sinks back into the mantle region) it is called subduction zone volcanism. A third, but less frequent, path of heat transfer results from basaltic magmas that rise through a plume to the surface. This process leads to volcanism further away from plate margins, so called hot-spot volcanoes (e.g. the Hawaiian islands or Iceland).

The geological setting influences the magma composition and gas content and therefore the shape and eruption style of a volcano. The evolution of magma from the point at which the rock melts to the time of an eruption influences the composition of the magma and - the most important aspect for this work - also the composition of gases released from volcanoes.

The processes involved in the formation of mid-ocean ridge volcanoes, subduction zone volcanoes and hot-spot volcanoes are shown in Figure 2.1 and briefly summarised below:

- Mid-ocean ridge volcanism occurs when two oceanic plates are pulled apart, e.g. by the sides of a plate that sinks under another plate (see below, subduction zone volcanoes). The spreading of the plates leads to a thinned oceanic lithosphere. As a result of the thinner lithosphere, material from the upper mantle that is solid at depths lower than 100 km ascends to shallower depths of approximately 50 km. At this depth, the pressure is low enough for the mantle material to start melting. This type of volcanism leads to basaltic magma (low SiO_2 content, relatively few volatiles and low viscosity) that rises further and replenishes the gap between the two plates.

- Continental rift zone volcanism is in a way similar to mid-ocean ridge volcanism. The process leading to volcanism in this case is a continental plate that splits into two diverging plates. One important example of continental rift zone volcanism is the Nyriagongo volcano in the Democratic Republic of Congo.

- Subduction zone volcanoes are caused by an oceanic plate converging under another oceanic or continental plate. This type of volcanism is, for example responsible for the Andes. Two of the volcanoes that were examined during this thesis, Popocatépetl in Mexico and Nevado del Ruiz in Colombia, are subduction zone volcanoes. The descending plate is dense enough to sink back into the lower mantle and contains many water-rich minerals and sediments. During the descent the temperature of the plate increases due to an uptake of heat from the surrounding warmer mantle material and frictional heating. At a depth of several hundred kilometres, the plate will reach a temperature at which it starts melting and consolidates with the mantle again. Beginning at an earlier stage of approximately 80 – 150 km, water from the water-rich descending plate evaporates and rises into

the mantle above. The increase in water content in the mantle material above the descending slab causes it to melt. The result of the melting process is water-rich magma with more volatiles than magma from mid-ocean ridge volcanoes. Most of the magma at subduction zone volcanoes consists mainly of andesite, but since it can consist of melt from various parts of the earth (subducting plate, the upper mantle and continental lithosphere) basaltic, dacite and rhyolite magmas can be found as well. The low viscosity magma at subduction zone volcanoes is one of the causes for the violent eruptions.

- Hot-spot volcanoes can occur in the middle of oceanic or continental plates. They are a rare manifestation (only 5% of the world's volcanoes) but include such important volcanoes as the Hawaiian islands, Yellowstone or Iceland. This type of volcano emerges when a hot spot at the core-mantle boundary inside Earth leads to a plume in the mantle, a pathway in which solid material rises. When the solid material reaches approximately 100 – 150 km depth it partially starts to melt and creates basaltic magma. During the further ascent the magma can interact with, e.g. continental crust, which in turn leads to rhyolitic, more-viscous magma. In some cases the solid material from the lower mantle consists of recycled lithospheric plates, which leads to a more complex magma.

After magma is formed from molten rock, it can ascend further depending on its buoyancy. At some depth the concentration of dissolved volatiles exceed the solubility in the magma and a gas phase is formed. This might lead to degassing from the volcano.

2.2 Volcanic degassing

Volcanoes emit large quantities of various gases during eruptions but also during phases characterized by quiescent degassing. Emissions of volcanic gases into the atmosphere can influence the climate and serve as a precursor of volcanic activity. Even more, in most cases the exsolution of volatiles from the magma is the driving force behind the volcanic eruption. This demonstrates the importance of studying volcanic gas emissions.

When measuring volcanic gas emissions it is crucial to understand the origin of the gas in order to find meaningful interpretations of the results. It is necessary to understand how gases are exsolved from the magma, how they are transported to the surface and which interactions during gas ascent can alter the gas composition. A simple model based on Henry's law can be used to explain degassing of volatiles from magma and the variability in the gas composition. Henry's law describes which equilibrium concentration c of a gas can be dissolved in a liquid with a Henry's constant k at a gas pressure p:

$$c = k \cdot p \tag{2.1}$$

In this model the melt starts at depth in a single liquid phase. As the magma rises the pressures decreases while c stays constant. When a volatile reaches saturation (i.e. $c > k \cdot p$) a second gas phase forms in addition to the liquid melt. This process is referred to as first boiling. The Henry's constant and thus the solubility of a volatile in the melt depend on the system's temperature as well as on the chemical composition of the liquid and the volatile. Another process called second boiling is caused by crystallization in magma that cools down. As most crystals contain almost no volatiles, the crystallization process leads to an increased concentration of volatiles in the melt, and can lead to degassing without changes of the system's pressure.

This model can help explain the importance of measuring the ratio between different trace gases. Figure 2.2 shows an example of degassing due to Henry's law. Figure 2.2 (a) shows the vesicularity[1] of a melt as a function of depth. The vesicularity is shown for different starting concentrations of CO_2 and for three values of the CO_2/H_2O ratio. Higher CO_2 concentrations lead to exsolution of gas at greater depth, as does a higher CO_2/H_2O ratio. A magma with a start concentration of 1000 mg CO_2 per kg melt and a CO_2/H_2O ratio of 5 has a vesicularity of 50% at a depth of approximately 300 m. At this depth practically all CO_2 and 70% of the H_2O are exsolved from the magma but only 20% of the SO_2 and almost none of the HCl are exsolved. When ascending further the degassing of HCl will start at a depth of 100 m while at this depth most of the H_2O has already exsolved. The composition of gases can therefore evolve, and in this example the SO_2/HCl ratio would decrease during magma ascent. Using

[1] The vesicularity V is related to the gas/melt volume ratio R by $V = 100 \cdot R/(1 + R)$.

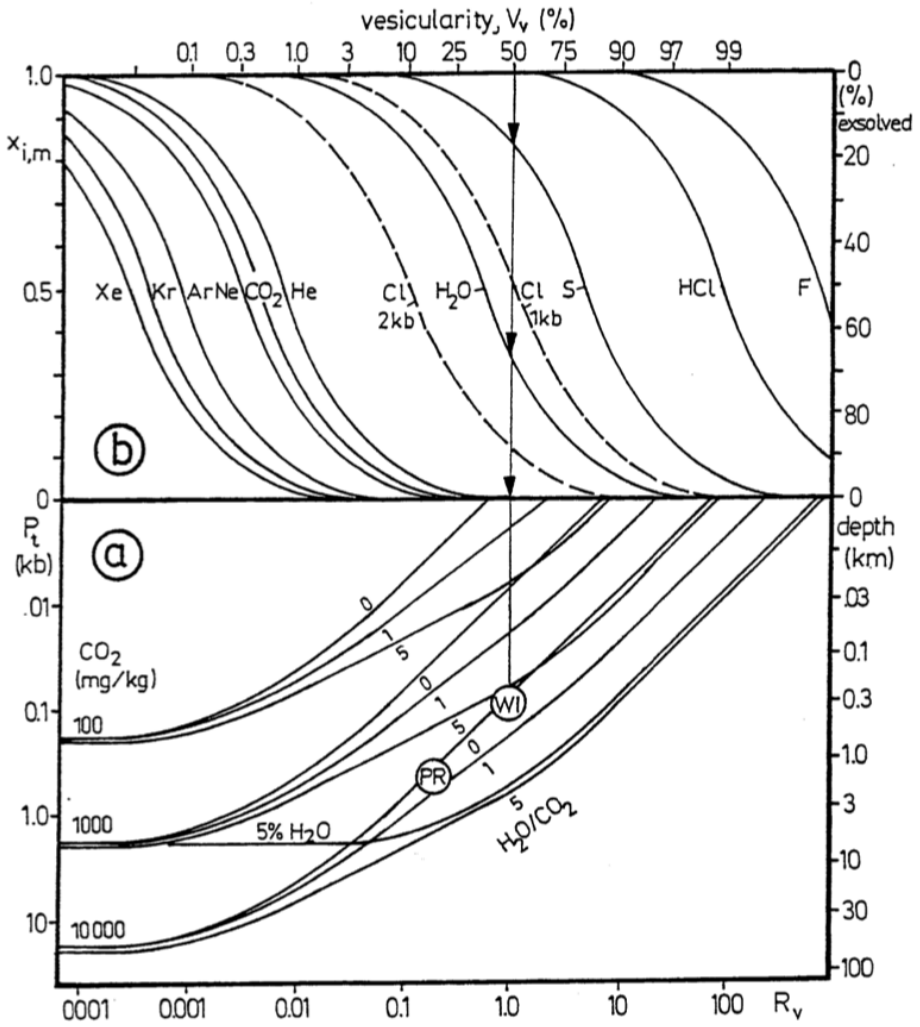

Figure 2.2.: Solubility of different volatiles in magma. The bottom plot shows the vesicularity of a melt in dependence of depth (or pressure P_t). Vesicularity is shown for different CO_2 concentrations and for three H_2O/CO_2 ratios. The upper plot shows how much gas is exsolved from the melt depending on the vesicularity. In this example, a melt with 1000 mg/kg CO_2 and a H_2O/CO_2 ratio of 5 leads to a vesicularity of approximately 50 % at a depth of 400 meters. At this depth, practically all CO_2 and 70% of the H_2O are exsolved from the melt, but only 20% of the sulphur and almost no HCl. As the magma rises further, it becomes depleted in H_2O and the HCl/sulphur ratio increases. Reproduced from Giggenbach (1996) with kind permission from Springer Science and Business Media.

this model gas compositions can give insights into processes at depth and the equilibrium temperatures at which the gas phase was formed as long as the gas phase remains unchanged during ascent (Edmonds, 2008).

In reality, however, exsolved gas bubbles need to rise to the surface to be observed. The rise of gas to the surface can alter the chemical composition and lead to patterns in the observed gas emission rates. While the mechanisms and how they can lead to degassing patterns will be described below, it is first necessary to address how the rise of gas can lead to variations in the chemical composition: Temperature changes of the ascending gas can lead to a re-equilibration (i.e., SO_2 reacts to H_2S at decreasing temperatures) and gases can also interact with crustal rock or groundwater during ascending. According to Giggenbach (1996) the composition of gases due to processes at depth does not vary during "conventional observational periods". The author claims that most variations observed are not caused by variations of the magma at depth but due to processes during the ascent of the gases. However, these processes and therefore also the gas composition might still vary with volcanic activity.

After gas bubbles are formed they need to ascend for degassing at the surface to occur. Two different models are frequently used to describe the behaviour of gas bubbles after their formation: the rise speed dependent (RSD) model and the collapsing foam (CF) model (Parfitt, 2004). In the RSD model bubbles form during magma ascent. As gas bubbles always have a lower density than the magma they are buoyant. Depending on the magma rise speed and the viscosity of the magma, the RSD model can explain two mechanisms for degassing.

In a low-viscosity magma that ascends with a low velocity, the gas phase can form bubbles that can rise to the surface separately from the magma. This is called open-system degassing. During their ascent gas bubbles can also coalesce and form larger bubbles that rise faster. If the gas phase can leave the magma, the viscosity of the magma decreases, which in turn slows down the ascent.

In magmas with higher viscosity and a relatively high rise speed the bubbles might not be able to coalesce but grow by diffusion and decompression. Gas bubbles cannot separate from the magma, but ascend together with the magma until it is erupted. This process is called closed-system degassing. The formation of a gas phase that rises together with the magma decreases the magmas density and can thus be a trigger for a faster magma ascent.

The RSD model can be used to explain periodicities in volcanic activity. A simple model with a one-dimensional volcanic conduit containing rising magma is explained in Sparks (2003a,b). In this system the magma can obtain the two different steady states described above, which can be summarized as:

- Slow-ascending magma, in which bubbles can coalesce and leave the magma and the viscosity increases.
- Fast-ascending magma, in which bubbles form but cannot coalesce and rise with together the magma. This leads to lower-density magma which accelerates even more.

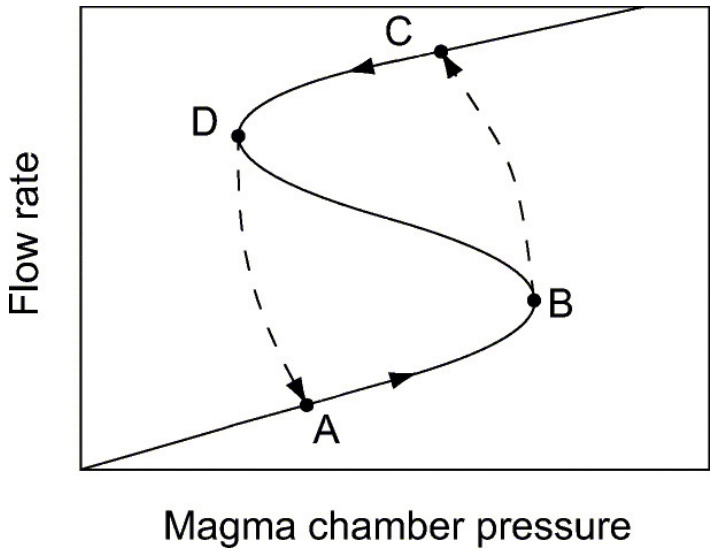

Figure 2.3.: Degassing as a periodical process. The lower branch (A-B) shows open-system degassing, where gas can escape the magma. With increasing pressure at point B, the system jumps to the upper steady state at C, where close-system degassing leads to explosive behaviour. Reproduced from Sparks (2003a) with permission from Elsevier.

Figure 2.3 shows the magma flow rate as a function of magma chamber pressure. Between A and B we have the steady state where gas can leave the magma (open-system degassing). If the pressure in the conduit increases further, caused by material originating from the magma chamber the flow rate increases. At point B, the magma rises too fast for bubbles to coalesce and the system jumps directly to state C (there is no steady solution between B and D). In this regime the magma rises too fast for bubbles to escape. The gas phase leads to a lower density and this further accelerates the magma, which leads to an eruption of the system. In the eruptive state between point C and D material is transported out of the conduit faster than it is replenished from the magma chamber and the systems pressure decreases. The decreasing pressure and flow rate lead to point D. At point D the magma chamber pressure is too low to keep up the explosive regime, and with a further decreasing magma chamber pressure the system drops back to open-system degassing at point A.

In the CF model magma is stored in a magma chamber or a dyke system at some depth (Parfitt, 2004). Bubbles form and rise to the top of the reservoir where they form a closely packed gas foam layer. Once the foam reaches a critical thickness, it collapses and forms a large gas bubble that rises up to the surface driving the volcanic eruption (Vergniolle, 1996). Depending on the viscosity of the magma either an annular flow (low viscosity) or a periodic series of gas slugs resulting from partial collapse of the foam (high viscosity) can be observed. The CF model can also explain periodicities in degassing patterns by the time needed to rebuild the foam layer to a critical thickness after its collapse.

Magma does not necessarily need to erupt for degassing to occur. Degassed

magma is more dense than volatile rich magma, and convection can lead to degassing, where the degassed magma sinks back into the magma chamber. This process can lead to substantial amounts of degassing without any erupted magma (Kazahaya et al., 1994; Stevenson and Blake, 1998). It is also often the case that more gas is released during an eruption than can be dissolved in the magma that was erupted. For example, during the 1982 eruption of El Chicón, Mexico, 40 times more gas was measured than was estimated from the erupted magma with petrological methods (Shinohara, 2008).

2.3 Volcanic gases in the atmosphere

Volcanoes emit large amounts of gases into the atmosphere. In descending magnitude the most important gases are H_2O, CO_2, various sulphur species led by SO_2 and H_2S and halogen compounds (see Table 2.1). While water vapour is the most abundant gas in a volcanic plume, and responsible for the condensation of the plume that can be observed at many quietly degassing volcanoes from large distances, the total abundance is negligible when compared to evaporation from oceans. CO_2 emissions are thought to have played an important role during the formation of Earth's atmosphere. However, today CO_2 emission from volcanoes are several orders of magnitude smaller than anthropogenic CO_2 emissions. While anthropogenic CO_2 emissions were roughly 35 Gt (gigatons) in 2010, volcanic CO_2 emission estimates ranged between 0.13 - 0.44 Gt per year, comparable to the CO_2 emissions from countries as Pakistan (0.18 Gt), Kazakhstan (0.25 Gt) or South Africa (0.44 Gt) (Gerlach, 2011, and references therein). However, on time scales of 10^5 a CO_2 degassing has an important role in the Earth system, since it offsets CO_2 burial in the sediments. SO_2 is the third most abundant gas and can be measured by remote sensing in the UV. It is therefore often measured as a proxy for volcanic activity. The yearly global SO_2 emissions by volcanoes range between 7.5 - 10.5 $TgSyr^{-1}$ (Halmer et al., 2002) and are therefore of the same magnitude as anthropogenic SO_2 emissions (55 $TgSyr^{-1}$ for the year 2000 were given in IPCC, 2013).

SO_2 and BrO are the two trace gases in volcanic plumes that are the main topic of this thesis. This chapter therefore gives a brief overview over the chemistry of SO_2 and BrO in the atmosphere after emission from the volcanic vent. The impacts of volcanic gas emissions on the environment and especially the influence of SO_2 on the Earth's climate will be discussed following Robock (2000). The part about SO_2 summarizes parts of the review paper by Oppenheimer et al. (2011) and the chemistry of BrO is based on the papers of Bobrowski et al. (2007) and von Glasow (2010). Both parts also contain ideas from von Glasow et al. (2009).

Species	H_2O	CO_2	SO_2	H_2S	COS	CS_2	HCl	HBr	HF
% /vol	50	1	1	1	10^{-4}	10^{-4}	1		$<$
	-	-	-	-	-	-	-	?	10^{-3}
	90	40	25	10	10^{-2}	10^{-2}	10		
Tg/year			1.5	1	0.006	0.007	0.4	0.0078	0.06
	?	75	-	-	-	-	-	-	-
		-	50	2.8	0.1	0.096	11	0.1	6

Table 2.1.: Compounds of degassing volcanoes at the emission vent and their estimated global source strengths. Adapted from Textor et al. (2004)

2.3.1 Sulphur species

Sulphur species, mainly SO_2 and H_2S are the third most abundant species in volcanic plumes after H_2O and CO_2. SO_2 contributes up to 25 % of the total volume of the volcanic plume and H_2S ranges between 1 - 10 % (see Table 2.1). As opposed to the two most dominant species, SO_2 does not have considerable background levels in the atmosphere. The SO_2 concentration in the atmosphere is usually below 1 ppb while the concentration in a volcanic plume can easily achieve levels of 1 ppm (Oppenheimer, 2003a). The low background values together with the stability and the relatively strong UV absorption make SO_2 an easily accessible tracer for volcanic gas emissions (see next Section 2.4).

After their release from the reducing conditions in the volcanic vent the gases enter the atmosphere, which is an oxidising environment. H_2S is slowly oxidized to SO_2 when released into the atmosphere. The first step is the reaction of SH with OH:[2]

$$H_2S + OH \xrightarrow[k=4.7\times10^{-12}]{} H_2O + SH \qquad (C\,2.1)$$

The SH radical then undergoes a series of reactions in the atmosphere that lead to the formation of SO_2 (Seinfeld and Pandis, 2006). Theoretically H_2S can react with the halogen radicals Cl and Br to form SH, which results in H_2S lifetimes of only a few seconds (Aiuppa et al., 2007). However, Aiuppa et al. (2007) could not reproduce these low H_2S lifetimes in measurements that showed a constant SO_2/H_2S ratio at distances up to several kilometres from the vent.

SO_2 is removed from the atmosphere by wet and dry deposition or oxidized to sulphuric acid. In the gaseous phase the reaction with OH to sulphuric acid is rather slow:

$$SO_2 + OH \xrightarrow[k=1.3\times10^{-12}]{M} HSO_3 \qquad (C\,2.2)$$

$$HSO_3 + O_2 \xrightarrow[k=4.3\times10^{-13}]{} HO_2 + SO_3 \qquad (C\,2.3)$$

$$SO_3 + H_2O \xrightarrow[k=5.7\times10^{4}\,s^{-1}]{M} H_2SO_4 \qquad (C\,2.4)$$

The rate constant k in Eq. C 2.4 is given for 50% humidity in Atkinson et al. (2004). Möller (1980) calculated an SO_2 loss rate of $k = 1.2 \cdot 10^{-6}\,s^{-1}$ for homogeneous reactions in the gas phase, or converted to hours a loss of 0.43% SO_2 per hour. In heterogeneous reactions, such as reactions of SO_2 on particles or in the liquid phase of particles, the oxidation process is much faster. Möller (1980) gave loss rates of $k = 0.1$ - $1 \cdot 10^{-5}\,s^{-1}$ for reactions of SO_2 on aerosol particles and $k = 5 \cdot 10^{-5}\,s^{-1}$ for liquid phase oxidation. The equations for the

[2] If not otherwise stated, second order rate constants are taken from Atkinson et al. (2004) and given in units of $cm^3\,molecules^{-1}\,s^{-1}$.

reaction of SO_2 in the liquid phase are (Möller, 1980):

$$SO_{2,g} + H_2O_{aq} \rightleftharpoons (SO_2 \cdot H_2O)_{aq} \quad \text{(C 2.5)}$$

$$(SO_2 \cdot H_2O)_{aq} + H_2O \rightleftharpoons HSO^-_{3,aq} + H_3O^+_{aq} \quad \text{(C 2.6)}$$

$$HSO^-_3 + H_2O \rightleftharpoons SO^{2-}_3 + H_3O^+ \quad \text{(C 2.7)}$$

HSO^-_3 and SO^{2-}_3 can be further oxidized to sulphuric acid or sulphate, e.g. by a reaction with OH (Platt and Stutz, 2008). The oxidation of SO_2 can also take place on aerosol particles by reactions with O_3, H_2O_2, HOCl, HOBr or oxygen if catalysts (iron, manganes) are available (von Glasow et al., 2009).

Considering these different pathways and regarding the importance of SO_2 as a tracer for volcanic activity and for the comparison of SO_2 with other trace gases, it is worthwhile to compare measured SO_2 loss rates with the values given above. There are only a few reports of high SO_2 loss rates. Jaeschke et al. (1982) and Oppenheimer et al. (1998) reported loss rates between $1 \cdot 10^{-3}\,s^{-1}$ and $7 \cdot 10^{-4}\,s^{-1}$, which would lead to an e-folding time between only 16 and 23 minutes. However, older data listed in Oppenheimer et al. (1998) showed loss rates between $5 \cdot 10^{-5}\,s^{-1}$ and $2 \cdot 10^{-7}\,s^{-1}$, therefore leading to e-folding times between 5 hours and several weeks. McGonigle et al. (2004) studied the depletion rate of SO_2 using the DOAS technique at Masaya volcano, Nicaragua. The authors found that there are negligible variations of up to 500 s - 2000 s after release from the volcano. Furthermore, the authors argue that Jaeschke et al. (1982) had problems with using CO_2 as a tracer to compare the SO_2 concentration. Meanwhile Oppenheimer et al. (1998) based the calculated loss rates on only a few traverse measurements, thus being influenced by variations in the total emission rate from the volcano as well as errors from wind speed and direction. Oppenheimer et al. (1998) measured ash plumes during the wet season at Soufriere Hills, Montserrat. Repeated measurements at the same volcano with more traverses during the dry season and ash-free volcanic plumes, found an one order of magnitude slower SO_2 loss rate (Rodríguez et al., 2008). Recent studies from satellites by Beirle et al. (2013) investigated the SO_2 loss rates at Kilauea, Hawaii. The authors found mean monthly SO_2 life times between 16 and 57 h, with the longer lifetimes in summer, when the cloud coverage is lower. While satellites are not able to assess potential SO_2 loss close to the volcanic vent due to restrictions of their spatial and time resolution, this study still shows slow SO_2 loss rates with robust observations over a long time-scale.

In this work it is assumed that SO_2 is stable during the time frame that usually occurs during ground-based remote sensing measurements (a few up to several tens of minutes during this thesis).

Environmental impacts of SO_2

Regardless of the path of SO_2 scavenging, dry or wet deposition or oxidation to sulfuric acid, the molecule can influence the environment in several ways. A local effect, especially compared to the influences on the Earth's climate, are direct influences of SO_2 on humans (respiratory problems, asthma) and plants in the areas affected by volcanic gases. Acid rain caused by volcanic plumes can prevent the growth of plants. Darrall (1989) reviewed the influences of SO_2 on photosynthesis, and found that long-term exposures with SO_2 concentrations between 100 - 250 ppb can inhibit photosynthesis of plants. Delmelle et al. (2002) measured SO_2 concentrations around Masaya volcano, Nicaragua. The authors found concentrations of up to 230 ppb and an area downwind of the volcano with a decreased number of plant communities. Similar studies were done by Longo et al. (2005), who studied SO_2 concentrations and fine aerosol downwind of Kilauea volcano on Hawaii. The authors found high SO_2 concentrations of over 61.9 ppb with atmospheric sampling in the Kau desert south of Kilauea crater. Despite these lower SO_2 concentrations, plant growth is largely diminished in the Kau desert. Fig. 2.4 gives an impression of plants in the Kau desert. It should be noted, though, that while SO_2 certainly has negative effects on plant life other species in the volcanic plume (e.g., HF) are most likely deposited within close proximity of SO_2 on the ground as well.

Figure 2.4.: Picture taken in the Kau desert in Hawaii. Despite moderate precipitation, this area features hardly any vegetative life.

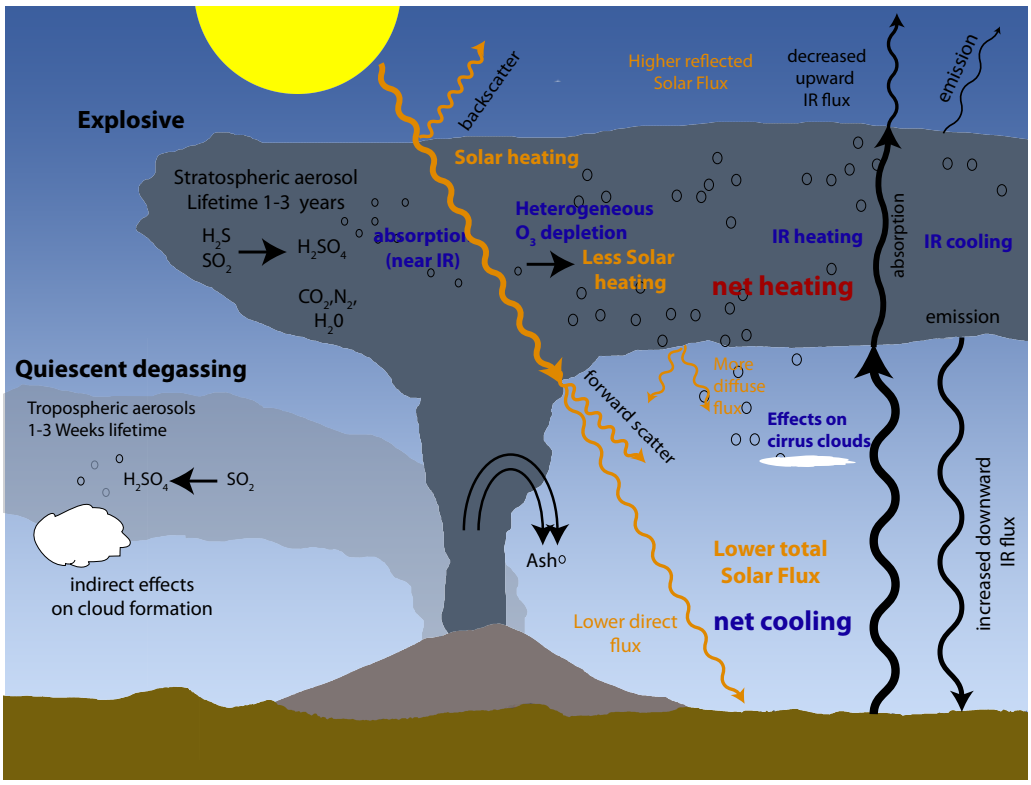

Figure 2.5.: The influences of eruptive and quiescent volcanic degassing on the Earth's climate. Redrawn on the basis of Robock (2000).

Sulphur influences on the Earth's climate

On a global scale, SO_2 and especially its oxidation product sulphuric acid have a large impact on Earth's climate. The total annual SO_2 emissions are low compared with anthropogenic emissions. Halmer et al. (2002) estimated mean annual S emitted as SO_2 by volcanoes between 1972 and 2000 to be in the range between 7.5 - 10.5 $TgSyr^{-1}$. The estimates for anthropogenic SO_2 emissions for the year 2000 have a mean value of 55 $TgSyr^{-1}$ (IPCC, 2013). However, Graf et al. (1997) suggested that the impact of volcanic SO_2 emissions is higher, since they are released into the free troposphere or into the stratosphere during eruptions, whereas most anthropogenic emissions are released into the planetary boundary layer. After emission into the atmosphere SO_2, is oxidised to sulphuric acid. The lifetime of sulphuric acid in the troposphere is only about 1 week compared with up to one year in the stratosphere (IPCC, 2013).

Sulphuric acid directly influences the climate by backscattering radiation from the sun and thus increasing the Earth's albedo. Even more importantly it serves as additional cloud-condensation nuclei (CCN), which results in more and finer condensed particles and therefore in whiter, more-stable clouds and also an increased albedo of Earth (Twomey, 1974, and Fig. 2.5). This leads to more back-scattered radiation (see Fig. 2.5) and more diffusively scattered

radiation. The net result of the back-scattered radiation is cooling of the Earth atmosphere, which is the dominating radiative effect of volcanic gases (Robock, 2000). Additionally, aerosol particles can also act as surfaces for heterogeneous reaction cycles that destroy ozone, especially in the stratosphere, which leads to an increased solar flux to the Earth. Larger aerosol particles can backscatter IR radiation emitted from the Earth's surface and the lower atmosphere and thus slightly reduce the net cooling effect in the lower troposphere. Absorption of direct UV and IR radiation from the sun as well as of radiation emitted by the Earth leads to net heating of the stratosphere. The 2013 IPCC report (IPCC, 2013) states that the radiative forcing caused by volcanoes was $-0.11\ \mathrm{Wm}^{-2}$ between the years 2008 and 2011 (for comparison, the radiative forcing of CO_2 was given as $1.68\,\mathrm{Wm}^{-2}$). Another, counter-intuitive effect is the winter warming in the Northern Hemisphere, which is caused by changes of the stratospheric and tropospheric circulation patterns due to strong temperature gradients between the Arctic and equatorial regions (Robock, 2000).

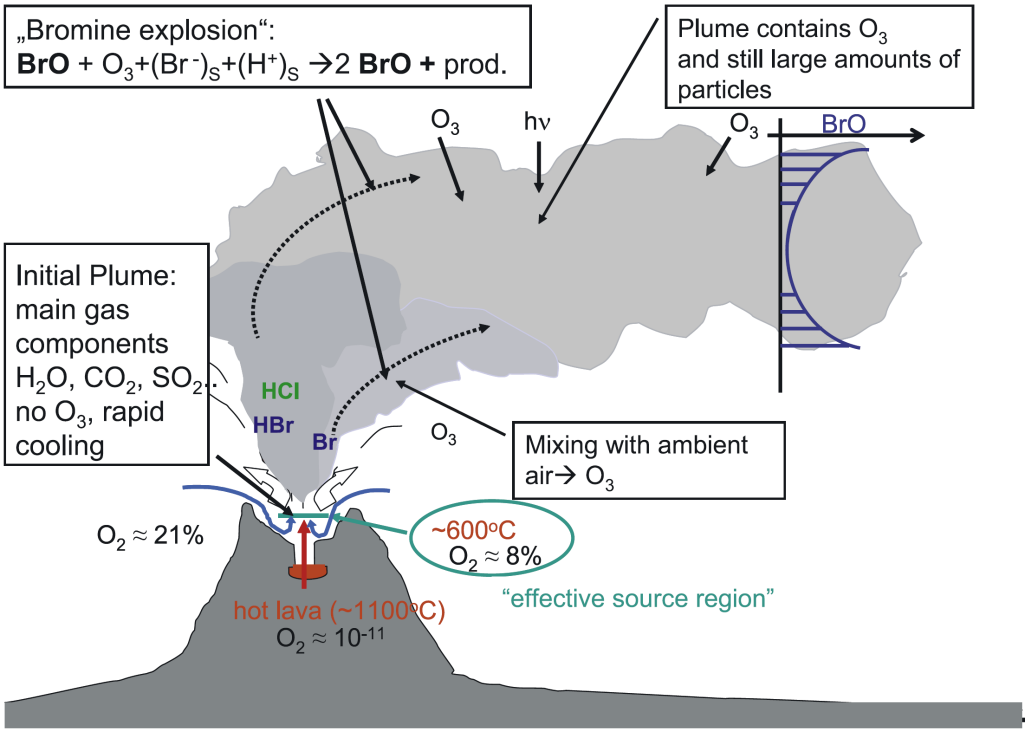

Figure 2.6.: Sketch of the Bromine Explosion. Volcanic gases mix in an effective source region with ambient air at high temperatures. The resulting Bromine species react to BrO while removing ozone from the plume. Reproduced from Bobrowski et al. (2007) with permission of John Wiley and Sons.

2.3.2 Bromine oxide

Bromine oxide (BrO) was detected for the first time at Soufriere Hills volcano (Montserrat) by Bobrowski et al. (2003). Since then, BrO has been detected at many volcanoes by ground-based measurements (e.g., Bobrowski and Platt, 2007; Bobrowski et al., 2007; Oppenheimer et al., 2006; Vogel, 2011) or from airborne platforms (Heue et al., 2011; Kelly et al., 2013). Theys et al. (2009) were able to detect BrO from satellite after the Kasatochi eruption in 2008, and Hörmann et al. (2013) were able to find BrO in volcanic plumes from 11 erupting volcanoes with data from the GOME-2 instrument.

However, it is actually mainly HBr, not BrO, that is emitted from volcanoes. BrO is formed after the volcanic gas mixes with ozone-rich ambient air. Gerlach (2004) and Martin et al. (2006) used thermodynamical equilibrium calculations to assess the source of bromine and found that there is not enough Br or BrO in hot magmatic gases to explain the BrO concentration measured, e.g. at Soufriere Hills by Bobrowski and Platt (2007). Instead, the volcanic gases mix with atmospheric air at high temperatures, in the so-called *effective source region* (Bobrowski et al., 2007), see Figure 2.6. This can be compared to a chimney, where hot air released from the volcano pulls in atmospheric air through the

permeable edifice (Gerlach, 2004). The mixing process at high temperatures ($\approx 600-1200°C$) changes the gas composition and leads to an increase in bromine species other than HBr such as Br, Br_2 and BrO (Martin et al., 2006; von Glasow, 2010). Further mixing with atmospheric air leads to cooling down to ambient temperatures where the so-called *Bromine Explosion* starts. The term Bromine Explosion originates from BrO observations in polar regions, where a similar non-linear increase in BrO concentration has been observed (Hönninger and Platt, 2002; Lehrer et al., 1997; Wennberg, 1999).

The Bromine Explosion mechanism can be summarized as:

$$HBr_{gas} \longrightarrow Br^-_{aq} + H^+_{aq} \quad \text{(C 2.8)}$$

$$HOBr_{(gas)} \longrightarrow HOBr_{(aq)} \quad \text{(C 2.9)}$$

$$HOBr_{(aq)} + Br^-_{(aq)} + H^+_{(aq)} \longrightarrow Br_{2(aq)} + H_2O \quad \text{(C 2.10)}$$

$$Br_{2,aq} \longrightarrow Br_{2,gas} \quad \text{(C 2.11)}$$

$$Br_2 + h\nu \longrightarrow 2\,Br \quad \text{(C 2.12)}$$

$$Br + O_3 \longrightarrow BrO + O_2 \quad \text{(C 2.13)}$$

$$BrO + HO_2 \longrightarrow HOBr + O_2 \quad \text{(C 2.14)}$$

$$BrO + BrO \longrightarrow 2\,Br + O_2 \quad \text{(C 2.15)}$$

$$BrO + BrO \longrightarrow Br_2 + O_2 \quad \text{(C 2.16)}$$

C 2.8 and C 2.9 describe the uptake of HBr and HOBr on the surface of an aerosol particle and subsequent transformation into the liquid phase. At low pH < 6.5 (Fickert et al., 1999) or at cold temperatures H^+, Br^- and HOBr react to form Br_2 (C 2.10) that is then released back into the gas phase (C 2.11). Br_2 reacts to Br via photolysis if sunlight is available (C 2.12). The necessity of solar radiation for the Bromine Explosion in volcanic plumes was verified by Kern et al. (2009), who could measure elevated BrO during daytime, but not at night at Masaya volcano, Nicaragua. In the next step Br that was formed from Br_2 and O_3 reacts to BrO (C 2.13). The role of O_3 in Eq. C 2.13 was shown by Bobrowski et al. (2007) and Louban et al. (2009) who measured higher BrO/SO_2 ratios at the edges of the volcanic plume rather than in the middle of the plume, where less ambient (ozone-rich) air is available. Kelly et al. (2013) was able to measure the evolution of ozone depletion in volcanic plumes from an airborne platform. BrO can react with HO_2 to form HOBr again leading back from C 2.15 to C 2.9. The result of this reaction cycle is the formation of BrO and the destruction of O_3. BrO can also react with another BrO molecule to form Br_2 or Br (C. 2.15 and 2.16), which in turn would react again to BrO. The Bromine Explosion reaction cycle is schematically shown in Figure 2.7.

Considering the multitude of chemical reactions that take part in the formation of BrO and because BrO is a secondary volcanic gas, there is some discussion as to whether BrO/SO_2 ratio can be a useful indicator of volcano activity. If BrO/SO_2

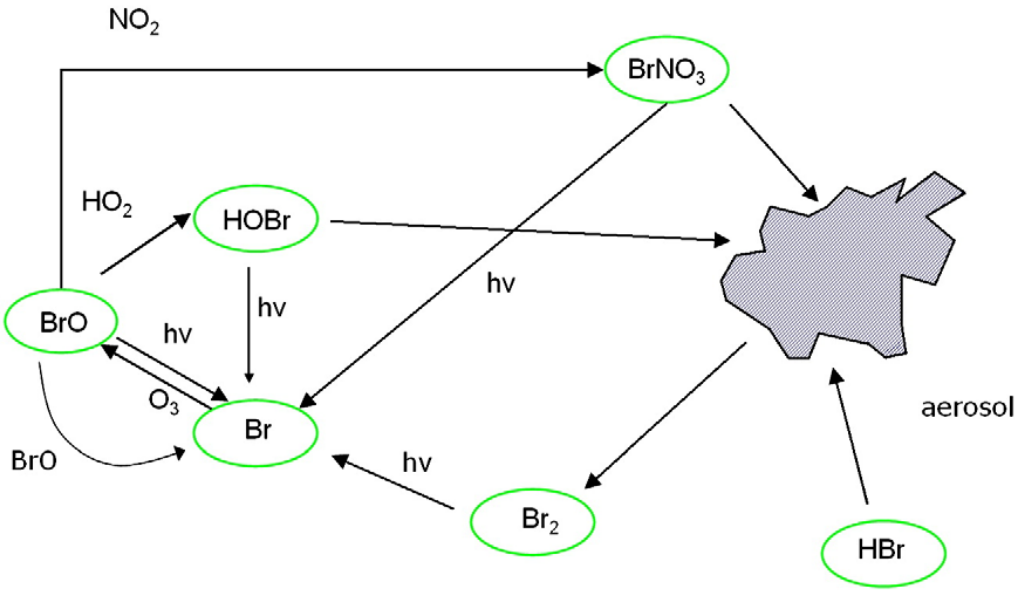

Figure 2.7.: Scheme of the chemical reactions that are part of the BrO explosion. The reaction cycle with NO_2 is not discussed in the text. Reprinted from von Glasow et al. (2009) with permission from Elsevier.

ratios are used as an indicator of volcanic activity, influences from the formation of BrO in the atmosphere have to be ruled out or characterized carefully. SO_2 can be regarded as stable during times that are typically observed in ground-based remote sensing observations (see above). Perspectives on the time scales of BrO formation have changed over the last couple of years. Bobrowski et al. (2007) and Roberts et al. (2009) estimated an increase in the BrO/SO_2 ratio up to several tens of minutes after release from the vent. Newer publications and an improving dataset led Bobrowski and Giuffrida (2012) to the conclusion that the BrO/SO_2 ratio increases in the first minutes after release from the volcano, and then stays constant for some time (see Figure 2.8). Vogel (2011) and Gliß (2013) were able to measure the evolution of the BrO/SO_2 ratio in the young plume of Pacaya volcano and Etna volcano respectively using horizontal DOAS scanning measurements and found a strong increase within the first five minutes after release. Vogel (2011) also measured the BrO/SO_2 ratios in ageing plumes at Mt. Etna and found a constant ratio for plume ages of up to two hours. It has not been sufficiently examined if the BrO/SO_2 ratio depends on the ratio of Br/S exsolved from the magma. Nevertheless, it is import to rule out influences of atmospheric chemistry in order to find a meaningful interpretation of BrO/SO_2 ratios. The influence of the time following the mixing of volcanic gas with the ambient atmosphere will be discussed in Chapter 5.

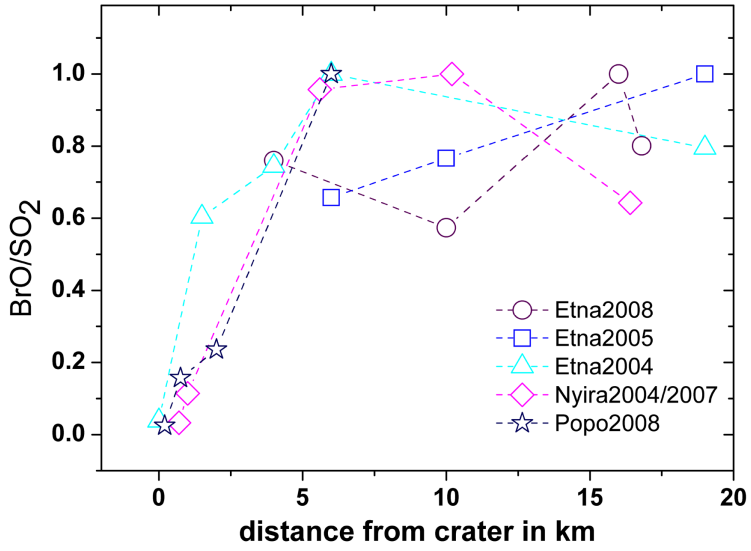

Figure 2.8.: BrO/SO_2 ratio as a function of distance from the volcanic vent (for a constant wind speed of 10 m/s). A strong increase can be observed for the first 5 km from the volcanic vent, afterwards the ratio is constant at least up to 20 km. Reproduced from Bobrowski and Giuffrida (2012)

2.4 Using volcanic gases to study volcanic activity

There are many factors influencing the degassing of volatiles and the composition of gases after and during the release from the volcanic vent. Furthermore the plume composition changes when it reacts with the oxidizing atmosphere. Therefore interpreting volcanic degassing data is complex. For example, Oppenheimer et al. (2011) reported in their review paper on SO_2 degassing, that decreasing SO_2 fluxes have been ascribed to:

- depletion of volatiles in a magma body
- decreased permeability of the magma in the conduit

The first process can be regarded as an indicator of decreasing volcanic activity. The second process can be caused by, for example, the formation of a plug when degassed magma starts crystallization. The plug leads to a build up of gas pressure and ultimately might lead to an eruption (Clarke, 2013). Therefore the observation of decreasing SO_2 emission rates can indicate an increase as well as a decrease of volcanic activity.

Despite these complications, measurements of volcanic gases can be an important additional tool for the forecasting of volcanic activity to accompany the classic monitoring techniques like seismicity or deformation measurements. The remote sensing of volcanic gases started with the correlation spectrometer COSPEC (Moffat and Millan, 1971; Stoiber et al., 1983) in the 1970 s. COSPEC

measurements together with fumarolic sampling helped, for instance, predict the eruptions of Mount St. Helens, USA, in August 1980 and June 1981 (Casadevall et al., 1983) or Pinatubo, Philippines, in 1991. The remote sensing of volcanic SO_2 experienced further spreading world-wide with the availability of miniature spectrometers (Galle et al., 2003) that measure the SO_2 column density by using Differential Optical Absorption Spectroscopy (DOAS, Platt and Stutz, 2008). Besides being smaller and cheaper, these miniature spectrometers using the DOAS technique have additional advantages for fieldwork in rugged environments, as they are lighter and consume less power. Additionally the availability of more spectral information allows for the correction of radiative transfer problems (Kern, 2009, and also Chapter 3) and to retrieve other trace gases (e.g. O_3, NO_2 or BrO). An important step towards continuous monitoring of volcanic SO_2 emission rates was made with the Network for Observation of Volcanic and Atmospheric Change (NOVAC, Galle et al., 2010). During this EU-funded project scanning DOAS instruments were installed at several volcanoes world-wide. The spectroscopic data for the BrO/SO_2 ratios evaluated within this thesis were recorded by the NOVAC network, which will be discussed in more detail in Chapter 5. Besides the monitoring instruments and the network itself, the detection of abnormally high SO_2 emission rates at Santa Ana volcano (El Salvador) before the eruption in 2005 was the first big success of the project (Olmos et al., 2007). These measurements helped to plan the evacuation of thousands of people living in the vicinity of Santa Ana volcano. Scanning DOAS instruments need approximately 5 – 15 minutes for one scan across the complete sky. These techniques are therefore rather suited to measure long-term variations in the SO_2 emission rates.

A lot of additional information can be gained when using instruments that allow emission rate measurements with a higher time resolution. Boichu et al. (2010) used two spectrometers with an optical system that led to a wide field-of-view covering the complete volcanic vent at Mount Erebus, Antartica. This set-up allowed SO_2 emission rate measurements with a time resolution of the order of 1 Hz. Frequency analysis of the data revealed patterns with periods between 11 and 24 minutes that allowed discussion of different models for the degassing at Mt. Erebus. The SO_2 camera, which is also used in large parts of this thesis, makes SO_2 emission rate measurements with a similar time resolution possible. Holland et al. (2011) used SO_2 camera measurements at Santiaguito, Guatemala to identify shear-fracturing as the main process leading to cyclic patterns of explosive eruptions rather than building of a viscous plug. Tamburello et al. (2013) applied SO_2 cameras at Etna, Italy, using a similar approach as Boichu et al. (2010), and suggested that periodic signals with periods between 40 – 250 s and 500 – 1200 s are caused by bursting of rising gas bubbles. First steps in the direction of the analysis of high time resolution SO_2 camera data are presented in Chapter 4 of this thesis.

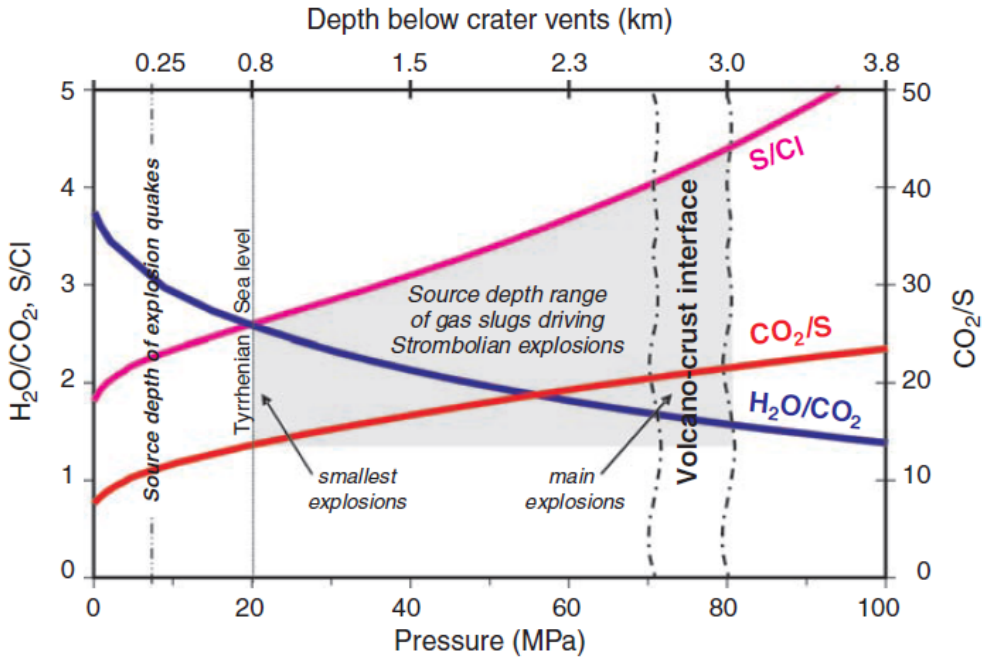

Figure 2.9.: Ratios of different volcanic gases and their evolution with depth at Stromboli Volcano, Italy. Reproduced from Burton et al. (2007). Reprinted with permission from AAAS.

In addition to the SO_2 emission rate, the ratio between different trace gases can be indicative of volcanic activity as well. The solubility of volatiles depends, e.g. on depth and chemical composition of the magma (see Chapter 2.1), therefore the composition of volcanic gases has been studied in depth. A good introduction to gas compositions and their interpretation can be found in Giggenbach (1996). A more recent review article about halogens in volcanic system was published by Aiuppa et al. (2009). Initial studies (e.g. Noguchi and Kamiya, 1963) investigated the Cl/S ratio by direct sampling. The authors found a decrease of the Cl/S ratio before an eruptive period (Noguchi and Kamiya, 1963; Stoiber and Rose, 1970). Later Pennisi and Le Cloarec (1998) found that Cl and F degas in a similar manner, while the Cl/S ratio varied between non-eruptive and eruptive periods. The authors argue that chlorine is exsolved from the magma at deeper levels (Cl/S > 1) while at shallower levels sulphur degassing dominates (Cl/S ≈ 0.1). Burton et al. (2007) measured volcanic gas composition (H_2O, CO_2, CO, SO_2 and HCl) by remote sensing using an open-path Fourier transform infrared spectrometer (OP-FTIR) at Stromboli, Italy. The authors found that the ratio of CO_2/SO_2 and SO_2/HCl were 3-5 times higher during explosions than during quiescent degassing. These observations paired with higher equilibrium temperatures lead the authors to the conclusion that the explosions are driven by gas slugs that originate from a deeper level than gas observed during quiescent periods. The authors then used melt inclusion data and a chemical model simulating degassing of magma to interpret the data. The S/Cl and H_2O/CO_2

ratios show that bigger explosions originate from a depth of approximately 2.7 – 3 km while smaller eruptions originate from depths as shallow as 0.8 km below the crater at sea level.

The BrO/SO_2 ratio has been measured using DOAS remote sensing measurements by several authors (e.g., Bobrowski and Platt, 2007; Bobrowski et al., 2003, 2007; Hörmann et al., 2013; Kelly et al., 2013; Oppenheimer et al., 2006; Theys et al., 2009; Vogel, 2011). However, despite naming the possibility to use BrO/SO_2 ratios as an additional tracer for volcanic activity, most of these studies focused on the formation of BrO in the atmosphere. First long-time measurements at Etna, Italy, were published by Bobrowski and Giuffrida (2012). The authors measured the BrO/SO_2 ratio covering the years 2005 - 2009 and found higher ratios during non-eruptive periods. During four eruptive periods BrO/SO_2 ratios were higher three months before the eruption compared to the ratios observed one month before the eruption. Studies on the seasonal variability and the influence of humidity did not reveal obvious correlations. The authors suggested a model in which bromine is released earlier than sulphur during the magma's ascent to explain the observed behaviour.

3

Remote sensing of volcanic gases

In this thesis, SO_2 and BrO in volcanic plumes are measured with two different remote sensing techniques, Differential Optical Absorption Spectroscopy (DOAS, Platt and Stutz, 2008) and SO_2 camera. Both techniques make it possible to measure volcanic gases by examining their interaction with radiation. This chapter will briefly describe absorption and scattering of radiation in the atmosphere in Section 3.1. The concepts of the two measurement techniques will be described in Sections 3.2 and 3.3. The chapter concludes with the effects of radiative transfer on remote sensing measurements in Section 3.4.

3.1 Absorption spectroscopy

3.1.1 Beer-Lambert Law

Atoms and molecules exist in several energy states with varying electron configuration. Molecules can additionally have different rotational and vibrational states. For simplicity, the basics of radiation transport in the atmosphere will be explained only for molecules in the following paragraphs.

If the energy of a photon matches the energy gap between two states of a molecule, the molecule can absorb the photon and enter the more energetic state. The transition can only occur if the lower energetic state is occupied and if the selection rules are fulfilled. The molecule can return to a lower state by collision with other molecules or emission of a photon. However, the direction of the emitted photon is usually not the direction of the incoming radiation. Therefore, the radiation intensity measured behind an absorbing medium (e.g. gases) decreases with increasing light-path through the medium.

This decrease is described by the Beer-Lambert law. For radiation of wave-

length λ and an initial intensity $I_0(\lambda)$ traversing a medium, the Beer-Lambert law gives the light intensity $I(\lambda)$ after passing through a path of length L,

$$I(\lambda, L) = I_0(\lambda) \cdot \exp\left(-\int_0^L \sigma(\lambda, p, T) \cdot c(l)\mathrm{d}l\right), \tag{3.1}$$

where $c(l)$ is the location-dependent concentration of the trace gas of interest and $\sigma(\lambda, p, T)$ is its absorption cross section. The absorption cross section is unique for each molecule and depends on pressure p as well as on temperature T.

The quantity measured with many optical remote sensing techniques is the optical density τ,

$$\tau = -\ln\left(\frac{I(\lambda)}{I_0(\lambda)}\right) = \sigma \cdot S, \tag{3.2}$$

where S is the column density, the concentration of the trace gas integrated along the light-path:

$$S = \int_0^L c(l)\mathrm{d}l \tag{3.3}$$

The concentration c for a constant trace gas distribution can be directly calculated from the column density S if the path length L is known.

For measurements in the atmosphere, the situation is more complex, with a multitude of different absorbers and scattering processes, such as Rayleigh scattering (see Section 3.1.2) and Mie scattering (see Section 3.1.2) that have to be taken into account. This is done by treating the scattering effects as pseudo-absorbers with their respective extinction coefficients ϵ_R for Rayleigh scattering and ϵ_M for Mie scattering. The extended Beer-Lambert Law reads:

$$I(\lambda, L) = I_0(\lambda) \cdot \exp\left(-\int_0^L \epsilon_R(\lambda, l) + \epsilon_M(\lambda, l) + \sum_j \sigma_j(\lambda, p, T) \cdot c_j(l)\mathrm{d}l\right) \tag{3.4}$$

This equation is valid for radiation traversing a medium of total length L, with several absorbing species j that can have variable concentrations c_j depending on the position l in the light path. The first two terms in the exponential function in Eq. 3.4 describe the extinction due to Rayleigh and Mie scattering in the atmosphere; the third term describes the absorption of various molecules. For simplicity, inelastic scattering and effects arising from turbulences in the atmosphere are neglected here. The most important effect of inelastic scattering, the Ring effect, will be described in Section 3.1.2 and 3.2.2.

3.1.2 Scattering processes in the atmosphere

Rayleigh scattering

Rayleigh scattering describes elastic scattering (the photon energy does not change) on particles much smaller than the wavelength of the incident radiation. It has a strong wavelength dependency, scattering at shorter wavelengths is stronger, which leads to the blue colour of the sky. Platt and Stutz (2008) gave a simplified estimate of the Rayleigh scattering cross section:

$$\sigma_R \approx \sigma_{R,0} \cdot \lambda^{-4} \text{ (with } \sigma_{R,0} \approx 4.4 \times 10^{-16} \text{cm}^2\text{nm}^4 \text{ for air)} \tag{3.5}$$

Rayleigh scattering is (as the name implies) a scattering and not an absorption process. However, in the narrow-beam approximation it can be treated as an absorption process. This approximation assumes that the probability of a photon that was scattered out of the light beam is scattered back into the light beam is negligible. The Rayleigh extinction coefficient ϵ_R for a number density of air molecules N_{air} is given by:

$$\epsilon_R(\lambda) = \sigma_R(\lambda) \cdot N_{air} \tag{3.6}$$

The angular distribution of Rayleigh-scattered photons is given by the Rayleigh phase function:

$$\Theta(\vartheta) = \frac{3}{4}(1 + \cos^2(\vartheta)) = \frac{I(\vartheta)}{I_0} \tag{3.7}$$

Forward or backward scattering is stronger by up to a factor of 2, when compared to a scattering angle of $\vartheta = 90°$.

Scattering and absorption by particles

Photons can also interact with particles that have a size comparable to the wavelength of the incident radiation (via scattering or absorption). For spherical particles this process is described by the Mie theory. Because these particles can absorb and scatter radiation, the Mie extinction coefficient is divided into two parts

$$\epsilon_M(r, \lambda) = \epsilon_a(r, \lambda) + \epsilon_s(r, \lambda), \tag{3.8}$$

with the particle radius r, the scattering coefficient ϵ_s and the absorption coefficient ϵ_a. Mie theory in general is very complex, even more for complex particle shapes. Therefore, only a few general remarks from Platt and Stutz (2008) will be given here.

The single scattering albedo (SSA) of an aerosol is defined as:

$$A_S = \frac{\epsilon_s(r, \lambda)}{\epsilon_a(r, \lambda) + \epsilon_s(r, \lambda)} \tag{3.9}$$

It defines the amount of radiation scattered by Mie particles, compared to the amount that was scattered or absorbed. An SSA of 1 describes pure scattering, whereas an SSA of 0 describes an aerosol that absorbs all radiation.

Mie scattering is, similar to Rayleigh scattering, not an absorption process; however, it can be described as an absorption process in the narrow-beam approximation as well. The wavelength dependency of the Mie extinction coefficient ϵ_M is:

$$\epsilon_M(\lambda) = \epsilon_{M,0} \cdot \lambda^{-\alpha} \tag{3.10}$$

Here α is the Ångström exponent (Ångströem, 1929, 1961), which is inversely related to the size of the aerosol particles. In general, Mie scattering exhibits a smaller wavelength dependency then Rayleigh scattering. Spinetti and Buongiorno (2007) measured the optical properties of aerosols in the plume of Etna, Italy and found Ångström exponents between 0.13 and 2.42 during episodes of quiescent degassing.

The Mie phase function, and thus the scattering direction, depends on the size parameter α_s:

$$\alpha_s = \frac{2\pi r}{\lambda} \tag{3.11}$$

In general it can be said, that forward scattering is more dominant in Mie scattering when compared to Rayleigh scattering, especially for increasing values of α_s.

Raman scattering

In addition to elastic scattering, inelastic Raman scattering (i.e. the energy of the photon changes during the scattering process) may also occur in the atmosphere if the atom/molecule changes its excitation state during the scattering process. The photon can transfer energy to the molecule (Stokes process) or take up energy from the molecule (anti-Stokes process). If only the rotational state ($\Delta\nu = 0$) of the molecule changes the process is called Rotational Raman scattering is used. When the vibrational excitation state changes as well, it is called rotational-vibrational Raman scattering. The cross sections for Raman scattering are orders of magnitudes smaller than those for Rayleigh scattering (Platt and Stutz, 2008). However, the influence of Raman scattering has to be considered for remote sensing applications. Due to the energy exchange during the scattering event, the incident photon has a different wavelength after the scattering process. This causes an effect known as the "Ring effect", which is named after Grainger and Ring (1962). The Ring effect describes a decrease in the optical depth of the Fraunhofer lines due to photons that are inelastically scattered. The Ring effect is described in more detail in Section 3.2.2.

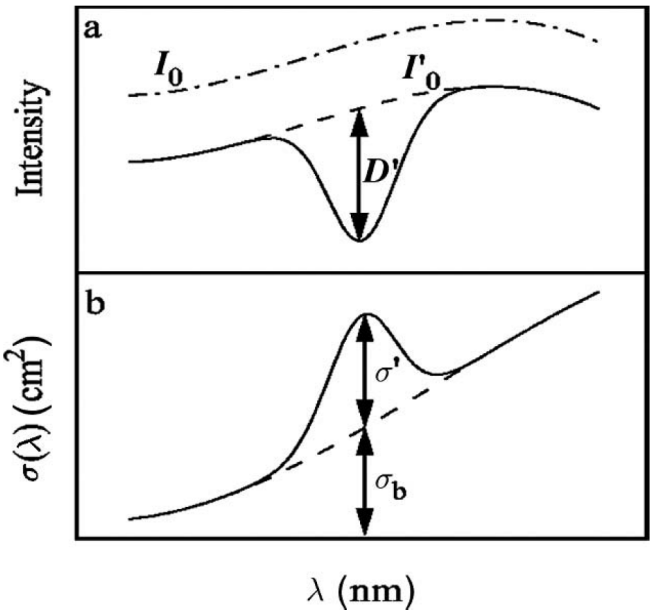

Figure 3.1.: The basic idea behind the DOAS approach: The initial spectrum spectrum I_0 is divided into a broad-band part I'_0 that only varies slowly with the wavelength and a narrow part D' that varies strongly with wavelength. In a similar manner the absorption cross section is divided into the narrow-band absorption σ' and a broad-band part σ_b. Reproduced from Platt and Stutz (2008) with kind permission from Springer Science and Business Media.

3.2 Differential Optical Absorption Spectroscopy

Eq. 3.4 cannot be applied to real measurements because obtaining the background intensity I_0 without absorbers would require removing the atmosphere. Additionally it is impossible to distinguish between the various broad-band effects, like scattering in the atmosphere or instrumental factors that influence the measured spectra. Differential Optical Absorption Spectroscopy (DOAS) is a technique that was invented in the late 1970s by Perner and Platt (1979) and that overcomes these drawbacks by using only the narrow-band absorption features of molecules to measure their column densities. This chapter will give a brief overview of the basic concepts applied in this thesis. More detailed information can be found in the comprehensive work by Platt and Stutz (2008), which was the foundation for this section.

3.2.1 The DOAS principle

The DOAS technique takes advantage of the fact that scattering effects as well as instrumental properties (i.e. the wavelength dependency of the spectrometer's optical system and grating) have a broad-band structure. The absorption cross section of trace gases on the other hand has spectral broad-band as well as

narrow-band features. It can be divided into the following two parts: a broad-band part $\sigma_b(\lambda)$ that only varies weakly with wavelength and a narrow-band part $\sigma'(\lambda)$ which varies strongly with wavelength:

$$\sigma(\lambda) = \sigma_b(\lambda) + \sigma'(\lambda) \tag{3.12}$$

The Beer-Lambert law (Eq. 3.4) can now be rewritten with the exponential function separated into one part that contains all broad-band effects (e.g., scattering as well as broad-band absorption features) and another part that only contains the narrow-band absorption features of the trace gases:

$$I(\lambda, L) = \overbrace{I_0(\lambda) \cdot \exp\left(-\int_0^L \epsilon_R(\lambda, l) + \epsilon_M(\lambda, l) + \sum_j \sigma_{b,j}(\lambda, p, T) \cdot c_j(l)\mathrm{d}l\right)}^{=:I_0'(\lambda)} \cdot \exp\left(-\int_0^L \sum_j \sigma_j'(\lambda, p, T) \cdot c_j(l)\mathrm{d}l\right) \tag{3.13}$$

The newly defined intensity $I_0'(\lambda)$ is the intensity without differential absorption, it differs from I_0 only in broad-band structures. Using I_0', the differential optical density τ' can be defined (note that in this equation the differential absorption cross sections σ_j' are used, see also Fig. 3.1):

$$\tau' = \ln\left(\frac{I_0'(\lambda)}{I(\lambda)}\right) = \int_0^L \sum_j \sigma_j'(\lambda) \cdot c_j(l)\mathrm{d}l = \sum_j \sigma_j'(\lambda) \cdot S_j \tag{3.14}$$

Eq. 3.14 can now be solved for the column densities S_j. For the simple case of only one trace gas with constant concentration c and a well-known light path L, the concentration can be directly calculated from τ':

$$c = \frac{\tau'}{\sigma' \cdot L} \tag{3.15}$$

In a DOAS measurement only the difference of the column density S_M in the measurement spectrum $I_M(\lambda) = I_0 \cdot e^{-S_M \cdot \sigma(\lambda)}$ and the column density S_R of the reference spectrum $I_R(\lambda) = I_0 \cdot e^{-S_R \cdot \sigma(\lambda)}$ is obtained. The optical density is given by:

$$\tau(\lambda) = -\ln\left(\frac{I_M}{I_R}\right) = \sigma(\lambda) \cdot (S_M - S_R) \tag{3.16}$$

In general for two spectra the obtained column density is called differential slant column density dS. In the case that the reference reference spectrum I_R does not contain the trace gas of interest ($S_R = 0$) it is called the slant column density (SCD), the column density along some light path. In volcanological

setting the ideal light-path is a straight line through the volcanic plume. In this thesis, it is usually assumed that the reference spectrum is gas free. Whenever the term column density is used it refers to the SCD. Only in Chapter 8 the distinction between dS and the SCD is explicitly made.

3.2.2 Technical implementation of the DOAS approach

The theory described above is based on an ideal instrument. In reality, instruments have limitations; spectrometers only have a finite optical and spectral resolution and temperature dependencies can further influence the signal. The chapter above also neglects the effect of inelastic scattering that causes the Ring effect and also the solar I_0 effect, an effect that influences the convolution of the high-resolution reference cross sections. All these effects will be described in this section. The section ends with a brief description of the DOASIS software's fitting routine (Kraus, 2006), which was used for the evaluation of spectroscopic data in this thesis.

Optical and spectral resolution of the spectrometer

The optical and spectral resolution of spectrometers is finite. This leads to a spectrum $I^*(\lambda)$ arriving at the detector that can be described as the convolution of the incident spectrum $I(\lambda)$ with the instrument line function (ILF) $H(\lambda)$:

$$I^*(\lambda) = I(\lambda) * H(\lambda) = \int I(\lambda - \lambda') \cdot H(\lambda, \lambda') d\lambda' \tag{3.17}$$

To correctly retrieve the column densities S_j, all reference cross sections σ_j used in Eq. 3.15 must have the same spectral resolution as the instrument used for recording the spectra. This can be achieved, for example, by recording absorption spectra and placing a calibration cell containing a known concentration of the trace gas of interest in the light path. However, this is difficult to achieve in many cases. Some species are too chemically reactive (e.g. the equilibrium between NO_2 and N_2O_4 depends on the temperature) and additionally calibration cells tend to leak. For O_3, the temperature dependency of the absorption cross section presents another problem. Therefore, cross sections $\sigma_j^*(\lambda)$ at instrument resolution are often calculated from high-resolution absorption cross sections $\sigma_j(\lambda)$ measured in a laboratory by convolving them with the ILF $H(\lambda)$:

$$\sigma_j^* = \sigma_j * H(\lambda) \tag{3.18}$$

In DOASIS, the convolved spectrum is interpolated to the spectral grid of the spectrometer after the convolution. Equation 3.18 is only an approximation that can be used for small optical densities. A more accurate solution is shown in the subsection about the solar I_0 effect.

The ILF $H(\lambda)$ that is needed for the convolution can be approximated by measuring the lines of a Mercury lamp. The spectral width of these lines is

typically only a few pm. Therefore, these lines can be seen as a delta peak in good approximation when compared to the resolution of a typical spectrometer (on the order of 0.6 nm for the instruments used in this thesis).

Effects from the detector

The spectrum I^* is recorded by a detector that only has discrete pixels. Therefore, a wavelength-interval is mapped onto a pixel i:

$$I'(i) = \int_{\lambda(i)}^{\lambda(i+1)} I^*(\lambda')d\lambda' \tag{3.19}$$

For the DOAS retrieval, it is important to know the relationship between the channels of the detector and the wavelength of the spectrum. The so-called wavelength-pixel-mapping for a detector with q channels can be described with a polynomial:

$$\Gamma_I : \lambda(i) = \sum_{k=0}^{q-1} \gamma_k \cdot i^k \tag{3.20}$$

The parameters γ_k describe which wavelength corresponds to which pixel. γ_0 corresponds to a shift of the spectrum, and a change in γ_1 describes a squeeze or stretch of the spectrum. The wavelength-pixel-mapping as well as the optical properties of the spectrometer depend on the instrument's temperature and the ambient pressure in many cases. The temperature dependency is discussed in more detail in Chapter 7.

To determine the wavelength-pixel-mapping, the peaks of a Mercury line spectrum are measured in many applications. From the known wavelength of the peaks and the pixels that correspond to these peaks the wavelength-pixel-mapping can be determined. More recently the wavelength-pixel-mapping is determined by comparing a high-resolution solar spectrum (Chance and Kurucz, 2010), which is convolved to the instrument's resolution with the measured spectrum (Lehmann, 2014; van Rozendael, 2013). The latter approach is used in this thesis, as Mercury line spectra for the NOVAC instruments were only available at room temperature.

Two other important temperature-dependent effects of the detector are offset and dark current. The offset is a low voltage that is added to the CCD signal to prevent negative signals that could result from noise at very low intensities. The analog-to-digital converter that converts the signal to a digital value cannot handle negative values. The offset structure is temperature dependent and each instrument has an individual offset structure. It can be removed by subtracting an offset spectrum, which can be created by recording n spectra with minimal exposure time and no radiation entering the spectrometer. The offset spectrum has to be rescaled to match the number of spectra summed up in the measurement spectrum.

The dark current of the CCD is caused by thermally excited electrons in the

semiconductor's depletion zone. The dark current signal increases linearly with increasing exposure times and exponentially with increasing temperatures and can be greatly reduced by cooling the detector. Additionally, it is signal dependent (Stutz and Platt, 1993), but a first-order correction can be made by subtracting a dark current spectrum from the offset-corrected measurement spectrum. The dark current spectrum should be recorded at the same temperature as the measurements, with no radiation entering the spectrometer and an exposure time longer than the measurement's exposure time. It has to be rescaled to match the measurements exposure time.

The complete process of how radiation is measured and the incident spectrum $I(\lambda)$ is altered by the instrument's optical system and subsequently mapped onto discrete channels recorded by the detector is depicted in Figure 3.2.

The Ring effect

Inelastic scattering leads to the Ring effect (named after Grainger and Ring, 1962) that can be observed as a filling of the Fraunhofer lines in spectra of scattered solar radiation when compared to direct sunlight measurements. Today, it is believed that the Ring effect is caused by rotational Raman scattering mainly on O_2 and N_2 in the atmosphere (Bussemer, 1993; Solomon et al., 1987). Solomon et al. (1987) suggested treating the Ring effect as a pseudo-absorber in the evaluation of spectroscopic data based on the calculation listed below.

The radiation arriving at the instrument I_{meas} consists of parts that were Rayleigh, Mie or Raman scattered in the atmosphere:

$$I_{meas} = I_{Rayleigh} + I_{Mie} + I_{Raman} = I_{elastic} + I_{Raman} \tag{3.21}$$

The logarithm of I_{meas} can be expanded when taking into account that Raman scattering is orders of magnitude weaker than elastic scattering processes:

$$\begin{aligned} \ln(I_{meas}) &= \ln\left(I_{elastic} \cdot \frac{I_{elastic} + I_{Raman}}{I_{elastic}}\right) \\ &= \ln(I_{elastic}) + \ln\left(1 + \frac{I_{Raman}}{I_{elastic}}\right) \approx \ln(I_{elastic}) + \frac{I_{Raman}}{I_{elastic}} \end{aligned} \tag{3.22}$$

The Ring spectrum that can be included as a pseudo-absorber in the DOAS evaluation is defined as:

$$I_{Ring} = \frac{I_{Raman}}{I_{elastic}} \tag{3.23}$$

The Raman Spectrum is needed for the calculation of the Ring effect. It can be measured by comparing the intensities of light that is polarized perpendicular and parallel to the scattering plane (Bussemer, 1993; Solomon et al., 1987). Another approach is to calculate the Raman spectrum from a measured spectrum using input knowledge on the concentrations of N_2 and O_2 in the atmosphere

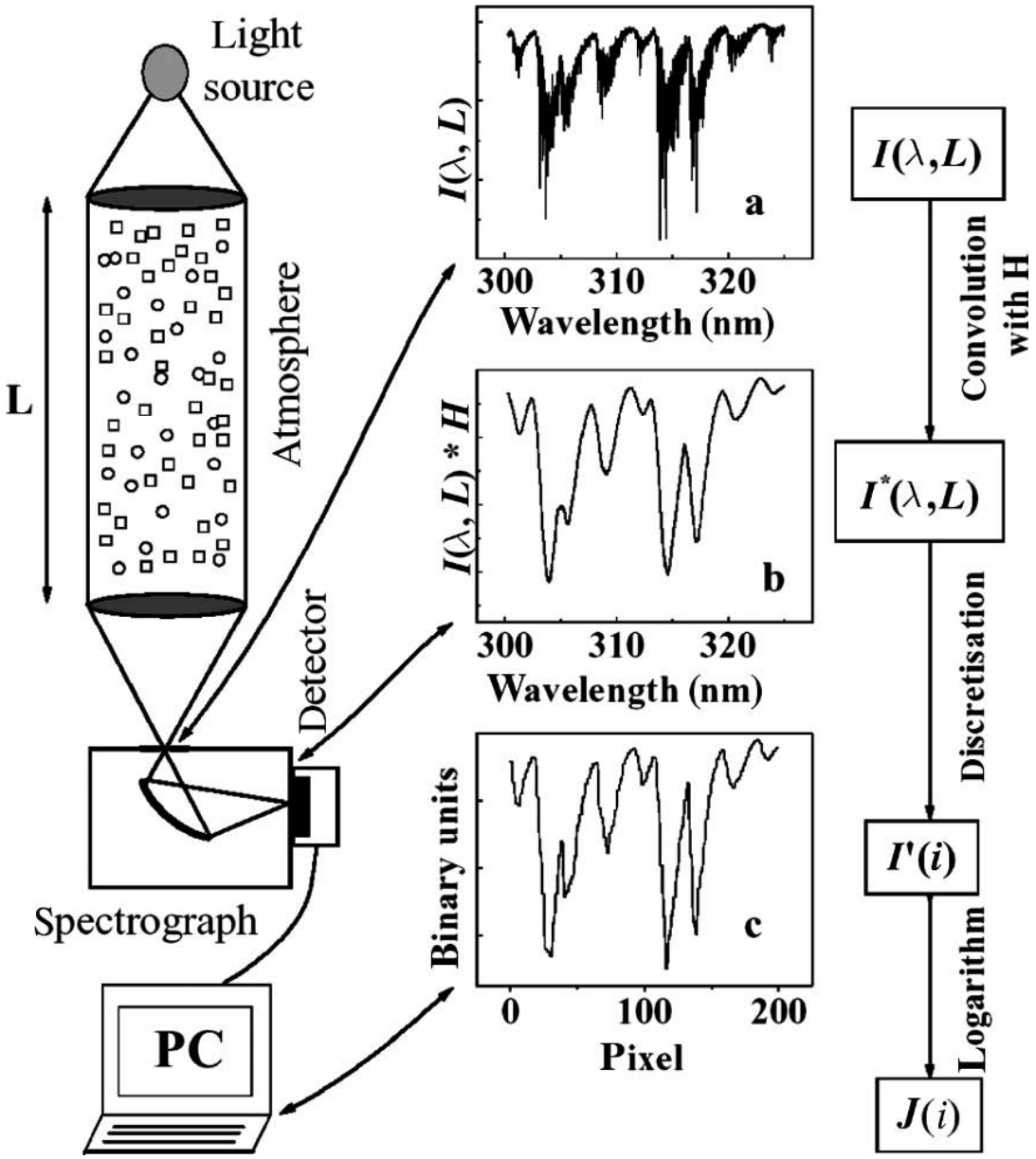

Figure 3.2.: Sketch of a DOAS measurement. Light from a source traverses the atmosphere and is focussed onto a spectrometer. The finite resolution of the spectrometer leads to a spectrum $I*$ arriving at the detector, where it is mapped onto discrete pixels and a spectrum I' is digitalised. Reproduced from Platt and Stutz (2008) with kind permission from Springer Science and Business Media.

(Bussemer, 1993; Chance and Spurr, 1997). In this thesis, the latter approach is used with the Ring spectrum being calculated from the DOASIS software package (Kraus, 2006).

In cases with multiple Rayleigh scattering in the atmosphere or scattering on clouds and aerosol particles, the wavelength dependency of the amplitude of the Ring spectrum can vary (Wagner et al., 2009). For these cases a second Ring spectrum, which is calculated from the original Ring spectrum by multiplying it by a wavelength dependent term ($\approx \lambda^4$), is included in the evaluation:

$$I_{Ring,2} = I_{Ring} \cdot \lambda^4 \tag{3.24}$$

In this work, the second Ring spectrum is orthogonalised against the first Ring spectrum in the retrieval range.

The solar I_0 effect

As outlined earlier in this section, typical spectrometers have a finite resolution that cannot resolve all the structures of the Fraunhofer lines. The absorption structures as seen by the spectrometer can therefore differ slightly from the absorption cross sections that were recorded in the laboratory with an unstructured light source and later convolved to match the instrument's resolution (Platt et al., 1997). Two effects called the *solar I_0-effect* and the *saturation effect* can occur. Both effects are caused by narrow spectral structures that are not accurately taken into account when using cross sections as outlined in Eq. 3.18. For the saturation effect, these are strong absorption lines that are smoothed out during the convolution of the cross section. For the solar I_0-effect, the causes are narrow Fraunhofer lines that weight a cross section differently in reality.

Mathematically this can be shown by comparing an ideal measurement (infinite resolution) with one trace gas with a real measurement. For an ideal measurement, the DOAS approach would yield the optical density:

$$\tau = \ln\left(\frac{I_0(\lambda)}{I(\lambda)}\right) = \sigma(\lambda) \cdot S \tag{3.25}$$

In reality, however, both intensities are measured with the instrument's spectral resolution (see Eq. 3.17) and the optical density τ^* is:

$$\tau^* = \ln\left(\frac{I_0^*(\lambda)}{I^*(\lambda)}\right) = \ln\left(\frac{I_0(\lambda) * H(\lambda)}{[I_0(\lambda) \cdot exp(-\sigma(\lambda) \cdot S)] * H(\lambda)}\right) \neq \sigma^*(\lambda) \cdot S \tag{3.26}$$

Therefore, for strong absorbers or a structured light source (as the sun in passive DOAS measurements), a correction has to be applied. Following Platt and Stutz (2008) and Lehmann (2014), the corrected absorption cross sections

can be calculated as:

$$\sigma_{I_0} = -\ln\left(\frac{I_K^*(\lambda)}{I_{0,K}^*(\lambda)}\right) \cdot \frac{1}{S} \tag{3.27}$$

In this equation $I_{0,K}^*$ is calculated by convolving a high resolution solar spectrum (e.g. Chance and Kurucz, 2010):

$$I_{0,K}^* = I_K(\lambda) * H(\lambda) \tag{3.28}$$

For the second spectrum I_K^* an absorbing term according to Beer-Lambert law is applied before the convolution:

$$I_K^* = [I_K(\lambda) \cdot \exp(-\sigma(\lambda) \cdot S)] * H(\lambda) \tag{3.29}$$

A good estimate of the true column density is therefore needed to create the corrected absorption cross sections. In this work, whenever solar I_0-corrected cross sections are used, the estimate was obtained by performing a fit using cross sections according to Eq. 3.18. The obtained column densities were then used as input parameters for Eq. 3.27.

The DOAS retrieval

The DOAS approach used in this thesis differs slightly from Eq. 3.14 and 3.15. The fitting routine from the DOASIS software (Kraus, 2006) was used to evaluate all spectroscopic data in this thesis.

Eq. 3.4 can be rewritten to:

$$\begin{aligned} \ln(I(\lambda, L)) &= \ln(I_0) + P(\lambda) - \int_0^L \sum_j \sigma_j(\lambda, p, T) \cdot c_j(l)\mathrm{d}l \\ &= \ln(I_0) + P(\lambda) - \sum_j \sigma_j(\lambda, p, T) \cdot S_j \end{aligned} \tag{3.30}$$

The term $P(\lambda)$ is a polynomial that accounts for all broad-band effects that differ between the background spectrum I_0 and the measurement spectrum I.

The DOAS fitting routine varies the polynomial $P(\lambda)$ and the column densities S_j to find a model function $F(\lambda)$ that resembles $\ln(I(\lambda))$:

$$F(\lambda) = \ln I_0 + P(\lambda) - \sum_i \sigma_j(\lambda) \cdot S_j \tag{3.31}$$

The DOASIS fit routine uses a combination of a standard least-squares fit and a Levenberg-Marquard algorithm to minimize χ^2:

$$\chi^2 = \sum_{i=\lambda_1}^{\lambda_2} (\ln(I(i)) - F(i))^2 \tag{3.32}$$

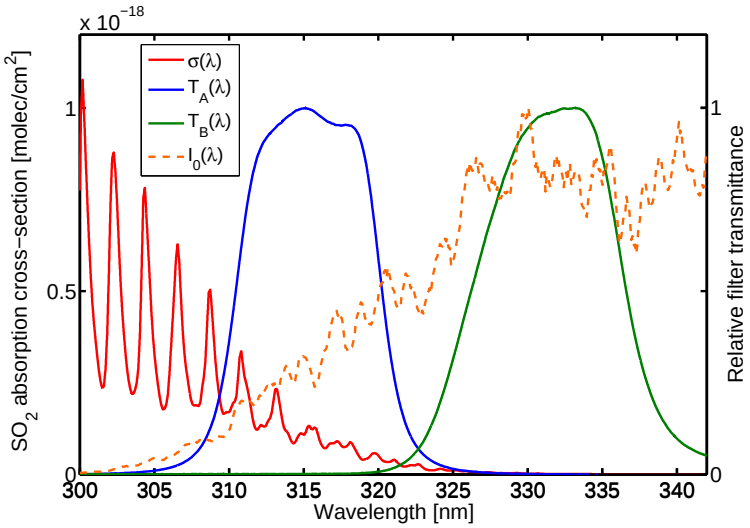

Figure 3.3.: Basic principle of the SO_2 camera. Two filters are used to measure the radiation intensity in a region where sufficient radiation intensity $I_0(\lambda)$ is available (dashed line). Filter A (blue curve) transmits light in a region where the SO_2 absorption cross-section (red solid line) still has prominent absorption features. Filter B (green line) corrects for ash and aerosol in a region where SO_2 absorption is negligible.

3.3 The SO_2 camera

The SO_2 camera is an optical remote sensing instrument for measuring volcanic SO_2 emission rates with a time resolution on the order of 1 Hz. These high time resolution measurements of the SO_2 emission rate can be used, for example, to perform time series analyses to investigate the degassing process inside the volcano (see Section 2.4 and Section 4.6). A large part of the work on the SO_2 camera during this thesis focussed on investigating the correct calibration of this relatively new technique. Parts of the SO_2 camera theory in this section are a revised version of the theory in Lübcke et al. (2013b).

The measurement principle of the SO_2 camera employs one or two band-pass interference filters and a UV-sensitive CCD detector to analyse the ultraviolet absorption of SO_2 using solar radiation scattered in the atmosphere as a light source (see Fig. 3.3). The measurement principle will be described in Section 3.3.1. Section 3.3.2 shows how the optical density measured by the SO_2 camera can be converted to an SO_2 column density. The SO_2 camera theory will conclude with a discussion of how the background intensity needed to calculate the optical density (Eq. 3.2) can be obtained (Section 3.3.3).

3.3.1 SO_2 camera theory

The SO_2 camera detects SO_2 in a narrow spectral window between 300 and 320 nm. In this region the absorption cross section of SO_2 still has strong

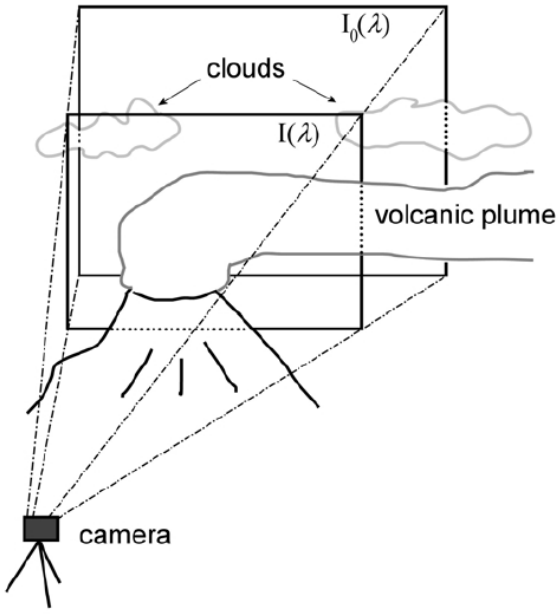

Figure 3.4.: The measurement geometry of the SO_2 camera. The SO_2 camera detects the incident radiation $I(\lambda)$ from the clear sky and the volcanic plume. To calculate the SO_2 column density, a proxy for the background intensity $I_0(\lambda)$ is needed. Reproduced from Kern et al. (2010b).

absorption features while sufficient solar radiation intensity is available to allow reasonable exposure times.

The optical density τ_A for Filter A can be written as:

$$\tau_A = -\ln \frac{I_{A,M}}{I_{A,0}}, \tag{3.33}$$

with incident spectral radiation intensity $I_{A,0}$ and radiation intensity $I_{A,M}$ after passing through the volcanic plume. $I_{A,0}$ is often obtained from background images that are recorded with a slightly different viewing direction. This will be discussed in section 3.3.3. A typical measurement geometry is depicted in Fig. 3.4. The optical density τ_A is influenced by SO_2 absorption, but other influences like ash, aerosol or plume condensation can influence it as well. A second filter, Filter B, can be used to perform a first-order correction of these effects. This filter is placed at a slightly higher wavelength, in a region where SO_2 absorption is negligible but the influence of the other effects is comparable. In this work, Filter B transmits radiation between 325 and 335 nm. The optical density τ_B for Filter B can be written similar to τ_A:

$$\tau_B = -\ln \frac{I_{B,M}}{I_{B,0}}, \tag{3.34}$$

and is only very weakly influenced by SO_2 absorption.

The optical density τ is the difference between τ_A and τ_B. It is often also referred to as apparent absorbance (AA):

$$\begin{aligned} \tau &= \mathrm{AA} = \tau_\mathrm{A} - \tau_\mathrm{B} = -\ln\frac{I_\mathrm{A,M}}{I_\mathrm{A,0}} + \ln\frac{I_\mathrm{B,M}}{I_\mathrm{B,0}} \\ &= \ln\frac{\frac{I_\mathrm{B,M}}{I_\mathrm{B,0}}}{\frac{I_\mathrm{A,M}}{I_\mathrm{A,0}}} = \ln\frac{I_\mathrm{B,M}}{I_\mathrm{A,M}}\cdot\frac{I_\mathrm{A,0}}{I_\mathrm{B,0}} \end{aligned} \tag{3.35}$$

The apparent absorbance is directly related to the SO_2 column density. However, to calculate the emission rate, the SO_2 camera has to be calibrated in a way that converts apparent absorbances values to SO_2 column densities.

3.3.2 Calibrating the SO_2 camera

To obtain SO_2 emission rates from SO_2 camera measurements, the AA values have to be converted to SO_2 column densities. Since the camera calibration depends on the incoming solar radiation and the measurement geometry (i.e. the solar zenith angle, solar azimuth angle and variations in the aerosol content of the atmosphere or the strength of stratospheric O_3 absorption), this has to be performed several times per day. Kantzas et al. (2010) studied the calibration and found that it is approximately constant on the order of an hour in the middle of the day and more variable near sunrise or sunset. Wöhrbach (2008) performed a series of laboratory studies and found a positive correlation between the solar zenith angle and the camera calibration constant. Similar studies at Etna by Huwe (2013) verified the dependence of the calibration on the solar zenith angle and showed variations with the relative solar azimuth angle during measurements in a volcanic plume.

The camera calibration can be performed with help of calibration cells or by conducting additional spectroscopic measurements. The advantages and disadvantages of the different methods will briefly be described here.

Calibration with calibration cells

Calibrating the SO_2 camera with calibration cells was the most commonly used method in the past (Dalton et al., 2009; Kantzas et al., 2010; Mori and Burton, 2006). The most simplistic approach is to place calibration cells in front of the camera manually. The SO_2 cameras built in our institute can automatically insert calibration cells in the light path, but this increases the complexity of the instrument. A set of images from both filters with a calibration cell covering the entire camera field-of-view (FOV) can be used to derive an AA value for each pixel of the camera. After conducting several measurements with calibration cells containing different concentrations of SO_2, a calibration curve can be derived.

Another method that has been used (for example in Dalton et al., 2009) is to place several calibration cells in the image simultaneously. Each cell covers a small area of the camera FOV and gives one calibration point for the calibration curve. While this approach certainly reduces the time needed to acquire a complete calibration curve (one set of camera images vs. one set of images for each calibration point), it has severe disadvantages. As was already suggested in Lübcke (2010) and will be shown later in this thesis (Sections 4.4.1 and 4.4.2), the camera's response to a given SO_2 column density varies with distance from the optical axis (e.g. centre of the image). If the calibration cells are placed at different distances from the image centre, the calibration curve can become unreliable.

An additional drawback of calibration cells is that depending on the position on the detector, rays entering the camera through the calibration cell have varying light paths in the calibration cell. This leads to a slightly different SO_2 column density, depending on the position. However, this issue can be corrected for by calculating the length of the light path through the calibration cell depending on the illumination angle.

The major problem with calibration cells is that they only show the reaction of the SO_2 camera system to pure SO_2 and that the calibration cannot be performed with the same viewing geometry as plume measurements. Influences from aerosols, ash or plume condensation cannot be assessed. Additionally cell calibration increases the manual effort. As the calibration has to be performed several times per day, the camera has to be turned away from the plume to measure calibration cells throughout the day.

The DOAS calibration method

A different approach for the calibration of the SO_2 camera is using additional spectroscopic data to calibrate the camera (Kern et al., 2010b; Lübcke et al., 2013b). A DOAS system measures the SO_2 column density in a small area that coincides with a part of the SO_2 camera image (see Figure 3.5). If the plume passes the DOAS FOV one obtains a set of SO_2 column densities and the corresponding AA values from the SO_2 camera. This set of SO_2 column densities and AA values can be used to create a calibration curve that is measured directly in the volcanic plume. This method is able to assess variations of the calibration curve due to changes in the incoming solar radiation and condensation or aerosols in the volcanic plume. Additionally the spectroscopic data from the DOAS instrument can be used to perform sophisticated radiative transfer corrections (Kern et al., 2010a, 2012, 2013). More details on the effects of radiative transfer are discussed in Chapter 3.4. To accurately calibrate the SO_2 camera with help of DOAS measurements, two conditions have to be fulfilled:

- The calibration should cover the entire range of SO_2 column densities that appear in the camera images. This might require changing the position of

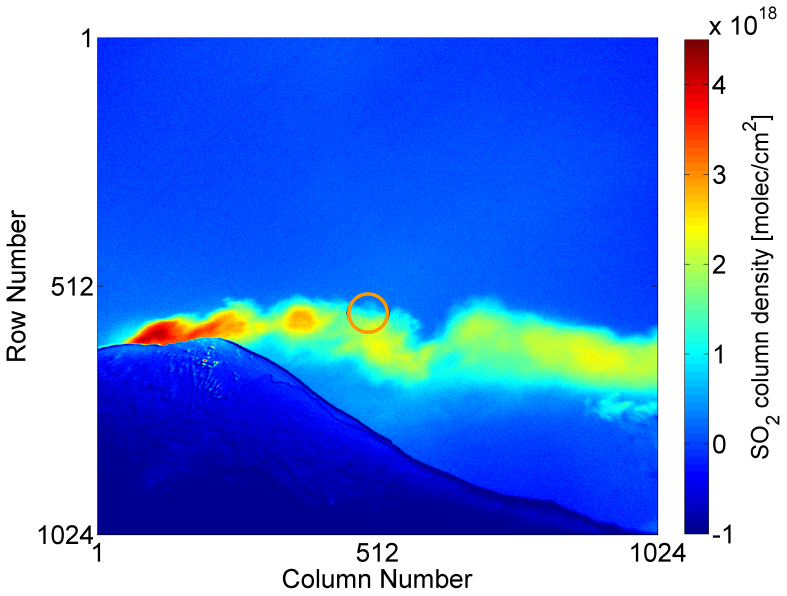

Figure 3.5.: SO_2 camera image acquired at Popocatépetl, Mexico on 1 March 2011. The orange circle in the middle of the image shows the approximate field-of-view of the spectrometer that was used for the calibration. Adapted from Lübcke et al. (2013b).

the DOAS FOV within the camera image, or changing the orientation of the complete SO_2 camera-DOAS set-up.

- The calibration is, as mentioned above, only valid in a small area within the camera image (the area where the FOV's of both instruments coincide). Ideally this is the centre of the camera image, but the position might vary depending on the measurement geometry. For all other parts of the SO_2 camera image, the sensitivity has to be characterized. This can, e.g. be done by taking images with several calibration cells, each cell covering the complete camera FOV (see above). If characterised carefully (e.g. in the laboratory) calibrating the SO_2 camera with a spectrometer can greatly reduce the need to perform calibration cell measurements in the field. This is especially advantageous if instruments should autonomously observe volcanic plumes.

The second condition can be verified with help of an imaging DOAS instrument (IDOAS) (see Section 4.4.3). The IDOAS combines the spectroscopic DOAS method with an imaging spectrometer and thus allows the retrieval of two-dimensional trace-gas distributions. However, the measurement set-up and data evaluation is complex and therefore a single DOAS telescope with a fixed viewing direction is preferable despite the advantages of two-dimensional spectroscopic data.

3.3.3 Background images

To calculate the AA according to Eq. 3.35, the background intensities $I_{A,0}$ and $I_{B,0}$ are needed. The real background intensity is not accessible, since it would require removing the volcanic plume from the measurement. Placing a camera behind the volcano with a similar viewing direction would still yield a somewhat different measurement geometry. Therefore, the background intensity is usually obtained by taking background images after turning the SO_2 camera to an area of the sky that is free of volcanic absorption structures and clouds (see e.g., Kick, 2008; Lübcke, 2010). These background images serve two purposes, they remove influences of the cameras optical system and they approximate the radiation intensity behind the volcanic plume in absence of SO_2.

The effects of the cameras optical system can be further divided into two main effects, lens vignetting and influences from the band-pass interference filters. Vignetting describes the effect that images become darker towards the edges of the image. The effect can be greatly reduced by reducing the aperture of the camera or characterized in the laboratory. The second effect is caused by the illumination angle dependence of band-pass interference filters (Lissberger, 1959; Lissberger and Wilcock, 1959). These filters shift their transmittance window towards smaller wavelengths with increasing illumination angle. The radiation intensity decreases with decreasing wavelength in the region used for SO_2 camera measurements. Therefore, the described effect also leads to a decrease of light intensity with increasing distance from the optical axis and is often mistakenly called vignetting as well. The variation of intensity caused by this effect depends on the spectrum of incoming radiation, it can therefore not be exactly characterized in the laboratory.

Besides influences from the optical system, the background images should also indicate the light intensity behind the volcanic plume. However, the viewing geometries of the background images is different from the measurement geometry. Since the background illumination of the sky depends on the solar zenith angle, the relative azimuth angle, the aerosol content of the atmosphere and clouds (if present) errors can occur. Both the colour (i.e. the ratio of radiation intensity between different wavelengths) and the absolute radiation intensity changes with the viewing geometry (Hernández-Andrés et al., 2003; Rossini and Krenzinger, 2007). This can lead to errors especially in the morning hours, when the solar zenith angle is large. Kantzas et al. (2010) compared three different methods to use background images:

- Background images were acquired adjacent to the plume. After calculating the AA according to Eq. 3.35 the AA value of the free sky was subtracted
- Background images were only used to correct for the optical effects of the camera system, a polynomial was fitted to free areas of the sky
- Background images were only used to correct for effects of the camera's

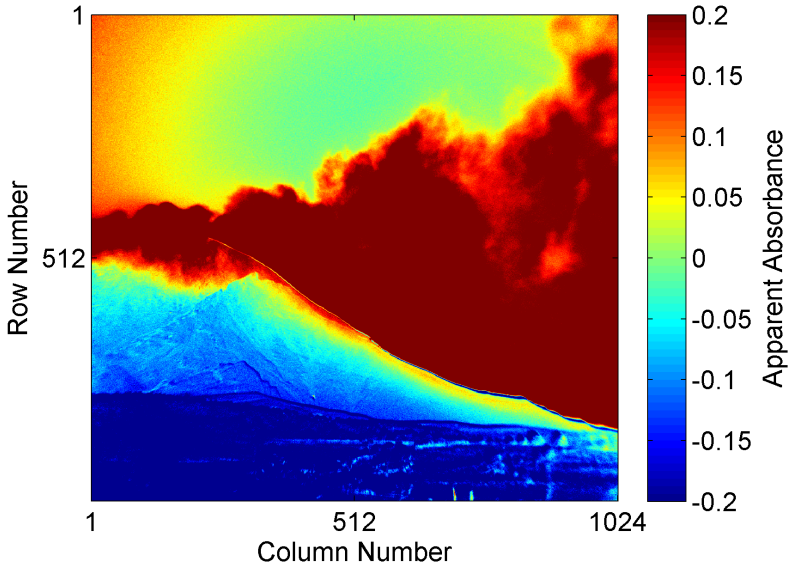

Figure 3.6.: SO_2 camera image acquired at Popocatépetl, Mexico on 2 March 2011 at 8:30 am. Besides the plume, which is covering the complete flank of the volcano, variations of the clear sky illumination can be observed. Under such conditions meaningful emission rate measurements are not possible.

optical system. The ratio of radiation at 310 and 330 nm was assumed to be constant and subtracted from the image.

The first and third method only differ in the question, where background images are acquired. The authors of Kantzas et al. (2010) found excellent agreement between the three methods. However, they restricted their measurements to geometries, where the relative azimuth between sun-camera-plume was larger than 90° to reduce inhomogeneous illumination across the FOV.

Measurements during this thesis at Popocatépetl, Mexico and Stromboli, Italy showed that the altitude also influences the degree to which the background illumination is homogeneous. During measurements (with an unfavourable measurement geometry) at Popocatépetl from a height of 3700 m and a summit height of 5426 m strong variations in the illumination across the FOV could be observed especially in the morning hours (see Fig. 3.6).

During measurements at Stromboli, which has a summit height of only 926 m no such large variations of the background illumination could be observed. A possible explanation for this behaviour is that measurements at Popocatépetl were performed at a higher altitude, where a larger fraction of radiation was only scattered once before entering the instrument. Therefore, the scattering angle dependency of Rayleigh scattering has a larger influence on the background illumination.

For meaningful SO_2 emission rate measurements, the plume has to be completely visible. Therefore a sufficiently large area of free sky should be available

to interpolate the measured intensity above and below the plume and thus eliminating errors arising from inhomogeneous sky illumination.

3.4 Radiative transfer effects on remote sensing measurements

For the optical remote sensing of volcanic gases, the ideal situation would be that all radiation is scattered in the atmosphere behind the volcanic plume only once before traversing the plume (where some intensity is lost depending on the trace gas concentrations). After traversing the plume radiation is detected by the instrument. However, already in the early days of volcanic gas remote sensing with the Correlation Spectrometer (COSPEC, Stoiber et al., 1983) influences from the radiative transfer in the atmosphere were detected (Millan, 1980; Moffat and Millan, 1971). In reality, effects like the light dilution effect or multiple scattering inside the volcanic plume can lead to an overestimation as well as an underestimation of the "true" SO_2 column density.

Light dilution describes the effect that light is scattered into the instrument between the instrument and the volcanic plume (Kern et al., 2010a; Millan, 1980; Mori et al., 2006). As both Rayleigh and Mie scattering are stronger at lower wavelengths, the light dilution effect influences these wavelengths stronger. The magnitude of the light dilution effect depends on the ambient atmosphere, type and concentration of aerosol, but also humidity and temperature (Mori et al., 2006). Mori et al. (2006) found an attenuation of up to 50% for a volcanic plume in a distance of only 2.6 km when evaluating the 309 nm absorption band of SO_2. Kern et al. (2012) showed by the use of radiative transfer calculations that volcanic plumes with a high AOD and SO_2 concentration can also lead to a decrease of of the measured SO_2 column density. In this case the aerosol leads to an optical thick cloud, that prevents photons from passing the complete plume. Depending on the measurement geometry as well as the wavelength range used for evaluation a considerable amount of radiation is scattered into the instrument without penetrating the plume (see also Figure 3.7).

Multiple scattering is caused by plume condensation, aerosols and also SO_2 molecules inside the volcanic plume. Therefore the path length of a photon can be considerably longer than a straight line through the plume (Kern et al., 2010a). Different from light dilution, multiple scattering leads to an overestimation of the true SO_2 column density. The various light paths possible during remote sensing measurements of volcanic gases are shown in Fig. 3.7.

While the effects of radiative transfer on volcanic gas measurements have been known for quite a while, only recently efforts were made to correct for these effects. Mori et al. (2006) quantified the light dilution effect by measuring SO_2 from various lateral distances. Kern et al. (2009) performed an extensive theoretical study on the influences of factors like lateral distance, plume and

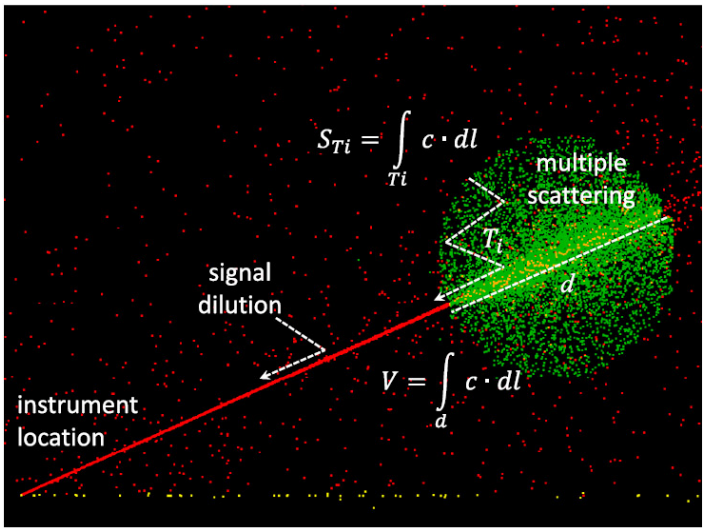

Figure 3.7.: Simulation of the radiative transfer in and around a volcanic plume. Red dots depict Rayleigh scattering events that are detected by the instrument. Green dots depict Mie scattering on aerosol in the volcanic plume, and roughly show the form of the volcanic plume. Yellow dots show scattering from the ground. Also shown is the straight line through the volcanic plume d, which is usually assumed for volcanic gas measurements. Figure adapted from Kern et al. (2012).

ambient aerosol load and SO_2 concentration on the retrieved column density. These theoretical studies were carried out using the 3D radiative transfer model McArtim (Deutschmann et al., 2011).

More recently different approaches to handle radiative transfer in volcanic plumes were explored, evaluating SO_2 in different wavelength window (Bobrowski et al., 2010; Hörmann et al., 2013), using an intensity fit that can assess the light dilution effect (Burton and Sawyer, 2013) or combining radiative transfer model calculations with a DOAS retrieval (Kern et al., 2010b, 2012, 2013).

Higher wavelength ranges are used as most scattering effects and strong SO_2 absorption potentially lead to larger problems at lower wavelengths. Bobrowski et al. (2010) suggested to evaluate SO_2 in the range between $360-390\,\text{nm}$. While the SO_2 absorption is several orders of magnitude smaller at these wavelengths, good results were obtained for high SO_2 column densities. Hörmann et al. (2013) evaluated SO_2 between $326.5-335.3\,\text{nm}$ for satellite measurements of the BrO/SO_2 ratios, if SO_2 had column densities exceeding $1 \cdot 10^{18}\,\text{molec/cm}^2$. A similar approach (with two different wavelength ranges) will be used in the evaluation of the NOVAC data in Section 6.1.

Another way to assess the complex radiative transfer in volcanic plumes is the use of radiative transfer models. Kern et al. (2012) described a model called Simulated Radiative Transfer (SRT) DOAS, that combines radiative transfer model calculations with DOAS measurements. Parameters for the RTM, in this case most importantly SO_2 column density and plume AOD, are varied until the modelled radiances match the measurement. The SRT-DOAS method was

applied to SO_2 camera measurements at Kilauea, Hawaii, USA and showed more than two times higher SO_2 emission rates when complex radiative transfer was taken into account (Kern et al., 2013). The SRT-DOAS method was applied to a set of spectra that was recorded during the work on this thesis at Stromboli volcano, Italy the results will be discussed in Section 4.5.3.

The 3d radiative transfer model McArtim (Deutschmann et al., 2011) was also used in Chapter 6 to assess the influences of radiative transfer on the BrO/SO_2 ratio. In particular the influences of distance between plume and instrument and clouds were studied by using the radiative transfer model.

4

SO_2 camera measurements

The SO_2 camera is a remote sensing instrument that can measure two-dimensional SO_2 column density distributions with a high spatial resolution and a high frequency on the order of 1 Hz.[1] Compared with the DOAS technique, SO_2 cameras only use extremely reduced spectral information. The measurement principle employs one or two interference filters and a UV-sensitive detector. One filter (Filter A) measures the optical density of SO_2, a second filter (Filter B) is used to correct for aerosol scattering and radiative transfer effects.

The theory of the SO_2 camera technique was already described in Section 3.3. This chapter will start with a brief description of the instruments that were used during the measurement campaigns in Section 4.1 and an overview of the measurement geometries at Popocatépetl, Mexico and Stromboli, Italy, in Section 4.2. Section 4.3 explains how SO_2 camera images were processed and how spectroscopic data from the narrow field-of-view DOAS (NFOV-DOAS) was evaluated. The calibration of the SO_2 camera will be discussed theoretically and with measurement results in detail in Section 4.4. Section 4.5 describes the calculation of SO_2 emission rates and presents the results from both campaigns. These SO_2 emission rates were analysed with help of the wavelet analysis technique in Section 4.6. The wavelet analysis is a first step to make SO_2 camera measurements accessible for volcanology.

[1] This Chapter is in large parts an updated version of Lübcke et al. (2013b). Most of the Mexico measurements and the work on the camera calibration were published there. The Stromboli measurements and the wavelet analysis are completely new content.

4.1 Instruments used during the measurements at Popocatépetl and Stromboli

Three different instruments (SO_2 camera, NFOV-DOAS and an imaging DOAS, also called IDOAS) were used during the measurement campaigns performed during this thesis. These instruments are briefly described in this section.

An SO_2 camera system with an integrated NFOV-DOAS system was designed and built at our laboratory in Heidelberg. This instrument is described in Lübcke (2010) and Lübcke et al. (2013b). Field measurements at Popocatépetl, Mexico were performed together with an IDOAS instrument, which was custom-built in the University of Heidelberg laboratory as well. More detailed information about the IDOAS can be found in Lohberger et al. (2004), Bobrowski et al. (2006) and Louban et al. (2009). The spatial resolution, FOV and the exposure times of the instruments used during the measurements in Mexico are summarized in Table 4.1.

For the measurements at Stromboli, Italy an updated SO_2 camera system was used. This instrument is described in more detail in Illing (2011) and Huwe (2013).

4.1.1 Design of the SO_2 cameras

Two different SO_2 camera prototypes were used during the measurements at Popocatépetl, Mexico, and Stromboli, Italy. This section will briefly describe the general design, before discussing the detector, lens and filters used in the respective cameras in seperate subsections.

Both SO_2 cameras consist of a CCD detector and a single plano convex fused silica lens. The band-pass interference filters are mounted between the CCD and the lens, to reduce influences from a variable filter illumination angle (see Section 4.4.1). As the light intensity might vary between different locations, times of day and environmental conditions, an iris aperture with variable diameter was installed in both cameras. Changing the aperture can lead to changes of the calibration curve (see Section 3.3.2) as well as influence the variation of sensitivity over the detector (see Section 4.4.1). Therefore reasonable aperture settings were adjusted at the beginning of the measurements and kept fixed for the rest of the campaign. In this context, reasonable means that exposure times do not fall below the minimum exposure time (mainly controlled by the speed of the mechanical shutter) at midday while still being as low as possible in the morning and evening, when less radiation is available.

Both SO_2 cameras use two band-pass interference filters that are installed in a custom-made filter wheel. Filter A is usually centred around 315 nm and Filter B is centred around 330 nm. The filter wheel consists of an aluminium mount, which holds the two filters, and a standard servo unit, which is operated by a Phidgets© USB servo controller (PhidgetAdvancedServo 8-Motor). The Phidget© controller

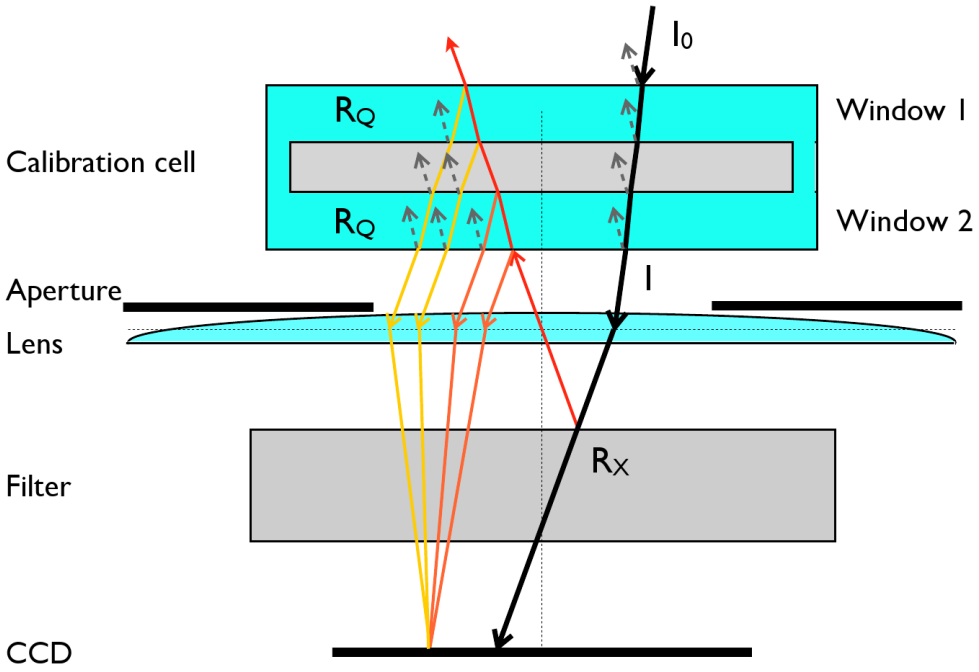

Figure 4.1.: Sketch of the optical set-up of the SO_2 camera (with a calibration cell in place). Reflections on the windows of the calibration cells, which are discussed in Sect. 4.4.1 are shown. Only part of the radiation arriving at the interference filter is transmitted (black line), radiation reflected from the interference filter (red) is – in turn – partially reflected on Window 1 (yellow) and Window 2 (orange) of the calibration cell. This radiation (some of which has passed the calibration cell three times) reaches the detector and leads to changes in the AA when arriving at the CCD. The grey dashed lines indicate additional reflections that are only accounted for as losses in the calculation of the reflections. Reflections on the lens are greatly suppressed by an anti-reflective coating. Reproduced from Lübcke et al. (2013b).

Table 4.1.: Optical parameters and settings of the instruments used during the measurements in Mexico, adapted from Lübcke et al. (2013b).

IDOAS	
Co-added exposures per spectrum	10
Exposure time	0.5 s–2.5 s
Resolution (pixel $h \times v$)	175×255
Solid angle per pixel	$0.26° \times 0.05°$
FOV per column	$0.26° \times 13.1°$
Scanned solid angle	$45.5° \times 13.1°$
SO_2-camera	
Exp. time Filter A	0.25 s–1 s
Exp. time Filter B	0.1 s–0.3 s
Resolution (pixel $h \times v$)	1024×1024
Solid angle per pixel	$0.02° \times 0.02°$
FOV	$22.4° \times 22.4°$
NFOV-DOAS	
Co-added exposures per spectrum	15
Exposure Time	0.3 s–0.6 s
FOV	2.5°

also controls two further servo motors. These servo motors can each insert one of two calibration cells containing known SO_2 concentrations in front of the aperture, each covering the entire FOV of the camera. The calibration cells can be moved in the light path separately or both at the same time, thus giving three measurement points for calibration. More calibration cells would improve the quality of the calibration curve but also drastically increase the mechanical complexity of the camera.

The SO_2 camera used at Popocatépetl

The detector of the SO_2 camera used during the Mexico measurements is an Apogee Instruments Alta U6 CCD array. The CCD has 1024×1024 pixels with a pixel size of $24 \times 24\,\mu$m resulting in a large detector area of 24.58×24.58 mm. The large detector area leads to short exposure times (approximately $0.2 - 0.4$ s) despite the fact that the detector quantum efficiency Q and the scattered radiation intensity are low ($Q \approx 0.06$) in the UV regions used in the measurements. Shorter exposure times were limited not by the radiation intensity but rather by the shutter opening time.

The optical set-up of the camera (see Figure 4.1) consists of a single 31.5 mm diameter plano-convex fused silica lens with a focal length of $f = 60$ mm and two band-pass interference filters mounted in a filter wheel between the lens and the detector. The iris aperture in this camera is installed directly in front of the lens. During the measurements at Popocatépetl an aperture of roughly $f/8$ was

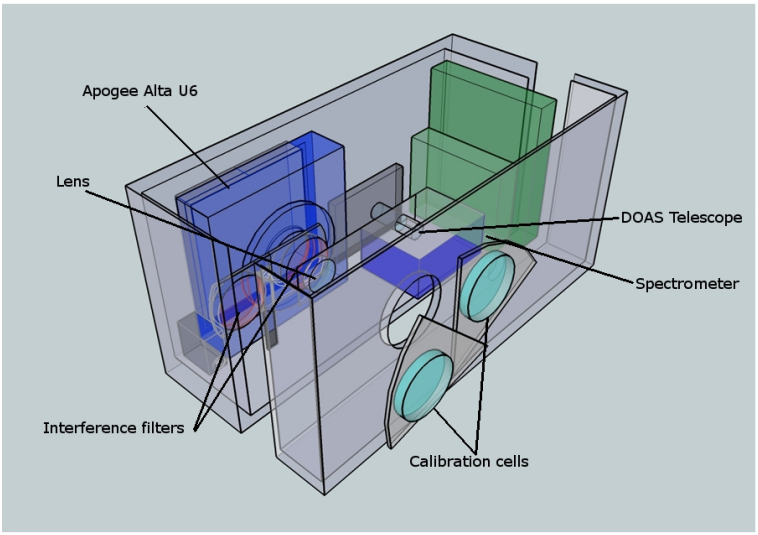

Figure 4.2.: Sketch of the SO_2 camera used for the measurements at Popocatépetl. Adapted from Lübcke (2010).

used. The two interference filters are manufactured by Eureca Messtechnik and have central transmittance wavelengths of 315 nm (Filter A , FWHM 10 nm), and 330 nm (Filter B, FWHM 10 nm). The calibration cells were filled with SO_2 concentrations corresponding to column densities of 3.5×10^{17} molec/cm^2 (140 ppmm) and 1.8×10^{18} molec/cm^2 (720 ppmm), respectively[2]. The instrument used during the measurements at Popocatépetl is described in more detail in Lübcke (2010), a sketch of this instrument is shown in Figure 4.2. After the measurements were conducted some drawbacks were discovered that lead to the development of a new SO_2 camera prototype. One of the main disadvantages is the relatively high read-out time of the CCD. The read-out time is approximately 1 s per image, thus leading to acquisition rates of the order of 0.25 Hz for a complete set of SO_2 camera images. The second problem concerns the shutter used in the Apogee U6 camera. The Melles Griot shutter used in this camera has an opening time of 1/60 s, which restricts the range of possible exposure times at the lower end. Additionally the expected life-time is only 100,000 cycles, which can be easily reached within a two week measurement campaign. The shutter was replaced by a shutter that is based on Pöhler (2009) after the measurement campaign in 2011. The SO_2 camera with the improved shutter was permanently installed at Popocatépetl in June 2011 to perform continuous measurements.

[2]The unit of ppmm is used similar to Kern (2009). The units molecules/cm^2 where converted to ppmm assuming standard pressure and a temperature of 20°C throughout the text: 1 ppmm=2.5×10^{15} molec/cm^2.

The SO_2 camera used at Stromboli volcano

The SO_2 camera used for the Stromboli measurement is an updated system using the same basic optical set-up as the camera used at Popocatépetl. This instrument is explained in more detail in Illing (2011) and Huwe (2013). The CCD is an e2v 4710 BI CCD with a custom-made read-out electronic by khs-electronics. The CCD is a back-thinned detector and thus has a very high quantum efficiency of $\approx 60\%$ in the UV region used for the measurements. The high quantum efficiency allows short exposure time even though the CCD has a smaller detector area of $13.3 \times 13.3\,\mu$m. The focal length is reduced to 32 mm which results in a FOV of $23.5° \times 23.5°$. In this instrument the aperture is installed directly behind the plano-convex lens. During the measurements at Stromboli a small aperture of $f/12$ was used. To minimize the size and the costs of the set-up the filters and the lens use standard optic components with a diameter of 25.4 mm. The interference filters have central wavelengths of 315 nm (Filter A) and 330 nm (Filter B) similar to the other camera model. The two calibration cells were filled with SO_2 concentrations corresponding to column densities of 1.14×10^{18} molec/cm^2 (456 ppmm) and 2.55×10^{18} molec/cm^2 (1020 ppmm).

4.1.2 The Narrow Field-of-View DOAS

For calibration purposes a Narrow Field-of-View DOAS (NFOV-DOAS) system was installed inside the camera housing. It measures the SO_2 column density at the approximate centre of the camera image (see Figure 3.5 and Kern et al., 2010b). The DOAS system consists of an Ocean Optics USB2000+ spectrometer, a 400 μm fibre, a Hoya U330 filter to reduce stray light, and a telescope with a quartz lens. A lens with a focal length of $f = 30$ mm and a diameter of 18.5 mm was used at Popocatépetl. At Stromboli a lens with a focal length of $f = 30$ mm and a diameter of 25 mm was used to obtain a smaller DOAS FOV of 0.46° (Illing, 2011). The telescope of the DOAS system is mechanically attached to the camera optics to minimize changes in the FOV relative to the camera images. The temperature of the spectrometer was stabilized to 15 °C for measurements at Popocatépetl and 20 °C at Stromboli. This was done with a peltier element controlled by an Arduino board (Arduino Uno manufactured by SmartProjects) running a PID control software, and an Analog Devices ADT7410 temperature sensor.

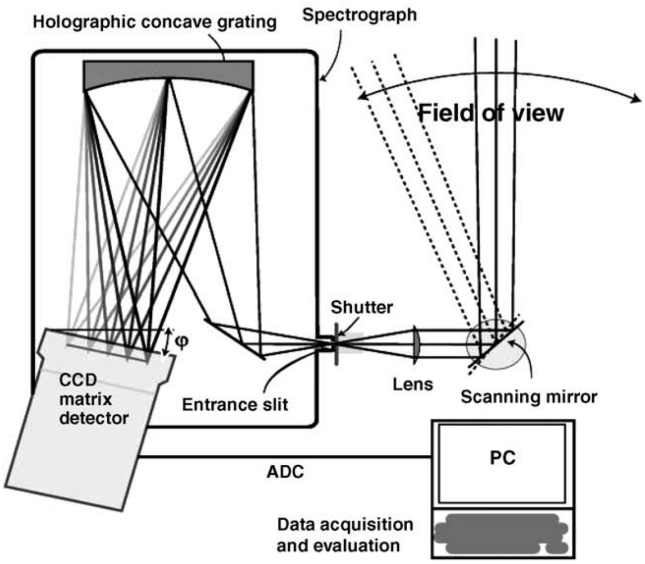

Figure 4.3.: Sketch of an IDOAS instrument consisting of the imaging spectrometer, a lens and a rotating mirror. Reprinted from Bobrowski et al. (2006) with permission from Elsevier.

4.1.3 The Imaging-DOAS instrument

The Imaging DOAS (IDOAS) is an instrument that uses a two-dimensional CCD as a detector in an imaging spectrometer to measure two-dimensional trace gas distributions (Bobrowski et al., 2006; Lohberger et al., 2004; Louban et al., 2009). Note that the IDOAS instrument determines the two-dimensional distribution of the SO_2 column densities – just as the SO_2 camera – however, using the DOAS technique rather than Eq. 3.35. During the measurements, the horizontal direction of the CCD resolved spectral information, while the vertical direction was used to capture one spatial dimension. The second spatial dimension (horizontal direction) is obtained by applying the push-broom method, realized by rotating a mirror to scan along the second spatial dimension (see Figure 4.3). The IDOAS instrument uses a quartz lens with $f = 30\,\mathrm{mm}$ ($d = 20\,\mathrm{mm}$) to image the incident radiation onto the entrance slit of the spectrograph (Jobin Yvon UFS-200, $f = 21\,\mathrm{cm}$, $f/\# = 3.2$, grating: $1200\,\mathrm{lines\,mm^{-1}}$); an Andor DV-420-OE (1024 pixel columns by 255 pixel rows) serves as a detector. Measurements were conducted simultaneously to the SO_2 camera observations on 4 March 2011 to compare the NFOV-DOAS calibration with a second instrument and to verify the calibration over the spatial extent of the complete image instead of only the small region captured by the NFOV-DOAS. Information about the spatial resolution, FOV and settings of the IDOAS are summarized in Table 4.1.

4.2 Measurement geometry for the two measurement campaigns

4.2.1 Measurement geometry at Popocatépetl

Measurements from Popocatépetl were acquired on 1, 2 and 4 March 2011. These measurements will be used to discuss the two calibration methods. For clarity, these days will be referred to as Day 1, Day 2 and Day 3, respectively, during the discussion of the calibration methods. Measurements were performed from the ranger's post at Paso de Cortés (longitude: -98.64694°E, latitude: 19.0867°N, $\approx$3700 m above sea level), approximately 7 km north of the volcano's vent. The viewing direction of the camera and the solar azimuth angle are shown in the top row of Figure 4.4, for the start and end times of measurements. The red line indicates the viewing direction used for calibration cell and background image acquisition. Photos giving an impression of the measurement conditions during the three days are shown in the bottom row of Figure 4.4. During all measurements, background images and calibration cell images were acquired before and after measurements if an area of clear sky was available. All calibration cell measurements presented here were performed in the morning hours (between 09:30 a.m. and 11:00 a.m. local time) with approximately the same viewing direction. Additional car traverses were performed with a zenith-looking DOAS instrument to determine the wind direction. However, the car traverses were usually not conducted at the same time as camera measurements.

4.2.2 Measurement geometry at Stromboli

Stromboli is a 926 m high volcanic island in the Tyrrhenian Sea (Italy). Measurements were conducted as a part of the Imaging Volcanic Plumes Workshop from the terraces of the Hotel Villagio Stromboli. The Hotel is located approximately 2.6 km North-East of the volcanic vents. The measurements were performed from approximately 20 meters above sea level during the 26, 28, 29 and 30 of June 2013. However, only data from 26 June, 2013 is presented in this thesis. Explosive activity in combination with the viewing geometry of the camera led to problems with the wind speed determination that is usually used for the calculation of the SO_2 emission rates (see Section 4.5.1). The measurement conditions during the here presented day were excellent, with clear sky during the complete time.

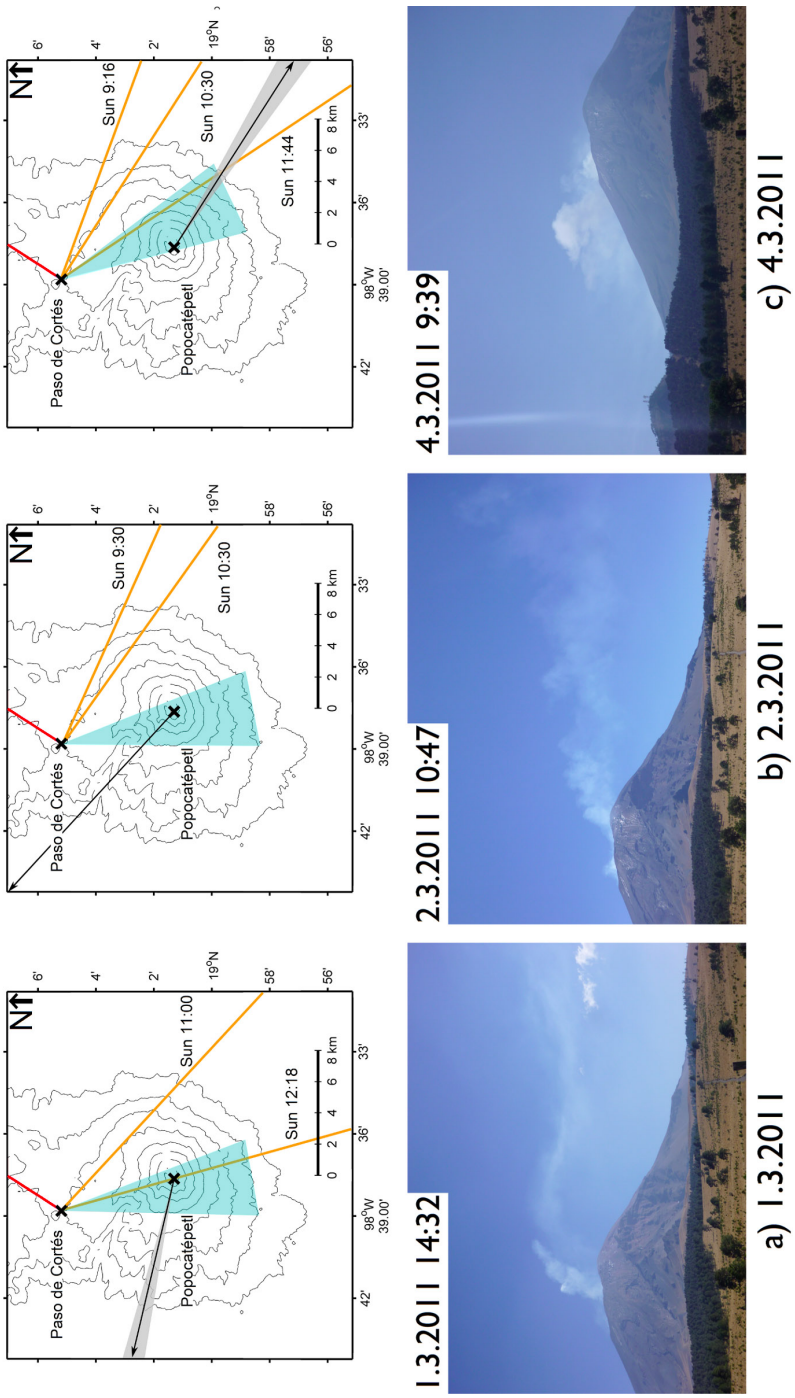

Figure 4.4.: Measurement geometry and photographs of the measurement conditions for the three days discussed in the text: **(a)** 1 March 2011, **(b)** 2 March 2011, **(c)** 4 March 2011. Top row: sketches of the measurement geometry. For all three measurement days the solar azimuth during the start and end time of the measurement is shown as orange lines. The camera field of view is depicted as a light blue area. The direction in which the calibration cell measurements were made is indicated by the red line. The black arrows show the general wind direction, the grey shaded areas indicate the range of wind directions. Bottom row: pictures of Popocatépetl and plume taken from the instrument position (Paso de Cortés) on all three days . The image from the 1 March 2011 was not taken simultaneously to the measurements, but the measurement conditions were similar. From Lübcke et al. (2013b)

4.3 Data acquisition and processing

4.3.1 SO_2 camera images

The SO_2 camera acquired images with both filters sequentially: exposure times were adjusted to keep the maximum measured intensity signal at about 85 % of the maximum intensity (65 536 counts with the 16 bit ADC). Before and after each measurement period, the camera was pointed towards a region of the sky free of clouds and volcanic gas (if available), to obtain background images for both filters. Normalisation with the background images removes vignetting from the camera images, as this effect occurs both in the background as well as in the measurement images. Whenever background images were acquired, images with the calibration cells inserted into the light path and reference spectra for the DOAS evaluation were also recorded.

As a first evaluation step all camera images were corrected for offset and dark current by subtracting a dark image. Next, the background images I_0 were scaled such that the average intensity in a gas-free subsection of the plume images I_{M} matches the average intensity in the same subsection of the respective background images. This step has to be performed to account for varying radiation intensities throughout the time of the measurements. The result are normalised intensities $I^*_{\mathrm{A},0}$, $I^*_{\mathrm{B},0}$:

$$I^*_{\mathrm{A},0} = c_{\mathrm{A}} \cdot I_{\mathrm{A},0} \tag{4.1}$$

$$I^*_{\mathrm{B},0} = c_{\mathrm{B}} \cdot I_{\mathrm{B},0} \tag{4.2}$$

with

$$c = \frac{\bar{I}_{\mathrm{M}}^{\text{Clear Sky}}}{\bar{I}_{0}^{\text{Clear Sky}}} \tag{4.3}$$

From the normalised background images $I^*_{A/B,0}$ and the measurement images $I_{A/B,M}$ the AA can now be calculated according to Eq. 3.35.

For the comparison with the SO_2 column densities obtained by the IDOAS and the calculation of the SO_2 emission rates, all AA images were corrected for higher sensitivity towards the edges of the detector by dividing each pixel of the AA images by the corresponding pixel of a correction mask (see Section 4.4.1). This mask was created by fitting a 2^{nd} order polynomial to the optical densities τ_A and τ_B from calibration cell images, not considering areas affected by reflections (Sections 4.4.1 and 4.4.2). From these fits a reflection free AA image of a calibration cell was calculated. The correction mask was then obtained by normalizing the AA with respect to the area where the DOAS telescope was pointing to.

4.3.2 Spectroscopic retrieval

The spectra recorded with the two spectrometers (NFOV-DOAS, IDOAS) were evaluated for SO_2 between 314.6 nm and 326.8 nm. The absorption cross sections of SO_2 (298K, Vandaele et al., 2009) and O_3 (both 221 K and 241 K, Burrows et al., 1999) were fitted to the measurement spectra along with a Fraunhofer reference spectrum (measured away from the plume in close time proximity). A Ring spectrum (Grainger and Ring, 1962), calculated from the Fraunhofer reference, was included in the fit as well. All cross sections were convolved to the instrument resolution using the measured instrument response to the 334.15 nm line of a mercury emission lamp. The Fraunhofer reference spectrum linked together with the Ring spectrum was allowed to be slightly shifted and squeezed against the measurement spectrum during the DOAS evaluation. All reference cross sections were also allowed to be shifted and squeezed together as a set. A maximum shift of ± 0.2 nm and squeeze of ± 2 % were allowed in both cases.

The DOAS fit for the IDOAS data was performed individually for each pixel using the same evaluation scheme as for the other spectroscopic data. As the instrument's slit function varies over the detector, the cross sections were individually convolved for each row of the detector. Due to problems with data logging, no exposure times were available for the IDOAS. Spectra were therefore only corrected for offset. However, later measurements, at the same detector temperature as during the measurements in Mexico, determined that the dark current can be considered below 0.1 % of the signal for exposures times of approximately 3 s, and is therefore negligible.

4.3.3 Determination of the DOAS FOV

To calibrate the SO_2 camera with a DOAS system, it is important to exactly know the area to which the NFOV-DOAS telescope points to. The viewing direction of the telescope relative to the camera's FOV was measured before the campaigns in the laboratory. This was done by coupling light from a halogen lamp into the spectrometer side of the optical fibre. The light beam from the DOAS telescope was then projected onto a wall. Afterwards images were acquired with the SO_2 camera to determine the position of the light spot on the wall in the camera image. However, after the measurements in Mexico were completed, we found that the FOV had changed during the transport to the measurement site or back to the laboratory. Therefore the size of the FOV and viewing direction of the telescope, relative to the camera's FOV, were estimated by searching for the best correlation between AA time series recorded by the SO_2 camera and SO_2 column density time series recorded by the NFOV-DOAS (as described in Kern et al., 2010b). The algorithm that was used is also described in more detail in Lübcke (2010). For this work, the technique was adapted with some minor changes. Instead of quadratic sectors a round FOV was chosen. This is a better approximation of the true FOV of the DOAS telescope, which is usually round.

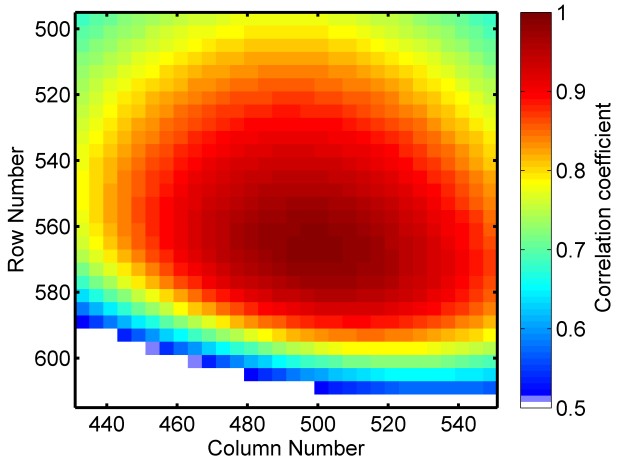

Figure 4.5.: The viewing direction of the NFOV-DOAS instrument was derived from the correlation coefficient between the SO_2 camera AA values and the NFOV-DOAS SO_2 column densities. The coordinates of highest correlation denote the position of the centre of the DOAS FOV in the camera image (Circle with a radius of 57 pixels). Correlation coefficients of 0.5 or below are shown white. Reproduced from Lübcke et al. (2013b).

The radius of the FOV was varied and for each radius, the FOV was shifted across the camera image. For each position an AA time series was created by calculating the mean AA value in the FOV as a function of time. As the acquisition time of the spectrograph generally is different from the acquisition time for the camera, the AA time series obtained from the camera images was interpolated to match the acquisition times of the DOAS spectra. After the time interpolation, the linear correlation between the AA time series and the SO_2 column density time series from the DOAS was calculated. This way the radius with the best correlation was obtained. A "correlation map" can be plotted, that shows where the correlation between the camera's AA time series and the DOAS's SO_2 column density time series has its maximum (see Figure 4.5). A stable design of the SO_2 camera-NFOV-DOAS assembly and laboratory calibration is preferable. However, since this is not always achievable, it is recommended to check the relative alignment by the method described above.

4.3.4 Comparison between SO_2 camera and IDOAS

The SO_2 camera and the IDOAS differ in temporal and spatial resolutions. While the SO_2 camera acquires an AA image approximately every 3 to 4 s with a quadratic FOV of roughly $22° \times 22°$, the IDOAS needs between 5 and 25 s to acquire one column of the image with a FOV of 13° (vertically) $\times$ 0.26° (horizontally). For example, the image that was used to validate the SO_2 camera calibration was recorded between 10:30 a.m. and 11:15 a.m. on 4 March 2011. It has a spatial extension of 13° (vertically) $\times$ 44.5° (horizontally). The SO_2 camera recorded 815 AA images during this time period. The data obtained

from the two instruments were carefully prepared to be comparable. As a first step, a transformation matrix was created to translate, rotate, shear and scale the SO_2 camera images to the IDOAS FOV. This was done by manually choosing feature points (e.g. vent of the volcano) that can be distinguished in both the SO_2 camera image and in the IDOAS image. This set of points was used to create the image transformation matrix. After the matrix was applied to all camera images, the images matched a sub-section of the IDOAS FOV (since the IDOAS image has a larger horizontally FOV than the SO_2 camera). The acquisition start and end time is known for each column of the IDOAS: for the corresponding image constructed from SO_2 camera measurements, the average of all camera images recorded between the start and end time were used to construct the corresponding column for the comparison.

The error induced by the image transformation was investigated by comparing several cross sections through the image in the horizontal and in the vertical direction. From these cross sections the maximum displacement was estimated to be below $\Delta x = 1$ pixel in the x-direction, and below $\Delta y = 2.5$ pixels in the y-direction. Next the gradients for the AA image $\frac{\Delta\tau}{\Delta x}$ and $\frac{\Delta\tau}{\Delta y}$ were calculated for each pixel. The uncertainty in τ originating from the image transformation was calculated using error propagation:

$$\Delta\tau = \sqrt{(\frac{\Delta\tau}{\Delta x} \cdot \Delta x)^2 + (\frac{\Delta\tau}{\Delta y} \cdot \Delta y)^2} \tag{4.4}$$

As this error estimation showed, that some pixel had rather large errors, we removed all values with an error above $\Delta\tau = 0.05$, this however did not change the calibration curve.

4.4 Calibration of the SO_2 camera

As already outlined in Section 3.3.2 the AA (see Eq. 3.35) has to be converted to SO_2 column densities before SO_2 emission rates can be calculated. The SO_2 camera was originally calibrated with the help of SO_2 calibration cells containing a known SO_2 concentration. More recently, Kern et al. (2010b) suggested to use a DOAS instrument for the calibration. During the work on this thesis both calibration methods were extensively studied. The two methods were compared with the data acquired at Popocatépetl in March, 2011. Possible pitfalls were identified. This section will show the results of the comparison. The results and large parts of the text in this section were already published in Lübcke et al. (2013b).

Several effects that can negatively influence the SO_2 camera calibration will first be treated theoretically in Section 4.4.1. Section 4.4.2 presents results acquired from calibration cell measurements. This includes reflections on the calibration cells that can falsify the calibration and variations of the SO_2 sensitivity across the detector. Section 4.4.3 concludes the discussion on the SO_2 camera calibration with a comparison of cell calibration and DOAS calibration during the measurements at Popocatépetl. It will be shown that aerosol and plume condensation can lead to wrong results when calibrating the SO_2 camera with calibration cells.

4.4.1 Theoretical considerations on the calibration

Non-uniformity of calibration across the field of view

Typically, SO_2 cameras show an increase in sensitivity for a given SO_2 column density with increasing distance from the optical axis (i.e. the sensitivity increases towards the corners of the image). The AA for a given SO_2 column density is influenced by the transmission curve of band-pass interference filters (Kern et al., 2010b). These interference filters show a shift of the filter transmission window towards shorter wavelengths when not illuminated perpendicularly. Since the SO_2 absorption cross section becomes larger towards shorter wavelengths (e.g. Vandaele et al., 2009), the optical density measured with Filter A also increases. Because the influence of SO_2 on the optical density of Filter B is negligible (also for non-perpendicular illumination) the AA increases considerably for off-centred illumination. As the mean illumination angles at the edges of the detector are larger than at the centre of the image, the AA increases towards the sides of the image. The transmission curve thus changes over the range of the detector depending on the filters chosen and the optical set-up. Every camera should be carefully characterised. The non-uniformity of the response can be eliminated by proper calibration.

Model calculations on the non-uniformity were shown in Lübcke (2010) and Kern et al. (2013). Lübcke (2010) showed, that a camera design in which the

filter is placed between lens and detector reduces the variation of the sensitivity. Based on these findings Kern et al. (2013) found an idealised design, that greatly diminishes the effects of non-uniform calibration through a short focal length in combination with a large aperture.

Reflections on the interference filters and gas cells

Radiation arriving at the interference filter is only partly transmitted even at the peak transmission wavelength. A small fraction is absorbed and a remaining, significant fraction is reflected. If the reflected radiation passes the aperture, part of it is reflected a second time on the windows of the calibration cell. Radiation reflected on the front window of the cell passes the inside of the calibration cell, and therefore the SO_2 concentration, two additional times before part of it reaches the detector (see Figure 4.1). Since the reflectivity of the two interference filters is different, the reflection effects do not cancel out in the calculation of the AA for a calibration cell image. Without reflection from the interference filter, radiation arriving at the interference filter (with a calibration cell in the light path) can be described by:

$$I(\lambda) = I_0 \cdot e^{-\sigma(\lambda)\cdot S} \cdot (1 - R_Q(\lambda))^4 \tag{4.5}$$

with the incoming solar radiation I_0, the SO_2 cross section $\sigma(\lambda)$, the SO_2 column density along the light path S and the Fresnel reflectivity R_Q at each quartz window of the calibration cell. The exponent of 4 results from the four transitions between quartz glass and air that influence radiation when passing through the calibration cell. When taking reflections on the inference filters into account, more radiation arrives at the interference filter. Neglecting higher orders reflection terms, i.e. using only radiation that was reflected once at the interference filter and reflected once at one of the different walls of the calibration cell into the direction of the detector and also neglecting the angle dependence of R_Q, we obtain an additional intensity:

$$\Delta I_X(\lambda) = I(\lambda) \cdot R_X(\lambda) \cdot R_Q \cdot \left(\sum_{n=1,2} (1 - R_Q)^{2\cdot(n-1)} + \right.$$
$$\left. + \sum_{n=3,4} e^{-2\cdot\sigma(\lambda)\cdot S} \cdot (1 - R_Q)^{2\cdot(n-1)} \right) \tag{4.6}$$

In this equation $R_X = 1 - T_X$ is the reflectivity of the interference filter and T_X is the transmittance. The terms for n = 1,2 describe reflections on Window 2 in Fig. 4.1, the terms n = 3,4 describe reflections on Window 1. Radiation that is reflected from Window 1 has to pass the inside of the calibration cell twice, and is influenced by SO_2 absorption during each traverse. The term $(1 - R_Q)^{2\cdot(n-1)}$ describes the losses at each quartz glass – air interface. For example, radiation

that was reflected from the interference filter passes three interfaces before it is reflected on the outer surface of Window 1 and it passes three additional interfaces before arriving at the interference filter again. Thus, losses for the 6 transitions are accounted for by the term $(1 - R_Q)^6$. Note that reflection on the lens has been neglected because its anti-reflection coating suppresses reflectivity well below that of the calibration cell windows.

A sample calculation for the central wavelengths of the interference filters will give an estimate of the magnitude of these effects. The central wavelength of Filter A is 315 nm with a transmission of $T_{\mathrm{A},315\,\mathrm{nm}} = 0.64$; the central wavelength of Filter B is 330 nm with $T_{\mathrm{B},330\,\mathrm{nm}} = 0.45$ (both measured in the laboratory). Quartz glass, as used for calibration cells, has a refractive index of $n = 1.4841$ at 315 nm and $n = 1.4808$ at 330 nm (Interpolated from Heraeus, 2012).

The Fresnel equations generally describe the reflection and refraction of radiation at the interface between two different media with refractive indices n_1 and n_2. The reflection coefficients for the polarization plane perpendicular to ($R_\perp$) and parallel to ($R_\parallel$) the plane of incidence are given by:

$$R_\perp = \left(\frac{n_1 \cos\alpha - n_2 \cos\beta}{n_1 \cos\alpha + n_2 \cos\beta} \right)^2 \tag{4.7}$$

$$R_\parallel = \left(\frac{n_2 \cos\alpha - n_1 \cos\beta}{n_2 \cos\alpha + n_1 \cos\beta} \right)^2 \tag{4.8}$$

Here α is the incidence angle and β is the refraction angle. For perpendicular ($\alpha = 0$) illumination of the interface between air ($n \approx 1$) and fused silica with unpolarized incident radiation, the equations can be simplified to:

$$R = \frac{R_\perp + R_\parallel}{2} = \left(\frac{n-1}{n+1} \right)^2 \tag{4.9}$$

We therefore obtain reflection coefficients of $R_\mathrm{A} = 3.81 \times 10^{-2}$ (315 nm) and $R_\mathrm{B} = 3.76 \times 10^{-2}$ (330 nm) respectively for perpendicular illumination of the calibration cell. These reflection coefficients inserted in Eqs. (3.35) and (4.6) lead to $\tau_\mathrm{A} = -0.0478$, $\tau_\mathrm{B} = -0.0714$ and thus to an AA of -0.0236 (corresponding roughly to an SO_2 column density of $\approx 2.4 \times 10^{17}$ molec/cm^2) for an empty calibration cell ($S = 0$, and assuming $I_{X,M}(\lambda) = I_X(\lambda) + \Delta I_X(\lambda)$). This means that the AA of a low concentration gas cell recorded at the centre of the image could be significantly skewed (by up to the equivalent of ~ 100 ppmm) towards lower values.

In reality the situation is even more complex. For one, we do not solely have perpendicular reflection. This leads to an increase in reflectivity (Eqs. 4.7 and 4.8). However, most rays that are reflected by the band-pass filter will be blocked by the aperture and thus do not arrive at the calibration cell again. Of those rays that arrive, only the ones that arrive at the interference filter

perpendicularly will be reflected to the same position on the detector. In general each ray will be reflected to another position on the detector. Another effect reducing the influence of the reflection is that the reflectivity of the interference filter in general is somewhat less than $R_X = (1 - T_x)$ as a fraction of radiation is absorbed inside the interference filter. The magnitude of the described effect strongly depends on the optical set-up but it will also occur for interference filters that are mounted in front of the lens and any calibration cells that are mounted reasonably parallel to the lens.

Aerosol influence on the calibration curve

SO_2 cameras that use a second filter to correct for plume condensation and aerosols in the volcanic plume usually assume that these effects are independent of wavelength in the region between 300 nm – 335 nm. However, as discussed in Section 3.1.2 both Mie scattering and Rayleigh scattering show a wavelength dependency.

Using Eq. 3.10 the ratio κ_{Mie} between the scattering cross sections σ_{Mie} at two different wavelengths λ can be written as:

$$\kappa_{\text{Mie}} = \frac{\sigma_{\text{Mie},\lambda_1}}{\sigma_{\text{Mie},\lambda_2}} = \left(\frac{\lambda_1}{\lambda_2}\right)^{-\alpha} \tag{4.10}$$

For Rayleigh scattering, the ratio κ_{Ray} between the scattering cross sections σ_{Ray} at two different wavelengths λ can be calculated from Eq. 3.5:

$$\kappa_{\text{Ray}} = \frac{\sigma_{\text{Ray},\lambda_1}}{\sigma_{\text{Ray},\lambda_2}} = \left(\frac{\lambda_1}{\lambda_2}\right)^{-4} \tag{4.11}$$

The effect of radiation being absorbed or scattered out of the camera's FOV on aerosols as it passes through the volcanic plume is wavelength dependent. With Eq. (4.10) we get the relationship between the aerosol optical depths (AOD) $\tau_{\text{A,aerosol}}$ and $\tau_{\text{B,aerosol}}$ at two wavelengths:

$$\tau_{\text{A,aerosol}} = \tau_{\text{B,aerosol}} \cdot \kappa_{\text{Mie}} \tag{4.12}$$

The influence on SO_2 camera measurements can be approximated by inserting the central wavelengths of the interference filters used during the experiments ($\lambda_1 = 315$ nm and $\lambda_2 = 330$ nm) into Eq. (4.12). An Ångström Exponent of 1.2 was chosen as this value is thought to be representative of a typical volcanic plume (Spinetti and Buongiorno, 2007):

$$\tau_{\text{A,aerosol}} = \kappa_{\text{Mie}} \cdot \tau_{\text{B,aerosol}} = 1.057 \cdot \tau_{\text{B,aerosol}} \tag{4.13}$$

This indicates that $\tau_{\text{A,aerosol}}$ would be 5.7 % higher than $\tau_{\text{B,aerosol}}$ for a given AOD. This means, while Filter B does certainly reduce the influence of aerosol on SO_2

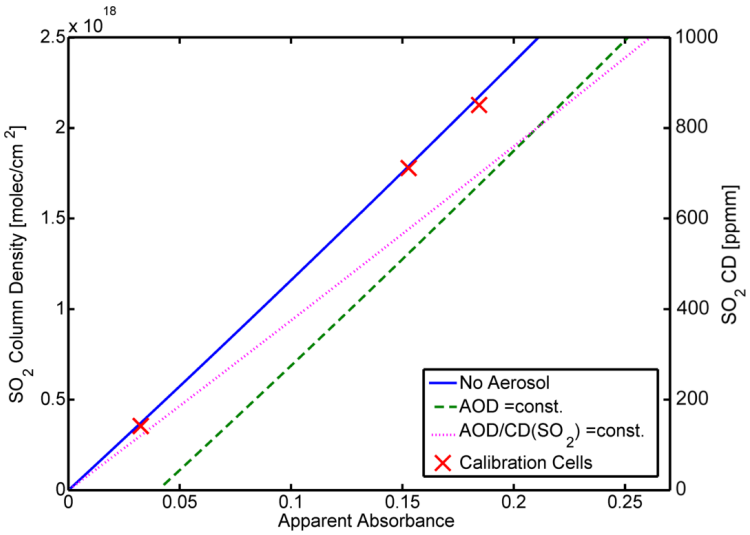

Figure 4.6.: Camera calibration curves simulated from a sky spectrum recorded with the DOAS spectrometer from Paso de Cortes, Mexico on 2 March 2011. The calibration curve for the no aerosol case (blue, slope of 1.185×10^{18} molec/cm^2) coincides with calibration cell measurements performed at the same time (red crosses). The curve for a constant AOD (shown for $\tau_{\text{B,Aerosol}} = 0.7$) (dashed green line) is parallel to the No Aerosol line, but is shifted by an optical density of 0.04. Assuming a linear relationship between the SO_2 column density and τ_{Aerosol}, as we might expect in a real plume, we obtain the red dotted line. We here assumed $\tau_{\text{B,Aerosol}} = 1.0$ for an SO_2 column density of 2.0×10^{18} molec/cm^2. The slope is reduced when compared to the other cases (9.57×10^{18} molec/cm^2). Reproduced from Lübcke et al. (2013b).

camera measurements, it does not completely remove it. For a constant AOD in the volcanic plume the calibration curve would be shifted towards higher AA values. However, it is likely that the AOD increases with increasing SO_2 column density. For a linear relationship between SO_2 and AOD we obtain a calibration curve with a lower slope (see Fig. 4.6).

Besides absorption or scattering radiation out of the camera's FOV, volcanic (as well as atmospheric) aerosols also scatter radiation not originating from behind the plume into the camera's FOV. The AA therefore changes, depending on the amount of radiation scattered into the FOV. We will here focus on scattering of radiation by volcanic aerosol. For the sample calculation we assume that the radiation scattered into the camera's FOV from aerosol is proportional to $I_{\text{A/B,M}}$. Geometrical considerations show, that the mean light path length for radiation that was scattered into the camera's FOV from inside the volcanic plume is close to the length of a straight line through the plume assuming a round plume cross section. The fraction δ of the measurement intensity $I_{\text{B,M}}$ at 330 nm is scattered into the camera's FOV. The additional intensity therefore is $\delta \cdot I_{\text{B,M}}$ for Filter B. For Filter A the fraction of additional radiation is different. We have to take into account, that Mie scattering on particles in the plume has a different wavelength dependency compared to Rayleigh scattering in the

background atmosphere. This is done by multiplying $\frac{\kappa_{\text{Mie}}}{\kappa_{\text{Rayleigh}}}$. The fraction of additional radiation for Filter A is then $\delta \cdot \frac{\kappa_{\text{Mie}}}{\kappa_{\text{Rayleigh}}}$.

$$\begin{aligned} \tau &= \tau_{\text{A}} - \tau_{\text{B}} = -\ln\left(\frac{I_{\text{A,M}} \cdot (1 + \delta \cdot \frac{\kappa_{\text{Mie}}}{\kappa_{\text{Rayleigh}}})}{I_{\text{A,0}}}\right) + \ln\left(\frac{I_{\text{B,M}} \cdot (1+\delta)}{I_{\text{B,0}}}\right) \\ &= \tau_{\text{SO}_2} + \underbrace{\ln\left(\frac{1+\delta}{1+\delta \cdot \frac{\kappa_{\text{Mie}}}{\kappa_{\text{Rayleigh}}}}\right)}_{\Delta\tau} \end{aligned} \tag{4.14}$$

Since $\frac{\kappa_{\text{Mie}}}{\kappa_{\text{Rayleigh}}}$ is less than one there is a shift of the calibration curve towards higher AA values if radiation is scattered into the FOV by Mie scattering (note: the DOAS technique is not affected by this since broad band structures are removed in the DOAS evaluation). For an Ångström exponent of 1.2 and $\delta = 0.2$ we obtain $\Delta\tau = 0.0206$, with the central wavelengths of the Filters used during this work. This means one can obtain a signal equivalent to an SO_2 column density of 2.5×10^{17} molec/cm^2 or 100 ppmm if 20% of the measured radiation intensity are scattered into the camera's FOV on aerosol in the volcanic plume.

4.4.2 General results from calibration cells

Figure 4.7 a shows the AA of a calibration cell with an SO_2 column density of 1.8×10^{18} molec/cm^2 (720 ppmm). The image was created by applying Eq. (3.35) to images taken in the background geometry with the calibration cell covering the entire FOV. As the viewing direction does not change, and the calibration cell measurements are performed within 5 minutes, no normalisation (Eq. 4.3) is necessary, i.e. $c_{\text{A}} = c_{\text{B}} = 1$. Two features can be seen in Figure 4.7 a: First, a clear increase in signal with increasing distance from the centre of the image can be observed. There is an increase in AA of up to 85 % between the centre, where AA is lowest, and the corners of the detector, where the highest AA values can be observed.

The second feature that can be seen in Figure 4.7 a is a (slightly off-centre) ring like structure (arrows) in the middle of the AA image of the calibration cell. This feature can be attributed to reflections on the windows of the calibration cell (Section 4.4.1).

Figure 4.7 b shows an AA image that was created by fitting two-dimensional 2^{nd} order polynomials to the variation of intensity of the calibration cell optical densities τ_A and τ_B, without considering the area affected by the reflection features. The residual between the polynomial fit and the calibration cell images was usually below 0.005 (again, only in the area not affected by reflection).

Figure 4.7 c shows τ_{B} from a calibration cell measurement: a circular structure can be observed in the centre of the image, where the optical density is lower, i.e. more radiation arrives in the centre of the detector than at the rest of

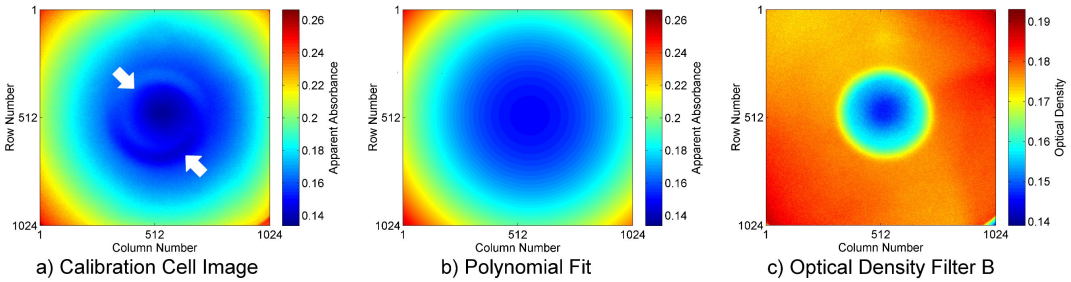

Figure 4.7.: **(a)** AA of a calibration cell with an SO_2 column density of 1.77×10^{18} molec/cm^2. A slight ring-like structure (arrows) is caused by reflections on the calibration cell. **(b)** AA image that was created from 2$^{\text{nd}}$ order polynomial fits to calibration-cell images. The area with reflections in the centre of the images was not considered when determining the best fits. These images were used as a mask to correct for higher sensitivity towards the edges in the IDOAS comparison and for the SO_2 emission rates. **(c)** Optical density τ_B for a calibration cell measurement with Filter B. Reproduced from Lübcke et al. (2013b).

the detector. As the intensity seen through Filter B is essentially unaffected by SO_2 absorption we would expect a flat signal over the complete detector. However, reflections on the calibration cell windows cause additional radiation to be reflected into the centre of the image (see Fig. 4.1).

4.4.3 Results from the field measurements

Calibration

The FOV of the DOAS instrument within the SO_2 camera image had to be derived for the DOAS calibration (see Section 4.3.3). The best correlation between the SO_2 column density time series and the AA time series was found for a circle with a radius of 57 pixels. Small changes in the viewing direction result in variations of the correlation coefficient (see Figure 4.5). Differences in the area with best correlation were found to be very low (on the order of 0.2°) between the different days thus indicating that the pointing of the DOAS telescope in relation to the camera optics had not changed. To assess the uncertainty of the calibration due to the alignment of the instrument's FOV, we investigated the calibration curve for all areas that have a correlation coefficient within 1 % of the maximum correlation coefficient. For these areas found changes of the slope of the calibration curve of up to 8 % when fitting a first order polynomial to the data (data from Day 3 was not included in these estimates as there was a slight deviation from linear behaviour, see Section 4.4.3). Also, the offset of the first order calibration polynomial varied between -2.2×10^{17} molec/cm^2 (~ -90 ppmm) and 1.5×10^{17} molec/cm^2 (60 ppmm) across this area. In future measurements, the uncertainty arising from the viewing direction of the DOAS telescope should be reduced by exactly measuring the DOAS FOV at the measurement site.

For calibration with cells we fitted a 2^{nd} order two-dimensional polynomial to

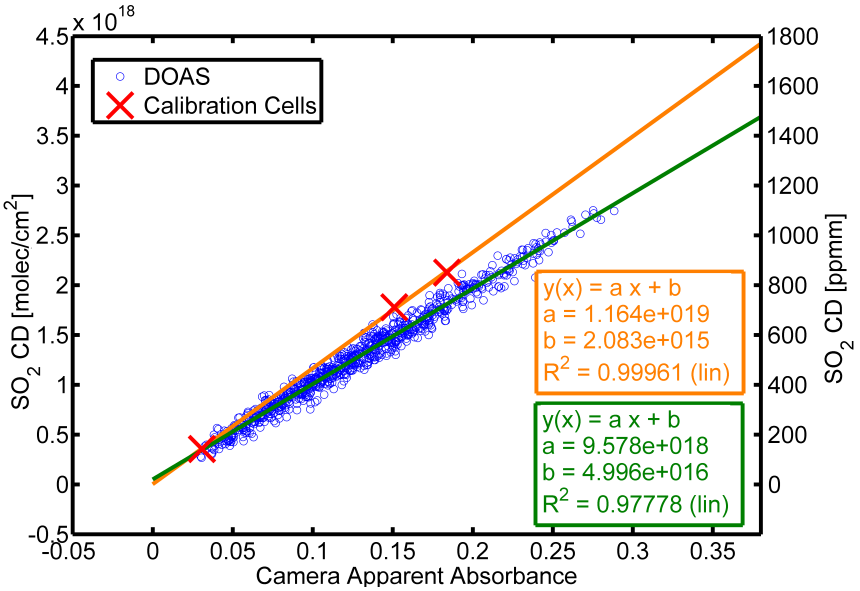

Figure 4.8.: Calibration curve for the SO_2 camera obtained from measurements performed on 1 March 2011 (Day 1). The SO_2 column density derived from the DOAS (blue circles) and calibration cells (red crosses) is shown as a function of the AA measured by the camera. Reproduced from Lübcke et al. (2013b).

the optical density images of the calibration cells (the areas with structures from reflections were removed from the fit, see Sect. 4.3), From these 2D-polynomials we created reflection free AA images. The residual between the 2D fits and the optical density images were usually below an optical density of 0.005 in the areas without reflection structures, thus leading to an uncertainty of approximately 5 % for the calibration curves. The AA value for the calibration curves was then calculated in the same area as the DOAS FOV to be able to compare the two methods. The calibration curves obtained with calibration cells during the three days (see next page) differ very little for all of the measurements. The slope of linear fits to the calibration cell AA/SO_2 column density pairs varied by only about $\sim$ 1 % during the entire measurement period. This indicates that the instrument was very stable and exhibited a nearly constant sensitivity towards SO_2 calibration cells (at close proximity to the instrument).

Day 1, 1 March 2011

On this day, the calibration curves from the calibration cells and the DOAS both showed a linear relationship between AA and SO_2 column density (Figure 4.8). The DOAS measurements correlated very well with the camera's AA time series (R^2 of 0.978). However the slopes derived by the two calibration methods differed by almost 20 %.

The optical densities τ_A and τ_B obtained for the two filters (Figure 4.9) each also showed a linear dependency on the DOAS-derived SO_2 column density.

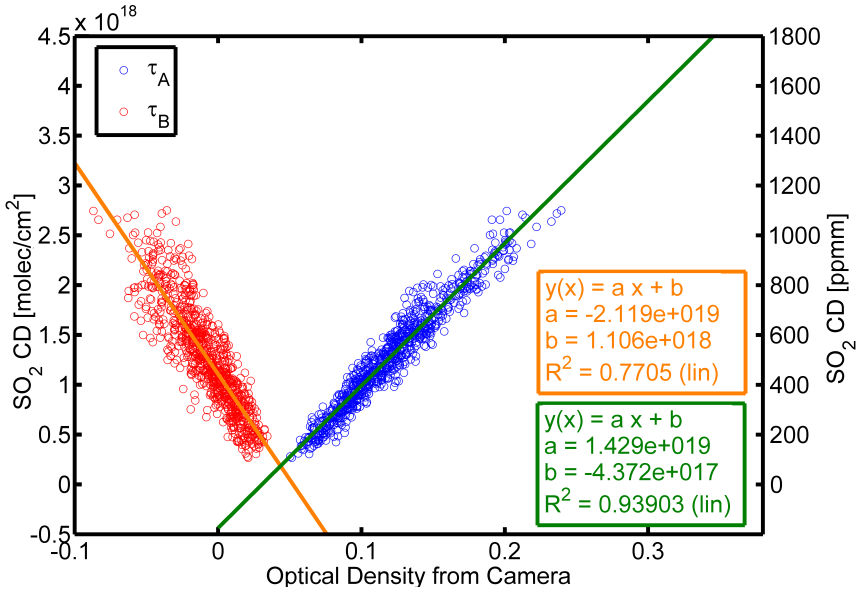

Figure 4.9.: The SO_2 column density from the DOAS plotted against τ_A and τ_B for measurements from 1 March 2011 (Day 1). Note the decreasing optical density τ_B for Filter B with increasing SO_2 column density caused by aerosol scattering in the plume. Reproduced from Lübcke et al. (2013b).

While τ_A exhibited the expected increase in magnitude with increasing SO_2 load due to absorption, τ_B actually decreased with increasing SO_2 column density. This can be explained by light being scattered toward the instruments on aerosol and cloud droplets that are generally co-located with areas of high SO_2 column density. Thus, the plume appears slightly brighter than the background at 330 nm, where SO_2 absorption is negligible.

Figure 4.10 shows the NFOV-DOAS time series in comparison to the SO_2 camera time series (average of the AA for all pixels coinciding with the DOAS FOV) from Day 1. After converting the AA to SO_2 column densities by multiplying with the calibration factor of 9.58×10^{18} molec/cm^2 ($\sim$ 3800 ppmm) obtained from the DOAS (see Figure 4.8, the offset was also taken into account), 95 % of the DOAS measurement values lie within $\pm 1.5 \times 10^{17}$ molec/cm^2 ($\sim$ 60 ppmm) of the camera data points.

Day 2, 2 March 2011

AA values derived in the DOAS FOV again showed very good correlation with the DOAS derived SO_2 column densities on Day 2 (see Figure 4.11). This time the calibration curves derived from the DOAS and the calibration cells showed good agreement. The slope differed by only about 5.6 %, well within the measurement uncertainty, and the offset between the two calibration curves was only 3×10^{16} molec/cm^2 (12 ppmm). The measurements show that the linear relationship between AA and SO_2 column density holds true for up to

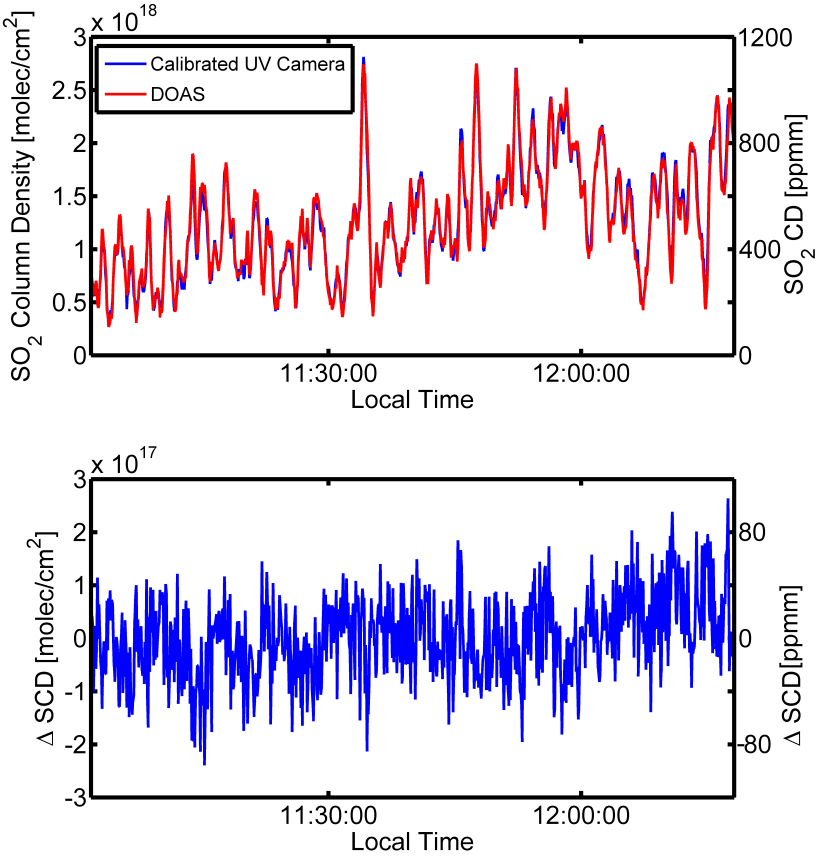

Figure 4.10.: Top: Time series of the SO_2 camera (average values of all pixels coinciding with the DOAS) and the DOAS from 1 March 2011 (Day 1). SO_2 camera values were calibrated with the DOAS. Bottom: Difference between the calibrated camera and the DOAS system. Note, there is a different y-scale in the bottom plot. Reproduced from Lübcke et al. (2013b).

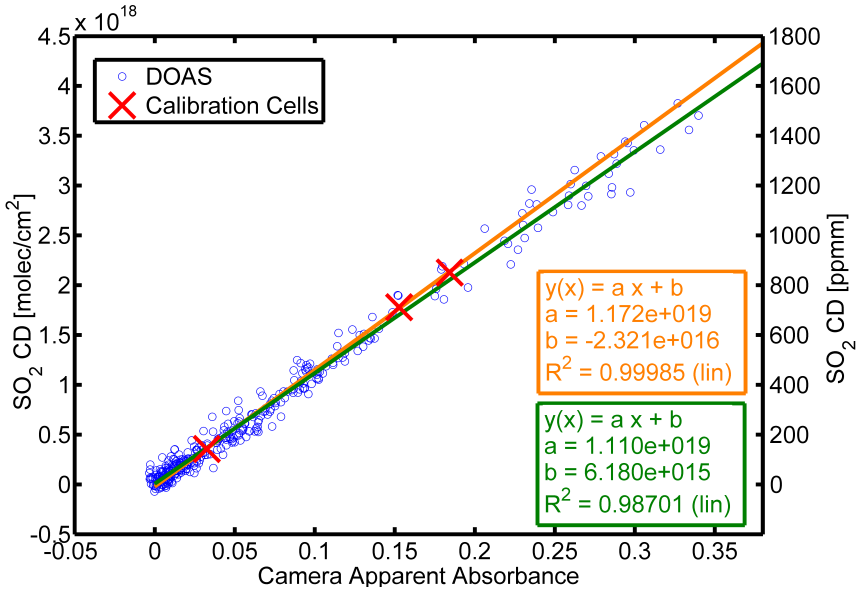

Figure 4.11.: Calibration curve for the SO_2 camera obtained from measurements performed on 2 March 2011 (Day 2). Reproduced from Lübcke et al. (2013b).

4×10^{18} molec/cm^2 (approx. 1600 ppmm) in this case. Figure 4.12 shows the individual optical densities $\tau_{A/B}$ for Filter A and Filter B. While the slope for τ_A is comparable to Day 1, the slope of τ_B is much steeper than on Day 1, i.e. there was less change of τ_B with changing SO_2 column density, likely indicating a smaller aerosol load in the plume on this day.

Day 3, 4 March 2011

On 4 March 2011 two time series were recorded, one between 09:15 a.m. and 10:00 a.m. the other between 10:38 a.m. and 11:45 a.m. From 09:15 a.m. until 09:36 a.m., the DOAS calibration curve (Figure 4.13) is similar to Day 1. This time interval will hence be referred to as "Part 1". For the rest of the measurements, however, the calibration curve deviates slightly from a linear relationship. For increasing SO_2 column densities all data points are shifted towards higher AA values compared to the calibration cells (Figure 4.15). This interval will be referred to as "Part 2". Figure 4.16 shows both time series. Calibration for this figure was performed with the green NFOV-DOAS curve from earlier in the day (Part 1, Fig. 4.13). Calibrated in this way, the camera overestimates the SO_2 column densities in Part 2 when compared with the DOAS for high SO_2 column densities.

The SO_2 column densities are plotted as a function of the optical densities for Filter A and B in Fig. 4.14. The optical densities τ_A and τ_B for Part 1 show similar behaviour as on Day 1. For Part 2 most data points are shifted towards higher optical densities.

Simultaneous IDOAS measurements (taken between 10:38 a.m. and 11:45 a.m.

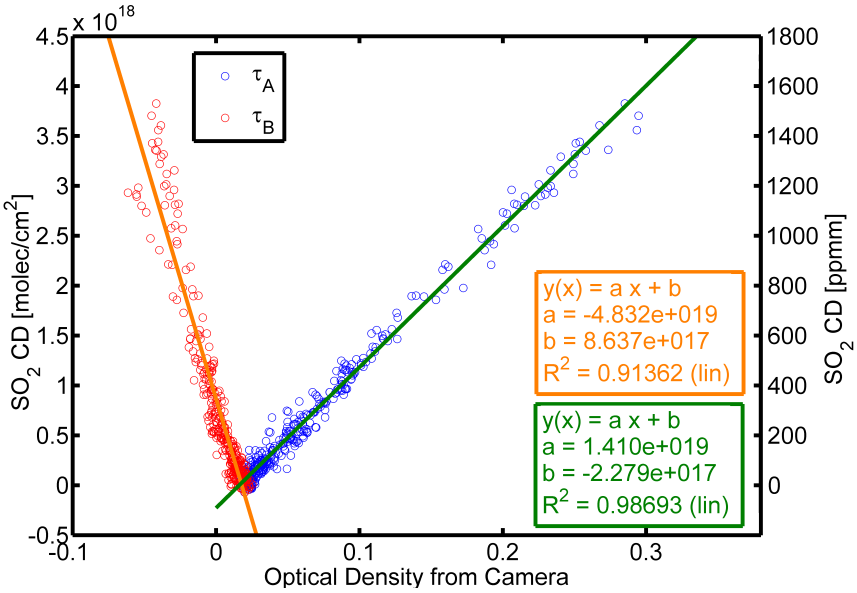

Figure 4.12.: SO_2 column densities from the DOAS plotted against the optical densities for Filter A and Filter B. Measurements from 2 March 2011 (Day 2) at Paso de Cortes. Reproduced from Lübcke et al. (2013b).

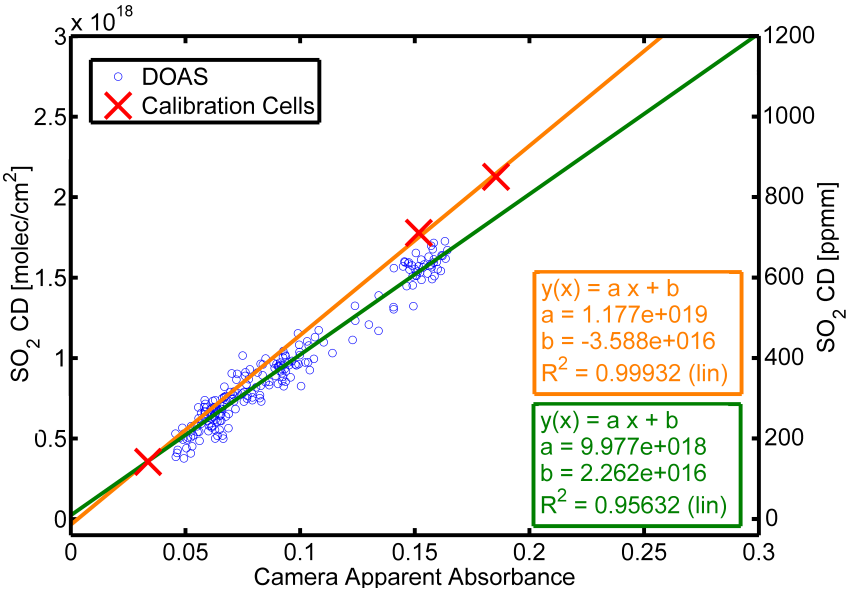

Figure 4.13.: Calibration curves for the SO_2 camera obtained from measurements performed between 09:15 a.m. and 09:36 a.m. on 4 March 2011 (Day 3). Reproduced from Lübcke et al. (2013b).

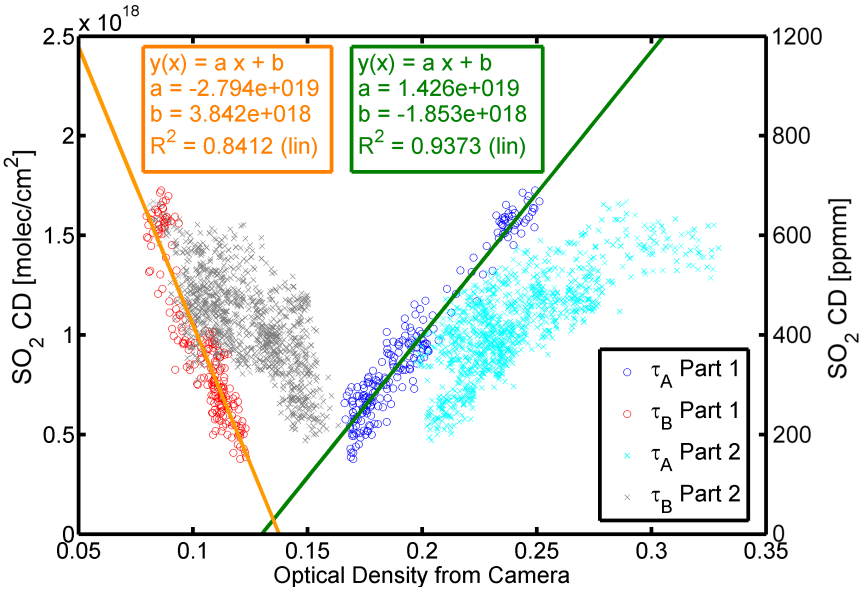

Figure 4.14.: SO_2 column densities from the DOAS measurements plotted against optical densities for Filter A and Filter B for the measurements on Day 3. The optical densities are shifted towards higher values for Part 2. Reproduced from Lübcke et al. (2013b).

on Day 3) were used to further investigate the calibration. Comparing the images constructed from the SO_2 camera (see Section 4.3.4) and the IDOAS measurement (Figure 4.17), the overall structure of the volcanic plume appears similar in both images. A noteworthy fact is that the SO_2 camera exhibits SO_2 columns of up to 2×10^{17} molec/cm^2 (~ 80 ppmm) in areas where the IDOAS shows no enhanced SO_2. This effect is caused by changes in the the background intensity over the FOV of the SO_2 camera. Due to the sun's azimuthal position (approximately in line with the azimuthal viewing direction of the camera, see Fig. 4.4), the ratio between the scattered radiation intensity at 315 nm and 330 nm is not constant over the entire image.

To further verify the calibration, the image size was reduced to 127 (horizontally) $\times$ 88 (vertically) pixels to reduce errors caused by imperfect image alignment. All values that were below a thresholds of 1.5×10^{17} molec/cm^2 (60 ppmm) for IDOAS measurements and below 0.01 AA for camera images were removed. The remaining data points were used to create a calibration curve that can be compared with the calibration curve obtained from the DOAS instrument incorporated in the camera. The result in Figure 4.15 shows that the calibration curve obtained with the NFOV-DOAS instrument is in general agreement with the IDOAS measurements. The calibration obtained from the IDOAS is slightly more noisy, probably due to an imperfect spatial and temporal alignment. Since the SO_2 camera images were spatially transformed to match the IDOAS FOV and averaged to match the IDOAS time resolution, small errors due to misalignment are possible. Both calibration curves clearly deviate from the calibration cell measurements for AA values above 0.1.

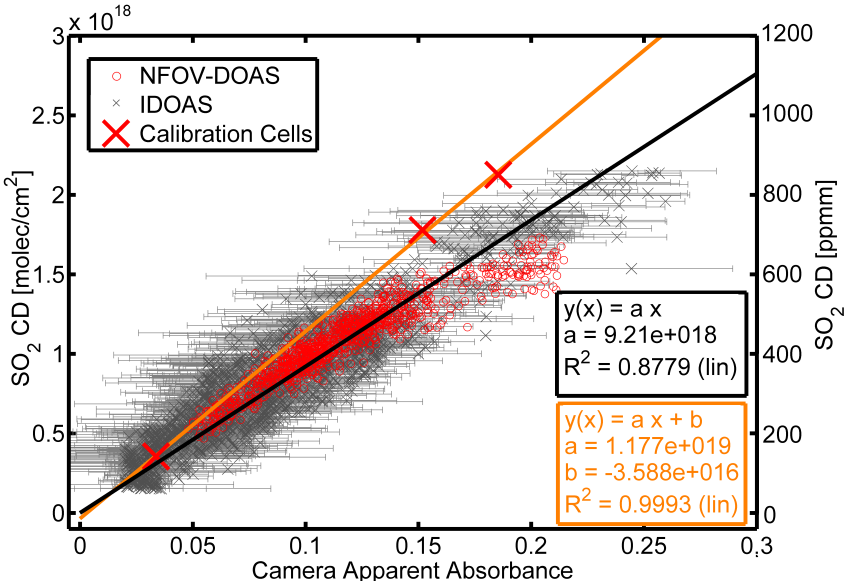

Figure 4.15.: Calibration lines from the NFOV-DOAS and from an IDOAS compared to the fit curve we obtained from the three calibration cells. For high AA values both DOAS instrument show a deviation from the calibration curve obtained from calibration cell measurements. The black curve is a linear fit to the IDOAS data that was forced through the origin. The data points from the NFOV-DOAS have higher AA values for high SO_2 column densities compared to this fit line. Reproduced from Lübcke et al. (2013b).

Discussion of calibration results

On all days the optical density for Filter B decreased with increasing SO_2 column density. This shows that more radiation is incident at 330 nm from areas with high SO_2 column densities compared to the background intensity, an indication for radiation being scattered on volcanic aerosol into the camera's FOV. Comparing the optical density τ_B for Day 1 and 2 (Figures 4.9 and 4.12) one can see that τ_B has a smaller slope on Day 1 compared to Day 2, possibly due to a higher abundance of volcanic aerosol on Day 1. However, the measurement geometry shown in Figure 4.4 also shows that the relative azimuth between the viewing direction of the camera and the sun's position is smaller on Day 1 compared to Day 2. Since forward scattering is dominant in Mie scattering, a larger fraction of radiation might have been scattered into the camera's FOV by aerosols or ash in the plume. As discussed in Section 4.4.1, Mie scattered radiation leads to an increase in AA and therefore to a decrease of the calibration curve. Comparing Figures 4.8 and 4.11 shows that the slope of the calibration curve on Day 1 is indeed lower than on Day 2, as expected for a higher aerosol influence on Day 1.

On Day 3 the situation is more complex. Between 09:15 a.m. and 09:36 a.m. (Part 1), both optical densities τ_A and τ_B and the AA behave similar to Day 1, indicating some radiation scattered into the camera's FOV (Figs. 4.13 and 4.14).

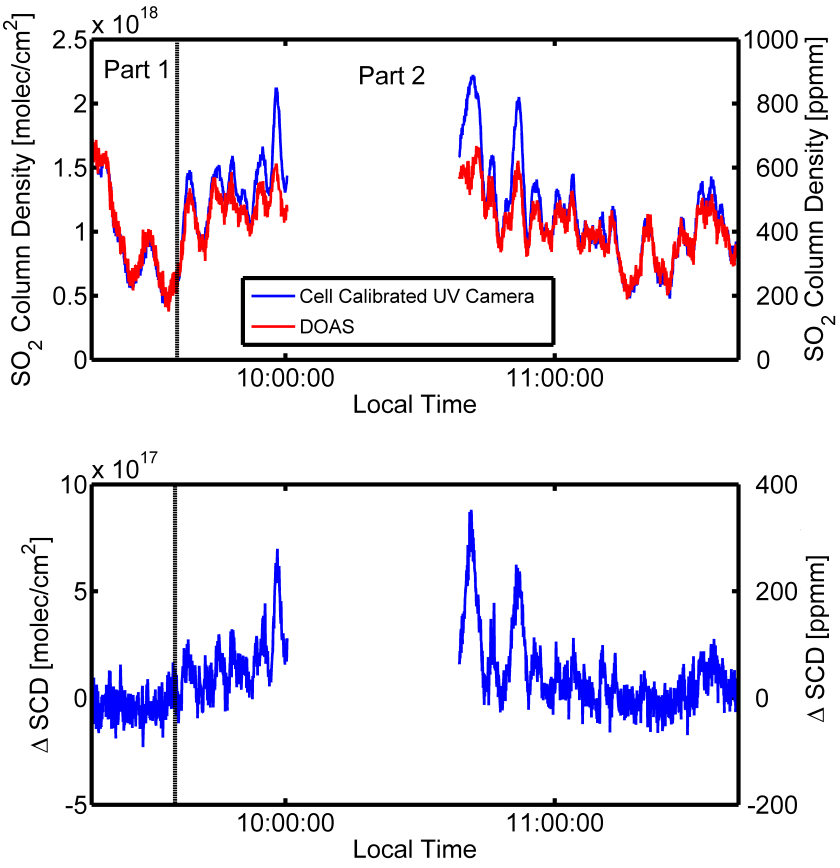

Figure 4.16.: Top: time series from the SO_2 camera on 4 March 2011 (calibration constant 9.98×10^{18} molec/cm^2 obtained from Part 1) compared to the DOAS measurements. Bottom: Difference between the camera and the DOAS system. Background images were acquired at 10:05 a.m. for the first time series and at 10:36 a.m. for the second time series. Reproduced from Lübcke et al. (2013b).

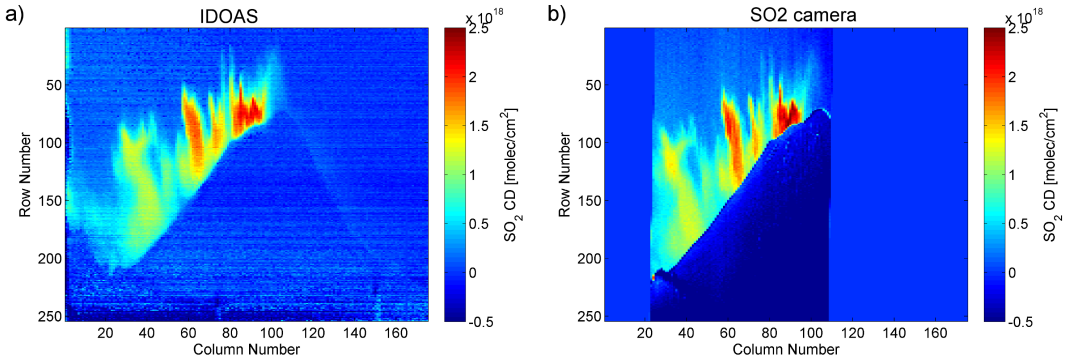

Figure 4.17.: **(a)** Image acquired with the IDOAS on the 4 March 2011 from Paso de Cortes. **(b)** Image constructed from the SO_2 camera measurements to match field of view and temporal resolution of the IDOAS measurements. For this image the camera images were calibrated with the black calibration line obtained from the IDOAS measurements depicted in Figure 4.13. Reproduced from Lübcke et al. (2013b).

For Part 2, both optical densities are shifted towards higher values compared to Part 1 (Fig. 4.14). Less radiation is arriving at the camera's detector for both wavelength channels, which could be caused by more absorbing aerosol in the volcanic plume. τ_B still shows lower values with increasing SO_2 column densities, indicating that besides aerosol absorption some radiation is still scattered into the FOV by ash or aerosol in the volcanic plume.

4.5 SO_2 emission rates

The SO_2 emission rate can be easily calculated by integrating the SO_2 column densities along a cross section through the volcanic plume and subsequently multiplying with the wind speed perpendicular to the viewing direction of the camera. The integral has the dimension of an area times average SO_2 concentration. When multiplying this integral with the wind speed (measured with the SO_2 camera, perpendicular to the viewing direction) the flux through the cross section is obtained. This section will briefly line out how this is implemented and how the wind speed is obtained from SO_2 camera images.

4.5.1 Calculation of SO_2 emission rates

The SO_2 camera has a finitely large pixel size. In practice, instead of integrating along a cross section through the volcanic plume the SO_2 column densities are multiplied with the extent h_i of a pixel i and subsequently summed up. The extent h_i of the pixel i in the image plane can easily be calculated from the distance between the SO_2 camera and the volcanic plume, the extent of a pixel on the detector and the focal length of the lens. The sum over the extent of a pixel times the SO_2 column density $S(\tau_i)$ of the pixel is sometimes called the integrated SO_2 column density χ:

$$\chi = \sum \Delta h_i \cdot S(\tau_i) \tag{4.15}$$

The emission rate is obtained by subsequently multiplying this sum with the wind speed v, perpendicular to the cross section through the plume (see Figure 4.18):

$$\Phi = v \cdot \chi = v \cdot \sum \Delta h_i \cdot S(\tau_i) \tag{4.16}$$

Ideally, the viewing geometry is chosen in a way that the cross section is perpendicular to the propagation direction of the plume, but in reality this is not always possible. During calculation of the SO_2 emission rate, non-perpendicular viewing directions cancel out if the wind speed is derived from SO_2 camera measurements since both, the derived wind speed and the SO_2 column density are functions of the viewing direction (see Mori and Burton, 2006; Wöhrbach, 2008, and Figure 4.19).

The time the plume needs to travel between two parallel plume cross sections is found by calculating the cross-correlation of time series of the integrated SO_2 column densities from the two cross sections. Using the travel time and the distance between the two cross sections, the wind speed can be calculated (Johansson et al., 2009; McGonigle et al., 2005).

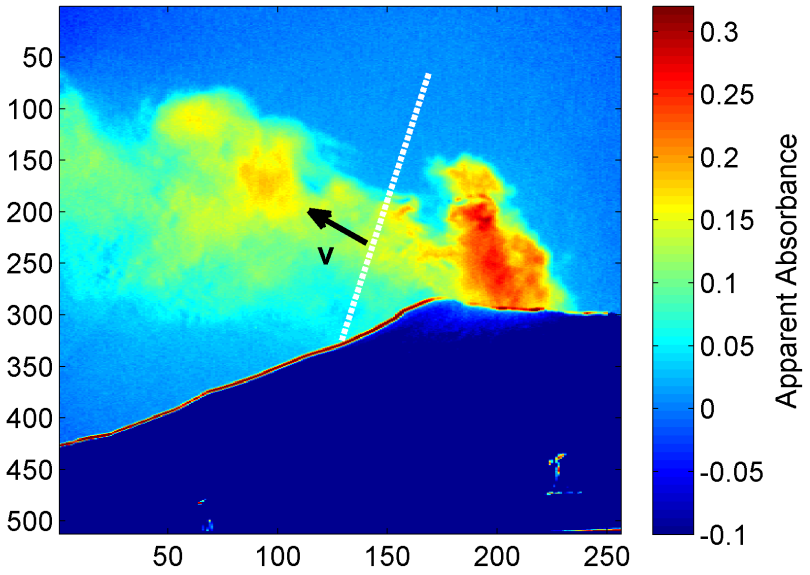

Figure 4.18.: SO_2 camera image acquired at Stromboli on 26 June, 2013. The white dashed line shows the profile along which the SO_2 column densities were summed up. The black arrow shows the wind direction.

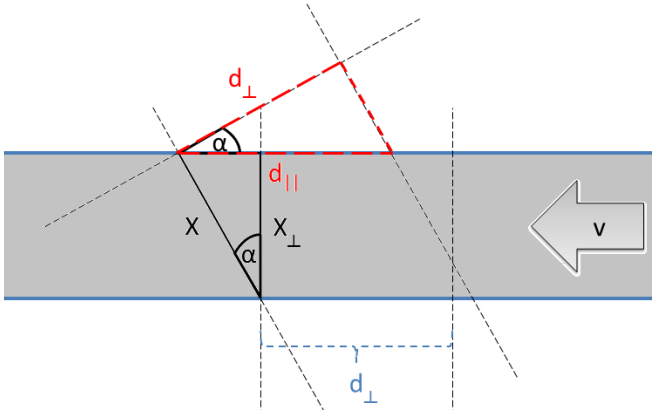

Figure 4.19.: Sketch of the SO_2 camera geometry for the calculation of the SO_2 emission rates. The grey shaded area denotes the volcanic plume. If the camera does not observe the plume perpendicular to propagation direction the light-path and thus the integrated SO_2 column density χ is larger by a factor of $1/\cos\alpha$. However, this cancels out in the calculation of the SO_2 emission rate, since the obtained wind speed decreases by a factor of $\cos\alpha$.

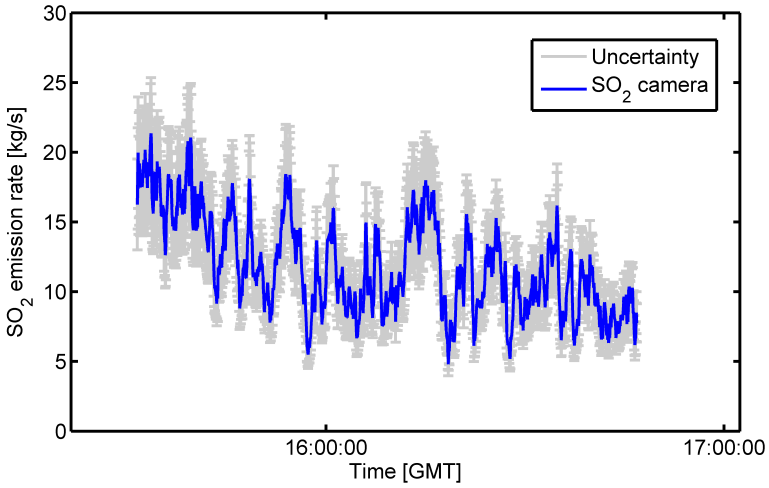

Figure 4.20.: SO_2 emission rate for the first time series on 1 March 2011. The shown emission rate is radiation dilution corrected, the shown error consists of the wind-speed and the calibration error.

4.5.2 SO_2 emission rates from Popocatépetl

SO_2 emission rates were calculated with cell calibration and DOAS calibration to test the influence of the calibration method on the results. If not explicitly stated all SO_2 emission rates were obtained using the DOAS calibration method. Information on the correction used to correct for the light dilution effect can be found in Appendix A.

On 1 March 2011 we obtained two long time series. The first one was recorded between 9:30 a.m. – 10:46 a.m., the second between 11:00 a.m. – 12:00 a.m. These were the only measurements at Popocatépetl that were able to capture the complete plume. The SO_2 emission rates were later investigated using the wavelet analysis technique (Section 4.6) and will therefore be discussed in more detail. The light dilution corrected SO_2 emission rate for the first time series is shown in Figure 4.20. The SO_2 emission rate varied between $4.8 \pm 0.8\,\mathrm{kg\,s^{-1}}$ and $21.4 \pm 4.0\,\mathrm{kg\,s^{-1}}$. The mean emission rate is $11.86\,\mathrm{kg}\,s^{-1}$. The SO_2 emission rate starts with higher values and declines until 10:00 a.m.. For the second time series the SO_2 emission rates are ranging between $4 \pm 0.7\,\mathrm{kg\,s^{-1}}$ and $23 \pm 3.9\,\mathrm{kg\,s^{-1}}$, with a mean emission rate of $10.56\,\mathrm{kg\,s^{-1}}$. Figure 4.21 shows the SO_2 emission rate for the second time series.

On Day 2 and 3 the obtained SO_2 emission rates are only a lower limit. On these two days, the plume was partly moving in front and behind Popocatépetl and we could thus not detect the complete gas emissions. Nevertheless, Day 2 shows the highest SO_2 emission rates, with a DOAS calibrated mean emission rate of $15.14\,\mathrm{kg\,s^{-1}}$. On Day 3, when most of the plume disappeared behind the volcanic edifice, we obtained the lowest SO_2 emission rate, with an average value of $5\,\mathrm{kg\,s^{-1}}$.

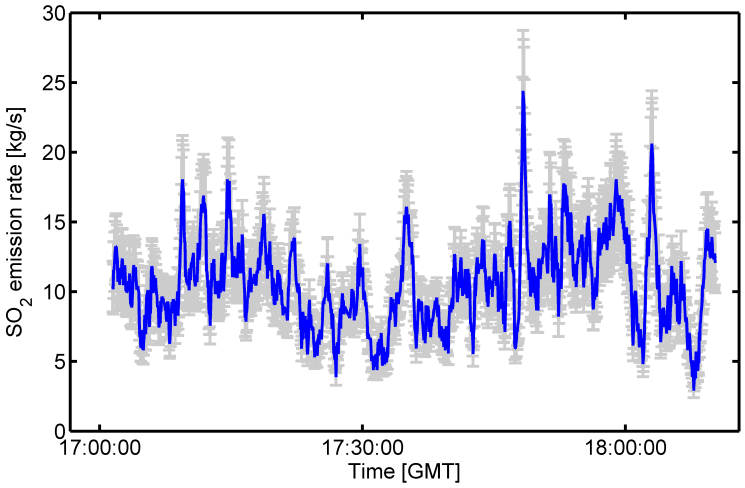

Figure 4.21.: SO_2 emission rate for the second time series on 1 March 2011.

Mean emission rates for all measurement periods with both calibration methods are shown in Table 4.2. While the SO_2 camera calibrated with cells can measure the SO_2 emission rate correctly under favourable conditions (only 6 % difference on 2 March 2011), differences in the emission rate of up to 25 % occurred (4 March 2011) when aerosols and condensed water in the volcanic plume significantly influenced the calibration. The difference in the emission rate is significantly lower, than the maximum difference of 60 % we found in the calibration curve on Day 3. This is due to the fact that during an emission rate measurements both, high and low SO_2 column densities can be observed. At lower SO_2 column densities the two calibration methods differ less than 60 % (see Figure 4.15).

4.5.3 SO_2 emission rates from Stromboli

Measurements were performed during the Imaging Volcanic Plume workshop on Stromboli between 26 - 30 June, 2013. Most data was not evaluated yet, since a combination of the measurement geometry and frequent eruptions of Stromboli prevented determination of wind speeds with the usual method described above. The SO_2 emission rate calculation fails, if eruptions pass the cross sections used for the plume speed determination. However, on 26 June, 2013 measurements were performed from the Hotel Villagio Stromboli in order to compare different SO_2 camera systems. While Stromboli also erupted on this day, the SO_2 emission rate determination was performed down-wind the plume, and thus lead to reliable results.

The viewing geometry and the cross section used for the calculation of the SO_2 emission rate is shown in Figure 4.18. The mean emission rate using the DOAS calibration was $0.92 \pm 0.08\,\mathrm{kg\,s^{-1}}$. The calibration curve and the SO_2

	Day 1 1 March	Day 2 2 March*	Day 3 4 March*
Measurement Time [GMT]	17:01–18:02	15:35–16:10	15:16–17:30
Wind direction [°]	283	313	119–125
Average Wind Speed [m s^{-1}]	10.2	9.4	8.0
Maximum SO_2 CD [molec cm^{-2}]	3.5×10^{18}	5.6×10^{18}	3.2×10^{18}
Distance [km]	6.8	6	8–8.5
DOAS calib. kg s^{-1}	11.21	14.34	4
Cell calib. kg s^{-1}	13.63	15.14	5
$\frac{\text{Flux Cell calib.}}{\text{Flux DOAS calib.}}$	1.21	1.06	1.25

Table 4.2.: Average SO_2 emission rates for the measurement conducted at Popocatépetl adapted from Lübcke et al. (2013b). For all days, mean emission rates are shown for DOAS calibration and cell calibration and with or without correction of the light dilution effect. * For 2 March and 4 March the emission rates are only a lower baseline for the emission rate. Note that the SO_2 emission rates on Day 1 differ from those published in Lübcke et al. (2013b), as additional data was evaluated.

emission rate time series are shown in Figure 4.22. The obtained SO_2 emission rates are of the same order of magnitude as measurements by other authors. Tamburello et al. (2012) measured SO_2 emission rates between $0.4 - 1.9\,\text{kg s}^{-1}$ with a mean emission rate of $0.7\,\text{kg s}^{-1}$ at Stromboli. For the spectra used for calibration C. Kern provided SRT-DOAS (Kern et al., 2013) corrected SO_2 column densities. These column densities showed a nice linear relationship to the usual DOAS evaluation and $\approx 18\%$ higher values. Therefroe, the true radiative transfer corrected SO_2 emission rate for Stromboli is $1.1\,\text{kg s}^{-1}$.

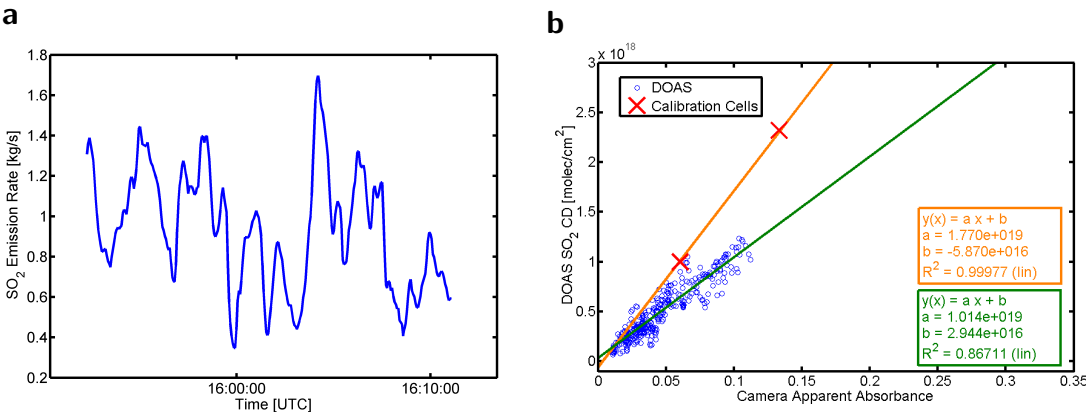

Figure 4.22.: **a** SO_2 emission rate from 26 June, 2013 at Stromboli. **b** The corresponding DOAS calibration curve that was used for camera calibration.

4.6 Wavelet analysis

Learning more about processes occurring below the Earth's surface is one of the declared goals of SO_2 camera measurements. The high time-resolution SO_2 emission rates gained by SO_2 camera measurements allow to look at periodicities in the degassing signal.

These periodicities can be identified with help of the well known Fourier analysis. The Fourier analysis shows how a signal can be approximated by of a sum of trigonometric functions. However, one pitfall is that it only gives information about the frequency content of a signal, not about the times at which frequencies appear in a signal. These problems can be partially solved by applying the windowed Fourier analysis during which a window-function is multiplied to the signal. The window function is zero everywhere except in the small interval that is analysed. However, the windowed Fourier analysis is not very efficient and the choice of the analysing window can superimpose structures on the signal (Torrence and Compo, 1998).

These problems can be overcome by using the so-called *wavelet analysis*, a technique that can determine the dominant frequencies and how they vary with time (Lau and Weng, 1995; Morlet, 1983). During the wavelet analysis a signal $s(t)$ is analysed with a wavelet function $\Psi_{b,a}(t)$ that is generated from the so-called mother-wavelet $\Psi(t)$ through dilation by a factor a and translation by a factor b (Lau and Weng, 1995):

$$\Psi_{b,a} = \frac{1}{a^{1/2}} \cdot \Psi\left(\frac{t-b}{a}\right) \tag{4.17}$$

$a^{-1/2}$ is a normalisation factor. Certain rules apply for a group of functions to be possible wavelets, however discussing all the mathematical details of the wavelet analysis is beyond the scope of this thesis. Readers interested in the practical application of wavelets are referred to the excellent practical guide by Torrence and Compo (1998), a more mathematically thorough treatment can be found in Teolis (1998). In this work, a complex Morlet wavelet given by

$$\Psi(x) = (2\pi)^{-0.5} \cdot e^{2i\pi x} \cdot e^{-x^2/2} \tag{4.18}$$

is used. This Morlet wavelet is also shown in Figure 4.23, it was chosen since the complex nature of the wavelet allows to gain information on the amplitude and phase of the signal (Torrence and Compo, 1998). Additionally, this type of wavelet is the only complex wavelet used in the sparse literature on the interpretation of high time-resolution SO_2 emission rate data (Boichu et al., 2010), thus making the results more comparable. The difference between the wavelets used in this study and Boichu et al. (2010) are just normalisation factors, which do not influence the qualitative discussion in this section.

For a wavelet analysis we assume our signal to be a discrete time series x_n (with n = 0,....,N-1) that is equally spaced in time with a distance δt between

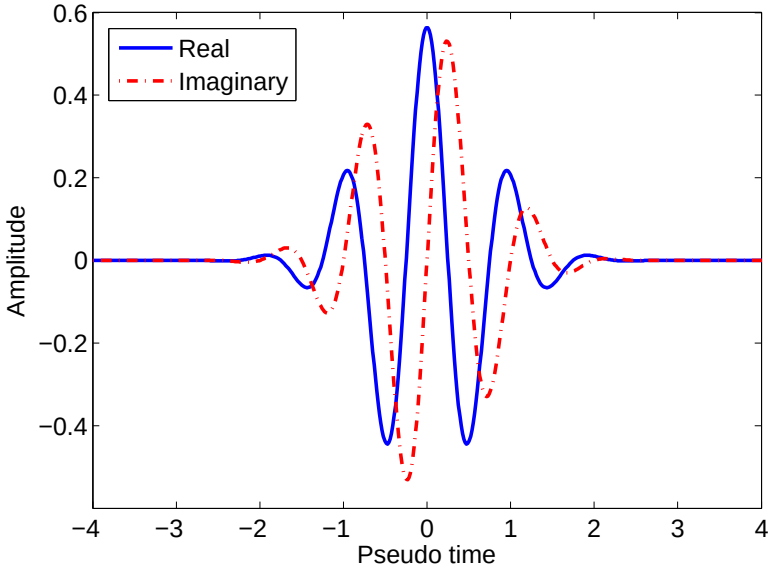

Figure 4.23.: Real (solid blue line) and imaginary (dashed red line) part of the complex Morlet wavelet (see Eq. 4.18) used in this work.

two data points (Torrence and Compo, 1998). The wavelet transform $W(n, s)$ for the time n and the scale s is given by:

$$W(n,s) = \sum_{n'=0}^{N-1} x_{n'} \cdot \Psi^* \left(\frac{(n'-n)\cdot \delta t}{s} \right) \tag{4.19}$$

In this equation Ψ^* is the complex conjugate of the wavelet. The scalogram, an image showing the amplitude for different scales (that correspond to different frequencies or periods) and times can be constructed by varying the time n and the scale s. The scalogram SC is then calculated as:

$$SC(n,s) = \frac{100 \cdot |W(n,s)^2|}{\sum_n \sum_S |W(n,s)^2|} \tag{4.20}$$

The scalogram shows the percentage of energy for each coefficient $W(n, s)$ relative to all coefficients. Comparing the absolute values of the scalogram coefficients is not straightforward. A small wavelet scale (high frequencies) leads to a very broad wavelet in frequency space and thus frequencies are smoothed out. On the other hand, a wavelet for lower frequencies is narrower in frequency space and thus low frequencies (or higher periods, for the discussion following later) have a larger amplitude in the scalogram.

In this thesis, periods found by application of the wavelet analysis are discussed only qualitatively. For a quantitative discussion, more care has to be taken, to fulfil normalisation criteria (see e.g. Torrence and Compo, 1998). Additionally, the significance of the signal has to be verified with more care, for example by

using tests with white-noise (constant noise power for all frequencies) or red-noise (higher noise power at lower frequencies) as explained in Torrence and Compo (1998). In the following discussion, we rely on the investigations of Heinzmann (2013). Heinzmann (2013) studied SO_2 emission rates from Popocatépetl that I recorded in 2011 (see Section 4.5) and that were re-evaluated with the wavelet analysis in this dissertation. The evaluation was performed with and without the addition of realistic noise to the SO_2 emission rates and the author found the same frequencies in both signals.

Before using the wavelet analysis, all SO_2 emission rates were interpolated to match an equally spaced time grid and the signal was padded with zeros in front and behind to reduce edge effects (Torrence and Compo, 1998). The wavelet analysis was then performed with the Matlab Wavelet Analysis toolbox using the Morlet wavelet given by Eq. 4.18.

4.6.1 Wavelet analysis of the SO_2 emission rates from Popocatépetl and Stromboli

The complete scalogram for the first time series is shown in Figure 4.24. A subset of the same scalogram only showing lower frequencies is shown in Figure 4.25. The white shaded areas in the scalogram denotes the cone-of-influence. In this area side effects from the edges of the signal can influence the obtained wavelet coefficients $W(n, s)$. In Figure 4.24 we can see periods between 15 and 20 minutes that are apparent throughout the complete region outside the cone of influence. These low frequencies most likely describe the decrease of the SO_2 emission rate that can be observed in Fig. 4.20. A period between 5 and 8 minutes can be observed from the beginning until minute 45 of the time series. A few minutes before these periodicities disappear, a signal with a period between 8 and 12 minutes starts. A short time later around minute 45 another signal with periods between 3.5 and 5.5 minutes appears for 10 minutes.

Figure 4.25 shows the shorter periods of this time series in more detail. A signal with a lower period of 2 minutes starts between 10 — 20 minutes and can be better seen in this figure. This signal later merges with the signal with periods between 5 and 8 minutes. Also several signals with periods between 1.5 and 2.5 minutes can be observed.

In the second time series (Figure 4.26), recorded between 11:00 a.m. and 12:00 p.m. at Popocatépetl, we see only a very small signal at large periods (between 13 and 17 minutes). A small signal with periods between 2.5 and 4.5 minutes can be seen in the beginning. This signal is followed by the most distinguishable feature with periods between 4.5 and 8 minutes that can be observed between minutes 22 and 40. At the end of the time series a signal with periods between 2.5 and 6 minutes can be observed. Also frequencies between 1.5 and 3 minutes occur again occasionally throughout the complete time series. However, the nicely noticeable signal around minute 45 with a period between

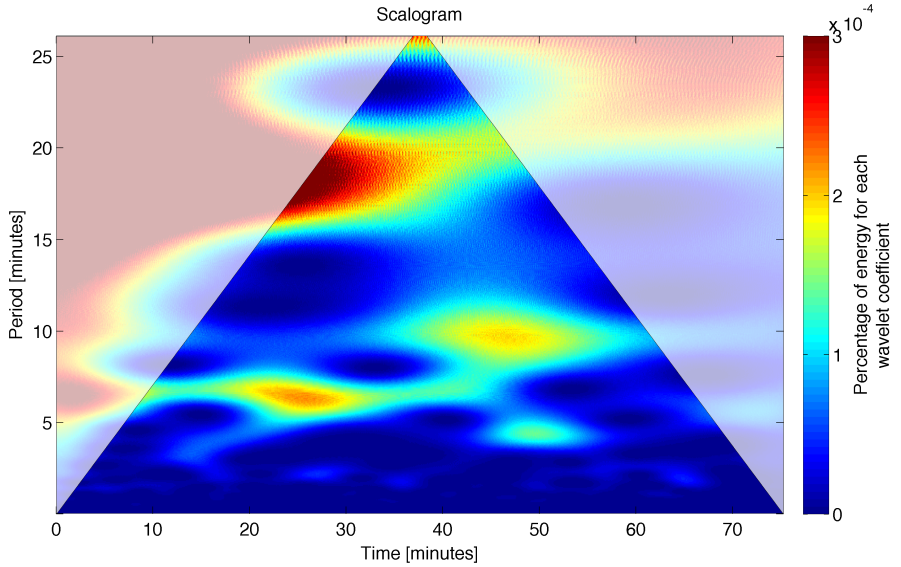

Figure 4.24.: Scalogram for the SO_2 emission rate time series between 9:30 and 10:46 am on 1 March 2011. The white blurry area shows the cone of influence, where insufficient information for the correct calculation of the wavelet coefficient is available.

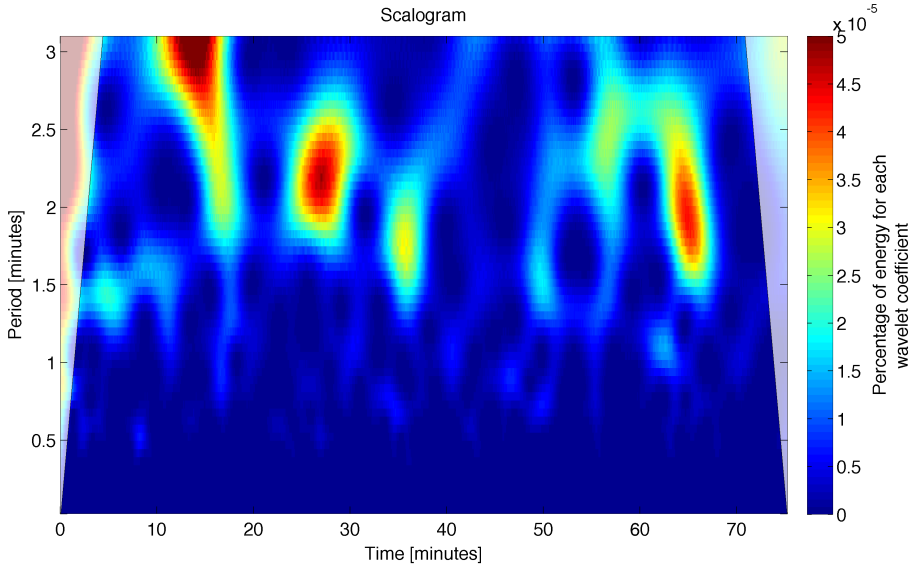

Figure 4.25.: The same scalogram as in Figure 4.24 but with a different scaling.

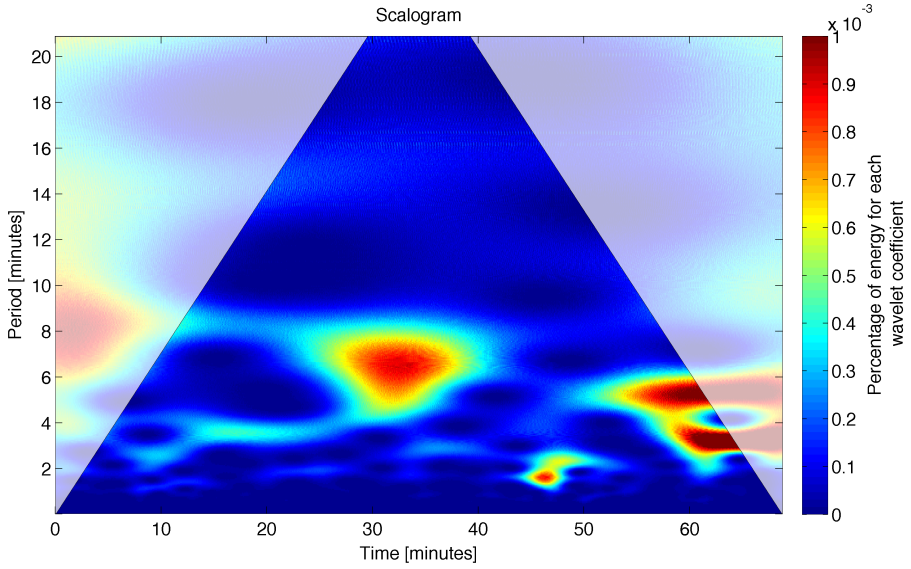

Figure 4.26.: Scalogram for the second SO_2 emission rate time series recorded between 11:00 am and 12:00 pm on 1 March 2011.

1.5 – 3 minutes was identified to be caused by slight movement of the SO_2 camera set-up.

Combining the results of these two time series five different periodicity ranges that occured in both time series could be identified for Popocatépetl. These intervals are 1.5 – 3 minutes, 2.5 – 6 minutes, 4.5 – 8 minutes, 8 – 12 minutes and 13 and 20 minutes.

From the Stromboli measurements only a 20 minute long time series was evaluated. The other measurements are yet to be evaluated. Frequent eruptions and thus varying plume speeds did not allow the usual emission rate evaluation procedure (see Section 4.5.1). The time series shown here, was not influenced by frequent eruptions. While eruptions could be observed in the SO_2 camera data, the wind speed determination was performed further downwind, and the signal from the eruptions did not prevent wind speed determination. The SO_2 emission rate was thus determined by using the standard SO_2 emission rate calculation procedure (see Section 4.5.1). The result is shown in Figure 4.27. Two different signals can be clearly identified; one with a period between 2 and 3 minutes, the other one with a period between 5 and 6 minutes. It should be noted though, that longer periods could not be registered due to the short time series.

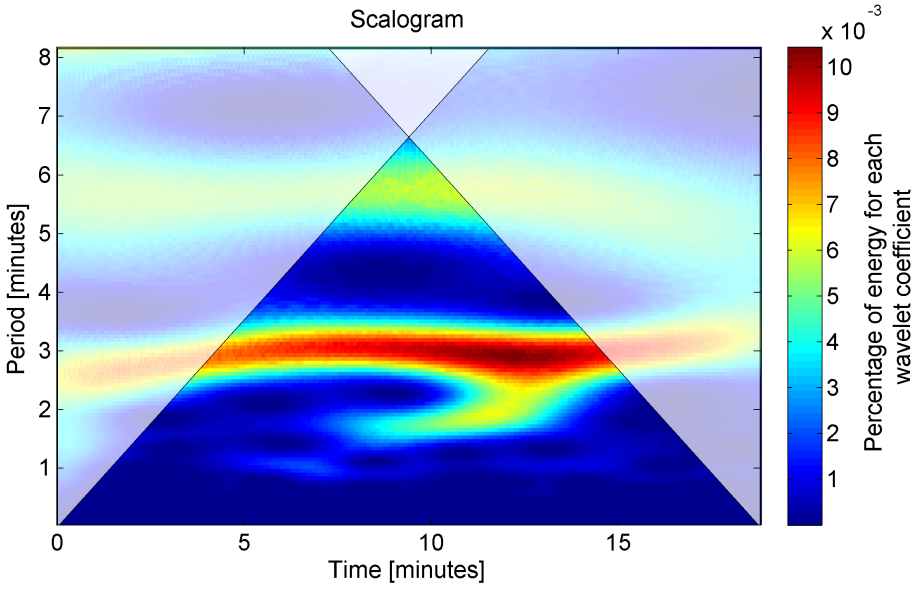

Figure 4.27.: Scalogram for the SO_2 emission rate measured between 3:52 pm and 4:11 pm on 26 June, 2013 at Stromboli.

Popocatépetel	Stromboli
1.5 - 3 minutes	2 - 3 minutes
2.5 - 6 minutes	
4.5 - 8 minutes	5 - 6 minutes
8 - 12 minutes	
13 - 20 minutes	

Table 4.3.: The various periods of the signals found from the wavelet analysis for the measurements performed at Popocatépetl.

4.6.2 Comparison with periodicities found in the literature

One of the goals of SO_2 camera measurements is to improve the understanding of volcanic systems. This can, for example, be done by looking at periodicities in the SO_2 emission rates. An interpretation of the SO_2 emission rates obtained at Popocatépetl and Stromboli would require additional geophysical parameters (e.g. seismicity, deformation measurements) which were not available and more/longer measurements. The few, relatively short time series that were acquired during the work on this thesis do not allow a meaningful interpretation of the observed periodicities. Regardless of the above mentioned restrictions, the periodicities that were obtained will be compared with periodicities from the recent literature. The intention of this comparison is to give an overview about possible processes that can lead to periodicities in the SO_2 emission rates. The weaknesses of this comparison should be clearly pointed out though. For one, the data sets used in this thesis as well as in the literature are only the result of relatively short measurement campaigns. Second, different volcanoes with a different geological

setting and magma composition cannot easily be compared. Additionally the frequency content of the SO_2 emission rates might be governed by the style of activity. To overcome these restrictions, and maybe allow comparison of different volcanoes, more data at a multitude of volcanoes are necessary.

The discussion starts with the periods obtained at Stromboli. For this volcano there is at least some literature on periodicities from degassing processes available, e.g., Harris and Ripepe (2007), Tamburello et al. (2012) and Spampinato et al. (2012). Popocatépetl, on the other hand, is an open-vent volcano, but has a andesite-dacite magma composition (Rose et al., 2013). There is no literature on periodicities comparable to our measurements at Popocatépetl. Therefore, the periods that were found will be discussed in combination with results from other volcanoes, in spite of possible differences between different volcanoes.

At Stromboli, Harris and Ripepe (2007) revealed gas released from bursting magma bubbles every 1 – 2 seconds. However, the sampling frequency of ≈ 0.25 Hz used during the measurements is too low to reveal these cycles. The 5 – 6 minutes period found during the Stromboli measurements falls into similar period ranges found by several authors (Spampinato et al., 2012; Tamburello et al., 2012). Tamburello et al. (2012) found cycles with periods between 5 – 12 minutes at Stromboli which the authors explained as a combination of the "intrinsically rhythmic nature of Strombolian explosions" and an up to two minute long coda (decay of the SO_2) signal. Spampinato et al. (2012) found a cycle of 5 – 8 minutes at Stromboli using thermal monitoring and explained them as "minor fluctuations within the vigorous puffing regime...that might result from changes in magma level within the vent". Both periodicities found at Stromboli (2- 3 minutes and 5- 6 minutes) fall into the broad range of 1-10 minutes that was categorized in Spampinato et al. (2012) as "bursting of hot, overpressured gas bubbles...at the magma-air interface". The authors based their findings on measurements of thermal cycles at Stromboli, Mt. Etna, Italy and Kilauea, Hawaii, USA.

At Popocatépetl a larger variety of periods was found (see Table 4.3). Due to the sparse data set from comparable volcanoes, also data from other volcano types will be discussed in spite of the obvious limitations. Generally speaking, the periodicities can be divided in two different regimes. Short cycles with periods below 20 minutes which are linked to bursting and movement of gas bubbles and longer cycles with periods longer than $\approx$ 10 minutes which are assumed to be connected to magma movement. A similar classification was made by Spampinato et al. (2012). The time limits here should not be seen as exact limits and additionally deviations can occur depending on the geological settings (e.g. magma viscosity).

For both regimes there are several observations in the literature:

- **Short cycles:** The periods of 1.5 – 3, 2.5 – 6, 4.5 – 8 and possibly 8 – 12 minutes at Popocatépetl can be classified as short cycles that are supposed to be connected to movement of gas bubbles. Boichu et al. (2010) observed periods between 1.5 – 3 minutes at Mt. Erebus that only occured occasionally, similar to these periods at Popocatépetl. However, unlike Mt. Erebus, Popocatépetl does not have an open lava lake. This could potentially influence bubble ascend and burst. On the other hand, these two processes are most likely governed by magma viscosity and the SiO_2 content, which is not too different for the two volcanoes ($57 - 64\%$ at Popocatépetl and $55 - 57\%$ at Mt. Erebus, Rose et al., 2013).

  Holland et al. (2011) performed SO_2 camera measurements at Santiaguito volcano, Guatemala, which is better comparable to Popocatépetl due to its magma composition and the volcanic conduit that does not feature an open magma-air interface. The authors found cycles with periods below 10 minutes that they associated with the "connectivity of bubble chains as degassing pathways through the shallow magma".

  A similar interpetation was made by Tamburello et al. (2013) who found periodicities between 8 –20 minutes at Etna. The authors interpreted their findings as "periodic bursting of rising gas bubble trains at the magma-air interface".

  As already mentioned above, Spampinato et al. (2012) interpreted cycles below 10 minutes with bursting of gas bubbles/trains of bubbles based on measurements at Kilauea, Stromboli and Etna.

- **Longer Cycles:** The longer periods of 8 – 12 minutes and 13 – 20 minutes measured at Popocatépetl might be in this regime, which is usually connected to magma movement. Boichu et al. (2010) observed long periods (11 – 22 minutes) and explained these cycles with periodic magma supply or the collapse of a magma foam that allows the gas to escape the magma. The periodicity of the magma is explained by either shear forces between descending and ascending magma or volatile dependend viscosity variations. A similar argument is made by Spampinato et al. (2012) for basaltic volcanoes. The authors explain periodicities between 12 – 90 minutes more generally as "reflecting dynamics occurring within the shallow magma supply system".

There are further interpretations for the longer periods observed at Popocatépetl that should at least be mentioned here. These periods most likely correspond to the decline of the SO_2 emission rate (see Figure 4.20). Nadeau et al. (2011) performed SO_2 camera measurements at Fuego volcano, Guatemala, a volcano with a basalt-andesite magma composition, and found a decrease of SO_2 emission rates that was interpreted as rheological stiffening of the volcanic conduit. The

rheological stiffening inhibits the release of gas from the volcano and thus leads to lower SO_2 emission rates.

It should also be mentioned that Boichu et al. (2010) explained periods between 5 – 10 minutes as a signal that was caused by turbulence in the atmosphere. However, this cannot be observed in the SO_2 camera measurements at Popocatépetl.

Instrumental artefacts can also not be ruled out completely. A strong peak in the period range between 1.5 – 3 minutes that was found in the second time series (see Figure 4.26) was identified to be an artefact caused by a slight shift of the instrument's field-of-view.

The periods between 13 – 20 minutes might be due to influences of the changing solar azimuth angle on the obtained SO_2 emission rates. The first time series, which shows the stronger features at these periods, was recorded in the morning hours at Popocatépetl. The SO_2 emission rate was calculated with a constant calibration factor. Changes of the SO_2 camera calibration due to variations of the incident radiation were not assessed by the evaluation procedure. Following this argumentation the observed pattern would only be an instrumental artefact. The time series recorded one hour later on the same day did not show these strong features in this period range.

The wavelet analysis of the SO_2 emission rates from Popocatépetl revealed that there are a multitude of processes happening in a relatively short time interval and partially even simultaneously.

These comparisons with the literature give some possible explanations for periodicities that were observed by different authors. Shorter cycles are usually linked to ascent and bursting of bubbles while the longer cycles are connected to movement of magma. However, volcanoes are complex systems and their degassing behaviour is governed by a multitude of processes. Even a single volcano might show different periodicities depending on its style of activity.

5

BrO/SO_2 ratios from NOVAC

This chapter covers the evaluation of spectroscopic data from the Network for Observation of Volcanic and Atmospheric Change (NOVAC) (Galle et al., 2010) for BrO and SO_2.[1] As outlined in Chapter 2 the ratio of halogens to sulphur is an additional parameter in a volcanologist's toolbox. The BrO/SO_2 ratio is a tempting proxy for a halogen to sulphur ratio as it can be retrieved by optical remote sensing measurements in the UV using the robust DOAS technique.

The chapter starts with a brief description of NOVAC, the instruments installed in the network and the measurement strategies that are used to obtain spectra (Section 5.1).

Section 5.2 discusses the algorithm that was developed for the automatic evaluation of NOVAC data and the parameters used for the DOAS evaluation for BrO and SO_2.

As a case study the automatic evaluation algorithm was applied to spectroscopic data from Nevado del Ruiz, Colombia. A brief overview about this volcano will be given at the beginning of Section 5.3. The performance of the DOAS evaluation, in particular the dependence of the DOAS fit error on the number of co-added spectra, will be discussed. A first long-term time series of BrO/SO_2 ratios recorded from two stationary DOAS instruments at Nevado del Ruiz was created. During this time the volcano showed interesting activity, including an eruption at the end of June 2012. Variations of the BrO/SO_2 ratio are linked to the volcanic activity by comparing them with SO_2 emission rates and seismic data. The results section ends with some insights into the variation of the BrO/SO_2 with increasing time since release from the volcano into the atmosphere.

[1] Large parts of this chapter are a revised version of Lübcke et al. (2013a)

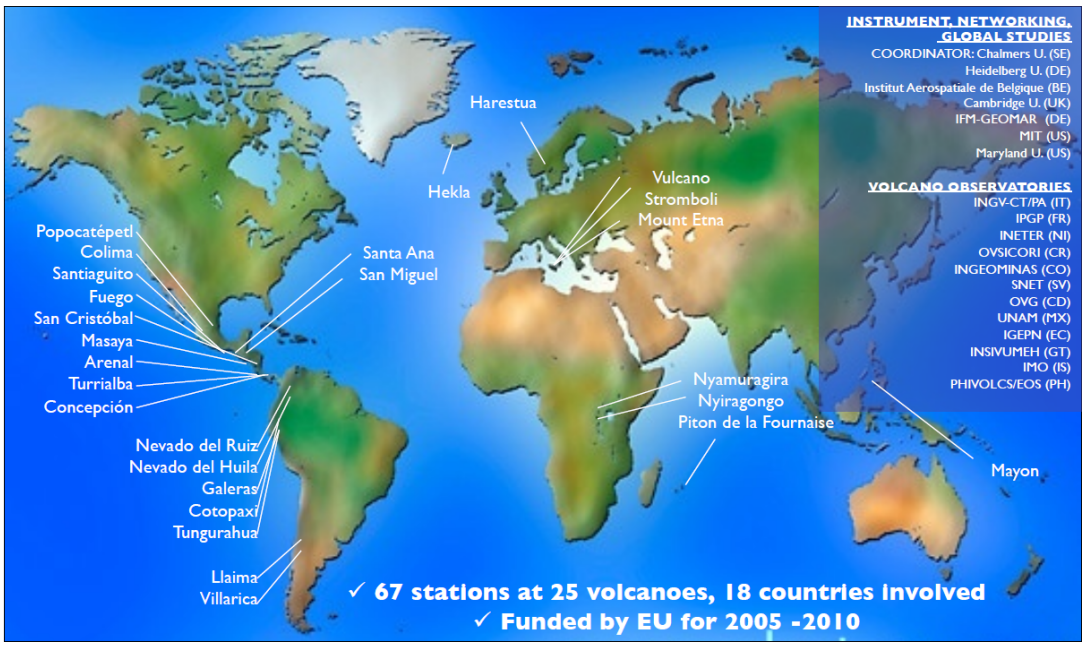

Figure 5.1.: Map of the world with the locations of the volcanoes that are included in the NOVAC network. Used with friendly permission of Santiago Arellano.

5.1 The NOVAC network

The Network for Observation of Volcanic and Atmospheric Change (NOVAC) was established during a 5-year EU-funded project that ended in 2010. The goal of the project was installing a network of scanning DOAS instruments to automatically monitor volcanic gas emissions (Galle et al., 2010). At current about 70 scanning DOAS instruments have been deployed at 26 volcanoes worldwide. Figure 5.1 shows a map with the locations of the volcanoes that are included in the NOVAC network. The NOVAC instruments are typically installed 5 – 10 km downwind of the volcano. They measure the volcanic SO_2 emission rate and gas composition by acquiring spectra of scattered solar radiation. About 100 scans are performed per day and routinely evaluated by the local observatories in order to obtain SO_2 emission rates. These SO_2 emission rates from NOVAC are used as part of the monitoring activities at the volcanoes.

5.1.1 Instruments used in NOVAC

Two versions of scanning DOAS instruments are used in the NOVAC network. The NOVAC Version 1 instrument is a robust, low energy consumption instrument that is described in Galle et al. (2003) and Galle et al. (2010). These instruments are not thermally stabilized in order to minimize power consumption and use a very simple entrance optic. This results in a robust, energy efficient instrument. The power consumption of the NOVAC type 1 instruments can usually be covered by a combination of batteries and a solar panel. A robust instrument is extremely important when operating instruments in remote locations that are sometimes difficult to access. However, temperature variations of the instruments can lead to errors in the spectroscopic retrieval. During the NOVAC project it was estimated that these variations lead to deviations below 10% of the retrieved SO_2 column densities (Pinardi et al., 2007). Influences from variations of the instrument's temperature are further discussed in Chapter 7.

The NOVAC Version 1 instruments use Ocean Optics S2000 spectrometers with an optical resolution of ≈ 0.6 nm which cover a wavelength range of 280 – 420 nm (Galle et al., 2010). The spectrometer measures radiation through a telescope with a quartz lens (field-of-view ≈ 8 mrad) that focusses light onto an optical quartz fibre. The viewing direction can be altered with the help of a mirror that is mounted on a stepper motor in front of the lens. Some instruments feature two spectrometers to allow measurements with slightly different viewing directions. In these instruments two optical quartz fibres are mounted at equal distance from the optical axis. This results in two different viewing directions with a fixed angular displacement, which makes it possible to determine the wind speed (Johansson et al., 2009). The NOVAC type 1 instruments come in two possible optical set-ups that result in different measurement geometries (flat scanning geometry and conical scanning geometry). These geometries will be further described in the scanning strategies section.

The NOVAC Version 2 instruments, which are described in Galle et al. (2010) and in more detail in Kern (2009), have a more sophisticated set-up to allow higher accuracy of spectroscopy and additionally more flexibility with regard to the measurement geometry. They use spectrometers with a better optical resolution (Ocean Optics HR2000 with an optical resolution of ≈ 0.4 nm, covered wavelength range 295 – 390 nm). The spectrometers are thermally stabilized by a thermoelectric Peltier element. The NOVAC Version 2 instruments use an advanced entrance optics consisting of a spherical mirror that is used to collimate incident radiation onto a 400 μm optical fibre. Using a mirror instead of a lens reduces chromatic aberrations. A dual-axis scanner is used to yield higher flexibility of the measurement geometry. However, these instruments have higher energy consumptions mainly due to the temperature stabilisation, which makes a reliable power supply necessary.

5.1.2 Scanning strategies

NOVAC instruments are typically installed between a few and up to ten kilometers downwind from the volcano. At most volcanoes two – three instruments are installed to cover a wide range of possible wind directions. An example of the three instruments installed at Nevado del Ruiz, Colombia, is shown in Figure 5.2. In this figure the blue shaded area shows the area in which the wind direction is directed in 70% of the time, while the yellow shaded areas show the wind direction in the remaining 30% of time. The solid lines show the viewing directions of the three instruments installed at Nevado del Ruiz. Figure 5.2 shows that the three instruments are set-up in a way to allow SO_2 emission rate measurements in most situations. The two scanning geometries that exist for the NOVAC Version 1 instruments are both used at Nevado del Ruiz. The instrument at Bruma Station (red lines, with the instrument number D2J2200) uses the flat scanning geometry, while the instruments at Alfombrales Station (blue lines, instrument number D2J2201) and Azufrado Station (black lines) use the conical scanning geometry.

Instruments using the flat scan geometry scan the complete sky from one horizon to the other horizon by rotating a mirror. All viewing directions of a scan lie in one plane (see Figure 5.3). In contrast, for the conical scanning geometry all viewing directions lie on the surface of a semi-cone that is facing towards the volcano (Galle et al., 2010). This measurement geometry is achieved by tilting the mirror and thereby changing the viewing direction. The two instruments at Nevado del Ruiz that use the conical scanning geometry have a tilt angle of $\beta = 60°$ (see Galle et al., 2010, or Figure 5.3 for a definition of the tilt angle). The advantage of the conical scanning geometry is that it has better spatial coverage in situations where the plume deviates from the ideal direction. Additionally the distance between instrument and plume is smaller (thus decreasing the effect of light dilution, see Section 3.4) in situations where the plume is not above the instrument. This set-up is also more robust with regards to errors in the wind direction used for the calculation of SO_2 emission rates (Galle et al., 2010).

The instruments used in the NOVAC network can be used in three different scanning modes, the plume speed measurement mode, the plume composition mode and the plume scan mode. In the plume speed measurement mode the SO_2 column density is measured at two distances from the volcanic plume simultaneously or subsequently with rapid alteration of the viewing direction. NOVAC Version 1 instruments can only use the plume speed measurement mode if the instrument contains two spectrometers. By calculating the cross-correlation of the SO_2 column density time series at these two points, the wind speed can be retrieved (Johansson et al., 2009; McGonigle et al., 2005). In the plume composition mode the sky is scanned to assess the location of the volcanic plume. Afterwards spectra are acquired by alternating between two viewing directions, one is directed towards the free sky and the other towards the approximate centre of the volcanic plume. This measurement mode is ideal for the evaluation

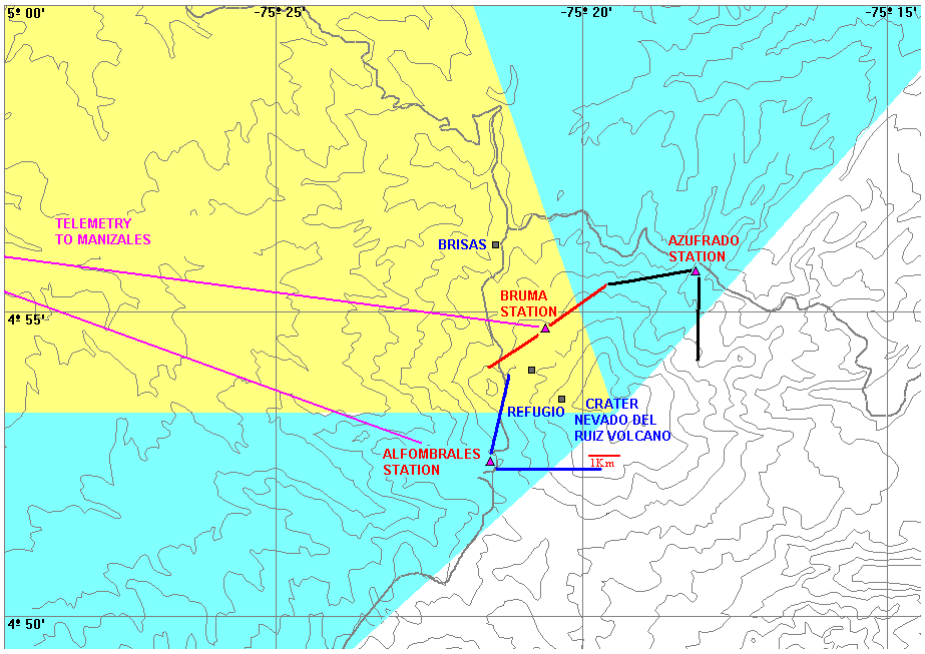

Figure 5.2.: Topographic map (contour levels every 200 m, the upper contour level is at 5200 m, Bruma station is at 4800 m above sea level) showing the location of Nevado del Ruiz volcano (Colombia) and the three NOVAC stations used for gas monitoring. The blue, red and black lines depict the viewing directions of the scanning DOAS systems. The two original instruments at Alfombrales station and Bruma station were installed in November 2009 and transmit data in real time to the volcanological observatory located at Manizales city. The third instrument at Azufrado station was installed in May 2012. Data from this instrument was not evaluated for this thesis, since only two month of data was available. The yellow background colour shows the wind direction for approximately 70 % of the time, the light blue shaded area shows the wind direction for the remaining 30 %. Reproduced from Lübcke et al. (2013a).

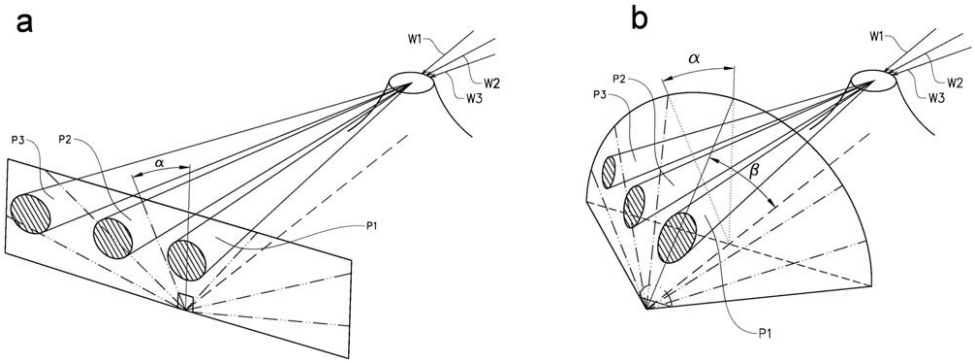

Figure 5.3.: Scanning geometries used in the NOVAC network **a** The flat scanning geometry **b** the conical scanning geometry. Reproduced from Galle et al. (2010) with kind permission of John Wiley and Sons.

of the BrO/SO_2 ratios. Unfortunately both, the plume speed mode and the plume composition mode are rarely used by the observatories. Several conditions have to be fulfilled before a wind speed measurement is performed; the plume has to be close to the zenith and a certain number of previous scans has to have a relatively stable direction of the plume centre (Johansson, 2009). Most observatories use the plume scan mode, in which a zenith-looking Fraunhofer reference spectrum is acquired before the complete sky is scanned from horizon to horizon. In this work only spectra with elevation angles between $\pm 75°$ (where an elevation angle of $0°$ describes a zenith-looking instrument) were evaluated to minimize problems with a long light path through the atmosphere and obstacles in the line of sight of the instruments.

While the plume scanning mode is optimal for the calculation of the SO_2 emission rates a higher signal-to-noise ratio (and thus more radiation intensity) is needed to successfully retrieve BrO. Therefore, ten spectra from the plume are summed up to obtain a collective plume spectrum with a higher intensity. The same is done for ten spectra that lie outside of the volcanic plume in order to obtain a collective Fraunhofer reference spectrum. This procedure will be explained in more detail in Section 5.2.1. The average step size between two viewing directions in NOVAC is $3.6°$ (Galle et al., 2010), therefore the collective plume and Fraunhofer reference spectrum contain spectra that cover a large field-of-view ($36°$).

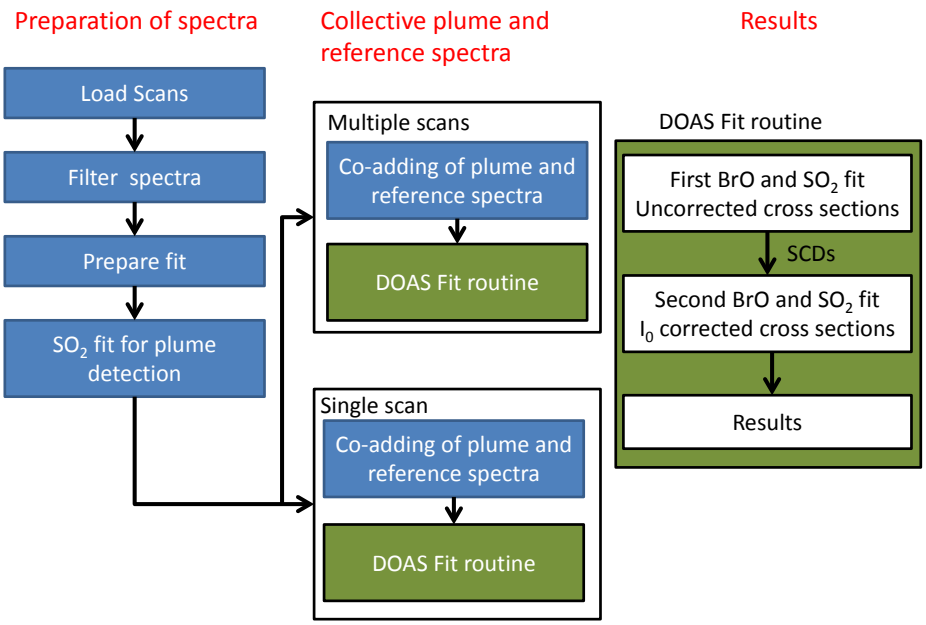

Figure 5.4.: Flow chart showing the main elements of the NOVAC BrO/SO_2 evaluation algorithm.

5.2 Evaluation of the BrO/SO_2 ratios

This section briefly describes the algorithm for the automatic evaluation of spectra from the NOVAC instruments for BrO and SO_2. The algorithm was developed during the work on this thesis, it is based on previous work by Vogel et al. (2011). The section starts with a description how the plume and Fraunhofer reference spectra for the DOAS retrieval are obtained by co-adding spectra from different viewing directions. Section 5.2.2 lists the settings for the DOAS retrieval. This includes among other things the wavelength range used for the evaluation and the absorbers that are included in the fit. A flow chart of the algorithm used for the evaluation of the NOVAC spectra is shown in Figure 5.4. A preliminary SO_2 evaluation is used to select spectra which are co-added to obtain collective plume and Fraunhofer reference spectra. These collective spectra are subsequently evaluated for BrO and SO_2 using the DOAS method.

5.2.1 Finding reference and plume spectra

The instruments of the NOVAC network are set-up in a way that they acquire spectra with a compromise of time resolution and sufficient signal-to-noise for the SO_2 evaluation. With this compromise there is too little radiation intensity for a successful BrO evaluation. While the BrO absorption cross section (e.g. Fleischmann et al., 2004) is roughly a factor of 150 larger than the SO_2 cross section (e.g. Vandaele et al., 2009) in the wavelength ranges that are commonly used for the DOAS evaluation, BrO has a lower abundance in volcanic plumes. Bobrowski and Platt (2007) studied the BrO/SO_2 ratio in the plumes of five volcanoes and found BrO/SO_2 ratios between 8×10^{-5} and 1×10^{-3}. Hörmann et al. (2013) used satellite measurements and found BrO/SO_2 ratios "ranging from some 10^{-5} to several 10^{-4}" at eleven different volcanoes. This leads to an optical density of BrO that is one to three orders of magnitude smaller than the optical density of SO_2.

To obtain a high enough signal-to-noise ratio for the BrO evaluation more radiation intensity is needed. The number of single exposures that are summed up for each spectrum cannot be changed retrospectively for the available NOVAC data, therefore a different approach is needed to obtain a better signal-to-noise ratio. In this work, several spectra (from a single scan from horizon to horizon) with different viewing directions (typically covering 36°) were co-added to obtain collective plume and Fraunhofer reference Spectra (FRS) for the DOAS retrieval of BrO and SO_2. To further increase the signal-to-noise ratio, the collective plume spectra and FRS obtained from several scans (of the complete sky) were co-added as well.

The first step is to determine which spectra (from one scan) are co-added for the collective plume spectrum and the collective FRS, respectively. Therefore, all spectra of each plume scan are pre-evaluated for SO_2 using a zenith spectrum acquired at the beginning of the plume scan as FRS. Underexposed and overexposed spectra (intensity below 15 % or above 85 % of the maximum exposure in the spectral region used for the DOAS evaluation) were removed from further evaluation. The ten adjacent spectra with the highest mean SO_2 column density value are selected and defined as the volcanic plume region. Similarly the set of ten adjacent spectra with the lowest mean SO_2 value is defined as the reference region (see Figure. 5.5). The spectra from the plume region are co-added to obtain a collective plume spectrum with higher signal-to-noise ratio, as well as the spectra from the reference region to obtain a collective FRS.

It should be noted, that this only a very basic approach to determine plume and reference spectra. With this approach only the centre of the plume is sampled in some cases (as in the example in Fig. 5.5). In other situations the collective plume spectrum might contain spectra from the plume edge as well as the centre of the plume. Previous measurements indicate that the BrO/SO_2 ratio increases at the plume edge (Bobrowski et al., 2007; Louban et al., 2009). Variations of the BrO/SO_2 ratio over the extent of the volcanic plume are not

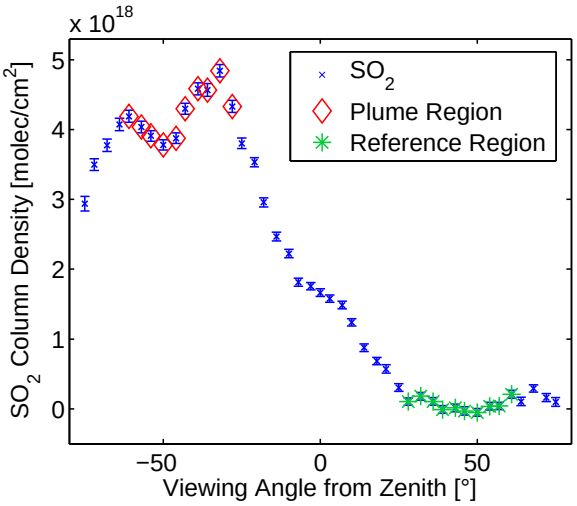

Figure 5.5.: Example of the SO_2 column densities from one complete scan ($-75°$ – zenith – $+75°$ elevation angle, measured clockwise when looking towards the volcano). The red diamonds show the column densities defining the volcanic plume region, while the green asterisks show the column densities defining the reference region. Reproduced from Lübcke et al. (2013a).

accounted for in the current version of the evaluation.

The collective plume spectra and FRS are evaluated using the DOAS method (see Section 3.2 and 5.2.2). To obtain an even better signal-to-noise ratio the collective plume spectra and FRS from several scans were co-added and the resulting spectra were evaluted by the DOAS method. Co-adding collective spectra from several scans further improved the DOAS retrieval errors, but led to a decrease of time-resolution. The dependency of the DOAS fit error on the number of co-added spectra is discussed in Section 5.3.1.

5.2.2 Spectroscopic retrieval for the BrO/SO_2 ratios

All spectra were evaluated with the DOAS method that combines a non-linear Levenberg–Marquard fit and a standard least-squares fit (Platt and Stutz, 2008) using the DOASIS software-package (Kraus, 2006, also see Section 3.2).

The FRS was wavelength calibrated using a high-resolution solar spectrum (Chance and Kurucz, 2010) that was convolved with the line shape of the 334.15 nm line of a low-pressure mercury lamp recorded with the same spectrometer. The plume spectra used the calibration from the respective FRS. The fit coefficient of the FRS was fixed to -1 in the DOAS fit. Two Ring spectra were included in the DOAS fit to correct for the Ring effect (Grainger and Ring, 1962). The first Ring spectrum was a standard Ring spectrum calculated using the DOASIS software-package; the second was created from the first Ring spectrum by multiplying it with a wavelength dependent term (in this work λ^{-4}) to account for multiple Rayleigh scattering in the atmosphere (Wagner et al., 2009).

A more detailed treatment of the Ring effect can be found in Section 3.2.2. A 3^{rd} order polynomial was included in the fit to account for broadband absorption structures and Rayleigh as well as Mie scattering structures in the spectra. An additional wavelength independent offset in the intensity space was allowed to correct for stray-light inside the spectrometer.

The SO_2 evaluation was performed in the wavelength range between 314.8 nm and 326.8 nm including one SO_2 absorption cross section at 298 K (Vandaele et al., 2009) and one O_3 absorption cross section at 221 K (Burrows et al., 1999).

The BrO evaluation was performed between 330.6 nm and 352.75 nm using the following absorption cross sections: BrO at 298 K (Fleischmann et al., 2004), the same SO_2 and O_3 as above, O_4 (Hermans, 2003), NO_2 at 298 K (Vandaele et al., 1998) and CH_2O at 298 K (Meller and Moortgat, 2000). An example of a BrO fit is shown in Fig. 5.6. The evaluation ranges and trace gases included in the SO_2 as well as in the BrO fit were chosen accordingly to Vogel et al. (2011), who performed a series of studies on the optimal evaluation wavelength range for BrO and SO_2 in a combination of real measurement data and theoretical studies. Chapter 7 discusses the choice of the evaluation range with regard to changes of the spectral response of the instruments due to temperature variations.

All trace gas absorption cross sections were convolved to match the instrument's spectral resolution using the 334.15 nm line of a mercury lamp, a sample of the instrument line function (ILF), recorded with the respective spectrometer. To account for the I_0-effect (Platt and Stutz, 2008, and also see Section 3.2.2) an iterative approach was used (see Figure 5.4). First, a fit was performed to retrieve uncorrected column densities of the trace gases; these column densities were then used to create I_0-corrected absorption cross sections (Wagner et al., 2002 and Section 3.2.2). In order to correct for small inaccuracies in the wavelength calibration, the FRS and both Ring spectra, as one set, and all trace gas absorption cross sections, as another set, were allowed to be shifted and first order squeezed against the measurement spectrum.

As an additional validation step both trace gases were additionally evaluated in further evaluation ranges. SO_2 was evaluated between 318.3 – 330 nm and 326.5 – 335.3 nm. BrO was evaluated between 327 – 347 nm to verify the stability of the DOAS retrieval. The smaller wavelength difference between these two SO_2 evaluation ranges and the BrO range was used to identify the influences of radiative transfer (e.g. light dilution). The results from different evaluation ranges are summarized in Section 6.1.

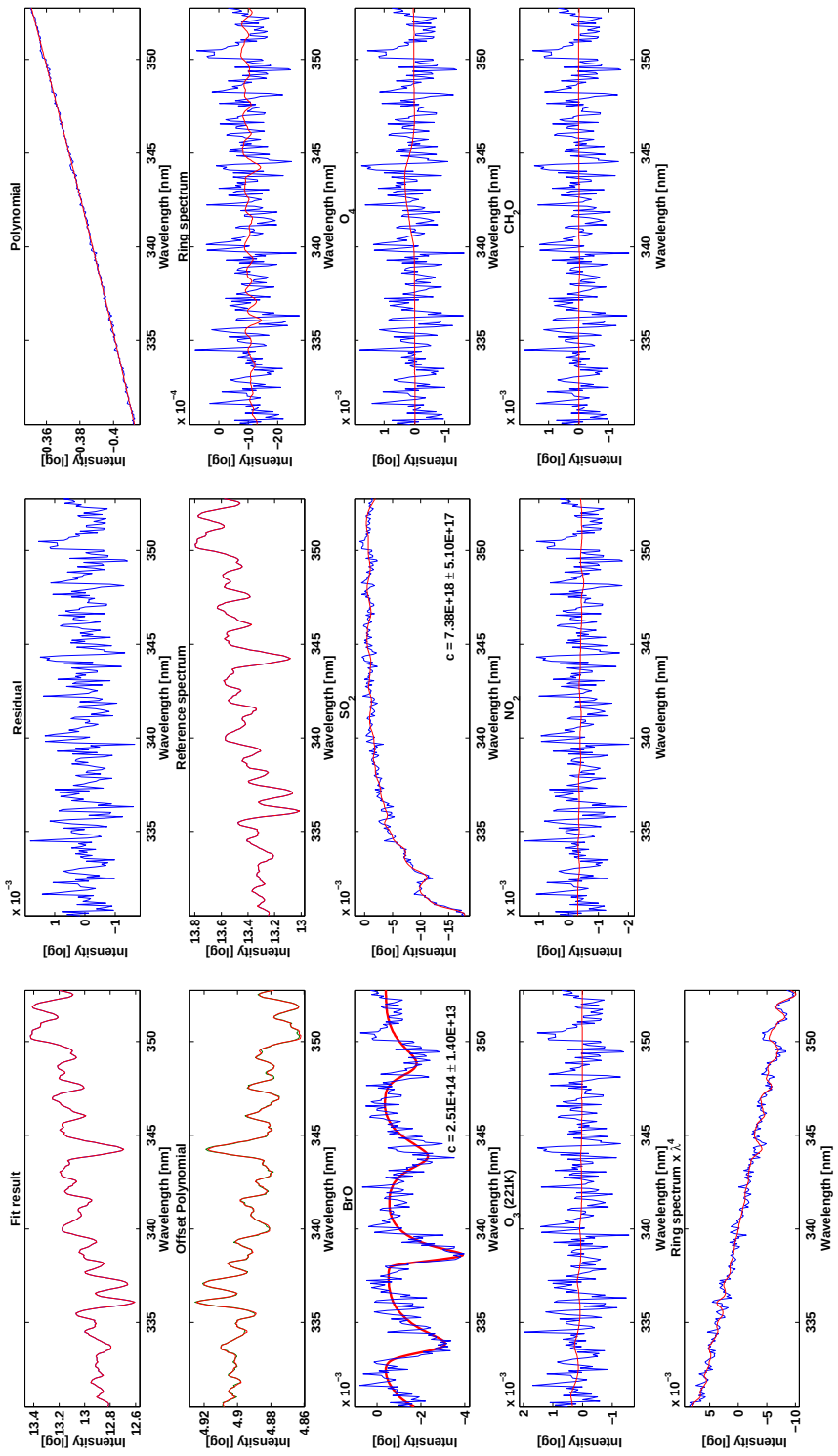

Figure 5.6.: Example of a DOAS BrO evaluation performed in the wavelength range of 330.6 nm – 352.75 nm. The red lines show the fit result, the blue lines the measurement data. A FRS and two Ring spectra were included in the DOAS fit. The BrO column density for this spectrum is 2.51×10^{14} molec/cm^2. Besides BrO, other trace gases (SO_2, O_4, O_3, NO_2, and CH_2O) were included in the DOAS evaluation. The spectra for this example were recorded on 31.10.2012 between 16:32 and 17:05 GMT. Reproduced from Lübcke et al. (2013a).

5.3 BrO/SO_2 ratios from Nevado del Ruiz

The algorithm for the retrieval of BrO/SO_2 ratios was tested by applying it to data from Nevado del Ruiz, Colombia. Almost four years of data, covering the time between November 2009 and June 2013 were automatically evaluated by the retrieval algorithm. Nevado del Ruiz was chosen as a first test site as it has a relatively complete dataset and interesting recent volcanic activity with high gas emissions.

Nevado del Ruiz is a 5400 m high stratovolcano located in the Andes in Colombia, approximately 130 km west of Bogotá. On 13 November 1985 Nevado del Ruiz tragically became known world wide, when the aftermath of an eruption killed approximately 25 000 people. The majority of people died in the small town of Armero that is located in a distance of approximately 50 km from the volcano. Lahars, debris and mud flows that were caused from glaciers melting due to pyroclastic flows from the volcano, buried the town of Armero and it's inhabitants.

After the eruption monitoring at Nevado del Ruiz has been enlarged. In November 2009 two NOVAC type 1 instruments were installed in the surroundings of the volcano. A third instrument was installed in May 2012. A map showing the location of Nevado del Ruiz, the currently three NOVAC instruments and their scanning directions is given in Fig. 5.2. The instruments whose data is used in this work were installed at Alfombrales station (blue lines in Figure 5.2) and Bruma station (red lines). The third instrument was not used in this thesis as data submission was intermitted only a few days after the instrument was installed.

At the end of 2010 seismicity and SO_2 emissions increased slowly. Higher activity with further increasing SO_2 emission rates started in the beginning of 2012 and on 30 June 2012 Nevado del Ruiz erupted, producing an ash plume with a height of 8 km above the crater (Smithsonian Global Volcanism Program, 2012).

This section starts with a discussion on the effect of co-adding spectra on the DOAS retrieval error before the BrO and SO_2 column densities as well as the BrO/SO_2 ratios will be discussed. An attempt of interpreting the results in a volcanological context follows in Section 5.3.3. This section ends with a discussion of how the release time from the volcanic vent into the atmosphere influences the BrO/SO_2 ratio.

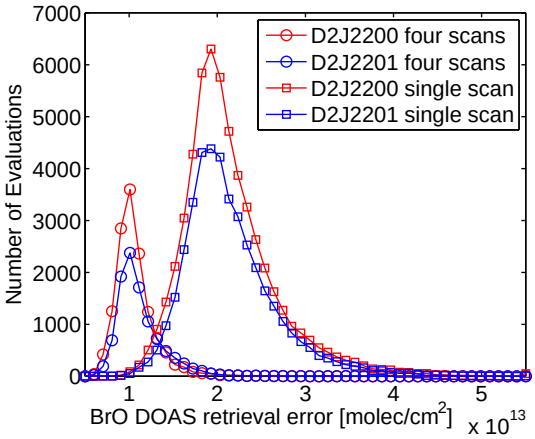

Figure 5.7.: The BrO DOAS fit errors for both instruments which data is presented in this study. The plot shows the results for spectra from single scans and for spectra co-added from four consecutive scans. The latter have a 50 % lower BrO DOAS fit error than single scans. Reproduced from Lübcke et al. (2013b).

5.3.1 Effect of co-adding spectra on the DOAS fit error

Spectra from one scan of the complete sky as well as spectra from various scans were co-added in order to increase the signal-to-noise ratio. In general a number of effects can lead to a strong increase of the residual as well as the DOAS fit error when co-adding spectra. For the NOVAC type 1 instruments the dominant error source is most likely caused by variations of the instrument's temperature (see Section 7). Changes of the instrument's temperature can lead to changes of the ILF and the wavelength-pixel-alignment, which can lead to a largely increased residual (see Section 7). Another possible error source are changes of the atmospheric conditions between spectra that are co-added. In the retrieval algorithm used in this work spectra are added in the intensity space. However, the optical densities are in the argument of the exponential function in the Beer-Lambert Law. As the exponential function and the sum are not commutative errors might occur, in particular at large optical depths. An simple example for optical depths of 0.5 and 0 shows the problem:

$$-\ln\left((e^{-0.5}+e^{-0})/2\right) \approx 0.2191 \neq 0.25 = -\ln\left(e^{-0.25}\right) \tag{5.1}$$

When co-adding spectra in intensity space, the resulting optical depth is not necessarily the average optical density of the single spectra. Additionally, this effect depends on the wavelength dependent optical density of the trace gases included in the spectra. Co-adding of spectra with varying optical densities of strong absorbers could increase the residual and therefore potentially hide weak absorbers.

The influence of co-adding spectra from several scans was investigated by using a subset of the Nevado del Ruiz data covering all scans between January

2011 and December 2012. The data was evaluated for BrO after the collective plume and reference spectra spectra from 1, 2, 4, 6 or 8 of scans were co-added.

An example of the number distribution of the BrO DOAS retrieval errors for both instruments and for spectra created from one and four scans is shown in Figure 5.7. The BrO retrieval error is similar for both instruments. For a single scan the fit error is centred around 2×10^{13} molec/cm^2, for the co-added spectra from four scans the fit error is centred around 1×10^{13} molec/cm^2. This means that the BrO retrieval error halves when comparing spectra created from one scan to spectra created from four scans, an indication that the evaluation is still limited by photon shot-noise.

The average BrO retrieval error plotted against the number of scans (1 – 8) from which spectra were co-added, is shown in Figure 5.8. The black curve shows a constant value divided by the square of the number of co-added scans, which denotes the ideal, photon shot-noise dominated case. The constant value, used for the black curve, is the BrO retrieval error from a single scan. It can be seen, that the BrO retrieval error deviates only slightly from the black curve when co-adding spectra from up to eight scans.

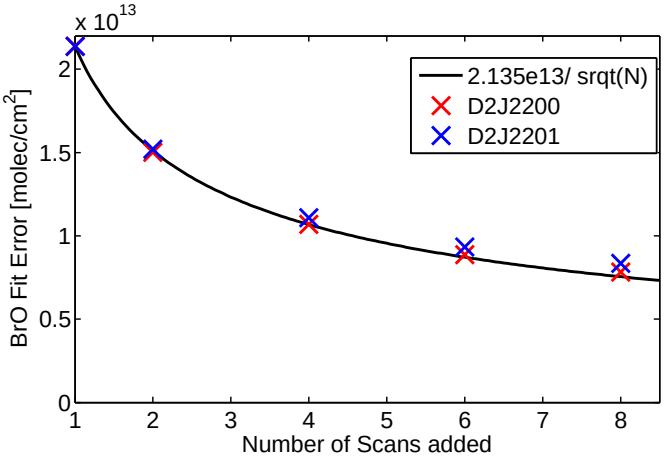

Figure 5.8.: The BrO DOAS fit errors for both instruments and its dependence on the number of consecutive scans from which the reference and plume spectra were created.

These result show that co-adding spectra greatly improves the BrO DOAS fit error. The BrO DOAS fit error appears to be mainly limited by photon shot noise. Problems that could lead to a deviation from the black curve (that denotes the photon shot-noise dominated case) cannot be observed. However, while the noise decreases, co-adding spectra from several scans can lead to losing absolute signal in some cases and generally losing time resolution.

For the rest of this section, spectra are used that were created by co-adding of four scans. This compromise leads to a low BrO retrieval error while still allowing a time resolution of approximately 15 – 30 minutes.

5.3.2 BrO/SO_2 ratios

Time series of the SO_2 and BrO column densities covering the time between November 2009 and June 2013 are shown in Figure 5.9.

The SO_2 column densities are below 2.5×10^{17} molec/cm^2 and BrO remains below the detection limit until the middle of April 2010. At the end of April, 2010 the SO_2 column densities increase noticeably for instrument D2J2200, while BrO only occasionally exceeds the detection limit. The BrO column densities significantly exceed the detection limit for the first time in September 2010 (marked by the first vertical dashed line in Figure 5.9). At the same time the SO_2 column densities and the SO_2 emission rates both show increasing values as well (Figure 5.9). At the beginning of 2012, the SO_2 and BrO column densities and the SO_2 emission rates drastically increase (third vertical dashed line). Towards the beginning of 2013, the SO_2 column densities start to decline while the BrO column densities stay elevated (which leads to increasing BrO/SO_2 ratios, see below).

Unfortunately, both instruments have some periods without transmitted data. D2J2201 has very few scans between July 2011 and November 2011 and the instrument with the serial number D2J2200 has a gap between June 2012 and September 2012. These gaps are due to technical difficulties that can occur when operating instruments in remote locations, i.e., the gap of D2J2200 after June 2012 can be explained by ash from the eruption falling onto the surface of the solar panels which led to a lack of power supply.

As there is only a relatively small amount of data points ($\sim$ 1–30) per day after the co-addition of scans, the usual approach of calculating the linear regression for a large amount of data points (Bobrowski et al., 2003) to find the BrO/SO_2 ratio cannot be used here. Instead, daily averages of the BrO/SO_2 ratios were calculated. Averaging over all ratios can lead to erroneous results, since the average would include many scans without significant volcanic gas and therefore negligible SO_2 and BrO column densities. Taking the ratio of two values (i.e., SO_2 and BrO column densities) that are close to zero gives unpredictable and unrealistic results. Therefore, spectra measured outside the volcanic plume have to be excluded. One possibility is setting a BrO threshold equivalent to a certain factor of the DOAS fit error as a BrO detection limit. An example of a time series created for all scans containing BrO above the detection limit (in this case 4 times the retrieval error was chosen) is shown in Figure 5.10. The BrO/SO_2 ratio is almost constant between January 2011 and January 2012 with a value of roughly $6-10 \times 10^{-5}$. Starting January 2012, the BrO/SO_2 ratio drops down to values as low as 2×10^{-5}, and increases again up to $4-6 \times 10^{-5}$ after an eruption on 30 June 2012 (red vertical bar in Figure 5.10). However, this approach is problematic since BrO is often close to the detection limit. In this case, setting a BrO threshold would remove low BrO values, and thus lead to elevated BrO/SO_2 ratios.

To avoid this problem, an SO_2 threshold of 7×10^{17} molec/cm^2 was used

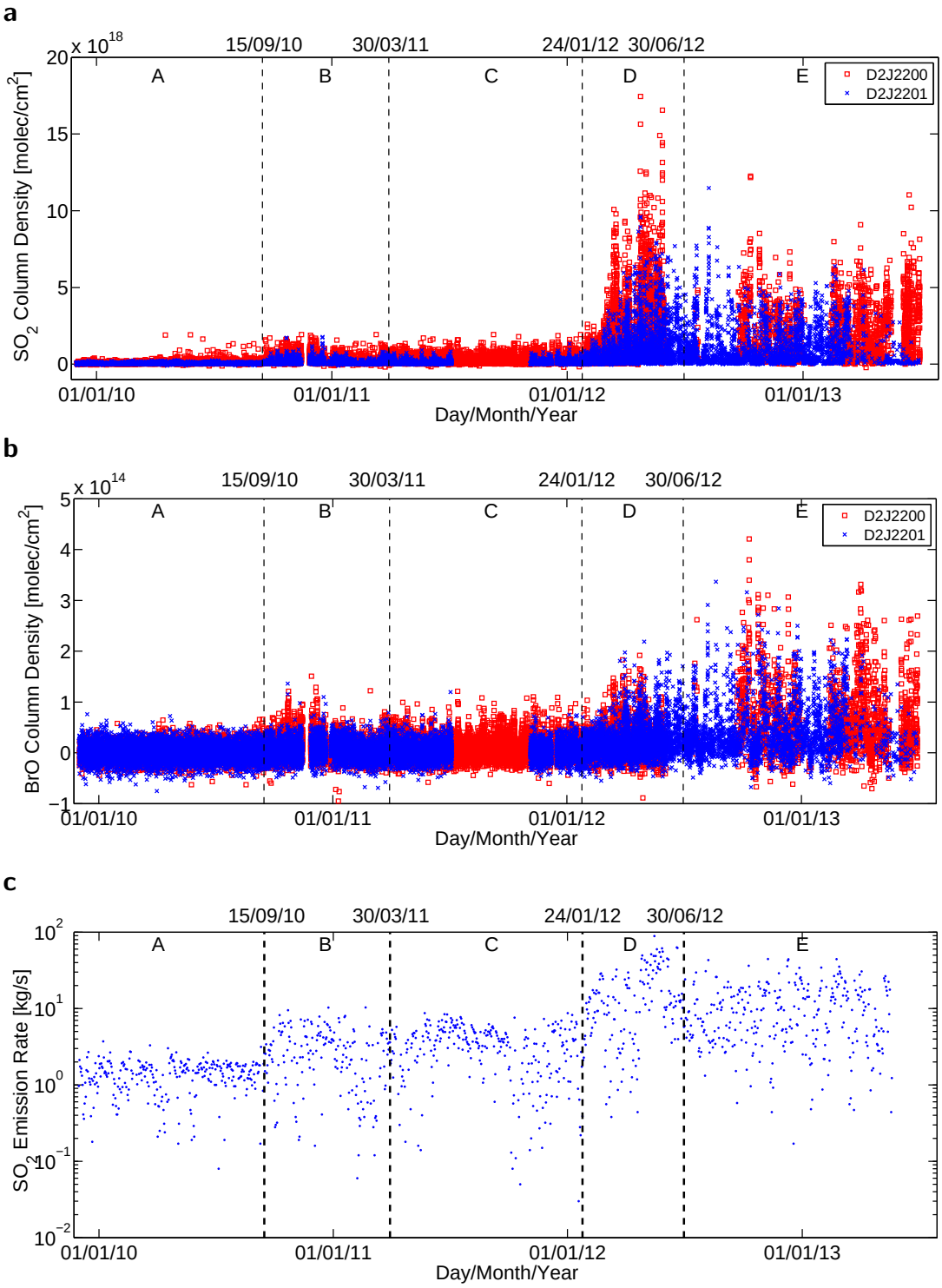

Figure 5.9.: Time series from the two instruments at Nevado del Ruiz. **a** SO_2 column densities, **b** BrO column densities. The spectra evaluated for the column densities were created from co-adding reference and plume spectra from four consecutive scans. **c** Daily averages of the SO_2 emission rates. The wind speed was taken from the ECWMF database, more details about the SO_2 emission rates in Galle et al. (2010) and Arrellano et al. (2013).

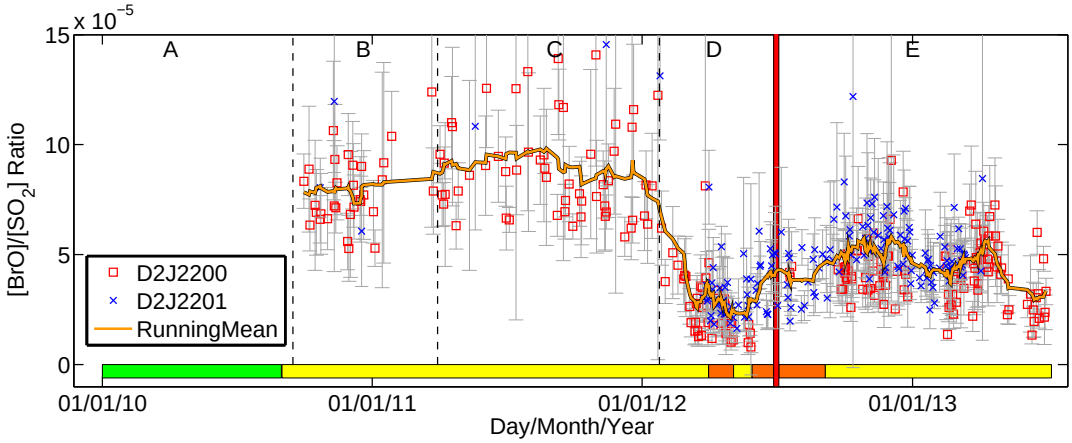

Figure 5.10.: Daily averages of the BrO/SO_2 molar ratios from Nevado del Ruiz from November 2009–June 2013. The criterion for a valid measurement is a BrO column density above four times the BrO DOAS retrieval error. The BrO/SO_2 ratio drops down to values below 5×10^{-5}, and increases again after the eruption on 30 June 2012 (red vertical bar). Also shown at the bottom of the image is the volcanic activity risk level defined by the Colombian Geological Survey (coloured horizontal bars). The black-orange line shows a running mean around 7 data points (from both instruments).

to select spectra for the evaluation of the BrO/SO_2 ratio. This threshold is a relatively high SO_2 column density. However, for the lower values of the BrO/SO_2 ratio in Figure 5.10 ($\sim 2 \times 10^{-5}$) this would result in a BrO column density as low as 1.4×10^{13} molec/cm^2, a value only slightly higher than the average DOAS retrieval error for BrO. This approach assures that scans not seeing significant amounts of volcanic gas are filtered out and thus will not significantly influence the BrO/SO_2 ratio. The result for the BrO/SO_2 ratio, using an SO_2 threshold as a selection criteria, is shown in Figure 5.11; the BrO/SO_2 ratio is again constant until January 2012 but with a lower value of 4×10^{-5}. In 2012 there is a drop to low SO_2/BrO ratios before the ratio increases again up to 4×10^{-5} after the eruption on 30 June, 2012. Afterwards the BrO/SO_2 ratio is mainly constant, independent of the spectra selection criterion, in June 2013 another drop of the BrO/SO_2 ratio can be observed. The trends found in the BrO/SO_2 molar ratios are similar irrespective of the plume selection criteria chosen for the calculation of the mean BrO/SO_2 ratio. Interestingly, the trends of the BrO/SO_2 ratio show a clear correspondence with the general evolution of the volcanic activity, as expressed by the levels of risks defined by the authorities (coloured bars in Figure 5.10 and 5.11). The decrease in the measured BrO/SO_2 ratio starts a few months before the main eruptive event on 30 June, 2012 that led to a rise of the alert to the highest (red) level. The drop in the BrO/SO_2 ratio occurs at a similar time as the increase in the total SO_2 emission rate. After the eruption the BrO/SO_2 ratio recovers again and reaches pre-eruptive values, when the level of activity decreases. The lack of BrO/SO_2 ratios from

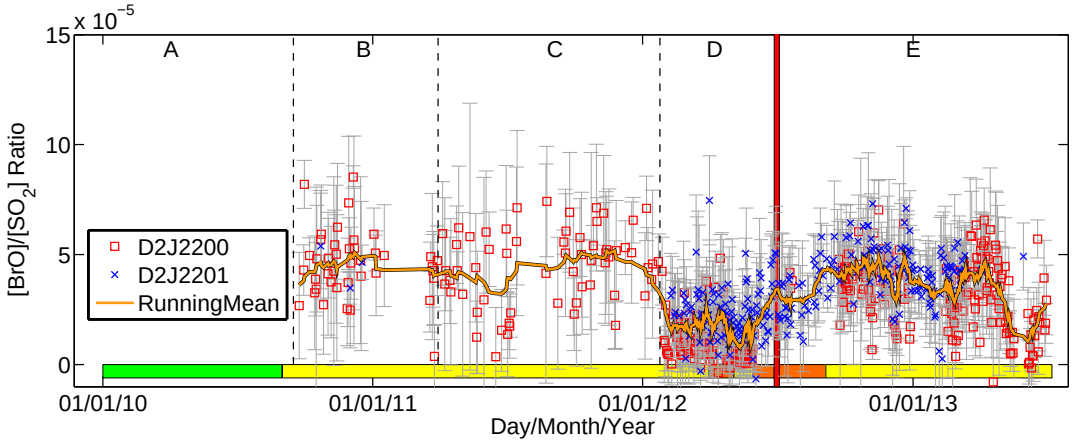

Figure 5.11.: Daily averages of the BrO/SO_2 molar ratios from Nevado del Ruiz from November 2009–June 2013. For this figure an SO_2 threshold of 7×10^{17} molec/cm^2 was chosen as the criterion for valid data points. The black-orange line shows a running mean around 7 data points (from both instruments). The dashed vertical lines and the letters A-D denote different periods of activity that are discussed in Section 5.3.3.

the spectrometer D2J2201 before January 2012 is due to the lack of spectra with high volcanic gas content, therefore no BrO or SO_2 could be detected above the detection limit. Whenever both instruments measure simultaneously the BrO/SO_2 ratio of both instruments agrees nicely.

The drop of the BrO/SO_2 ratios starts at the same time as the increase of the SO_2 emission rates. One could argue that the decrease of the BrO/SO_2 ratio does not have the same geological reason as the increase of the SO_2 emission rates, but rather is caused by increased gas emissions. A possible argument is, that during times of higher SO_2 emissions the volcanic plume does not mix well with the ambient air. If insufficient O_3 is available, the bromine explosion takes place slower and thus the observed BrO/SO_2 ratios decrease. One could reason against this explanation when looking at Figure 5.12; while the BrO/SO_2 ratio decreases with increasing SO_2 emission rate, there are also low BrO/SO_2 ratios on days with low SO_2 emission rates. This indicates that the BrO/SO_2 ratio does not only exhibit low values because of high SO_2 emission rates.

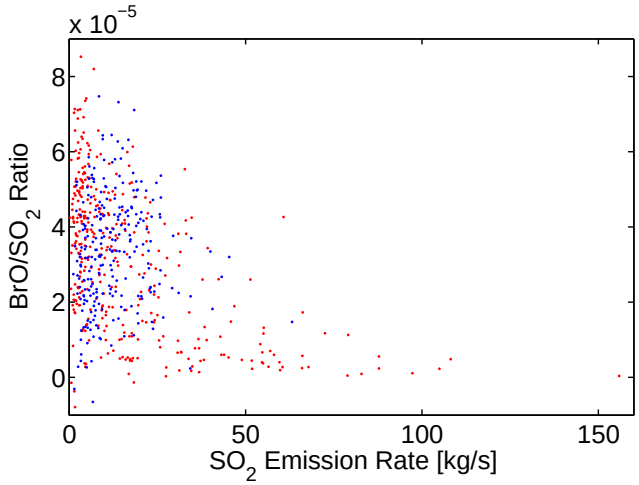

Figure 5.12.: Daily averages of the BrO/SO$_2$ ratio plotted against the daily average of the SO$_2$ emission rate.

5.3.3 Interpretation of the BrO/SO$_2$ ratio time-series

Many causes can produce the observed decrease in the BrO/SO$_2$ molar ratio, as for example the injection of an SO$_2$ rich batch of magma into a magma chamber, ascent of magma in the magmatic system or atmospheric effects like a different depletion rate of the two species due to scavenging by aerosols and ash in the plume. In this section the observed BrO/SO$_2$ ratios are compared with seismic activity and the SO$_2$ emission rate. It is suggested that the observed variations of the BrO/SO$_2$ ratio are indicative of the magma's ascent. An earlier model of the magmatic system at Nevado del Ruiz that was suggested by Stix et al. (2003) is used to interpret the data. In this model two different magma reservoirs are assumed below the volcano. A main, deep magma reservoir and a shallow reservoir. The main magma reservoir is between 9 – 15 km depth. The shallower magma chamber is located between roughly 2 – 5 km below the volcano.

The knowledge on bromine in magma and its distribution in the lithosphere is generally relatively sparse. However, Bureau et al. (2010) studied a synthethic magma that had similar concentrations of the main constituents (SiO$_2$ 72.2 wt.%, Al$_2$O$_3$ 11.4 wt.%, Na$_2$O 4.17 wt.%, K$_2$O 4.0 wt.%.) as melt inclusions from Nevado del Ruiz that were studied by Stix et al. (2003). Bureau et al. (2010) proposes that Br degasses from magmas together with water in subduction zone volcanoes. Based on the assumption that water exsolves from magma at earlier stages than sulphur (as e.g. suggested by Giggenbach, 1996, also see Figure 2.2), it is assumed that bromine is less soluble in magma than sulphur. Information about seismic activity, that is used in this section, is taken from Herrick (2012), who summarized and translated technical reports by INGEOMINAS[2].

[2]Instituto Colombiano de Geología y Minería, now called Servicio Geológico Colombiano. `http://www.sgc.gov.co`, last accessed: 11.02.2014.

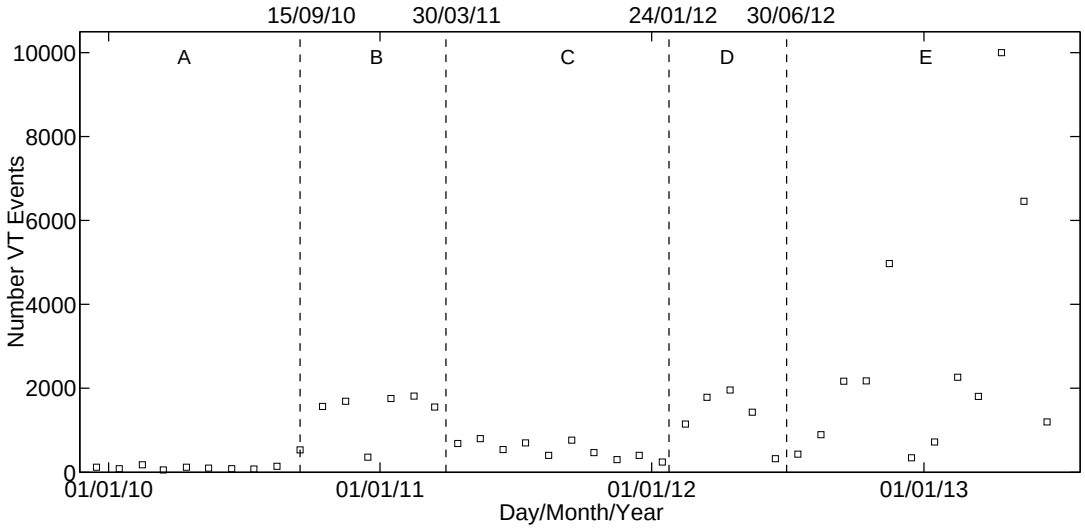

Figure 5.13.: Number of volcano-tectonic seismic events per month. Data taken from Herrick (2012) and from the technical reports of the SGC from `http://www.sgc.gov.co/`.

For a magma with high water content (4.4 wt%) and low CO_2 content (350 ppm) Stix et al. (2003) suggests that the H_2O content of the magma continuously decreases during the magma's ascent. The interpretation that follows is based on two assumptions; water only exsolves during the magma's ascent and water is less soluble in magma than sulphur. It should be noted though that this is only one possible explanation and that it is not totally certain if these assumptions are valid. For example, Giggenbach (1996) suggests that water exsolves from the magma earlier than sulphur, while in the same book an article by Martini (1996) suggests that sulphur is exsolved from the magma before water. Oppenheimer et al. (2014) summarizes the problem of gas exsolution from magma as follows: "The interactions of multiple phases (e.g., CO_2 and H_2O) are not well understood but are important". However, additional information (e.g. melt inclusions), which is not available, would be required to constrain the parameters. In the following the BrO/SO_2 ratios will therefore be interpreted using the above made assumptions:

Interval A: Herrick (2012) reports numerous seismic events between 2007 and August 2010 with a depth 1 – 12 km below Nevado del Ruiz. The SO_2 emission rates (available since the end of 2009, see Figure 5.9) were very low until September 2010, with average daily SO_2 emission rates between 0 – 2 kg/s. This period was interpreted as movement of magma from depth into the main magma reservoir between 9 – 15 km. At this depth both bromine and sulphur are most probably still soluble in the magma and almost no gas is exsolved.

Interval B: In September 2010, Herrick (2012) reports noticeable increase of seismic activity. This time is marked by the first vertical dashed line in the various plots (see Figures 5.9 - 5.14). We can see an increase of both volcano-tectonic

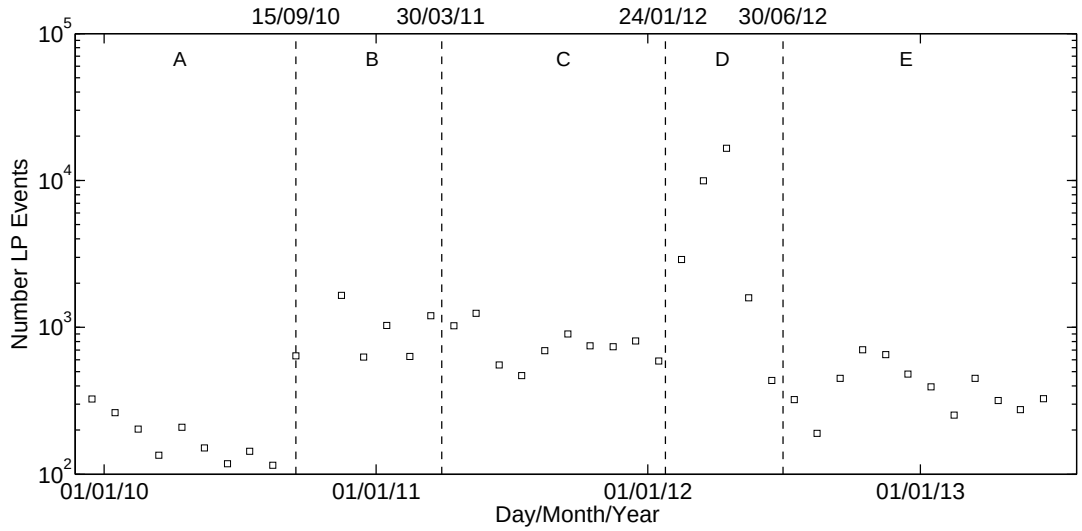

Figure 5.14.: Number of long-period seismic events per month. Data taken from Herrick (2012) and from the technical reports of the SGC from `http://www.sgc.gov.co/`.

(VT, see Figure 5.13) and long-period (LP, see Figure 5.14) seismic events. The SO_2 emission rates increase up to values of 10 kg/s, and the gas column densities are high enough to successfully obtain BrO/SO_2 ratios of $\approx 4-5 \times 10^{-5}$. This period was interpreted as ascent of magma from the deep reservoir up to the shallower reservoir between 2 – 5 km. At this depth the pressure is assumed to be low enough for bromine and some sulphur to exsolve at least partially from the magma. The increased number of VT events might be a hint that cracks are formed in the rock and magma is forming a path for it's ascent. LP events are often related to the movement of fluids. Assuming that bromine is less soluble than sulphur, the magma looses a considerable amount of bromine but only a small fraction of its sulphur content (see Figure 5.15).

Interval C: At the end of March 2011 (second vertical dashed line) the number of VT events decreases, while the number of LP events and the SO_2 emission rate stay constant. Maybe some new magma ascents into the shallow reservoir as indicated by the LP-events, however no new paths for the magma's ascent are formed (low number of VT events). At this time the magma is assumed to pond in the shallow reservoir with some additional magma, which is moving up from depth, filling up the shallow reservoir. While the magma is ponding it continues to degas, the pressure of the system and thus the BrO/SO_2 emissions are constant.

Interval D: At the end of Januar 2012 (shown by the third dashed line) a strong increase in VT and LP events can be observed (note that there is a logarithmic scale for the LP events in Figure 5.14). At the same time all observables, the SO_2 emission rate, SO_2 and BrO column densities start to increase as well. These observations were interpreted as a magma that is buoyant again and continues to rise towards the top of the volcano. Cracks that lead to a reduction

of the system's pressure or crystallization in the magma are possible reasons for exsolution of volatiles from magma. If the exsolved volatiles cannot escape the magma they decrease the magma's density and can thus lead to magma that is buoyant again (only a small fraction of the gas is able to escape the magma). As magma ascends the pressure and thus the solubility of bromine and sulphur further decreases (see Figure 5.15) and a larger fraction of both species is exsolved. Now a considerable fraction of sulphur exsolves and since there is much more sulphur in magma than bromine the BrO/SO_2 ratio decreases to values around $\approx 1 - 2 \times 10^{-5}$. In June 2012 the SO_2 emission rate strongly increase with daily averages of up to 88.85 kg/s. On 30 June 2012 an explosion of Nevado del Ruiz took place, leading to an ash plume with a height of up to 8 km (Herrick, 2012).

Interval E: After the explosion the number of VT and LP events goes back to lower, pre-eruptive values, but there are three month with largely increased numbers of VT events in interval E. The BrO/SO_2 ratio recovers and has still values similar to intervals A and B. However, the SO_2 emission rate has values of up to 40 kg/s (daily average), considerably higher than in intervals A and B. One interpretation for this behaviour is, that there is still a significant amount of gas that exsolves from the magma in the shallow magma chamber at the end of the observation period. Another possibility is that the earlier activity opened pathways for volatiles to escape and that a continuous convection in the magmatic system (see Chapter 2) leads to a supply of fresh, volatile rich magma. As the magma is at the same depth as in Interval A and B the BrO/SO_2 ratio is similar to these periods.

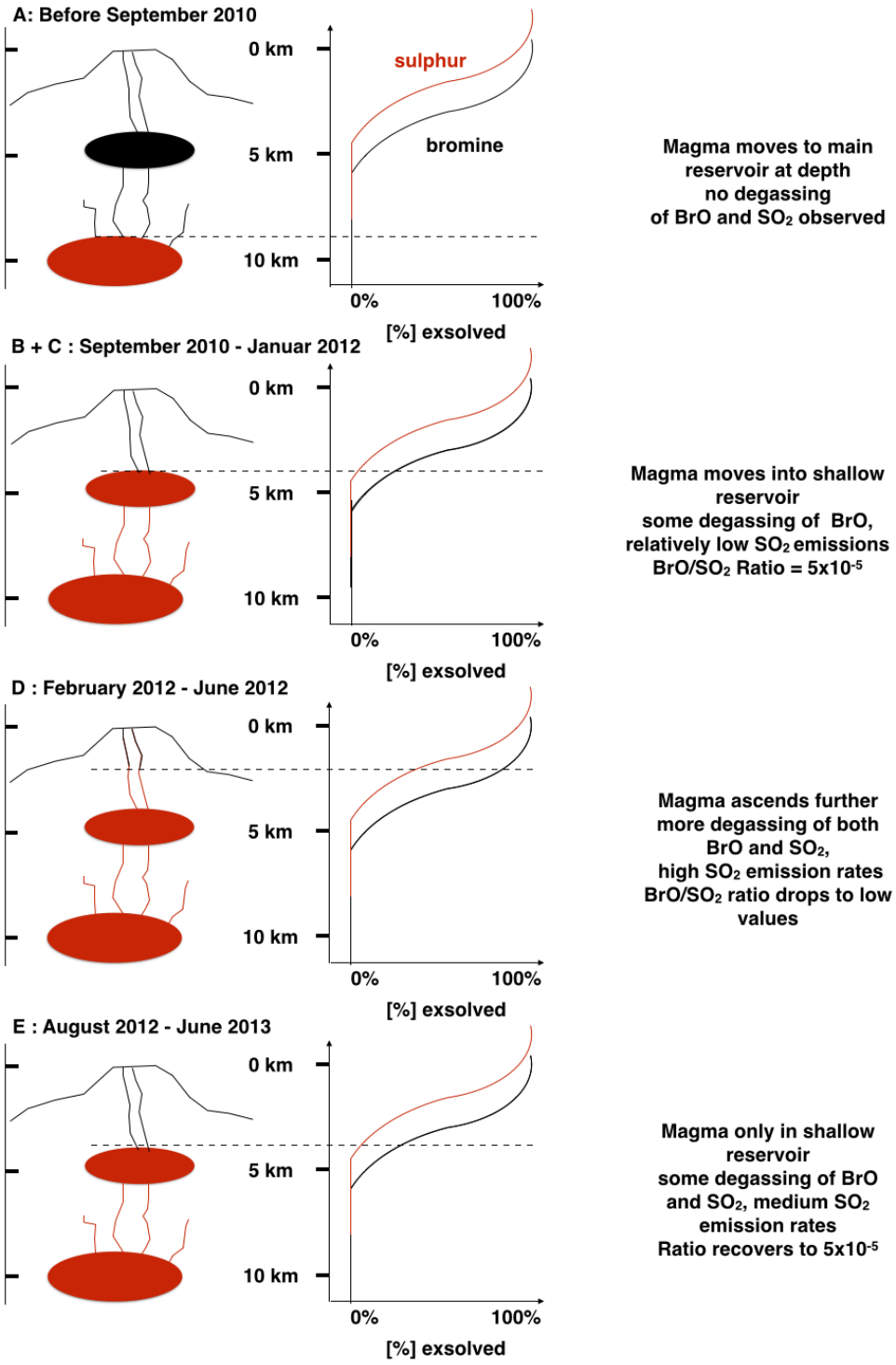

Figure 5.15.: The different phases of the magma ascent and the corresponding bromine and sulphur solubilities. If magma reaches higher levels gases start to exsolve. Bromine starts to exsolve earlier in this model. When the magma reaches high levels in period **D** a significant amounts of sulphur exsolves and the BrO/SO_2 ratio decreases.

5.3.4 BrO formation at Nevado del Ruiz

BrO is not directly released from the volcano, but formed when the volcanic gases mix with the surrounding atmosphere via the so-called "bromine explosion" (see Section 2.3.2). The large NOVAC dataset allows to investigate the timing of the BrO formation. Knowing the time evolution of the BrO formation is important in order to use BrO/SO_2 ratios as a tracer of volcanic activity. If the amount of BrO produced for a given amount of its precursors (e.g. HBr) released from the volcano is not constant during the measurement, it is unclear if changes in the BrO/SO_2 ratio are due to volcanic activity or due to BrO formation.

The residence time of the volcanic plume in the atmosphere is calculated from the viewing direction at which the plume was detected and the wind speed and direction from the ECMWF database. The ECMWF data that was used for the SO_2 emission rates in Figure 5.9 was also used for these investigations (both data sets were provided by Santiago Arellano, personal communication). First the distance between the volcanic vent and the point of measurement was calculated from the viewing direction of the instrument and the wind direction. This distance was then divided by the wind speed to gain the plume's residence time in the atmosphere. All BrO/SO_2 ratios with a residence time in a distinct interval were averaged. For times below 400 s an interval of 50 s was chosen (i.e., 0-50 s, 50-100 s,...) as we are interested in the dynamic changes of the BrO/SO_2 ratio in young volcanic plumes. For times above 400 s an interval of 200 s was chosen to account for the lower number of measurements at these plume ages.

These averages show a high degree of uncertainty. Besides the DOAS retrieval error there are additional sources of uncertainty, mainly the wind speed and direction from the ECMWF database and the exact direction at which the plume is detected. Therefore, the BrO/SO_2 ratios of both instruments were averaged to obtain better statistics.

The result of the averaging process is shown in Figure 5.16. In this figure data points for which more than 20 BrO/SO_2 ratios were averaged are shown in black, other data points are shown in red. Below release times of approximately two minutes, a total of only 18 scans were detected in four years of measurements. In comparison, about 40 scans are in the next interval (between 100 and 150 s). All other intervals between 150 and 1100 s contain more than 145 scans (see Table B.1 and Figure B.1 in Appendix B). Figure 5.16 shows a strong increase of the BrO/SO_2 ratio up to a residence time of roughly 8 minutes. Between 8 and 40 minutes the BrO/SO_2 ratio is constant.

The increase of the BrO/SO_2 ratio within the first minutes can be compared to measurements at Pacaya, Guatemala in February, 2010 by Vogel (2011) and with measurements at Etna in 2012 by Gliß (2013). Both authors used a DOAS instrument and scanned the plume in horizontal direction to investigate the time evolution of the BrO/SO_2 ratio. Vogel (2011) found a strong increase of the BrO/SO_2 ratio between 2-5 minutes after release from the volcano. Unfortunately, the measurements by Vogel (2011) only cover times up to 5 minutes after release,

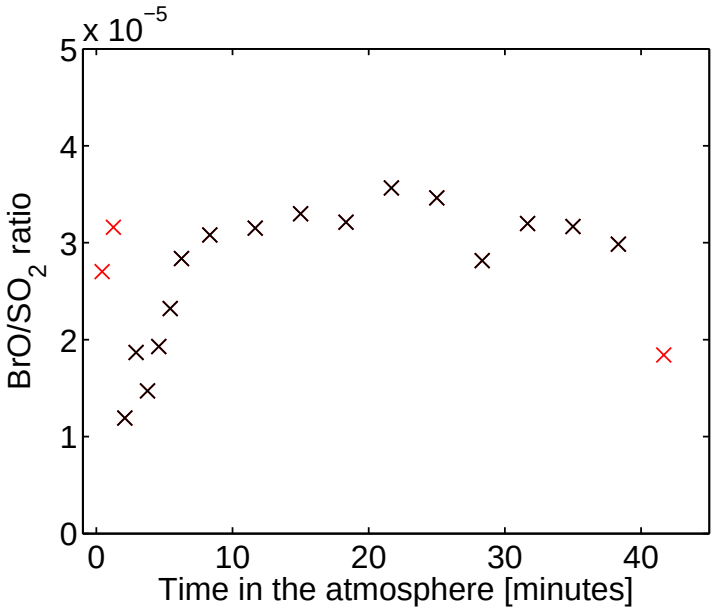

Figure 5.16.: Variation of the BrO/SO$_2$ ratio as a function of the time since release from the volcano. The black crosses show intervals with more than 20 scans, red points show all intervals where only few data points are available.

and no statement can be made, if the BrO/SO$_2$ ratio is constant at later times. Gliß (2013) measured the evolution of BrO/SO$_2$ at Etna and found an increase within the first few minutes. The author argues, that after 2-3 minutes the BrO/SO$_2$ ratio is constant. These measurements seem to indicate, that the BrO/SO$_2$ is constant earlier than in the results from Nevado del Ruiz. Additional scanning DOAS measurements by Vogel (2011) at Etna showed constant BrO/SO$_2$ ratios for up to 120 minutes, after the initial formation phase, these findings are in good agreement with the constant BrO/SO$_2$ ratio in Figure 5.16.

One possible explanation for the slower increase of the BrO/SO$_2$ ratio at Nevado del Ruiz is that the plume is not well mixed with the ambient air, and that therefore not enough O_3 is available for the bromine explosion. Roberts et al. (2014) recently suggested that higher gas emission rates from volcanoes might lead to lower BrO/SO$_2$ ratios. When comparing the SO$_2$ emission rates from Nevado del Ruiz with Pacaya, this seems to be one possible explanation, assuming that a higher SO$_2$ emission rate corresponds to a larger and therefore less well-mixed plume. While Nevado del Ruiz showed SO$_2$ emission rates above 10 kg/s at many times, the emission rates at Pacaya are usually well below 10 kg/s (Andres and Kasgnoc, 1998; Dalton et al., 2010). However, Etna, which also shows a much faster evolution of the BrO/SO$_2$ ratio, has SO$_2$ emission rates that are comparable to the SO$_2$ emission rates even during the eruptive phase at Nevado del Ruiz.

Another possible explanation is that both the chemical composition of the

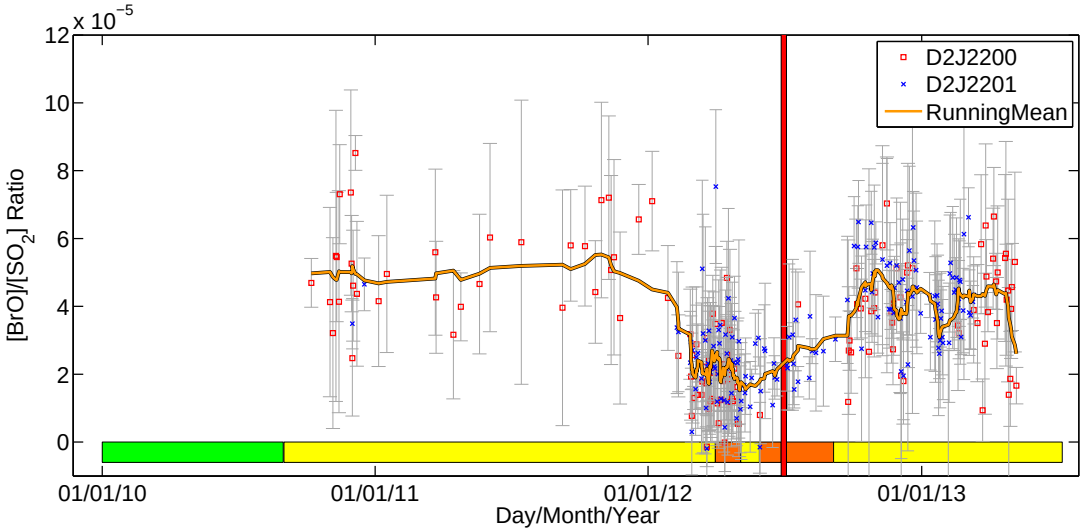

Figure 5.17.: Time-series of the BrO/SO_2 ratio after all scans with a plume age below 8 minutes were removed from the data set.

plume when released from the volcano and the mixing with ambient air in the "effective source region" (see Chapter 2.3.2) might be different at Nevado del Ruiz. Model calculations by Bobrowski and Platt (2007), von Glasow (2010) and Bobrowski et al. (2014) show that these parameters can influence the BrO formation in volcanic plumes. While Etna has four distinct craters, Nevado del Ruiz has only one main crater which might result in less mixing with ambient air in the effective source region and thus lead to a slower BrO formation.

The time evolution of the BrO/SO_2 ratio measured at Nevado del Ruiz is faster than model calculations by von Glasow (2010) and Roberts et al. (2009). These model studies suggest a constant BrO/SO_2 ratio at plume ages older than 15 minutes. The data from Nevado del Ruiz is an additional piece to the puzzle of halogen chemistry occurring in volcanic plumes.

To investigate if the BrO formation influences the BrO/SO_2 ratio time series (Figure 5.11), the data set was filtered and all scans with a plume residence time in the atmosphere below 8 minutes were removed. The result is shown in Figure 5.17. The general shape of the BrO/SO_2 ratio time series is similar to Figure 5.11. However, there are fewer data points and the scatter of the BrO/SO_2 ratio is lower, especially for the instrument D2J2200 before January 2012. The time series shown in Figure 5.17 ends earlier than Figure 5.11, because no SO_2 emission rates and therefore wind speeds and directions were available at the time of this thesis.

This investigation of the BrO formation shows that BrO is formed within the first 8 minutes after release from the volcano at Nevado del Ruiz. However, filtering *young plumes* from the data set did not lead to a significant variation of the BrO/SO_2 time series shown in Figure 5.17.

6

The influence of radiative transfer on the BrO/SO_2 ratio

The assumption for an ideal optical remote sensing measurement of volcanic gases is that radiation from the sun is scattered into the direction of the instrument from behind the volcanic plume. After this one scattering event, photons traverse the plume in a straight line and are, depending on their wavelength, absorbed by different trace gases before arriving at the instrument. The measured column density would thus give the integral of the mean trace gas concentration along a straight line through the volcanic plume.

In reality the radiative transfer in the volcanic plume and in the atmosphere can largely influence the path of radiation on its way to the instrument (see Section 3.4). There are mainly two processes that have an impact on the measured column densities. On the one hand, not all radiation that is detected by the instrument has actually passed the volcanic plume. A fraction of photons is scattered into the viewing direction of the instrument between the volcanic plume and the instrument diluting the measured signal, an effect that is often called light-dilution. This effect, which was already known for the COSPEC in the 1980s (Millan, 1980), leads to an underestimation of the measured column density. Empirical data by Mori et al. (2006) showed attenuations of the SO_2 retrieved at 309 nm between 30 – 50% for a distance of only 2.6 km. On the other hand multiple scattering events can also lead to a largely extended light path through the volcanic plume, which leads to an overestimation of the trace gas column density (Kern, 2009). Meteorological clouds are known to extend the light path of photons (Erle et al., 1995; Pfeilsticker et al., 1998) but can, depending on the measurement geometry, also shield radiation from penetrating the volcanic plume.

When measuring SO_2 emission rates the influences of radiative transfer that were described above can largely falsify the obtained results. The advantage of using the ratio between BrO and SO_2 is that both gases absorb radiation in a relatively narrow wavelength range and that the effects of radiative transfer are thus comparable for both gases. Therefore, the ratio of the two gases is assumed to be more robust than SO_2 emission rates. However, the mean wavelength range used in this thesis for the DOAS retrieval of the two trace gases is roughly 20 nm apart (see Section 5.2). Therefore, the path through the atmosphere is not exactly the same for both gases. Potential influences of radiative transfer on the BrO/SO_2 ratio have to be quantified.

In Section 6.1 the spectroscopic data from Nevado del Ruiz is evaluated with the DOAS approach in different wavelength intervals. Using wavelength ranges with a shorter spectral distance minimizes the differences between the column densities of the two trace gases due to radiative transfer effects.

A different approach, using simulations from a radiative transfer model (RTM), was used in Section 6.2. Model calculations using the 3D RTM McArtim (Deutschmann et al., 2011) were performed to quantify the variations of the BrO/SO_2 ratio caused by the distance between instrument and volcanic plume and the influence of meteorological clouds. Section 6.2 describes the McArtim simulations and the results for the BrO/SO_2 ratios.

The chapter concludes with a brief discussion on the possibility to detect clouds directly from the spectra recorded by the NOVAC instruments (Section 6.3).

6.1 Evaluating BrO and SO_2 in different wavelength ranges

The spectroscopic data from Nevado del Ruiz was evaluated in additional wavelength ranges in order to validate the results retrieved in the standard evaluation ranges and further assess influences of radiative transfer on the results. SO_2 was evaluated in two additional wavelength ranges between 318.3 – 330 nm and 326.5 – 335.3 nm. The starting wavelength of these two evaluation ranges is higher and they are thus closer to the range used for the BrO evaluation. Additionally the optical density of SO_2 is lower at larger wavelengths. The influences of radiative transfer on the BrO/SO_2 ratio should therefore be smaller than for the standard SO_2 range between 314.6 – 326.8 nm. The range between 326.6 – 335.3 nm was already used by Hörmann et al. (2013) as an alternative SO_2 retrieval range for the evaluation of satellite measurements. BrO was additionally evaluated in the range between 327 – 347 nm. This range was suggested by Kelly et al. (2013) and is used to validate the BrO results obtained in our standard evaluation range. The details of the DOAS retrieval are described in Section 5.2.

As one example for the SO_2 evaluation in different wavelength intervals the results for instrument D2J2201 are shown as a correlation plots in Figure 6.1.

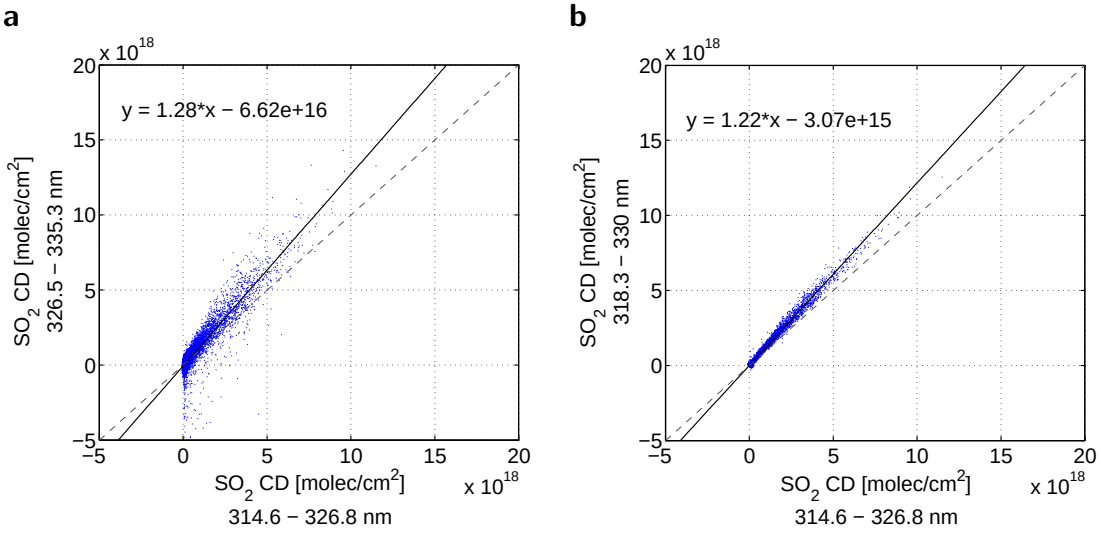

Figure 6.1.: Scatter plot of the SO_2 column densities for the instrument D2J2201 evaluated in two different wavelength ranges. Shifting the evaluation range to higher values results in higher SO_2 column densities. **a** 314.6 - 326.8 nm vs. 326.5 - 353.3 nm, **b** 314.6 - 326.8 nm vs. 318.3 - 330 nm.

The SO_2 results from evaluations between 314.6 – 326.8 nm and 326.5 – 335.3 nm are shown in Figure 6.1 a. The results for an SO_2 evaluations between 314.6 – 326.8 nm and 318.3 – 330 nm is shown in Figure 6.1 b. For the BrO evaluation the column densities for instrument D2J2200 evaluated between 330.6 – 352.75 nm and 327 – 347 nm are shown in Figure 6.2. The complete results for all retrieval ranges and both instruments can be found in Appendix C.

The DOAS SO_2 retrieval between 318.3 – 330 nm (Figure 6.2 b) showed an excellent linear correlation with the standard evaluation range but the SO_2 column densities are $\approx 20\%$ higher. For instrument D2J2201, the DOAS retrieval error in our standard range is $\approx 50\%$ lower, compared to an evaluation between 318.3 – 330 nm. Instrument D2J2200 has similar DOAS retrieval errors; however, from mid April 2010 3 – 4 times higher DOAS retrieval errors can be observed for the first and last scan of a day occasionally when using the alternative evaluation range.

Comparing the standard evaluation range with a DOAS retrieval performed between 326.5 – 335.3 nm (see Figure 6.1), a good correlation between the SO_2 column densities can be observed, with $\approx 30\%$ higher SO_2 column densities for the evaluation at larger wavelengths. The DOAS retrieval between 326.5 - 353.3 nm does not encompass the strong SO_2 absorption bands at lower wavelengths, which results in a DOAS retrieval error that is higher by more than a factor of 10 when compared to the standard evaluation range. For instrument D2J2200 there are also a few ($\approx$150) spectra where the fit completely fails and yields negative SO_2 column densities.

The BrO column densities (see Figure 6.2 and Appendix C) are similar in both

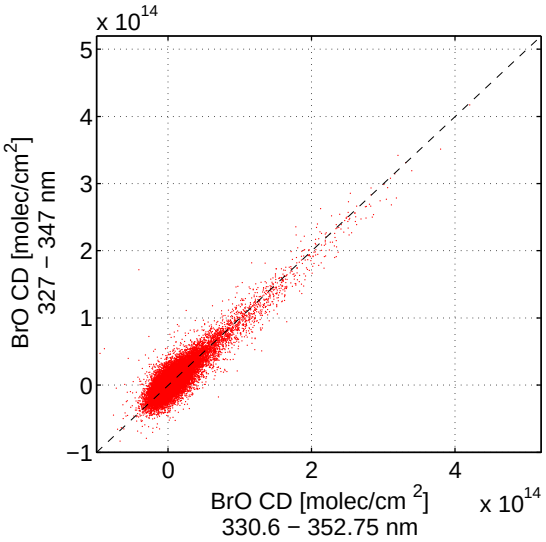

Figure 6.2.: Correlation plot of the BrO column densities for the instrument D2J2200 evaluated in two different wavelength ranges. In general both evaluation ranges yield the same results. The black dashed line shows the unity line.

evaluation ranges. The agreement is especially good for BrO column densities above 5×10^{13} molec/cm^2. Instrument D2J2201 has more prominent deviations at BrO column densities below this value. However, the BrO retrieval error in the standard evaluation range is $\approx 30\%$ lower than in the other range, suggesting that this wavelength range is better suited for the BrO DOAS retrieval.

To answer the question of how the choice of the evaluation range for the DOAS retrieval influences the BrO/SO_2 time series, plots similar to Figure 5.11 were created for four combinations of evaluation ranges:

- *Set 1* SO_2: 314.6 – 326.8 nm, BrO: 330.5 – 352.75 nm; this are the standard evaluation ranges used in the rest of this thesis
- *Set 2* SO_2: 314.6 – 326.8 nm, BrO: 327 – 347 nm
- *Set 3* SO_2: 326.8 – 353.5 nm, BrO: 330.5 – 352.75 nm
- *Set 4* SO_2: 326.8 – 353.5 nm, BrO: 327 – 347 nm

The SO_2 evaluation between 318.3 – 330 nm was not used in this comparison since the good linear relationship to the standard SO_2 evaluation range only leads to a lower BrO/SO_2 ratio but little other variations. To create the BrO/SO_2 time series an SO_2 threshold of 7×10^{17} molec/cm^2 (obtained in the respective SO_2 range) was chosen as a criterion to select scans similar to the results in Chapter 5. As one example for a different set of evaluation ranges the time series for Set 2 is shown in Figure 6.3. Due to the large number of data points it is hard to distinguish differences to Figure 5.11.

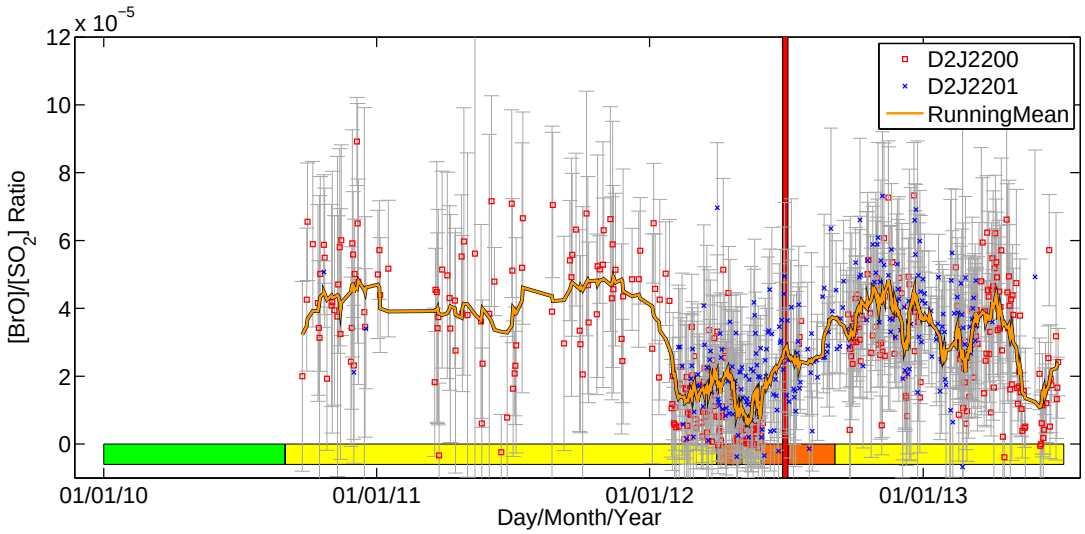

Figure 6.3.: Time-series of the BrO/SO_2 ratio. SO_2 was evaluated between 314.6 – 326.8 nm. The BrO evaluation was performed between 327 – 347 nm. The red vertical line shows an eruption of Nevado del Ruiz on 30 June 2012.

A better comparison is possible by looking at the running mean of the BrO/SO_2 ratio (over 7 days) for all four sets in Figure 6.4. The BrO range between 327 – 347 nm in combination with the standard SO_2 retrieval range (Set 2) leads to slightly lower BrO/SO_2 ratios. Similarly evaluating SO_2 at larger wavelengths between 326.5 – 335.3 nm, while using the standard BrO retrieval range (Set 3), leads to lower BrO/SO_2 ratios. The behaviour for the alternative SO_2 evaluation range is expected, as radiative transfer effects, such as the light-dilution effect (see Section 3.4 and 6.2) usually lead to an underestimation of the true SO_2 column density when evaluating at lower wavelengths. Even though the BrO/SO_2 ratios seem to agree better for the low values after February 2012, these values are lower as well for an SO_2 evaluation at larger wavelengths. This can be clearly seen in the zoomed-in-section in the upper part of Figure 6.4.

However, regardless of the difference between the absolute values of the BrO/SO_2 ratio, the main variations and the sharp drop roughly 5 months before the eruption at the end of June 2012 can be observed independently of the evaluation ranges chosen for the BrO and SO_2 DOAS retrieval.

Using the alternative SO_2 evaluation range leads to noticeably lower BrO/SO_2 ratios between June and the end of 2012. One possible explanation are variations in the volcanic plume composition (more ash or more plume condensation) that potentially lead to an increase of radiative transfer effects following the time of the eruption on 30 June 2012.

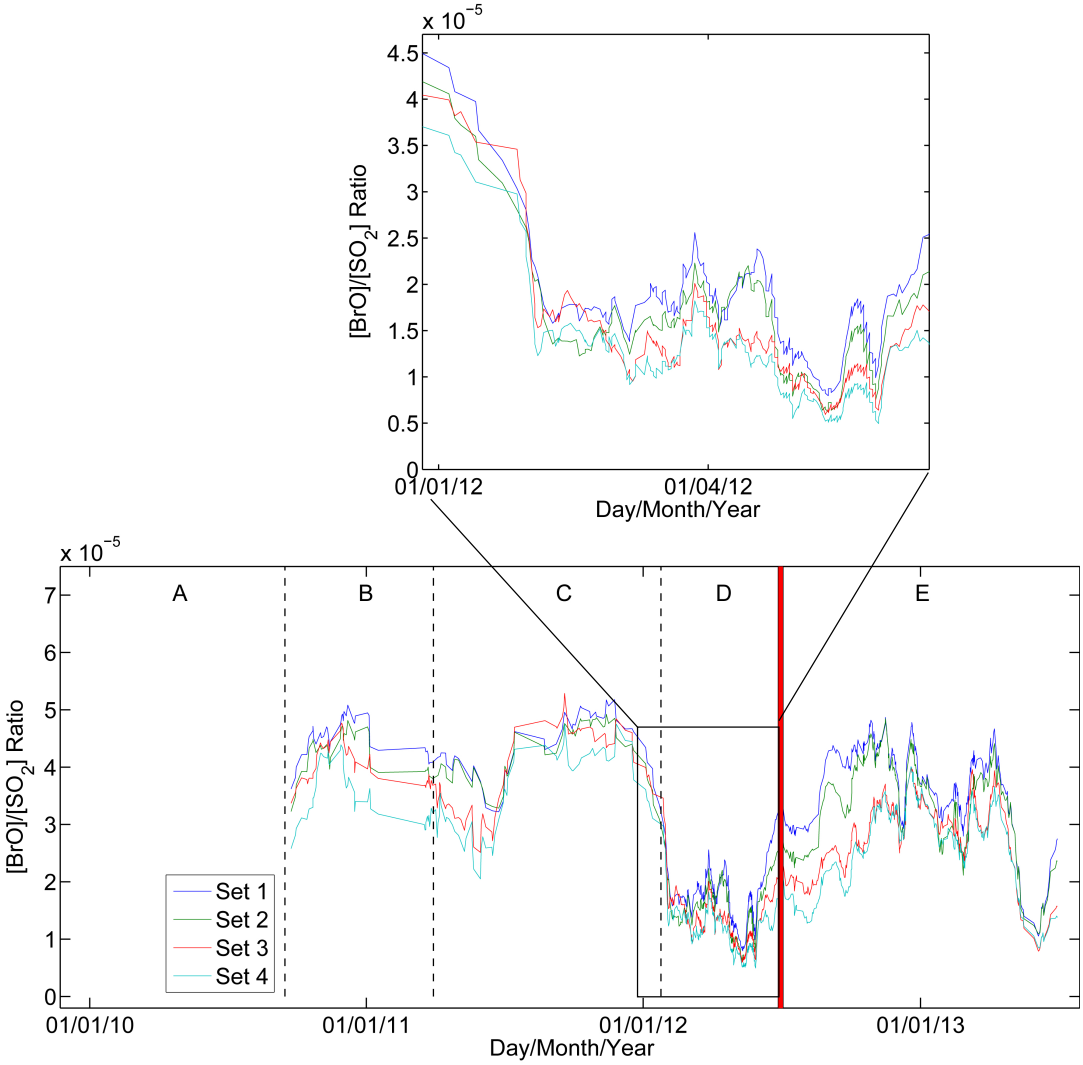

Figure 6.4.: Running mean over the BrO/SO_2 ratio for 7 days. Set 1 – 4 denote different combinations of the wavelength ranges used for the DOAS evaluation of BrO and SO_2. While the absolute value of the BrO/SO_2 ratio varies between the different evaluation ranges, the absolute variations are similar and the sharp drop, 5 months before the eruption on 30 June 2012, appears independent of the evaluation ranges used for the DOAS retrieval.

6.2 Radiative transfer modelling

The distance between instrument and volcanic plume or meteorological clouds can both influence the retrieved BrO/SO_2 ratio. In order to get a better numerical estimate of these influences simulations with the 3D RTM McArtim (Deutschmann et al., 2011) were performed. Section 6.2.1 describes the different geometries that were simulated, then the results are discussed in Section 6.2.2.

6.2.1 Simulation geometry

McArtim was set up to simulate a cylindrical volcanic plume that is indefinitely extended in the y-direction and has a round shape in the x-z plane. The plume has a diameter of 1000 m and is located between heights of 5500 m and 6500 m above sea level. The concentration of SO_2 inside the plume was set to $c = 1 \times 10^{13}$ molec/cm^3. This concentration results in an SO_2 column density of $S = 1 \times 10^{18}$ molec/cm^2 for a straight line through the centre of the plume. The BrO concentration was set to $c = 1 \times 10^9$ molec/cm^3, which leads to a BrO/SO_2 ratio of 10^{-4}. Besides volcanic absorbers typical profiles of O_3, NO_2 and O_4 were included in the simulations (see Figure D.1 in Appendix D).

The instrument was simulated at a height of 4500 m above sea level, similar to the instruments at Nevado del Ruiz. To investigate the influence of the distance between plume and instrument, the instrument was placed at five different lateral distances from the volcanic plume. Results were simulated for lateral distances of 0, 1.5, 3, 4.5, 6 km. The elevation angle of the instrument's viewing direction was adjusted so that the instrument was directed towards the middle of the volcanic plume.

To investigate the influence of clouds different cloud layers were simulated. These simulations were performed for the two instrument geometries with a lateral distance of 0 and 1.5 km, which results in an elevation angle of 90° or 45° respectively. Three different cloud layers with an infinite extent in the x-y plane but different extents in the z-direction were simulated. The first cloud scenario I has a cloud layer between 5500 m and 6500 m, encompassing the volcanic plume. Scenario II and III use clouds with a vertical extent of 500 m directly above or below the volcanic plume (see Figure 6.5). Cloud Scenario IV simulates results for an aerosol layer that is co-located with the volcanic plume.

An Ångströem exponent of 1, a single scattering albedo (SSA) of 1 and an asymmetry factor of $g = 0.85$ were used to simulate Mie scattering on cloud particles. The SSA of 1 means that the cloud is purely scattering; the asymmetry factor was chosen for clouds according to Wagner et al. (2013). Two different aerosol extinction scenarios were investigated for each cloud layer. The aerosol extinction coefficient was chosen in a way so that the aerosol optical density (AOD) for an upward looking instrument was 4 or 12 at 340 nm. The AOD at 320 nm was calculated with help of the Ångströem exponent resulting in AODs

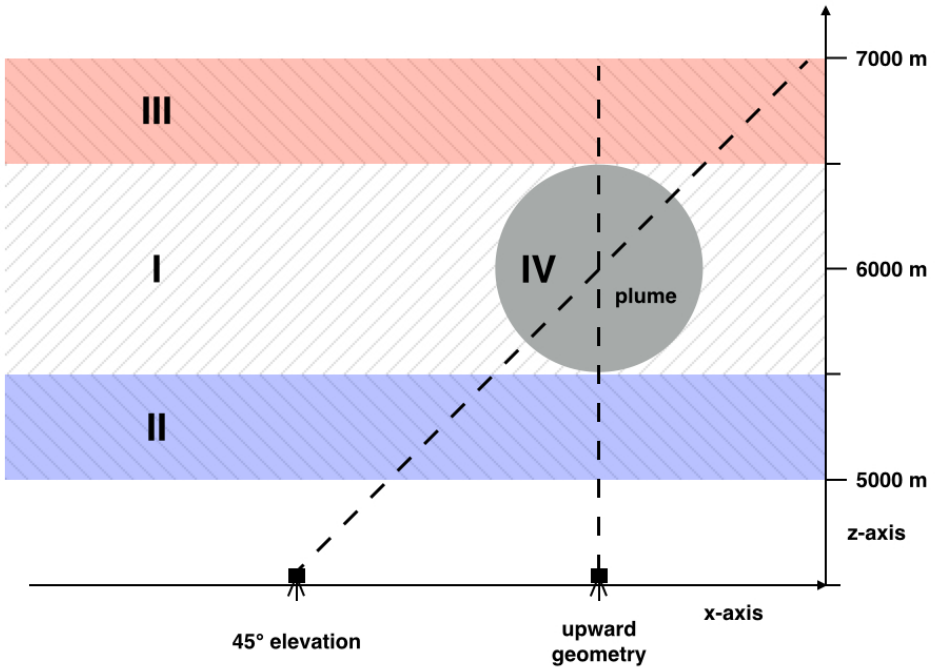

Figure 6.5.: Sketch of the simulated geometries for the McArtim simulations. A round plume with a diameter of 1 km was simulated with the instrument either directly below the volcanic plume or at a horizontal distance. The hatched areas indicate the three different regions in which clouds were simulated. The fourth cloud scenario is a cloud co-located with the volcanic plume (round grey area).

of 4.25 or 12.75, respectively.

6.2.2 Results

The results for different lateral distances between the instrument and the volcanic plume are shown in Figure 6.6. For both trace gases, the centre of the wavelength range used for the DOAS retrieval (see Section 5.2.2) was chosen as an indicator of the influence of radiative transfer on the results. Results were simulated at 320 nm for SO_2 and at 340 nm for BrO. However, radiative transfer effects can also depend on the optical density of the trace gases. Additional radiation that is scattered into the instrument's FOV leads to a larger dilution at large optical densities. Kern (2009) showed by using RTM simulations that the SO_2 air mass factor correlates with the shape of the SO_2 cross section. To account for this, SO_2 column densities were also simulated at 315.39 nm, which is the strongest SO_2 absorption band used in the DOAS retrieval in Chapter 5. As there is only a small wavelength difference between 320 nm and 315.39 nm the simulations at

this wavelength used the same aerosol distribution as the simulations at 320 nm.

Figure 6.6 a shows the variation of the SO_2 and BrO column densities for an increasing lateral distance in an atmosphere without clouds. The column densities of both trace gases decrease with increasing distance. The SO_2 column density decreases more with increasing distance since Rayleigh scattering, the dominant source of the light-dilution effect, has a larger scattering cross section at lower wavelengths (see Eq. 3.5). Only 75% of the true SO_2 column density (at 320 nm) and 79% of the BrO column density were retrieved at a lateral distance of 6 km. At 315.39 nm it can be observed that the light-dilution effect is stronger for large optical densities, only 71% of the true SO_2 column density were retrieved. However, the effect on the resulting BrO/SO_2 ratios (shown in Figure 6.6 b) was much smaller than the effect on the trace gas column densities. Even for the largest simulated distance of 6 km, the error is below 7% (for SO_2 at 320 nm) or $\approx$ 12% (for SO_2 at 315.39 nm). Since BrO is less influenced by the light-dilution effect, an increasing distance leads to an overestimation of the true BrO/SO_2 ratio.

The decrease of the SO_2 column density with lateral distance is smaller than in the simulations of Kern (2009). The explanation for this is that Kern simulated an instrument that was located at sea level. On the other hand, in this thesis, the instrument was simulated at a height of 4500 m above sea level to mimic the measurement situation at Nevado del Ruiz. Fewer scattering particles are available at this height, leading to a decrease of the light-dilution effect. It should also be noted once more that the light-dilution effect depends on the optical density of the trace gas of interest. At higher SO_2 column densities the light-dilution effect can have a more severe impact than in the calculations presented here.

The results for the different cloud layers for an AOD of 4 (for simplicity only the AOD at 340 nm will be given in the rest of this discussion) are summarized in Table 6.1 and Table 6.2. The results for an AOD of 12 are given in Table 6.3 and Table 6.4. The results for an AOD of 4 and 12 have different absolute numeric values, however the general behaviour is similar. For simplicity, the results below are mostly discussed for an AOD of 4. Where results for an AOD of 12 are reviewed, it is explicitly mentioned.

The results for no clouds are the same as in the simulations discussed above with a slight overestimation of the BrO/SO_2 ratio. An extended cloud at the height of the volcanic plume (Cloud Scenario I) and a cloud co-located with the volcanic plume (Cloud Scenario IV) both led to an extended light path inside of the volcanic plume. For both scenarios the retrieved column densities are between 1 and 9% higher than the true value. In the case of an extended plume the result also depends on the measurement geometry. The deviation of the BrO/SO_2 ratio is higher when SO_2 is simulated at 315.39 nm but are below 1.2% for a zenith-looking instrument. For an instrument with an elevation angle of 45° the ratio is similar to the simulations without clouds, with an overestimation

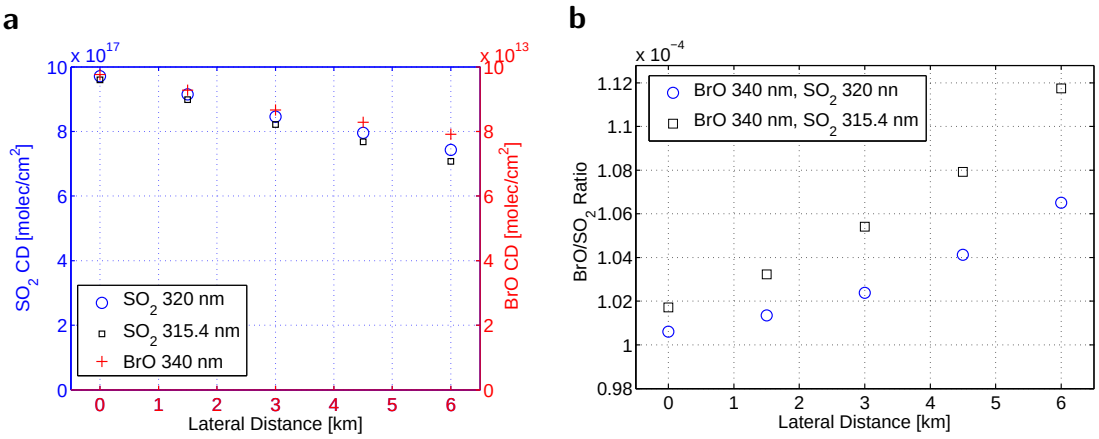

Figure 6.6.: The influence of an increasing lateral distance of the instrument. For all calculations the volcanic plume was simulated 1.5 km above the instrument. The SO_2 column densities were calculated at 320.00 nm and 315.39 nm, the BrO column densities at 340.00 nm. **a** shows the influence on the SO_2 and BrO column densities. **b** shows the resulting, lower variation of the BrO/SO_2 ratio.

of up to 3.9% (with SO_2 simulated at 315.39 nm). For an AOD of 12 both the retrieved trace gas column densities and the BrO/SO_2 ratio show larger variations. The cloud/aerosol layer leads to an extended light-path that results in up to 40% higher column densities. The BrO/SO_2 ratio has a deviation of 8% from the true value for an instrument with an elevation angle of 45° in CS I and SO_2 simulated at 315.39 nm. This is the largest deviation of all simulations. As in the no-clouds case, this overestimation is probably caused by the light-dilution effect that is larger at lower wavelengths as well as for larger optical densities.

A cloud that is located below the volcanic plume (Cloud Scenario II) resulted in the largest variations of the light-path through the volcanic plume. For an upward-looking instrument, the BrO column densities are only slightly lower than in the no-clouds case, while the SO_2 column density is 5 – 7% below the true value. The BrO/SO_2 ratio is overestimated by 3 – 5%. For an AOD of 12, significantly lower column densities are detected: For example only 78% of the true SO_2 column density has been found at 315.39 nm for an upward-looking instrument. The deviations of the BrO/SO_2 ratio are up to 6.7%. For the geometry with an elevation angle of 45° and a cloud below the volcanic plume the retrieved column densities are reduced to only 26 – 30% of the true value for an AOD of 4 and even ≈ 20% for an AOD of 12. Figure 6.7 shows the scattering and absorption events from a simulation for this geometry. Even though this simulation was performed at a lower wavelength (to achieve better visibility of the volcanic plume), it indicates that a large fraction of photons is scattered inside the cloud layer into the direction of the instrument without having penetrated the volcanic plume. However, even in this case, the BrO/SO_2 ratio is correct within 7% (for SO_2 simulated at 315.39 nm).

If clouds are located above the instrument (CS III), the retrieved column

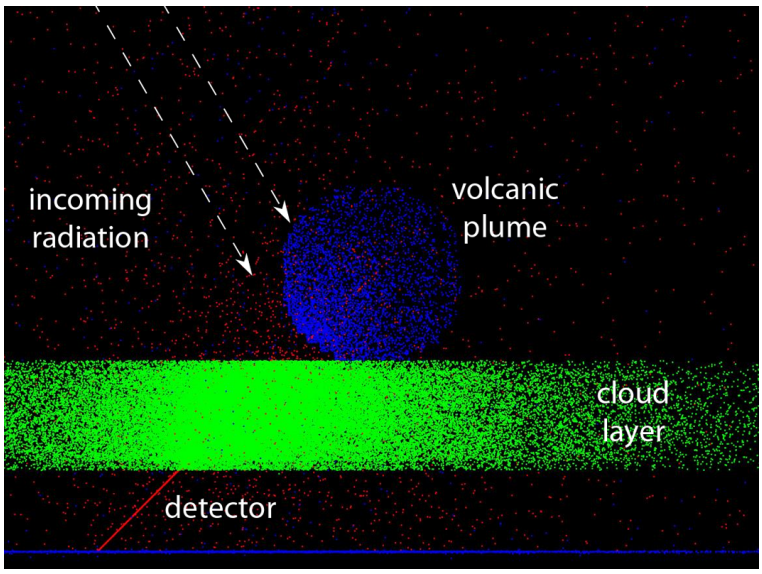

Figure 6.7.: Result of a McArtim simulation with an instrument at a lateral distance of 1.5 km from the volcanic plume. The volcanic plume has a diameter of 1 km and starts at 1 km above the instrument. A cloud layer is placed between a height of 500 and 1000 m. Red dots show Rayleigh scattering events, green dots Mie scattering events. Absorption by trace gases in the atmosphere and on the ground is depicted by blue dots. Note that the simulations for this image were performed at 304.19 nm. This corresponds to an SO_2 absorption band and leads to a better visibility of the SO_2 absorption events.

densities are only influenced marginally. The column densities for an elevation angle of 45° are closer to the true column density and the BrO/SO_2 ratio is within 2% of the true value for all scenarios and wavelengths used for the SO_2 column density simulation. This is caused by an increased amount of light that is scattered on cloud particles behind the volcanic plume. The increase of radiation scattered behind the volcanic plume reduces the influence of the light-dilution effect.
As expected, the results from the McArtim simulations indicate that the BrO/SO_2 ratio is more robust than the column densities themselves. The uncertainty caused by an increasing lateral distance and clouds was below 6% for SO_2 simulated at 320 nm and below 12% for SO_2 simulated at 315.39 nm. The variations from the different cloud layers were below 8.0% in all cases for SO_2 simulated at 315.39 nm. The simulations for SO_2 at 320 nm resulted in smaller deviations from the true BrO/SO_2 ratio that were below 3.5%.

However, while these results show that the BrO/SO_2 ratio is relatively robust, larger deviations can be caused under certain conditions. For one, the measurement geometry that was simulated was chosen to resemble the situation at Nevado del Ruiz. The instrument and the volcanic plume were simulated for an altitude between 4.5 and 6.5 km. The light-dilution effect that caused errors of up to 12% will lead to larger deviations at other volcanoes with a lower

$\lambda(SO_2)$: 320.00 nm $\lambda(BrO)$: 340.00 nm AOD: 4.25 / 4		SO_2 [molec/cm^2] $\times 10^{18}$	BrO [molec/cm^2] $\times 10^{14}$	BrO/SO_2 Ratio $\times 10^{-4}$	Deviation [%]
0	90°	0.97	0.98	**1.006**	0.6
	45°	0.92	0.93	**1.014**	1.4
I	90°	1.09	1.09	**1.000**	0.0
	45°	1.04	1.05	**1.013**	1.3
II	90°	0.95	0.97	**1.028**	2.8
	45°	0.28	0.27	**0.976**	−2.5
III	90°	0.96	0.96	**1.000**	0.0
	45°	1.01	1.02	**1.008**	0.8
IV	90°	1.08	1.08	**0.999**	−0.1
	45°	1.07	1.09	**1.013**	1.3

Table 6.1.: Results for the four different cloud scenarios described in the text. The true BrO/SO_2 ratio for the simulated volcanic plume is 1×10^{-4}. The results shown here are for an AOD of 4/4.25 for an upward-looking instrument and an instrument with an elevation angle of $45°$. SO_2 was simulated at 320.00 nm, BrO at 340.00 nm.

$\lambda(SO_2)$: 315.39 nm $\lambda(BrO)$: 340.00 nm AOD: 4.25 / 4		SO_2 [molec/cm^2] $\times 10^{18}$	BrO [molec/cm^2] $\times 10^{14}$	BrO/SO_2 Ratio $\times 10^{-4}$	Deviation [%]
0	90°	0.96	0.98	**1.017**	1.7
	45°	0.90	0.93	**1.032**	3.2
I	90°	1.08	1.09	**1.012**	1.2
	45°	1.01	1.05	**1.039**	3.9
II	90°	0.93	0.97	**1.050**	5.0
	45°	0.26	0.27	**1.044**	4.4
III	90°	0.96	0.96	**1.005**	0.5
	45°	1.01	1.02	**1.018**	1.8
IV	90°	1.07	1.08	**1.007**	0.7
	45°	1.05	1.09	**1.035**	3.5

Table 6.2.: Results for the four different cloud scenarios described in the text. The true BrO/SO_2 ratio for the simulated volcanic plume is 1×10^{-4}. The results shown here are for an AOD of 4/4.25 for an upward-looking instrument and an instrument with an elevation angle of $45°$. SO_2 was simulated at 315.39 nm, BrO at 340.00 nm.

$\lambda(SO_2)$: 320.00 nm $\lambda(BrO)$: 340.00 nm AOD: 12.75 / 12		SO_2 [molec/cm^2] $\times 10^{18}$	BrO [molec/cm^2] $\times 10^{14}$	BrO/SO_2 Ratio $\times 10^{-4}$	Deviation [%]
0	90°	0.97	0.98	**1.006**	0.6
	45°	0.92	0.93	**1.014**	1.4
I	90°	1.37	1.36	**0.997**	−0.3
	45°	1.17	1.20	**1.023**	2.3
II	90°	0.81	0.83	**1.034**	3.4
	45°	0.22	0.22	**0.996**	−0.4
III	90°	0.99	0.99	**0.999**	−0.1
	45°	1.03	1.04	**1.006**	0.6
IV	90°	1.26	1.26	**0.999**	−0.1
	45°	1.20	1.22	**1.024**	2.4

Table 6.3.: Results for the four different cloud scenarios described in the text. The true BrO/SO_2 ratio for the simulated volcanic plume is 1×10^{-4}. The results shown here are for an AOD of 12/12.75 for an upward-looking instrument and an instrument with an elevation angle of $45°$. SO_2 was simulated at 320.00 nm, BrO at 340.00 nm.

$\lambda(SO_2)$: 315.39 nm $\lambda(BrO)$: 340.00 nm AOD: 12.75 / 12		SO_2 [molec/cm^2] $\times 10^{18}$	BrO [molec/cm^2] $\times 10^{14}$	BrO/SO_2 Ratio $\times 10^{-4}$	Deviation [%]
0	90°	0.96	0.98	**1.017**	1.7
	45°	0.90	0.93	**1.032**	3.2
I	90°	1.32	1.36	**1.030**	3.0
	45°	1.11	1.20	**1.080**	8.0
II	90°	0.78	0.83	**1.067**	6.7
	45°	0.20	0.22	**1.071**	7.1
III	90°	0.98	0.99	**1.006**	0.6
	45°	1.02	1.04	**1.006**	1.5
IV	90°	1.23	1.26	**0.999**	2.0
	45°	1.16	1.22	**1.024**	5.8

Table 6.4.: Results for the four different cloud scenarios described in the text. The true BrO/SO_2 ratio for the simulated volcanic plume is 1×10^{-4}. The results shown here are for an AOD of 12/12.75 for an upward-looking instrument and an instrument with an elevation angle of $45°$. SO_2 was simulated at 315.39 nm, BrO at 340.00 nm.

altitude. Also no ambient aerosol was simulated, but cloud scenario II, in which a cloud was simulated below the volcanic plume, can be seen as a proxy for these situations.

Additionally, all simulations were performed for an Ångströem exponent of 1. This Ångströem exponent leads to a difference of only 6.25% between the aerosol optical depths at the two wavelengths. Different Ångströem exponents, for clouds or aerosol in the volcanic plume, can lead to a larger deviation. Still, with the range between $\alpha = 0.13 - 2.42$ given for volcanic plumes by Spinetti and Buongiorno (2007), these variations are still fairly low (between 0.8% and 15%). The value of the AOD will also play a role. However, for the AODs of 4 and 12 used in the simulations, the variations of the BrO/SO_2 ratio were comparable. Most importantly the light-dilution effect depends on the optical density of the trace-gases of interest. This could, e.g. be observed when comparing the SO_2 column densities simulated at 315.39 nm with those simulated at 320.00 nm. This means that errors due to the light-dilution effect depend on the absorption cross section and on the column density of the trace gas (which is especially important for SO_2 that oftentimes is a strong absorber in volcanic environments). Many of these problems due to strong SO_2 absorption can be minimized when evaluating SO_2 at larger wavelengths, where the absorption cross section is smaller (see Chapter 6.1). An SO_2 DOAS fit usually encompasses several absorption bands (strong and weaker absorption structures). One interesting question for future research is which SO_2 column density is retrieved from a complete spectrum (instead of simulating the column density at distinct wavelengths). This question can be answered by simulating complete spectra and subsequently evaluating them with the DOAS method.

In conclusion it can be said that the BrO/SO_2 ratio is very robust with regards to influences from radiative transfer. A comprehensive treatment of all radiative transfer effects is beyond the scope of this work. Nevertheless, the RTM calculations indicate that variations below 20% can be expected for the measurement geometry at Nevado del Ruiz and for the SO_2 and BrO column densities used in the simulations presented here. Variations of the ratio due to the light-dilution effect are much lower than the variations of the trace gas column densities. A distance of up to 6 km led to an overestimation of the BrO/SO_2 ratio of $\approx 12\%$. Variations due to simulated meteorological cloud layers were found to be below 8.0%.

6.3 Detecting clouds in DOAS scans

While the results in Section 6.1 and 6.2 showed that the BrO/SO_2 ratio is extremely robust against radiative transfer effects and especially clouds, there are good reasons to identify clouds in the spectroscopic data from the NOVAC network. For one, clouds can lead to an underestimation of the true SO_2 and BrO column densities and thus to large underestimations of the emission rates of these gases. Additionally, identifying clouds in the data set allows, for example, to study the influences of meteorology on the BrO formation (see Section 5.3.4).

Clouds can be identified by several measurement quantities that they influence. Since Mie scattering is dominant in clouds, the radiation scattered on a cloud has a different colour than the Rayleigh sky as can be easily observed by the white colour of clouds. Therefore clouds can, for example, be identified by looking at the ratio of the measured intensity at two wavelengths, a so-called colour index. For a zenith-looking instrument clouds usually enhance the measured radiation intensity. Other observables that can be influenced by clouds are the retrieved O_4 column density or the strength of the Ring effect (Wagner et al., 2013). In this work the two most accessible parameters, the radiance and a colour index, are investigated and interpreted. O_4 column densities were investigated as well. However, the O_4 absorption band at 360 nm was often overexposed. Using only the 343 nm O_4 absorption band did not lead to reasonable results, most likely due to the small evaluation range in combination with the rather broad absorption structure.

Three days with varying cloud conditions were identified with help of Terra MODIS satellite images of the cloud cover[1]. 1 January 2011 is one of the few days with very low cloud cover in the satellite image (see Figure E.1 in Appendix E). 2 February 2011 has a some more clouds in the vicinity of Nevado del Ruiz and a higher cloud optical thickness (see Figure E.2). 5 May 2011 has large clouds covering several degrees of latitude and longitude around Nevado del Ruiz (see Figure E.3). While no SO_2 can be observed on 1 January and 2 February, there was some SO_2 (up to 1.3×10^{18} molec/cm^2) detected on 5 May 2011. A large number of other days were investigated as well, but usually showed signs of a cloud cover, in good accordance with the high average cloud fraction at Nevado del Ruiz (usually above 80% in the montly averages from MODIS).

The radiation intensity was investigated by means of the number of counts at 381 nm divided by the exposure time for each scan. For a zenith-looking instrument and an ideal Rayleigh atmosphere, the optical depth of the atmosphere is relatively small. When clouds or aerosols are present, more radiation is scattered into the FOV of the instrument and the detected intensity increases (Wagner et al., 2013). This behaviour can be observed in Figure 6.8, where the lowest intensities can be seen on 1 January 2011, a cloudless day. The radiation

[1] `http://ladsweb.nascom.nasa.gov/data/search.html`, last accessed: 28.01.2014.

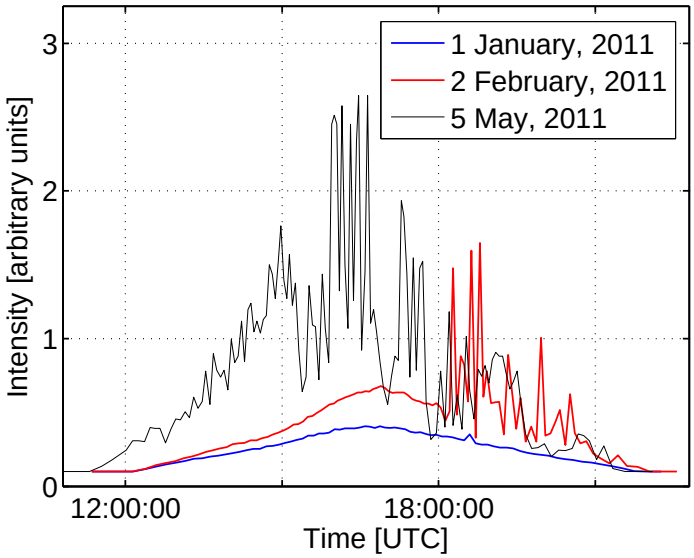

Figure 6.8.: Normalized radiation intensity for all three days. On the cloudless day (1 January 2011) the intensity varies smoothly and has its maximum value during the middle of the day. On 2 February 2011 intensity peaks occur when clouds appear. 5 May 2012 a completely cloudy day shows the largest intensities throughout the complete day.

intensity on this day varies smoothly. On 2 February, the intensity is higher and more variable in the afternoon when clouds appear. 5 May has the largest intensities which are noisy throughout the complete day. A cloudless sky shows less temporal and spatial variations of the radiation intensity or colour index (e.g. Wagner et al., 2013).

The Colour Index (CI) in this work was calculated between 329 nm and 381 nm. The two wavelengths were chosen as they are as far apart as the filter used for stray-light prevention in the spectrometers allows. On the other hand, the lower wavelength avoids the deep UV range where SO_2 and O_3 absorption plays a dominant role. When clouds are present more radiation from larger wavelengths arrives due to Mie scattering in the cloud. Therefore, the CI decreases when clouds are present. The results of the CI for the zenith-looking direction are shown in Figure 6.9. On 1 January, 2011 the CI varies smoothly with two minor dips in the afternoon. On 2 February 2011 the CI values are slightly lower in the morning and around noon when compared to 1 January and vary smoothly in time. According to Wagner et al. (2013) lower CI values with a smooth time variation can be caused by an aerosol load in the atmosphere. In the afternoon the CI values are lower and there is a higher time variation, indicating a broken cloud cover. For all of 5 May, the CI values are lower than for the whole 1 January, and there are some small variations of the CI throughout the day with three peaks. The satellite images from this day (see Appendix C) indicate that clouds were covering a large area around the volcano.

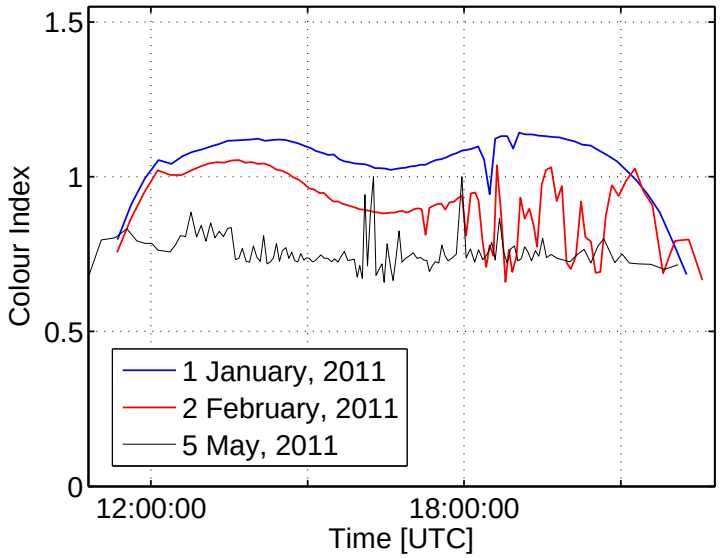

Figure 6.9.: Colour Index (329 nm/381 nm) for all three days. On 1 January, a mostly cloudless day, the variation of the CI is smooth with only two dips in the afternoon. On 2 February, 2011 the CI shows lower values and indicates some clouds in the afternoon. On 5 May low CI values with more variation can be observed.

When looking at a colour-coded image of the CI (where the UTC time is the x-direction and the y-direction shows the viewing direction), the cloud cover can also be identified. Figure 6.10 shows the smooth variations of the CI for 1 January 2011. A few clouds might be present for elevation angles between $-40°$ and $-80°$ in the afternoon. On 2 February Figure 6.11 nicely shows the lower CI values in the afternoon; at the same time when lower CI values appear, the variation between different viewing directions disappears. On 5 May, the day with the largest cloud cover, the CI values are lower during the complete day and there are hardly any variations between the different viewing directions.

When plotting the CI in dependence of the SZA (Figure 6.13), two different branches, corresponding to the morning and the evening, exist for all three days. For an ideal measurement, these two branches should fall together, and the CI should be symmetric in the morning and evening. One possible reason for the two CI branches are problems with the time saved in the spectra. The NOVAC instruments determine the measurement time with help of a GPS receiver and should thus be correct. In case of a failing GPS receiver all spectra are saved with the measurement time increasing subsequently. Considering measurements that take place from 8 a.m. until 4 p.m. each day and a GPS receiver that fails on day one, the subsequent measurements from the next day would be saved with timestamps of 4 p.m to 12 p.m. However, this behaviour cannot be observed for the measurements investigated here. Another possibility are problems during the conversion from local time to UTC. This option was ruled out after shifting

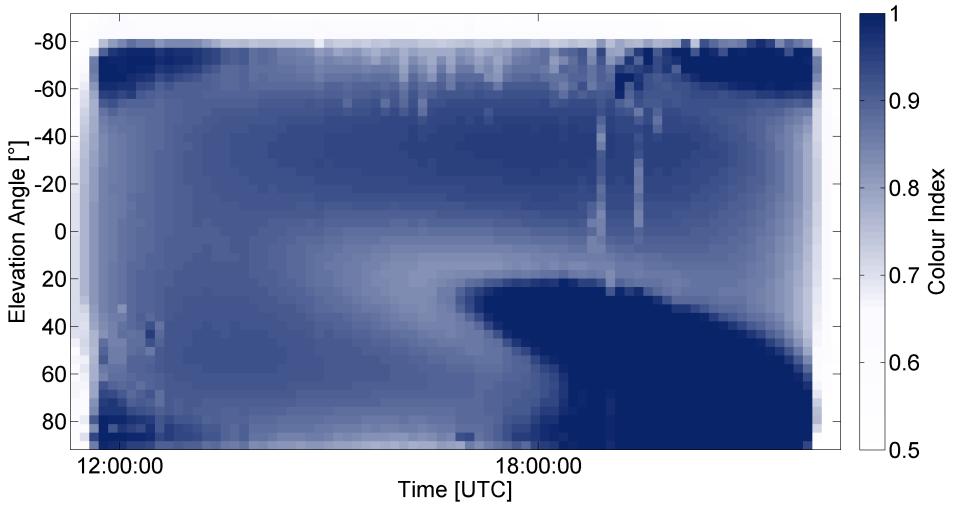

Figure 6.10.: Variations of the colour index (329 nm/381 nm) with viewing direction and time of day. This example is from 1 January 2011, a mostly cloudless day. The variations of the CI are smooth throughout the day. An elevation angle of $0°$ denotes a zenith-looking instrument. The low values at elevation angles below $-70°$ (see y-axis) are caused by an obstacle in the light-path. High values in the bottom-right corner are due to overexposed spectra.

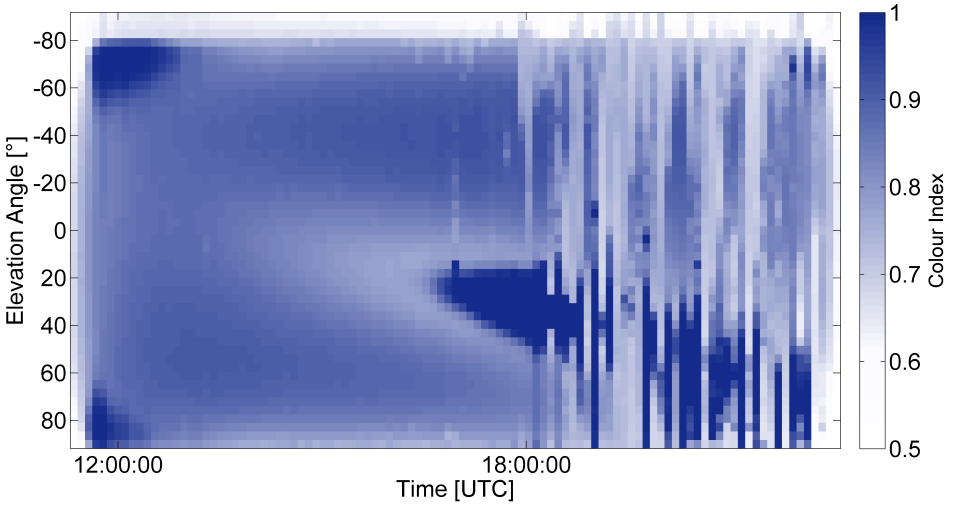

Figure 6.11.: Similar colour index plot as shown in Figure 6.10. This plot shows the CI for 2 February 2011 as a function of viewing direction and time of day. After 18:00 UTC a broken cloud cover can be observed as white values that do not vary smoothly with viewing direction.

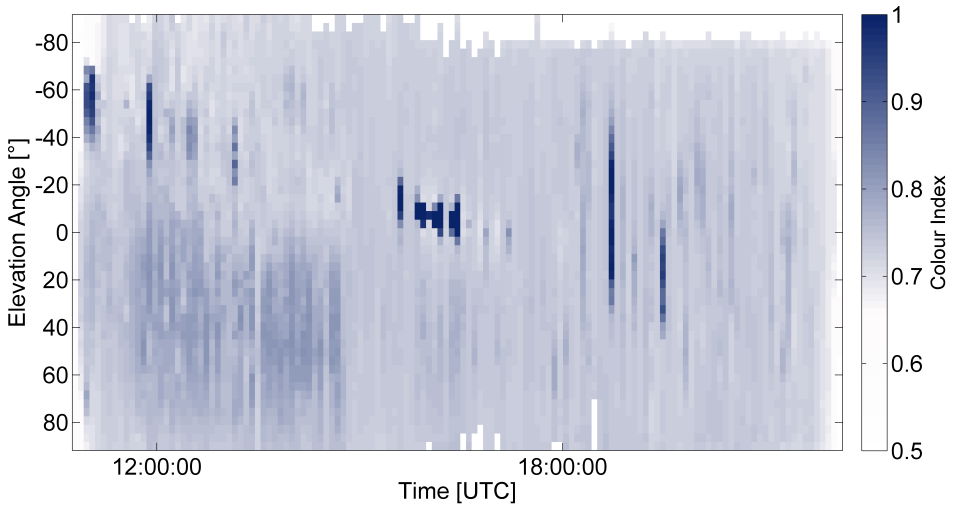

Figure 6.12.: Colour index between 329 nm and 381 nm as a function of viewing direction and time of day for 5 May 2011. On this day there was a constant cloud cover throughout the whole day.

the measurement time and re-calculating the SZA for each measurement. With a time shift of 30 minutes the two branches fall together. Another possible explanation is an instrument that is not exactly aligned. A tilted instrument could lead to different viewing directions and would have had an influence of the relative azimuth between instrument and the sun and would thus induce variations of the CI.

The CI values from 1 January 2011 were compared to McArtim radiative transfer calculations. The McArtim scenario described in Section 6.2 was adapted for these calculations. An aerosol layer was added and the volcanic plume was removed from the simulations. The aerosol profile for tropical summer from SCIATRAN (Rozanov et al., 2005) was used, and re-scaled to match an AOD of 0.16. The AOD value was chosen as a typical AOD value from the two closest Aeronet[2] stations at Medellin and Manaus. Aerosol was simulated with the Henyey–Greenstein phase function with an SSA of 1 and an asymmetry parameter of 0.68 (the asymmetry parameter was chosen similar to Wagner et al., 2013). After radiances were simulated for different SZAs the CI was calculated and re-scaled to match the measured CI. The re-scaling is justified by the spectrometer's quantum efficiency that is not simulated in McArtim. After calculation of the CI, the simulated CI values were shifted 30 minutes towards earlier times and plotted together with the measured CI (Figure 6.14). There is a fair agreement between the simulated CI and the measured CI. A more accurate description of the aerosol layer and the viewing directions could possibly improve the agreement between measurement and simulation, but is beyond the scope of this thesis. In a sensitivity study the aerosol layer was removed from the

[2] `http://aeronet.gsfc.nasa.gov`, last accessed: 17.02.2014.

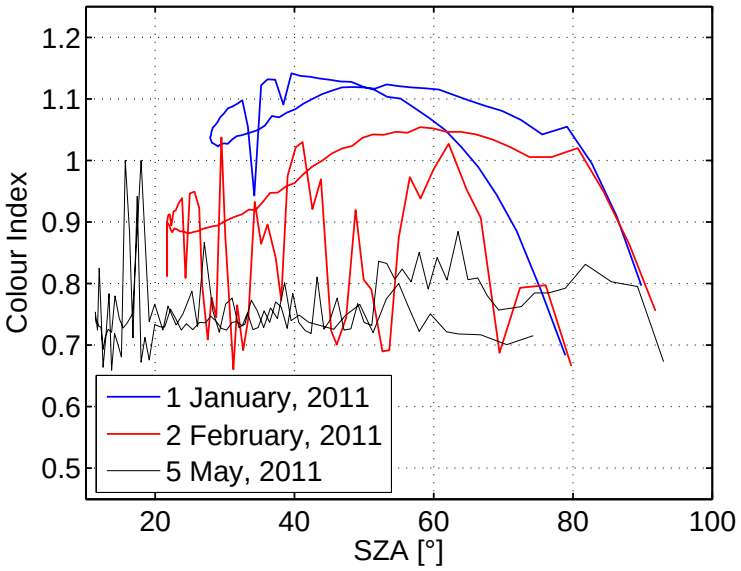

Figure 6.13.: Colour indices for both days as a function of SZA. One can clearly see the two branches for the morning and evening hours. Reasons for the shift of the SZA between the two branches are discussed in the text.

atmosphere, which led to a removal of the broadband dip of the CI at low SZAs.

The results from the study on clouds are promising and show that the cloud detection shown in Wagner et al. (2013) can most likely be implemented for the NOVAC instruments. The agreement between the McArtim simulation and measurement results is already good but can be further improved if the simulation is adapted to be closer to the measurement situation. However, some problems with the NOVAC measurements were identified. Overexposed spectra at 360 nm prohibited the O_4 retrieval. This problem can be easily solved by adapting the exposure time automatic, which is currently adjusted for maximum intensity in the SO_2 retrieval range. Additional problems with the instrument time or the exact viewing direction of the instrument were identified. These problems can be easily solved during a field-trip to the instruments where the exact alignment and instrument time can be verified. However, this was not possible during the work on this thesis.

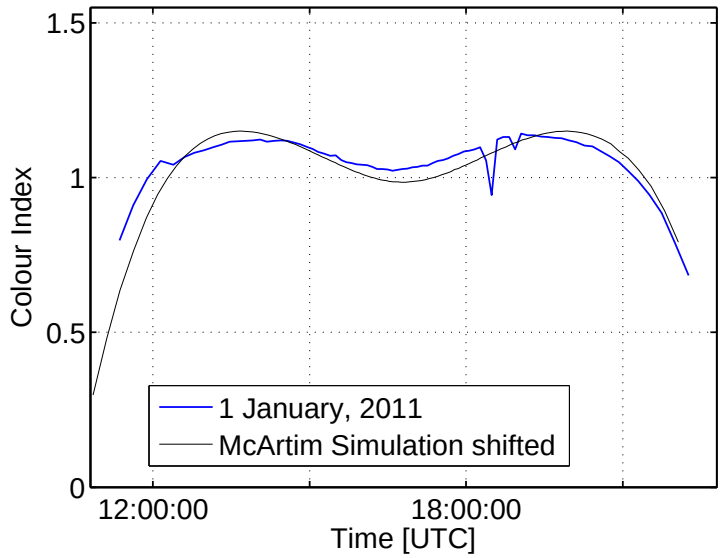

Figure 6.14.: Comparison of the CI on 1 January, 2011 with radiative transfer calculations from McArtim. Note that the McArtim results where shifted by 30 minutes and rescaled to mimic the form of the measurement data.

7

Effects of instrument temperature on the data evaluation

The NOVAC type 1 instruments installed at Nevado del Ruiz are not thermally stabilized. A variable instrument temperature can lead to misalignments of the spectrometer's optical system which can lead to changes in the pixel-to-wavelength alignment and variations of the instrument line function (ILF). These changes can lead to erroneous results of the DOAS retrieval. A good overview of temperature induced variations of the spectrometer's optical properties, from the instruments used in the NOVAC network can be found in Pinardi et al. (2007) and Kern (2009).

Figure 7.1 shows the variability of the instrument line function (ILF) and the pixel-to-wavelength alignment with changing instrument temperature for one of the spectrometers at Nevado del Ruiz. For this example, an FRS with zenith viewing direction was fitted to spectra from half a year of data (Januar - June 2011) with a fit range covering the SO_2 and the BrO evaluation range. Both, shift and squeeze of the reference spectrum clearly vary with changes of the ambient temperature.

Two different situations can occur if the ILF varies during the measurements. One problem occurs, if the ILF used for the convolution of the trace gas absorption cross section is different from the ILF during the measurement. In this case, the convolved absorption cross section has a different shape than the real absorption structure in the measurement. To depict this effect the absorption cross sections of SO_2 and BrO after convolution with different ILFs are shown in Figure 7.2 (SO_2) and Figure 7.3 (BrO). The high-resolution reference cross sections were convolved with a Gaussian profile with three different full width half maximum (FWHM) values. The values of 0.4 nm, 0.6 nm and 0.8 nm represent the range

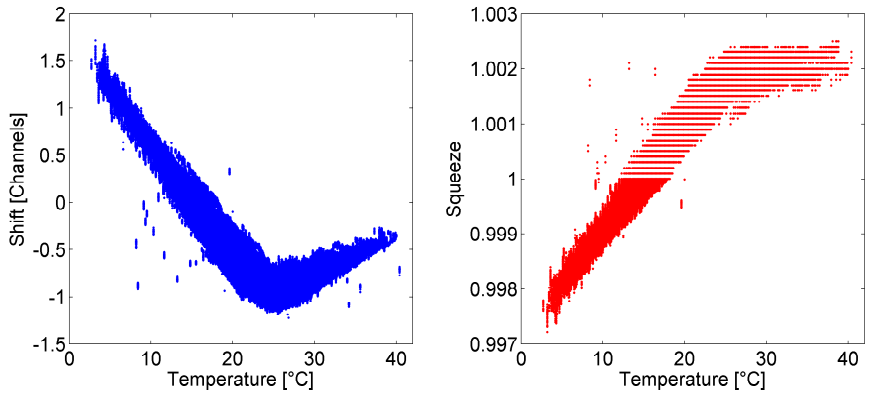

Figure 7.1.: Shift and squeeze for a DOAS fit only containing one reference spectrum with an instrument temperature of 15 °C. For this plot half a year of data (January - June 2011) was evaluated. It can be clearly seen, that the instrument pixel-to-wavelength alignment is influenced by changes in the ambient temperature.

of values for miniature spectrometers as used in the NOVAC network.

These two figures show that the amplitude of the differential absorption structures decreases with increasing FWHM. The effect is larger for SO_2 which has narrower absorption lines than BrO. When comparing the SO_2 cross section convolved with an FWHM of 0.4 nm to the one convolved with 0.8 nm the differential absorption structures are $\approx 40\%$ smaller (for the absorption maxima at 300 and 314 nm and the neighbouring minima). For BrO the differential absorption structures are only $\approx 25\%$ smaller (for the 338 nm absorption maximum and the neighbouring minima). The lower amplitude of the absorption features leads to changes in the sensitivity of the instrument for a specific trace gas and to incorrectly retrieved column densities. Furthermore, additional interferences can occur between the absorption features of different trace gases during the DOAS evaluation. For SO_2 one common problem are the O_3 Huggins bands (300 - 374 nm) that have a comparable wavelength width and absorption features in the UV (Platt and Stutz, 2008).

The situation is even worse, if the measurement spectrum and FRS are recorded with a different ILF. In this case, narrow band structures in the spectrum are resolved differently, which leads to a greatly enlarged residual. Figure 7.4 shows the optical density for a simulated measurement spectrum with an SO_2 column density of 1×10^{18} molec/cm^2. The blue line shows the optical density for a measurement spectrum and FRS that have the same ILF. The red line is clearly noisier, it shows the optical density for a measurement spectrum that has a different ILF than the FRS.

In a usual DOAS retrieval several trace gas cross sections, a Fraunhofer reference spectrum (FRS) and a Ring spectrum are fitted to the measurement spectrum (see Chapter 3 or Section 5.2). It is difficult to find the magnitude of error arising from variations of the ILF, since the error can be caused by a

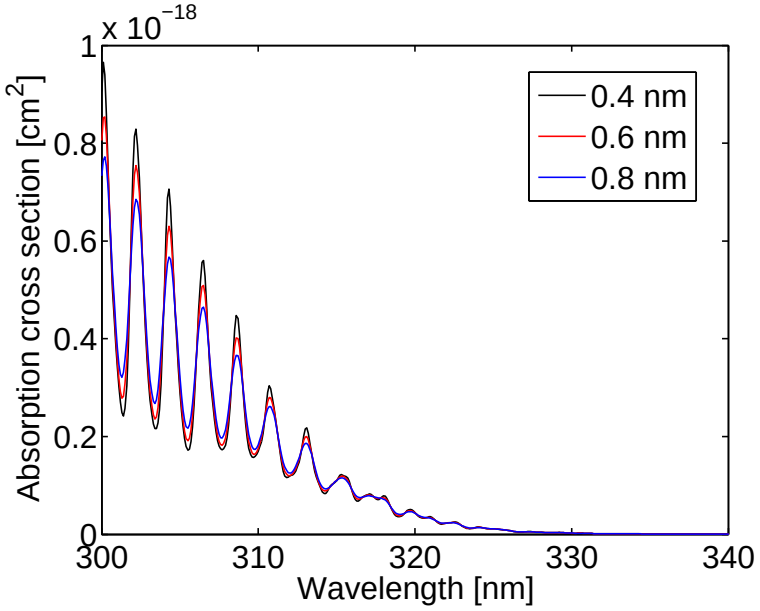

Figure 7.2.: SO_2 absorption cross section convolved with a Gaussian profile with three different FWHMs. The amplitude of the differential structures decreases for wider instrument slit functions.

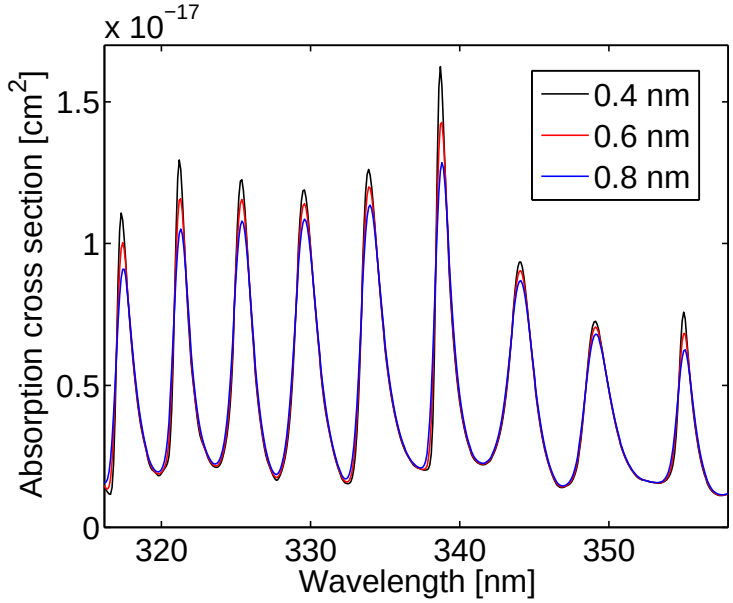

Figure 7.3.: BrO absorption cross section convolved with a Gaussian profile with three different FWHMs. As the BrO absorption cross section has wider absorption features, the effect of a changing instrument function is smaller than for SO_2.

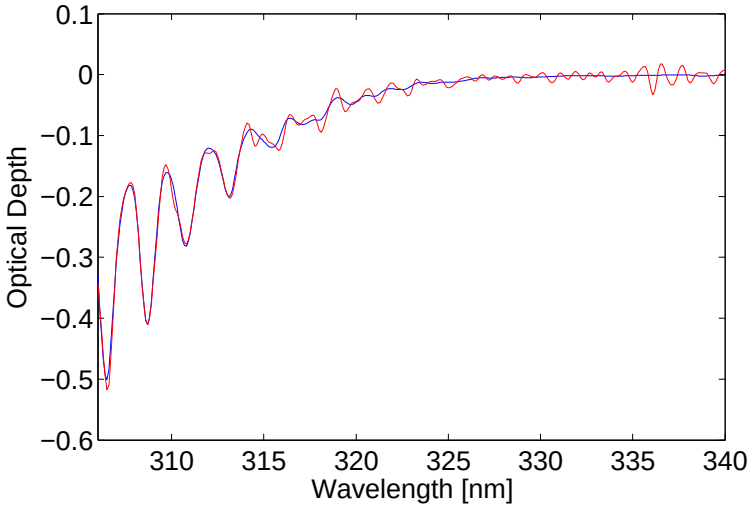

Figure 7.4.: Simulated optical densities for an SO_2 column density of 1×10^{18} molec/cm^2. For the blue line I and I_0 both were created by convolving a high resolution spectrum with a Gaussian profile with an FWHM of 0.6 nm. For the red line I was created with a Gaussian profile with an FWHM of 0.55 nm, while the same I_0 as before was used. The much noisier structure in the red curve can be easily seen.

combination of cross-interferences. In this thesis, a combination of theoretical studies and measurements was performed to assess the magnitude of errors arising from variations of the ILF.

7.1 Temperature influences on the NOVAC instruments

Pinardi et al. (2007) studied the influence of a changing instrument temperature for ten Ocean Optics S2000 spectrometers that were installed in the NOVAC network. Figure 7.5 shows the variation of different mercury emission lines (296 nm, the three lines around 365 nm and 404 nm) with changing instrument temperature for one of the spectrometers. While the shape and amplitude of the lines at 365 nm does not change significantly, the 296 nm and the 404 nm lines change both in shape and amplitude.

Pinardi et al. (2007) investigated the variation of the ILF for ten spectrometers from the NOVAC network by fitting a Gaussian profile to the 302 nm mercury emission line recorded at different temperatures (see Figure 7.6). According to the data sheet all these spectrometers should have an optical resolution of 0.7 nm. While the behaviour is individual for each instrument, we can see two general trends; there is an increase in FWHM with decreasing temperatures and the FWHM becomes independent of temperature above 30°C. None of the instruments showed a range of variation larger than 0.2 nm.

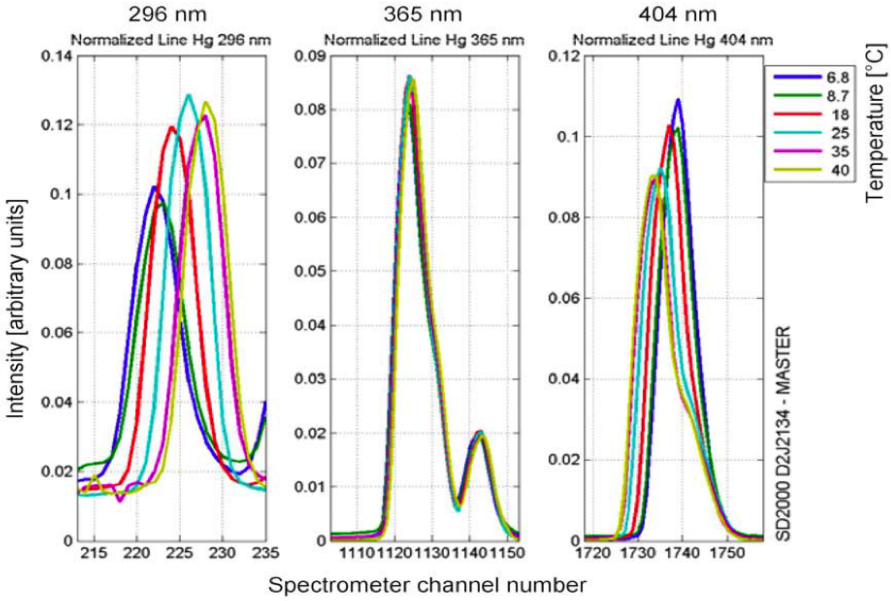

Figure 7.5.: Variation of different mercury emission lines (296 nm, three lines at 365 nm and 404 nm) with changing temperature for one of the spectrometers from the NOVAC network. Reproduced with permission Pinardi et al. (2007).

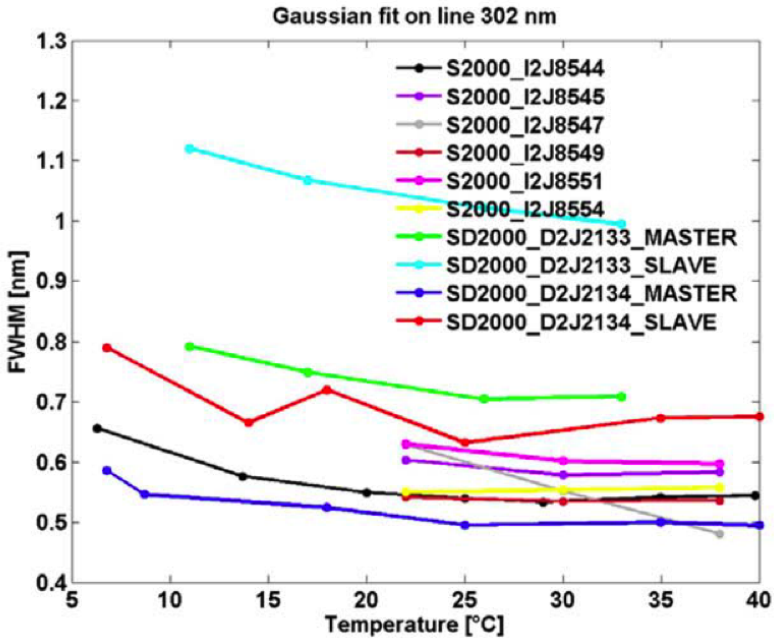

Figure 7.6.: Variation of the FWHM of the 302 nm line of a mercury emission lamp for ten different spectrometers from the NOVAC network. Reproduced with permission from Pinardi et al. (2007).

7.2 Investigation of temperature effects with modelled spectra

To assess the magnitude of errors that are caused by variations of the slit function theoretically a study with synthetic spectra, similar to Vogel (2011), was performed. Spectra were simulated at a high resolution and then convolved with Gaussian profiles of varying FWHM to match the lower resolution of a theoretical instrument. These spectra were then evaluated in DOASIS with different realistic evaluation scenarios for SO_2 and BrO. To keep the results comparable to Vogel (2011) the main parameters of the study were chosen similarly: The detector for the theoretical study has 1024 channels and covers a wavelength range of 300 nm - 402.3 nm with a linear pixel-to-wavelength alignment (0.1 nm/pixel).

Three different spectra were created at high resolution:

1. An FRS only containing stratospheric absorbers
2. A simulated measurement spectrum containing additional tropospheric absorbers but no volcanic plume gases. This spectrum is used to estimate errors arising from other tropospheric absorbers and differences of the Ring structures on the retrieval.
3. A simulated measurement spectrum containing tropospheric absorbers and additionally BrO and SO_2, to find the errors in a volcanic plume measurement.

The different trace gases with their corresponding column densities and the absorption cross sections that were used in this study are listed in Table 7.1, they were chosen according to Vogel (2011). For simplicity the simulated measurement spectra are only referred to as measurement spectra for the rest of this section.

The first step for the modelling of synthetic spectra is applying the trace gas absorption by using Beer-Lambert's law. The cross sections of the different trace gases were interpolated to match the resolution of the high-resolution solar atlas (Chance and Kurucz, 2010). After interpolation Beer-Lambert's law was applied with the column densities given in Table 7.1. A Raman spectrum was calculated in DOASIS to simulate the Ring effect. For the FRS the Raman spectrum was added to the spectrum rescaled in a way, that its total intensity over all channels accounts to 5% of the total intensity of the resulting spectrum. For the two measurement spectra the Raman spectrum was rescaled in a way that the total intensity is 2% of the resulting spectrum, similar to the study of Vogel (2011). The measurement spectra and the FRS were then convolved to match the instrument's resolution with a Gaussian profile with varying FWHM.

The measurement spectra were evaluated using a DOAS retrieval as described in Section 5.2.2. For SO_2 two additional evaluation ranges were investigated to identify the most robust evaluation range with regard to temperature variations:

Trace Gas	Temp. [K]	Absorption Cross-Section	Reference Spectrum [molec/cm^2]	Measurement Spectrum [molec/cm^2]
O_3	221	Burrows et al. (1999)	8×10^{18}	8×10^{18}
O_3	241	Burrows et al. (1999)	2×10^{18}	2×10^{18}
NO_2	220	Vandaele et al. (1998)	5×10^{15}	5×10^{15}
BrO	298	Fleischmann et al. (2004)		0
				1.5×10^{14}
O_3	273	Burrows et al. (1999)		1×10^{18}
NO_2	294	Vandaele et al. (1998)		2×10^{16}
SO_2	298	Vandaele et al. (2009)		0
				1×10^{18}
CH_2O	298	Meller and Moortgat (2000)	1×10^{16}	2×10^{16}
O_4		Hermans et al. (2003)		1×10^{42}
Ring Eff.			5%	2%

Table 7.1.: The different trace gases used for the study of temperature effects. The different scenarios are adapted from Vogel (2011).

- Range 1: 314.6 nm – 326.8 nm: This wavelength range was found to be "the best compromise of a robust fit and low influence of radiative transfer effects" in Vogel (2011).
- Range 2: 307.7 nm – 326.8 nm
- Range 3: 310.0 nm – 326.8 nm

Compared to the standard evaluation range, the second and third fit range encompass three or two additional SO_2 absorptions bands respectively. During the determination of wavelength range 1 in Vogel (2011), the instrument function was chosen to be constant. The idea behind the two different wavelength ranges is that the additional SO_2 absorption bands might lead to a more robust DOAS retrieval. However, since they encompass lower wavelengths, these ranges might be more vulnerable to errors due to radiative transfer and interferences from O_3.

The Ring spectrum was calculated from the FRS at low resolution after the convolution, to resemble a realistic evaluation. A Gaussian profile with an FWHM of 0.65 nm was chosen for the convolution of the absorption reference cross sections of all trace gases.

Two different scenarios that could both occur during the evaluation of the NOVAC data were investigated:

- Scenario 1: The ILF of the FRS and measurement spectrum is the same. However, the absorption cross sections are convolved with a different ILF. This is usually the case in the NOVAC network: measurement spectra and FRS are recorded in close time proximity (within approximately 10 minutes). They have the same instrument temperature and thus also the same ILF. The mercury emission lines for the convolution of the absorption reference cross sections, on the other hand, were only recorded once at room temperature.

- Scenario 2: The FRS has the same ILF as used for the convolution of the reference cross sections, but the measurement spectrum was recorded with a different ILF. This is, for example, the case when using a fixed FRS for the evaluation of data from a complete day or when using a high resolution solar reference spectrum for the evaluation (as in Chapter 8).

For both scenarios the measurement spectra were convolved with a Gaussian profile with varying FWHM. The FWHM was varied with steps of 0.025 nm between 0.525 nm and 0.775 nm. For the first scenario the FRS was convolved with the same Gaussian profile as the measurement spectrum. For Scenario 2 the FRS was convolved with a Gaussian profile with an FWHM of 0.65 nm. In both scenarios the trace gas cross sections were convolved with a Gaussian profile with an FWHM of 0.65 nm.

Results from Scenario 1 for SO_2

Scenario 1 describes the case, that the FRS is convolved with the same ILF as the measurement spectrum. All trace gas absorption cross sections were convolved with a Gaussian profile with 0.65 nm FWHM. Two fit scenarios were used, in the first fit scenario all absorption cross sections were convolved without I_0 correction, the second fit scenario used I_0 corrected cross sections. In the latter case corrected absorption cross sections were calculated using the correct column density of the respective trace gas (see Table 7.1) for the I_0 correction.

For a measurement spectrum not containing any volcanic absorbers (SO_2, BrO) no significant amounts of SO_2 were detected independent of the FWHM of the FRS and the measurement spectrum. The results for the spectrum without volcanic absorbers were similar for all three evaluation ranges. Therefore, only the results for 314.6 – 326.8 nm are shown as an example in Figure 7.7 a. However, while no significant amounts of SO_2 were found, there was a slight decrease of the O_3 column density with increasing FWHM. Even if FRS and measurement spectrum were both convolved with the same FWHM that was used for the convolution of the reference cross sections, the true O_3 and SO_2 column densities were not retrieved exactly. This is most likely due to other absorbers that are

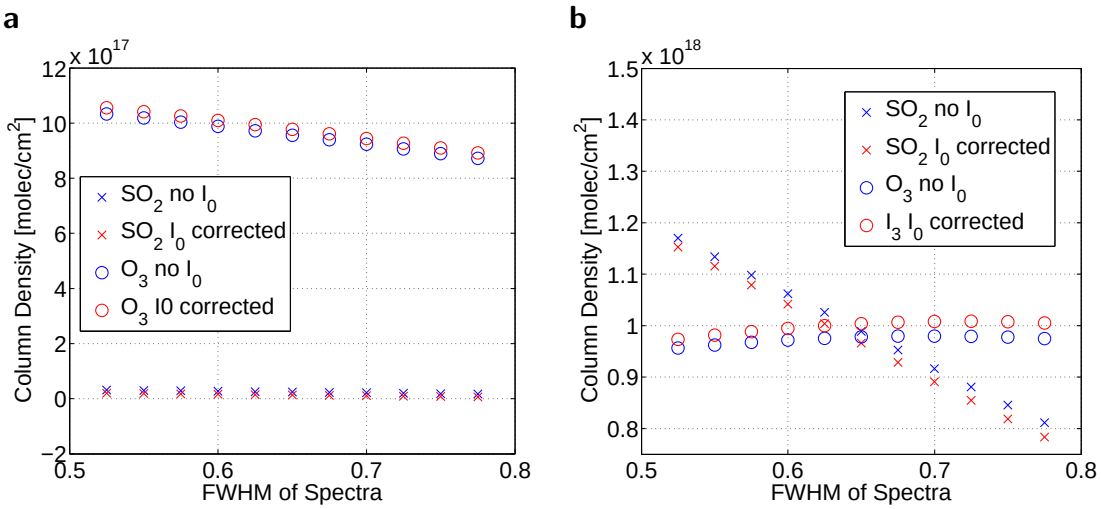

Figure 7.7.: SO_2 and O_3 column densities from synthetic spectra for evaluation range 1. For this plot the FRS and the measurement spectrum were convolved with a Gaussian function with varying FWHM (see x-axis), while all trace gas absorption cross sections were convolved with at FWHM of 0.65 nm. **a** shows a measurement spectrum without SO_2, **b** shows a measurement spectrum with an SO_2 column density of 1×10^{18} molec/cm^2.

present in the measurement spectrum but were not included in the fit (NO_2 as well as BrO have small absorption structures in the UV range used for the SO_2 evaluation, which are usually neglected when evaluating spectra for SO_2) or problems due to an incorrect calculation of the Ring spectrum. When the Ring structures were not included during the simulation of the spectra, accurate column densities were retrieved. The I_0 corrected cross sections yielded better results, but only of a negligible magnitude. The results for SO_2 and O_3 spectra without volcanic absorbers were similar in all three evaluation ranges.

This changes when volcanic absorbers were present in the measurement spectrum, the different evaluation ranges were not equally robust. Figure 7.7 b shows the results for O_3 and SO_2 in wavelength range 1. Both trace gases were included in the measurement spectrum with a column density of 1×10^{18} molec/cm^2. O_3 only had minor deviations from the true column density independent of I_0 correction. The retrieved O_3 column densities lie within 10% of the true value independent of the FWHM used for the convolution of the spectra. SO_2 showed larger deviations from the true column density. There was a deviation of approximately 3% even for a set of spectra that was convolved with the same FWHM as the reference cross sections (0.65 nm). Furthermore, a strong decline in SO_2 column density, with increasing FWHM used for the convolution of FRS and measurement spectrum, can be observed. The retrieved SO_2 column densities had deviations of up to 22% from the true value and exhibited an almost linear dependency on the FWHM.

Figure 7.8 a shows the same kind of plot as Figure 7.7 for evaluation range 2. The variation of retrieved SO_2 column density with changing FWHM of the

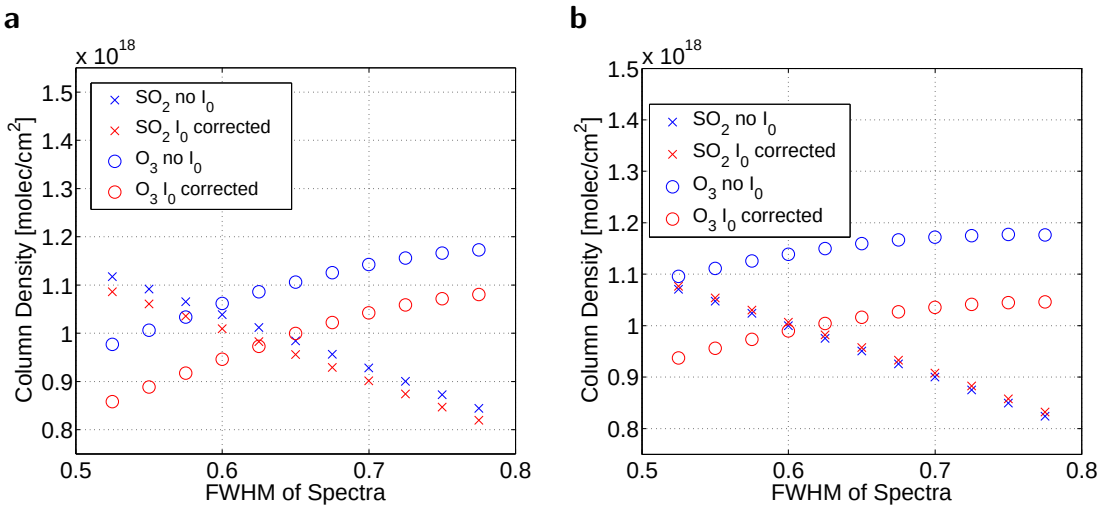

Figure 7.8.: SO_2 and O_3 column densities from synthetic spectra with an SO_2 column density of 1×10^{18} molec/cm^2 in the measurement spectrum. **a** shows results for range 2 (307.7 - 326.8 nm), **b** shows results for range 3 (310.0 - 326.8 nm).

Gaussian profile is smaller in this case. The O_3 column densities vary more and there is a shift between I_0 uncorrected and I_0 corrected reference cross sections. The I_0 corrected cross sections led to the correct O_3 column density when using the correct ILF for convolution.

The results for the spectra with SO_2 in the third range are shown in Figure 7.8 b. SO_2 looks similar to range 2. The slope of the curve for SO_2 is slightly lower. For O_3 the variation with varying ISF is smaller compared to range 2 while the shift between uncorrected and I_0 corrected cross sections is larger. The I_0 corrected cross sections again led to the correct O_3 column density if the correct ILF was used for the convolution of measurement spectrum and FRS. To get a better numerical estimate of the variation of the SO_2 column density with varying ILF, a linear fit was applied to the SO_2 column densities. The slope of the linear fit for all three evaluation ranges is shown in Table 7.2.

If the error of the retrieved SO_2 column densities is caused by an interference with other trace gases, the magnitude of variations of the retrieved SO_2 column densities should depend on the absolute value of the SO_2 column density. Spectra with all absorbers as stated in Table 7.1 but a higher SO_2 column density (2×10^{18} molec/cm^2) were simulated to investigate this issue. The relative variation of the SO_2 column density was comparable to spectra with an SO_2 column density of 1×10^{18} molec/cm^2. An example plot for evaluation range 1 is shown in Figure 7.9.

These results indicate that the evaluation range between 310.0 nm - 326.8 nm gives the most robust SO_2 column densities if the ILF varies during the measurements. As the O_3 column density increases when the SO_2 column density decreases this is the most likely explanation for the observed variations. However, while range 1 has the most robust O_3 column density it shows the

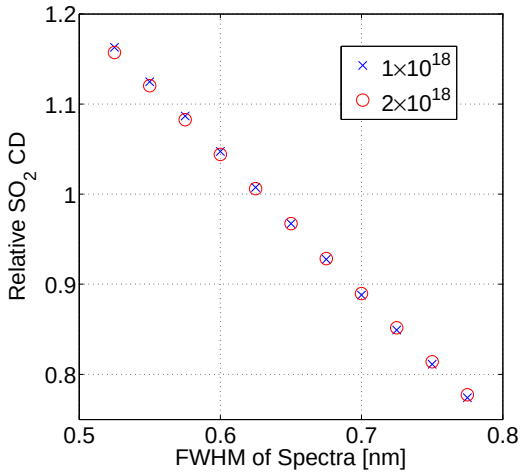

Figure 7.9.: Relative variation of the retrieved SO_2 column density for evaluation range 1 and two spectra with different SO_2 column density. There is no significant difference between the two spectra with different SO_2 content.

largest variations of SO_2 column density. Range 3 has a 50% smaller variation with changes of the ILF when compared to range 1 and 10% smaller variations when compared to range 2. Another advantage of range 3 compared to range 2 is that during real measurements of scattered solar radiation the radiation intensity decreases strongly with decreasing wavelength in this wavelength range, thus leading to increased noise.

Evaluation Range	314.6 - 326.8 nm	307.7 - 326.8 nm	310.0 - 326.8 nm
Slope $[\frac{molec}{cm^2 \cdot nm}]$	-1.48×10^{18}	-1.07×10^{18}	-9.8×10^{17}

Table 7.2.: Slope of the linear fit to the variation of the SO_2 column density with varying FWHM of the Gaussian profile used for the convolution of FRS and measurement spectra.

Results from Scenario 2 for SO_2

In Scenario 2 the FRS is convolved with the same ILF as the reference cross sections of the trace gases. The ILF for the convolution of the measurement spectra was varied. This is, e.g. the case when evaluating a complete data set with only one FRS recorded around noon time or in the case of the NOVAC data, when evaluating data with a high resolution solar atlas that was convolved with a fixed ILF as a Fraunhofer reference spectrum (see Chapter 8.1). As the differences between I_0 corrected and uncorrected reference cross sections were found to be only of minor importance, only I_0 corrected results are presented in this section.

For the measurement spectrum without volcanic absorbers (see Figure 7.10 **a**) one can see, that evaluation range 1 has a large variation of the retrieved

SO_2 column density while the two other ranges are more constant. Evaluation range 2 shows a slight overestimation of the true column density for FWHMs below 0.6 nm. Even for 0.125 nm deviation from the true FWHM the difference is below 2×10^{17} molec/cm^2.

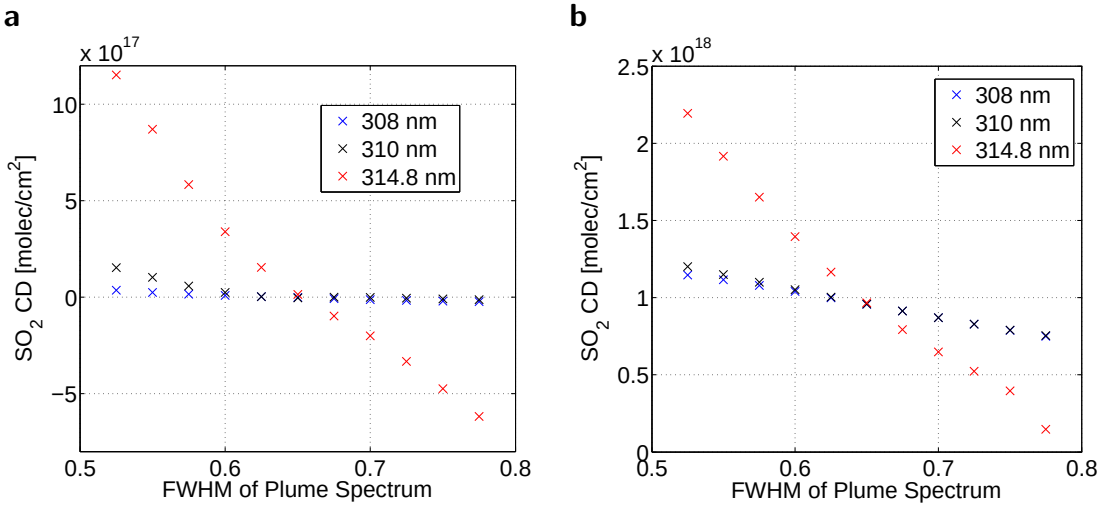

Figure 7.10.: SO_2 column densities retrieved in Scenario 2. **a** shows results for a measurement spectrum without SO_2, **b** shows results for a measurement spectrum with an SO_2 column density of 1×10^{18} molec/cm^2. One can see, that 314.6 – 326.8 nm has larger differences from the true value than the two other ranges. The two other ranges retrieve similar good results as in Scenario 1.

For the measurement spectrum with volcanic absorbers the situation (see Figure 7.10) looks similar. While evaluation range 1 shows large variations with varying FWHM, evaluation ranges 2 and 3 show comparable behaviour and under 25% error even for the largest deviations of the FWHM (±0.125 nm). The course of the O_3 column densities looks similar for both spectra, with or without volcanic absorption structures. An example of the retrieved O_3 results for the measurement spectrum with volcanic absorbers is shown in Figure 7.11. Here the O_3 column density varies for all three evaluation ranges, but the variation for evaluation range 3 is below 20% in any case, while evaluation range 1 shows the largest deviations from the true O_3 column density.

These tests also show that the two evaluation ranges which encompass more SO_2 absorption bands are more robust against variations of the ILF. Even though the performance of range 2 and 3 is comparable in these theoretical study, range 3 (310 – 326.8 nm) is advantageous since this range makes less use of lower wavelengths (with low light intensity). Additionally it is less vulnerable towards spectrometer stray-light (see Section 7.3), as more radiation is available.

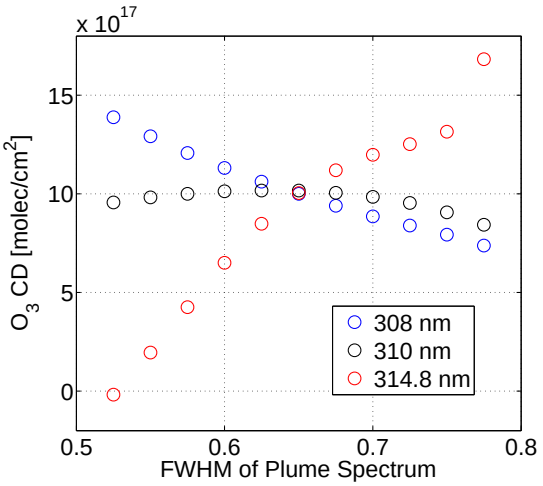

Figure 7.11.: O_3 column densities from the SO_2 evaluation in Scenario 2 for all three evaluation ranges. The evaluation was performed for a spectrum without any SO_2. The FWHM of the FRS was 0.65 nm, the FWHM used to create the plume spectra was varied. The true O_3 column density was 1×10^{18} molec/cm^2

Results from BrO for both scenarios

The BrO evaluation of a spectrum without any volcanic absorbers shows an offset for both the I_0 corrected and the I_0 uncorrected cross sections in Scenario 1 (Figure 7.12 a). The offset is roughly 6×10^{12} molec/cm^2 for I_0 uncorrected cross sections and 8×10^{12} molec/cm^2 for I_0 corrected cross sections. This offset is most likely due to an interference with the other cross sections or the Ring effect. If no Raman spectrum was added during the calculation of the synthetic spectra, the offset vanished. The retrieved BrO column density decreased with increasing FWHM of the Gaussian profile. The behaviour for the spectrum with a BrO column density of 1.5×10^{14} molec/cm^2 (see Figure 7.12 b) is similar when using a set of FRS and measurement spectrum that were convolved with the same Gaussian profile (Scenario 1). There is an offset even if all spectra and the cross sections were convolved with the same Gaussian profile. This offset is larger for the I_0 corrected case. It should be noted, that similar offsets can also be seen in the studies of Vogel (2011), whose findings led to the settings for BrO DOAS retrieval that was applied in this thesis. However, Vogel (2011) advised the wavelength range of 332.5 – 352.8 nm after additional studies using real measurement spectra. The BrO values decreased with increasing FWHM of the Gaussian profile, but the deviation from the true BrO column density is below 10% for all FWHMs that were simulated.

The variations of the BrO and SO_2 column densities both showed the same direction with varying FWHM of the ILF (decreasing column densities with increasing FWHM). When calculating the BrO/SO_2 ratio, the error from a varying ILF is therefore smaller than for the trace gas column densities themselves. The effect on the BrO/SO_2 ratio is shown in Figure 7.13. Here SO_2 was evaluated

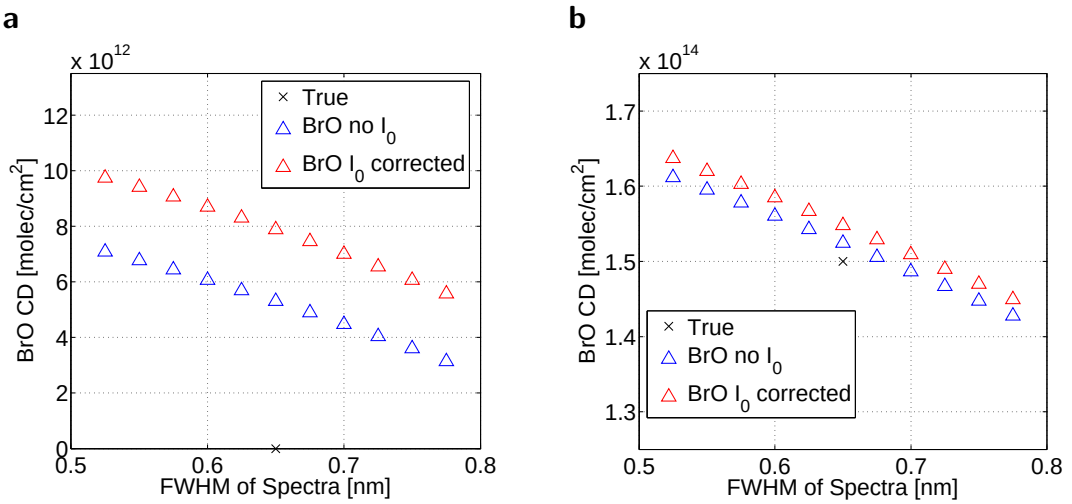

Figure 7.12.: BrO column densities for I_0 corrected and I_0 uncorrected cross-sections for Scenario 1. **a** shows a measurement spectrum without volcanic absorbers, **b** shows a spectrum with a BrO column density of 1.5×10^{14} molec/cm^2

in evaluation range 1, to show the magnitude of error for the BrO/SO_2 ratios in Chapter 5. It can be seen that the variation from the BrO/SO_2 ratio obtained with a correct set of ILF is below 15% for all simulated FWHM.

BrO is a relatively weak absorber, therefore variations of the other trace gases can have a more severe effect on the retrieved BrO column densities. A spectrum with a higher BrO column density (3.0×10^{14} molec/cm^2) but all other absorbers as stated in Table 7.1 was created. For a spectrum with higher BrO content lower relative variations of the retrieved BrO column density can be observed (Figure 7.14) This indicates that the variations of the BrO column density are at least partially caused by interferences with other absorbers. A future study that investigates variations of the SO_2 and BrO column densities when varying all other trace gases could help to identify these cross-interferences.

For Scenario 2 again only results using I_0 corrected cross sections are shown (see Figure 7.15). In this scenario large differences in the retrieved BrO column densities can be observed even for a change of the FWHM of only 0.025 nm. It is interesting to note, that there is only a shift between the two measurement spectra (with and without SO_2 and BrO). This indicates that the problems in the evaluation are not caused by volcanic absorbers but by the tropospheric absorbers or the Ring spectrum. However, no clear correlation with only one specific of the other trace gases was found. While the increase with larger FWHMs correlates well with a similar structure for the SO_2 column density retrieved in this wavelength range, there is no such a clear correlation for the behaviour for smaller FWHMS.

In general, this study hints, that the BrO column densities only vary up to 10% (for the range of ILFs investigated) if the FRS and the measurement spectrum are both recorded with the same ILF. Furthermore, the variation from the true

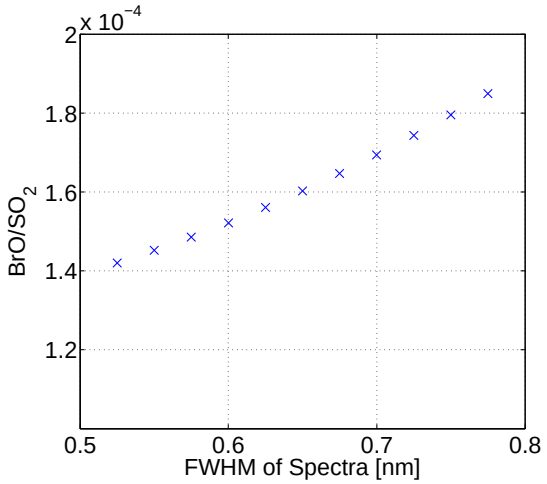

Figure 7.13.: Retrieved BrO/SO_2 ratios for spectra with an SO_2 column density of 1.0×10^{18} molec/cm^2 and a BrO column density of 1.5×10^{14} molec/cm^2. The SO_2 column densities were evaluated in wavelength range 1, to show the variations that can occur in the BrO/SO_2 ratios presented in this work.

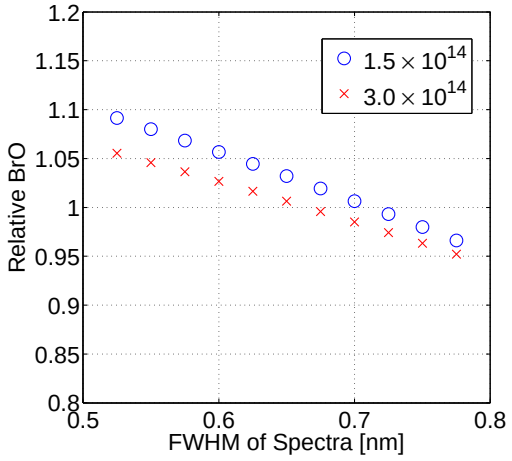

Figure 7.14.: Relative variation of the retrieved BrO column density for two spectra with a BrO column density of 1.5×10^{14} molec/cm^2 and 3.0×10^{14} molec/cm^2 respectively.

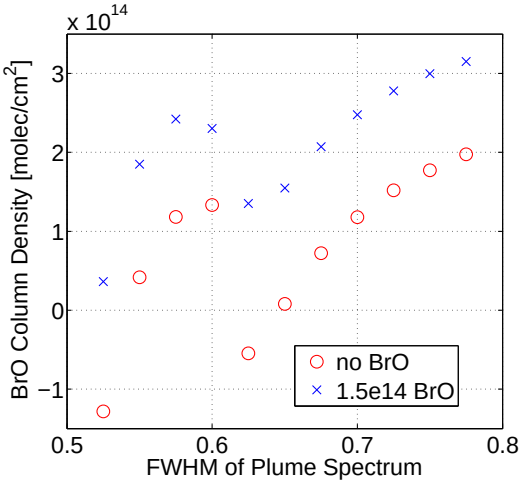

Figure 7.15.: BrO column densities for one spectrum with no apparent BrO and one spectrum with a column density of 1.5×10^{14} molec/cm^2. Only results for I_0 corrected cross sections are shown for Scenario 2. One can see, that even small differences between the ILF of the measurement spectrum and the Fraunhofer reference spectrum lead to strong variations in the retrieved column density.

column density shows in the same direction for BrO and SO_2, and leads to a variation of the BrO/SO_2 ratio of below 15%. However, if the FRS and the measurement spectrum are recorded with a varying ILF, the BrO evaluation seems to fail even for small variations.

7.3 Comparison with calibration cell measurements

The results from the model calculations, in particular the robustness of evaluation range 3, were verified by measuring spectra with SO_2 calibration cells in front of the spectrometer at different temperatures. For this validation, the spectrometer from the SO_2 camera, an Ocean Optics USB2000+, which has a comparable optical set-up to the instruments used in the NOVAC network, was used. As evaluation range 2 and evaluation range 3 show largely similar results, only range 1 and range 3 will be compared in this section.

Measurement procedure

At each temperature a measurement cycle was started after the instrument's temperature was stable for 5-10 minutes. Each measurement cycle started with measurements of a mercury emission line spectrum, dark current and offset spectra. Afterwards a sequence of: clear sky - Calibration Cell 1 - clear sky - Calibration Cell 2 - clear sky was recorded. At the end of each cycle another set of mercury emission line spectrum, dark current and offset was recorded in order to verify the stability of the instrument during the measurements.

The first measurement cycle was performed at 8°C, the second at 16°C and the last at 24°C. All measurements were performed between 11:40 am and 12:40 pm on 25 November, 2013. Measurements were started during a clear sky period. However during the short time frame of the measurements some clouds appeared on the sky (see Figure 7.16).

Evaluation

All spectra were evaluated according to the procedure described in Section 4.3.2. To rule out cross-interferences between two O_3 cross sections only one O_3 cross-section (Burrows et al., 1999, at 241K) was used in the evaluation. The 334.15 nm line of the mercury emission line was used for the convolution of the reference cross sections. I_0 corrected reference cross sections were used for the DOAS retrieval.

To verify the SO_2 column density of the calibration cells all spectra were first evaluated using a set of correct data, e.g. the FRS as well as the mercury emission line spectrum used for the convolution of the reference cross sections were recorded at the same temperature as the measurement spectrum. During this initial evaluation of the cell spectra it was found that the retrieved SO_2 column density depends on the evaluation range. Choosing a lower start wavelength of the DOAS retrieval led to lower SO_2 column densities. This might, e.g. be caused by spectrometer stray-light. In theory, the effect of stray-light should vanish, when using an additional polynomial in the intensity space during the DOAS retrieval. However, in reality using the offset polynomial in DOASIS did not improve the results.

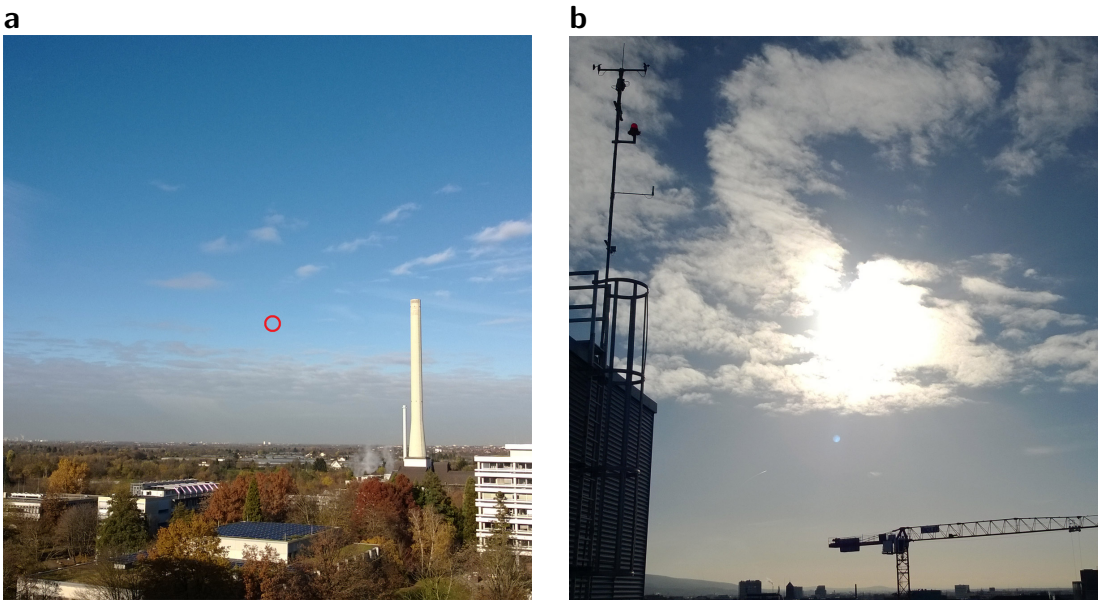

Figure 7.16.: Images acquired during the calibration cell measurements from the rooftop of the IUP in Heidelberg. **a** shows an image taken into the direction the spectrometer was pointing. The red circle marks the approximate position of the spectrometers field-of-view. **b** shows the viewing direction towards the Sun.

Therefore, the SO_2 column densities of both calibration cells were measured using an Acton 500 spectrometer with a Roper Scientific (NTE-2) camera and a broad-band laser driven light source. These measurements, with an instrument with lower stay-light fraction, did not reveal any wavelength dependency of the SO_2 column densities, and therefore these values are thought to be the correct SO_2 column densities of the calibration cells. Comparing the different retrieved SO_2 column densities in Table 7.3, one can see that range 2 between 310 – 326.8 nm underestimates the true column density by $\approx 10\%$ while in range 1 between 314.6 – 326.8 nm the underestimation is only $\approx 4\%$.

	Cell 1 $[molec/cm^2]$	Cell 2 $[molec/cm^2]$
Acton 500	$1.14 \times 10^{18} \pm 0.2 \times 10^{16}$	$2.55 \times 10^{18} \pm 0.8 \times 10^{16}$
310 – 326.8 nm	$1.02 \times 10^{18} \pm 1.0 \times 10^{16}$	$2.30 \times 10^{18} \pm 3.3 \times 10^{16}$
314.6 - 326.8 nm	$1.08 \times 10^{17} \pm 1.5 \times 10^{16}$	$2.41 \times 10^{18} \pm 6.0 \times 10^{16}$

Table 7.3.: Column density retrieved with the Acton 500 and for two different wavelength intervals retrieved with the Ocean Optics USB2000+.

After this first evaluation, the calibration cell measurements as well as the background spectra obtained before and after each measurement were evaluated with partly incorrect data sets to mimic Scenario 1 and 2 from the modelled spectra. For Scenario 1, all data was evaluated using the 334.15 nm line of a

mercury emission line recorded at 16°C as the ILF for the convolution of the reference cross sections. The FRS recorded at the same temperature as the measurement spectra were used in the DOAS retrieval of Scenario 1. For Scenario 2 the FRS as well as the mercury emission line recorded at 16° were used for the DOAS retrieval.

Results

The variation of the ILF with changing temperature, represented by the mercury emission lines at 302.15 nm and 334.15 nm, is shown in Table 7.4. The FWHM of a Gaussian profile fitted to the 302.15 nm Mercury emission line varied by almost 0.1 nm between the measurement at 8°C and 24°C while the 334.15 nm line varied only by 0.07 nm.

Temperature	302.15 nm	334.15 nm
8°	0.693	0.609
16°	0.617	0.552
24°	0.599	0.543

Table 7.4.: The FWHM of a Gaussian profile fitted to the 302.15 nm and 334.15 nm mercury emission lines for different temperatures.

The results for the calibration cells in Scenario 1 (see Figure 7.17) show only a low variation of the retrieved SO_2 column density. The clear sky spectra, acquired before and after the cell measurements, are used to see the magnitude of error, when no SO_2 is measured. For Scenario 1 no significant amounts of SO_2 are retrieved. The difference between the SO_2 column density retrieved with a correct data set and the incorrectly retrieved value is below 4% for both wavelength ranges. The retrieved SO_2 column density decreases with increasing FWHM of the measurement and Fraunhofer reference spectra, similar to the study with modelled spectra in Section 7.2. The theoretical study indicates slightly larger deviations with changing FWHM. For 8°C, where the 334.15 nm line is ≈ 0.06 nm wider, the theoretical study would result in an overestimation of 7.8%. However, in the theoretical study also other absorbers changed, while in the measurements evaluated here only the calibration cell containing SO_2 was inserted into the light-path.

For Scenario 2 a larger difference between the two evaluation ranges can be observed, similar to the study with modelled spectra. Figure 7.18 shows the results for both evaluation ranges. For evaluation range 1 (Figure 7.18 a), background spectra of the clear sky showed an overestimation between $4 - 5 \times 10^{17}$ molec/cm^2 at 8°C and 24°C. For calibration cell spectra recorded with an FWHM of 0.54 nm (24°) we see an overestimation of the SO_2 column density that is also between $4 - 5 \times 10^{17}$ molec/cm^2 for both calibration cells. For calibration cell spectra recorded with an FWHM of 0.61 nm (8°C) there is a

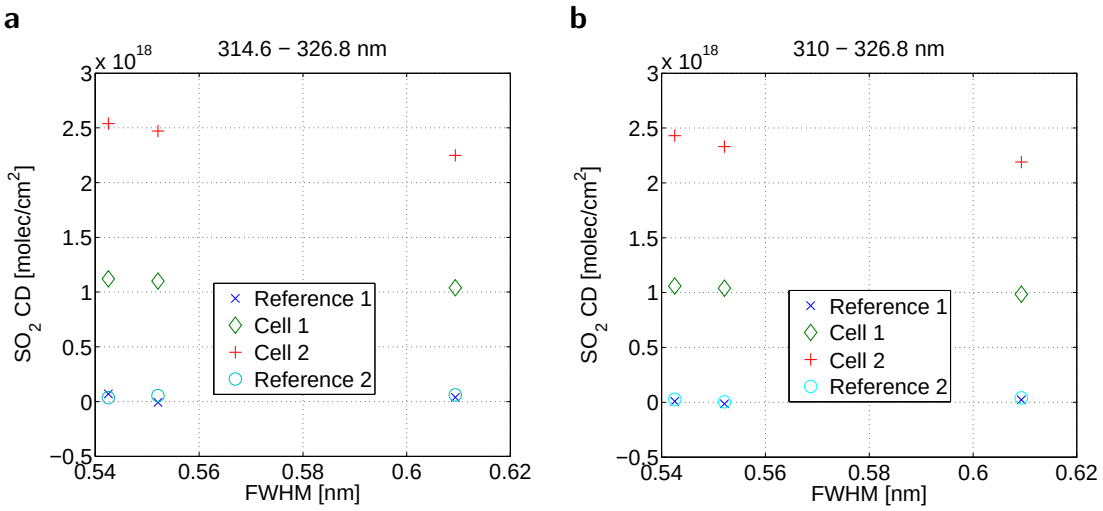

Figure 7.17.: Column densities retrieved for background and cell measurements, using a Fraunhofer reference spectrum recorded at the same temperature. All absorption cross sections were convolved using the 334.15 nm line recorded at 16°C, which has an approixmate FWHM of 0.55 nm. **a** shows data evaluated in Range 1 (314.8 - 326.8 nm), **b** shows data evaluated in Range 3 (310 - 326.8 nm).

linear relationship between the overestimation of the retrieved and the true SO_2 column density. For the background spectra, an SO_2 column density of $\approx 5 \times 10^{17}$ molec/cm^2 is retrieved, while for Cell 2 the true SO_2 column density is underestimated by only $\approx 2.2 \times 10^{17}$ molec/cm^2. These results cannot reproduce the clear linear dependency between the FWHM and the retrieved SO_2 column density that was found in the model calculations in Section 7.2. However, the measurement conditions changed during the time of the measurements. While clear sky conditions were observed in the beginning, some clouds appeared during the measurements. The variations might be partially due to this change of atmospheric conditions (e.g. different strength of the Ring structure).

The results for evaluation range 3 in Figure 7.18 **b** show far less variation of the true SO_2 column density. For the background spectra SO_2 amounts of up to $\approx 1 \times 10^{17}$ molec/cm^2 are detected, a value 4-5 times lower when compared to evaluation range 1. The difference between the retrieved SO_2 column density from the calibration cell spectra and the true value is below $\approx 7\%$.

For both evaluation ranges the DOAS fit error is approximately 3 times higher when using an incorrect FRS and absorption cross sections convolved with an incorrect ILF. While the results for Scenario 2 do not exactly reproduce the results from the theoretical study, they show that evaluation range 3 (310 – 326.8 nm) yields much better results if the instrument is not thermally stabilized. However, this does by no means say, that the findings in Vogel (2011) are invalid. The choice of the SO_2 retrieval range depends on the situation. For thermally stabilized instruments during a measurement campaign, evaluation range 1 clearly showed advantages (Vogel, 2011). As the DOAS retrieval is performed at

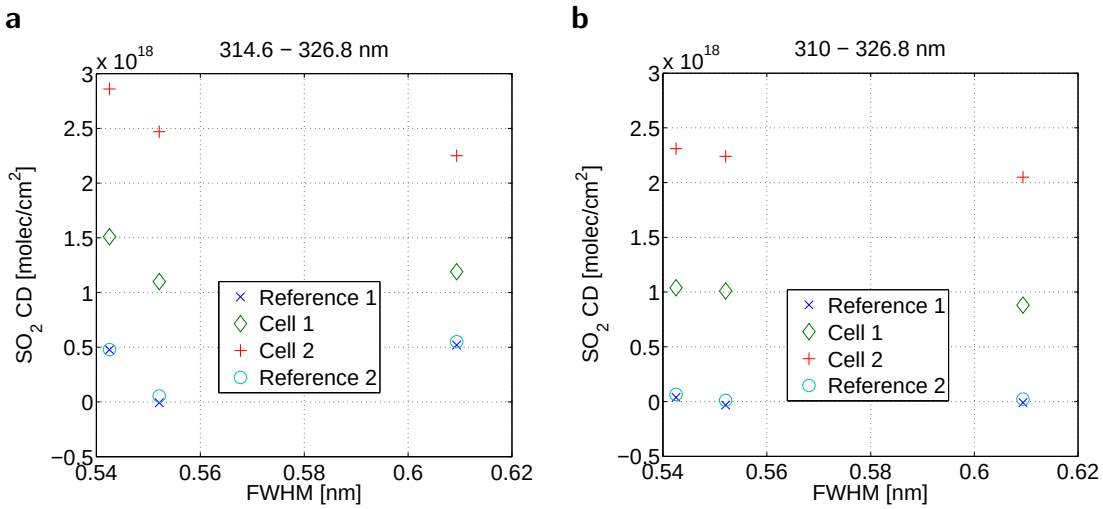

Figure 7.18.: Column densities retrieved for background and cell measurements, using a Fraunhofer reference spectrum recorded at 16°C. All trace gas reference cross sections were convolved using the 334.15 nm line recorded at 16°C, which has an approixmate FWHM of 0.55 nm. **a** shows data evaluated in Range 1, **b** shows data evaluated in Range 2.

larger wavelengths, the influences of radiative transfer (in particular the light dilution effect and saturation effects) on the retrieved SO_2 column densities are lower. However, in other applications, as for example the SO_2 retrieval with a high-resolution solar atlas as an FRS (Chapter 8), it is more important to use an evaluation range that is robust against changes of the ILF.

7.4 Determining the instrument line function from measurements

As described above, the form of the ILF can have severe effects on the DOAS evaluation. Unfortunately, for the instruments used in the NOVAC network, only measurements of a Mercury emission lamp, which were performed at room temperature at the beginning of the project, are available as a proxy for the ILF.

There are attempts to retrieve the ILF by adding it as an additional parameter in the DOAS fit. The Chance and Kurucz (2010) solar atlas convolved with varying ILFs is used as an FRS in these evaluations. The most simple version of this approach, convolving the Chance and Kurucz (2010) solar atlas with a Gaussian profile of varying FWHM was compared to a more sophisticated method that is currently being implemented in DOASIS (Kraus, 2006). However, the DOASIS implementation by Lehmann (2014) is still in development and the performance and possible pitfalls are not fully determined. The software package WinDOAS has a similar function (van Rozendael, 2013), which is in a more robust status. However, the WinDOAS documentation does lack a description of the exact implementation. Additionally WinDOAS cannot be used for batch processing of a larger amount of spectra. Therefore, WinDOAS will only be used for a brief comparison in the later part of this section, as it is a software-package used by many spectroscopy groups world-wide.

For the comparison of the different methods for finding the ILF, clear sky spectra from the measurements described in Section 7.3 were used. The ILF of the Ocean Optics USB2000+ used during these measurements is well known at certain wavelengths, as mercury emission line spectra were recorded directly before and after the measurements.

The different approaches from our institute that were compared are:

- Gaussian Profile: Fitting the convolved Chance and Kurucz (2010) high-resolution solar atlas to the clear sky spectrum. The solar atlas was convolved with a Gaussian profile of varying FWHM (for this comparison the FWHM was varied in steps of 0.005 nm) as an FRS for the DOAS fit. A Ring spectrum was calculated from the FRS. The absorption cross sections of O_3 and NO_2 were also convolved with the same Gaussian profile and included in the fit. The FWHM for which χ^2 of the DOAS fit is minimized is assumed to be the FWHM of the Gaussian ILF.

- The DOASIS software-package has a new optimization function implemented. This function was written by Lehmann (2014). It consists of two parts, the so-called wavelength-pixel-mapping (WPM), which is used to correctly calibrate the spectrum and the slit-function modelling (SFM) that is used to obtain the ILF. The basic concept is, similar to the first method, based on varying the ILF and performing a DOAS fit with the Chance and

Kurucz (2010) solar atlas as an FRS. However, in this approach the variation of the ILF is implemented directly into the DOAS fit routine which should theoretically improve the performance when compared with the brute-force approach described above. This function supports a variety of options (different line shapes, such as a Gaussian profile or an asymmetric Gaussian profile) and can also account for a wavelength variability of the ILF. Trace gas absorption cross sections of O_3 and NO_2 were also included in the fit. In this work a wavelength-dependent Gaussian profile was chosen as a possible ILF. However, one large drawback of this approach is, that the performance and possible pitfalls are yet to be determined by Lehmann (2014).

The two approaches were applied to clear sky spectra that were recorded at three different instrument temperatures (see Section 7.3). The results are then compared to measurements of a mercury line that were performed directly after the clear sky spectra were acquired and at the same temperature. Before using the different approaches to find the ILF, all spectra were calibrated with the DOASIS wavelength-pixel-mapping function. This function finds the spectral calibration of the instrument by comparing the measurement spectrum with a convolved Chance and Kurucz (2010) solar atlas.

In a first attempt, both methods were applied on the clear sky spectra in the wavelength range between 306 - 335 nm. This range does not cover the 302.15 nm Mercury emission line. Extremely low radiation intensities below 306 nm lead to increased noise and instability of both approaches. As the first method does not take any wavelength dependencies into account, and the SFM approach only showed a low wavelength dependency, interpolating the results for the 302.15 nm line only led to a negligible error.

It should be noted, that a DOAS fit using only the convolved Chance and Kurucz (2010) solar atlas without including O_3 and the Ring effect led to large errors. Figure 7.19 shows the residual of a fit that did not include O_3. A large residual structure that correlates with the differential structure of O_3 can be observed. The main stratospheric absorbers O_3 and NO_2 as well as a Ring spectrum were therefore included in the DOAS fits to find the ILF.

For the SFM function a Gaussian profile with a wavelength dependent FWHM was chosen as a proxy for the ILF. The wavelength dependency of the ILF is described by a 2^{nd} order polynomial. A start value for the FWHM of the ILF has to be given for the SFM function, in this work a value of 0.6 nm was chosen. Absorption cross sections of NO_2 (Vandaele et al., 1998, recorded at 220 K) and O_3 (Gorshelev et al., 2013; Serdyuchenko et al., 2013, recorded at 223 K) were included in the fit to account for typical stratospheric absorbers. Note that a different ozone cross section than in the rest of this work was used. This new cross section was recorded at higher resolution, which is advantageous for the task performed here.

The results for the 302.15 nm line are shown in Fig. 7.20 a. The SFM approach

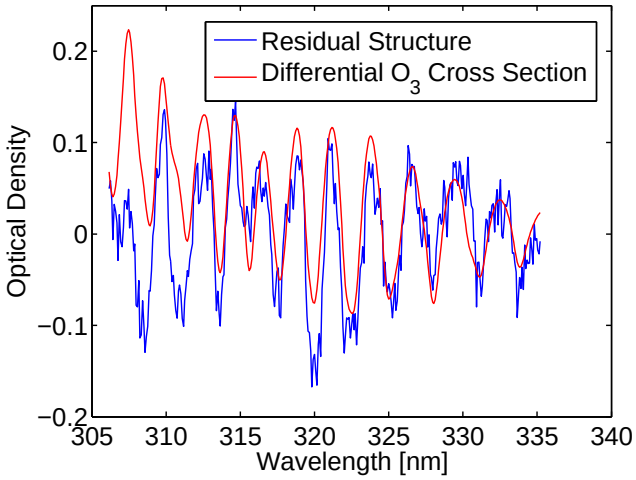

Figure 7.19.: Residual from fitting the Chance and Kurucz (2010) solar atlas to the measurement spectrum after convolution with a Gaussian profile (blue curve). The residual clearly correlates with the differential structure of O_3 (red line).

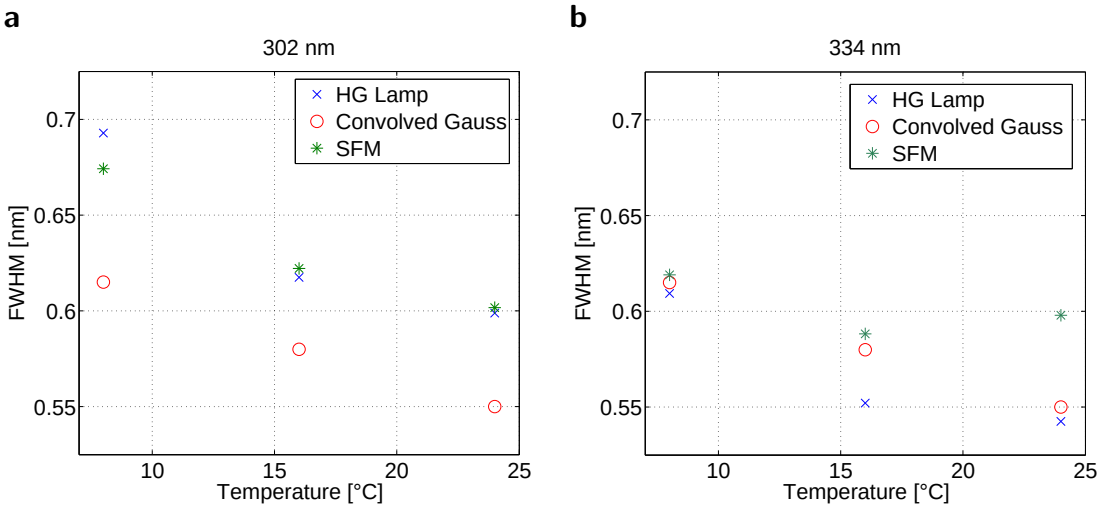

Figure 7.20.: The FWHM of a Gaussian curve determined for three clear sky spectra at different temperatures in the wavelength range between 301-335 nm. Convolving the Chance and Kurucz (2010) high-resolution solar atlas with a Gaussian clearly deviates from the FWHM of the ILF as measured by the Mercury emission line shape at 302 nm but shows goot agreement at 334 nm. **a** shows the results for the 302.15 nm line, **b** for the 334.15 nm.

corresponds well to this mercury emission line (the largest deviations at 8°C are below 0.02 nm). The convoluted Gaussian profile underestimates the FWHM at all temperatures, at 8°C the FWHM of the Gaussian profile is 0.08 nm below the value from the Mercury emission line. For the 334.15 nm line (see Fig. 7.20 b) the constant Gaussian profile and the Mercury emission line agree better. The largest deviation is 0.03 nm at 16°C. The SFM approach overestimates the FWHM of the 334.15 nm line at 16°C and 24°C. It is not exactly clear why the SFM approach is unable to find the correct ILF at 334.15 nm. A possible explanation for the large deviations of the constant Gaussian profile at 302.15 nm can be found by looking at χ^2 obtained for different FWHMs (see Figure 7.21). This plot shows, that χ^2 does not have a sharp minimum, but low values can be observed for a large range of FWHMs. Table 7.4 shows that at 8°C, the FWHM varies by almost 0.1 nm between 302.15 nm and 334.15 nm. A larger FWHM led to better agreement at lower wavelengths, while a smaller FWHM leads to a better agreement at larger wavelengths. The constant Gaussian profile cannot assess the wavelength dependency of the FWHM. In this case, the results from the constant Gaussian profile agree nicely at 334.15 nm and therefore cannot show the correct result at 302.15 nm.

To further validate the performance of the SFM function it was used with settings to mimic the constant Gaussian profile. The wavelength dependency is described by a constant (i.e., no wavelength dependency). This setting should lead to the same results as the first method. However, when using the SFM with these settings, the results of the FWHM lie within 0.01 nm of the 302.15 nm line, and therefore clearly do not agree with the first method. The test was repeated using a FWHM of 1.0 nm as the initial value of the ILF in the SFM function. The results varied up to 0.02 nm, which unfortunately shows that the SFM routine is sensitive to the initial settings, for example the initial value of the ILF. The most likely explanation for these deviations is the plateau of the χ^2 values as well (see Figure 7.21). All values that were obtained by the SFM function lie within this χ^2 plateau.

Both methods were also used in the wavelength range between 324.15 - 344.15 nm. This interval encompasses 10 nm on both sides of the 334.15 nm peak. More radiation intensity is available at these wavelengths and the influence of the strong O_3 absorption is lower. Additionally variations of the ILF are typically larger at the sides of the detector than in the centre. This setting was also compared with two additional method. First the DOASIS optimization toolbox also allows combining SFM and WPM, in this setting the calibration is further updated while the ILF is retrieved. In some cases this can result in a more accurate calibration.

As an additional comparison, the WinDOAS calibration method was used as well. WinDOAS is another spectroscopy software package that is applied by several work-groups. WinDOAS was set up to mimic the convoluted Gauss function. No wavelength dependency was allowed and only one fit window between 324.15 - 344.15 nm was chosen. Already without taking other absorbers

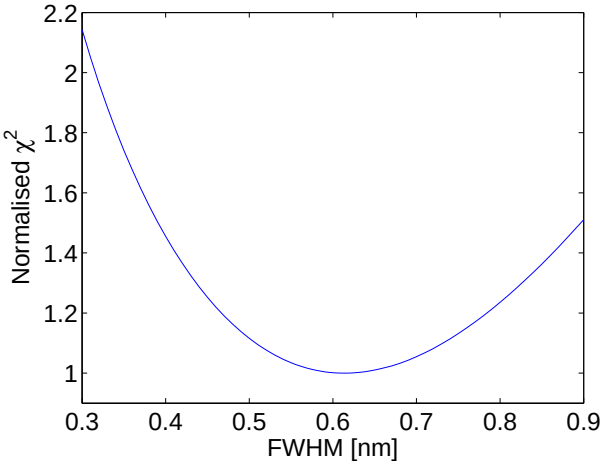

Figure 7.21.: χ^2 for a DOAS fit with a (Chance and Kurucz, 2010) solar atlas that was convoluted with a Gaussian profile with varying FWHM. It can be clearly seen, that χ^2 has low values in a rather large intervall, instead of a sharp minimum.

(O_3 and NO_2) or the Ring effect into account WinDOAS showed excellent agreement with the mercury emission line (see Figure. 7.22). The result are suprising, considering the fact that neither stratospheric absorbers nor the Ring effect were included in the evaluation (which led to problems for the convolved Gaussian). However, the possibilities of WinDOAS were not investigated further, as it is not possible to use the software package in a scripted form, which would be needed to include this function in the evaluation of the NOVAC data.

The results for all methods are shown in Figure. 7.22. The constant Gaussian profile underestimates the FWHM, but is in all cases within 0.05 nm of the true FWHM. The two DOASIS optimization functions also find the ILF within 0.05 nm in all cases. It should be noted though, that there is a shift of 0.04 nm depending on if only the SFM function or a combination of WPM and SFM is used to retrieve the ILF. It cannot be judged from these measurements which approach works better. While using only the SFM function fits the Mercury emission line at 8°C, the combination of SFM and WPM leads to better results at the two other temperatures.

In general it can be said that all different methods performed fairly well and retrieved the correct FWHM within 0.05 nm of the value from the mercury emission line. If the ILF can be retrieved to an accuracy of 0.05 nm the BrO/SO_2 ratios obtained with this ILF are within 5% of the correct value, which would be an excellent result. For improvements beyond the threshold of 0.05 nm a more detailed study, that investigates the different implementations by DOASIS and WinDOAS in depth, is needed.

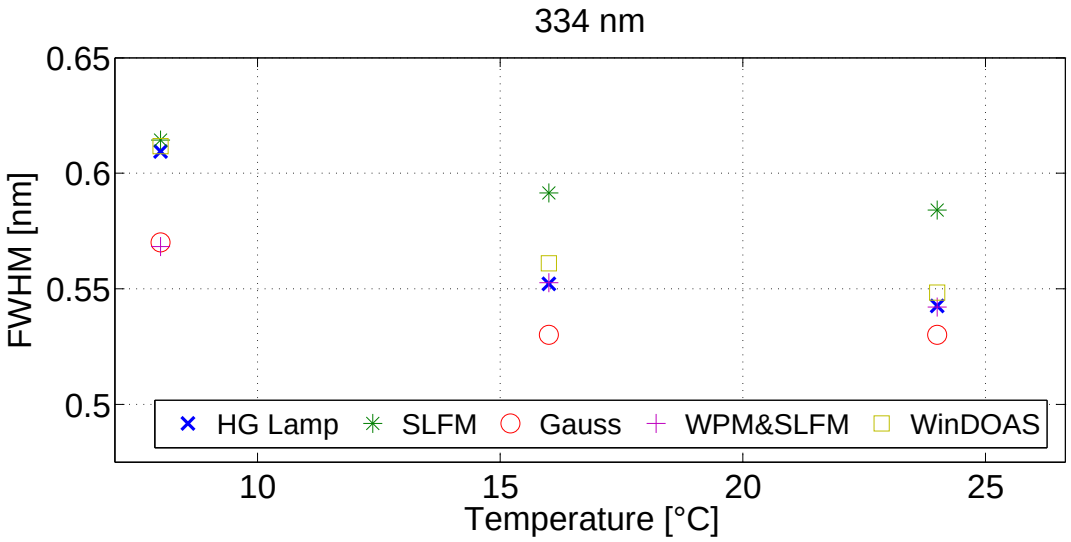

Figure 7.22.: The FWHM of the ILF determined for three clear sky spectra at different temperatures.

8

Using a high-resolution solar atlas as a reference spectrum

Since the solar spectrum (i.e. $I_0(\lambda)$) is highly structured by solar Fraunhofer lines (see Section 3.2) the evaluation of the NOVAC data requires a Fraunhofer reference spectrum (FRS) which is free of volcanic absorbers. In principle a FRS is recorded with the instrument looking in a direction where no volcanic plume is present. During the calculation of the SO_2 emission rates in the NOVAC project a zenith looking spectrum is used as an FRS in the DOAS retrieval. After this initial evaluation 20% of the lowest SO_2 dSCDs are assumed to be free of volcanic gases. Their average is subtracted from all retrieved dSCDs in order to convert them to SCDs. If all spectra of one scan through the complete sky are contaminated with SO_2 in the light-path, all retrieved SCDs will be erroneous and the SO_2 emission rate will be underestimated. For the evaluation of the BrO/SO_2 ratios the situation is slightly better. A reference spectrum that is contaminated with BrO and SO_2 does not influence the BrO/SO_2 ratio, if it contains the same ratio of both gases as the plume spectrum. However, in this case the signal-to-noise ratio still decreases.

An approach to evaluate spectra without a reference spectrum was investigated in order to find how frequently all viewing directions of a scan are influenced by volcanic gases. Instead of using a reference spectrum recorded with the same instrument, a high-resolution solar atlas (Chance and Kurucz, 2010) was used as an FRS for the evaluation. The big advantage of using a high-resolution solar atlas is that it is certain that the spectrum contains no SO_2 (or at least negligible amounts when compared to volcanic emissions). A drawback of this method is that the high-resolution solar atlas spectrum was not recorded with the same instrument as the measurement spectra, which complicates the DOAS retrieval.

The idea of using a high-resolution solar atlas as a reference spectrum is based on a similar approach that was published by Salerno et al. (2009). However, a different technical implementation was developed during this thesis. The details of the DOAS retrieval are outlined in Section 8.1. Section 8.2 compares the evaluation using the Solar Atlas by Chance and Kurucz (2010) with the NOVAC evaluation. Finally, Section 8.2.2 investigates reasons for the differences between the two evaluation methods.

8.1 Evaluation procedure

The spectra for the two instruments at Nevado del Ruiz (see Section 5.3) were evaluated with three different methods. Besides the two afore-mentioned methods all spectra were also evaluated using one fixed, gas-free FRS recorded with the same instrument. The big difference between the three methods is that it is uncertain in the NOVAC approach if the FRS, or any spectra from the respective scan, is gas free, therefore only dSCDs are obtained. The two other methods use SO_2 free FRS, the DOAS evaluation therefore yields SCDs.

The three methods compared in this chapter are:

- NOVAC: All spectra were evaluated using a reference spectrum that is acquired with a zenith-looking viewing geometry at the beginning of each scan. Since the FRS can contain SO_2 absorption structures, a baseline value is subtracted from all retrieved SO_2 dSCDs. In NOVAC, this baseline is the average of the SO_2 dSCDs from the 20% spectra with the lowest SO_2 content (Galle et al., 2010).

- Solar Atlas: Instead of an FRS from the same instrument a high-resolution solar atlas convolved to match the instrument's resolution is used as an FRS. In this work the solar atlas by Chance and Kurucz (2010) is used. The high resolution solar atlas is convolved using the 334.15 nm emission line of a mercury lamp that was measured in the laboratory at room temperature at the beginning of the NOVAC project. This approach is referred to as the Solar Atlas method.

- Fixed Reference: For each instrument a zenith-looking spectrum was identified as plume free through comparison of the results from the two other, above mentioned, methods. This fixed FRS was used for the evaluation of all scans. This method is utilized to verify the results of the Solar Atlas method.

The Ring spectrum for all three methods is calculated from the respective FRS. Similar to the SO_2 camera evaluation in Chapter 4, one SO_2 cross section (at 298K, from Vandaele et al., 2009) and two O_3 cross sections (both 221 K and 241 K from Burrows et al., 1999) were included in the DOAS retrieval. Additionally, it

was found that the Solar Atlas evaluation resulted in an almost constant residual for all evaluations (see result section below). The first component of a principal component analysis (PCA, Pearson, 1901) of the residual structures was included in the fit as well. A good introduction on the PCA is given by Smith (2002), more information on the use of the PCA in DOAS evaluations can be found in Lampel (2010, 2014).

The FRS and the Ring spectrum as one set, and all absorption cross sections as another set were allowed to be shifted by ± 0.2 nm and stretched/squeezed by a factor of $0.98 - 1.02$. The first principal component included in the Solar Atlas evaluation was allowed to shift ± 0.05 nm and squeeze by a factor of $0.98 - 1.02$.

The DOAS evaluation was performed in the wavelength range between 310 – 326.8 nm following the findings from Section 7. This evaluation range is more robust regarding variations of the instrument's temperature than the range used in Chapter 4 and 5.

8.2 Results

Residual for the Solar atlas evaluation

The first important observation when evaluating data with the Solar Atlas as an FRS was that the residual spectra have a dominant structure that is apparent in most spectra. Some deviations from this structure were found at large SZAs above 80°. These deviations might be due to temperature variations of the instrument (see Chapter 7) or a wavelength dependency of the O_3 dSCD when the SZA is large. Figure 8.1 shows a colour-coded image of the residual's intensity from instrument D2J2201 in January 2011. For this plot all spectra with an SZA below 80° and spectra that were under- or overexposed (under 25% or over 85% of the maximum intensity after dark current and offset correction) were removed. Also some spectra where the fit clearly failed (identified by a large χ^2 value) were not taken into account. It is obvious, that there is a dominant structure apparent in all spectra, with minor variations of the residual in the morning and evening hours.

A PCA was performed on the spectra from January 2011 fulfilling the above mentioned selection criteria. For the instrument D2J2200 the χ^2 criterion was set to a threshold of 0.016. The fit quality for D2J2201 was slightly better and a χ^2 threshold of 0.013 was chosen. Spectra above the χ^2 threshold only appeared in the morning and evening hours. The first principal component for both instruments is shown in Figure 8.2. Both instruments clearly show the same broad-band variation but also some narrower features are apparent for both instruments. As can be seen in Figure 8.1, the strength of these features was constant throughout most scans. A small wavelength shift can be observed between the narrow-band features of the two instruments.

The narrow-band features might be caused by variations of the sensitivity

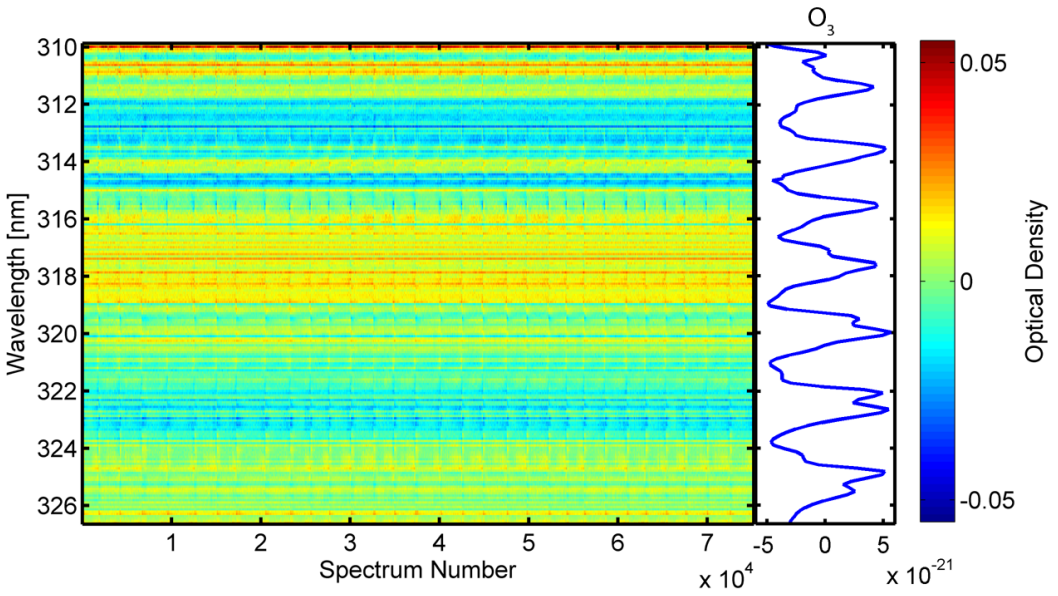

Figure 8.1.: Colour-coded image of the residual for spectra from instrument D2J2201. The plot shows all spectra from January 2011, that fulfil the criteria mentioned in the text (e.g., SZA<80°, sufficient intensity). The vertical lines are due to small variations of the residual in the morning and evening hours. On the right side the differential O_3 absorption cross section is shown for comparison.

of the detector pixels or inaccuracies of the ILF. Convolving the Chance and Kurucz (2010) Solar Atlas with different ILFs leads to a slightly different shape of the resulting spectrum. When fitting a Solar Atlas convolved with one ILF to a Solar Atlas convolved with a different ILF the residual shows comparable narrow-band features. The 334.15 nm mercury emission line was used for the convolution over the complete wavelength range. This mercury emission line cannot be seen as a good representation of the ILF for the complete wavelength range (see Chapter 7).

Instrumental effects like the quantum efficiency of the CCD or the efficiency of the spectrometer's grating can explain the broad-band variations of the residual. When using an FRS recorded by the same instrument these effects cancel out in a DOAS retrieval. When using a Solar Atlas as a reference spectrum the effect of the quantum efficiency and the grating efficiency leads to a constant term. For the quantum efficiency of the detector this can be shown by adding a wavelength dependent term $C(\lambda)$ accounting for the quantum efficiency to Equation 3.17. The radiation intensity I_{meas} as measured by a real instrument can be expressed by the following expression:

$$I_{meas}(\lambda) = I^*(\lambda) \cdot C(\lambda) = (I(\lambda) * H(\lambda)) \cdot C(\lambda) \tag{8.1}$$

Here $I(\lambda)$ is the incoming radiation that is convolved with the ILF $H(\lambda)$, the detector has a certain wavelength dependent quantum efficiency that is accounted for by multiplying $C(\alpha)$. For the FRS spectrum it is assumed in this

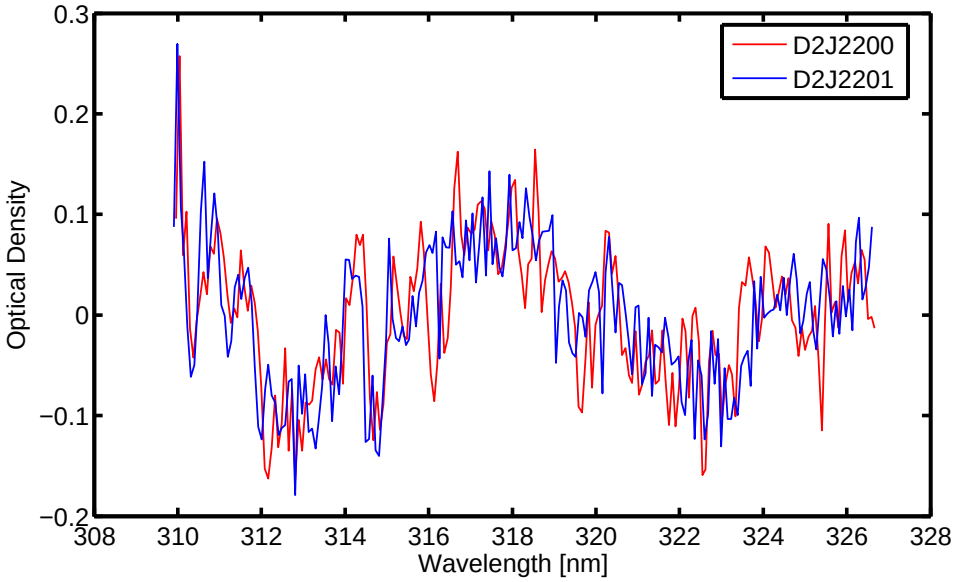

Figure 8.2.: Figure showing the first principal components for both instruments. Spectra from January 2011 were used for the PCA of both instruments.

thesis that the Chance and Kurucz (2010) Solar Atlas is a good representation of the incoming solar radiation. It should be noted though that other Solar Atlas spectra with some minor differences exist (e.g. Gurlit et al., 2005; Thuillier et al., 2004). The Solar Atlas spectrum $I_0(\lambda)$ is convolved with the ILF $H(\lambda)$ and used as an FRS in the calculation of the optical density. For simplicity the following calculation is shown for one absorber as in Equation 3.25. The optical density τ for an evaluation with a Solar Atlas becomes:

$$\tau = \ln\left(\frac{I_0^*(\lambda)}{I_{meas}(\lambda)}\right) = \ln\left(\frac{I_0(\lambda) * H(\lambda)}{[I(\lambda) * H(\lambda)] \cdot C(\lambda)}\right) = \sigma(\lambda) \cdot S - \ln(C(\lambda)) \quad (8.2)$$

This equation shows that a constant term, that is independent of the trace gas absorption has to be expected in the DOAS retrieval. Therefore, the first principal component of the residual is supposed to be a combination of instrumental effects that has to be taken into account when evaluating spectra with a Solar Atlas. The constant residual structure was included in the DOAS retrieval with the Solar Atlas as FRS as a pseudo-absorber.

8.2.1 Performance of the DOAS retrieval

An example of a DOAS retrieval using the Solar Atlas as FRS is shown in Figure 8.3. It can be seen that the SO_2 column density of 4×10^{17}molec/cm^2 can be clearly identified. The residual structure is mostly unstructured and has a peak to peak value of $\approx 10^{-2}$. In general the quality of the DOAS fit is similar to the regular NOVAC SO_2 retrieval that uses a reference spectrum recorded with the same instrument as an FRS. The principal component that was included in the fit is found extraordinarily well in most spectra.

The SO_2 DOAS fit error

The DOAS fit error was usually $\approx 1 \times 10^{16}$molec/cm^2 for scans with an SZA below 55°, at larger SZAs the retrieval error increased (Figure 8.4). It is interesting to note, that the fit error of instrument D2J2200 increased already at SZAs of 55°, while instrument D2J2201 had low fit errors up to SZAs of 75°. Three possible explanations for the increase of the DOAS fit error can be given. First, the light-path through the stratosphere and thus the O_3 column increase with increasing SZA. This can lead to a wavelength dependent O_3 column density, which was not accounted for in the DOAS fit. The second cause can be temperature variations of the instrument. The ambient temperature at Nevado del Ruiz varies between 0°C and 40°C in the course of a day. As was shown in Chapter 7, variations of the instrument temperature can lead to large errors in the DOAS retrieval. If one of the instruments has smaller variations of the instrument function with temperature, or is better thermally insulated, this might lead to smaller errors with variations of the ambient temperature. Unfortunately, for both instruments neither the spectrometer's temperature nor data about the variation of the instrument function with temperature was available. Therefore, this question cannot be definitively answered here. Additionally, less radiation intensity is available at at large SZAs, thus leading to longer exposure times and thus a larger dark current signal. This can result in a larger DOAS fit error.

The SO_2 DOAS fit errors for instrument D2J2200 with all three evaluation methods were compared for 1 January 2011. This day was one of the few almost completely cloudless days available in the data set (see Section 6.3). The SO_2 DOAS fit errors and their variations during the course of a day are shown in Figure 8.5. For the NOVAC method there are relatively large values for the first two scans in the morning. Afterwards a strong decrease of the fit error, to values around 1×10^{16} molec/cm^2, can be observed. The fit error for the Solar Atlas method and the fixed reference showed elevated values for a longer time and reached similar values as the evaluation with the NOVAC reference around 15:00:00 UTC (9:00 am local time). For low SZA values the Solar Atlas retrieval even shows smaller DOAS fit errors than the NOVAC evaluation. In the evening the fit error for all three methods showed a large increase.

Looking at the DOAS fit error as a function of SZA (Figure 8.6), one can

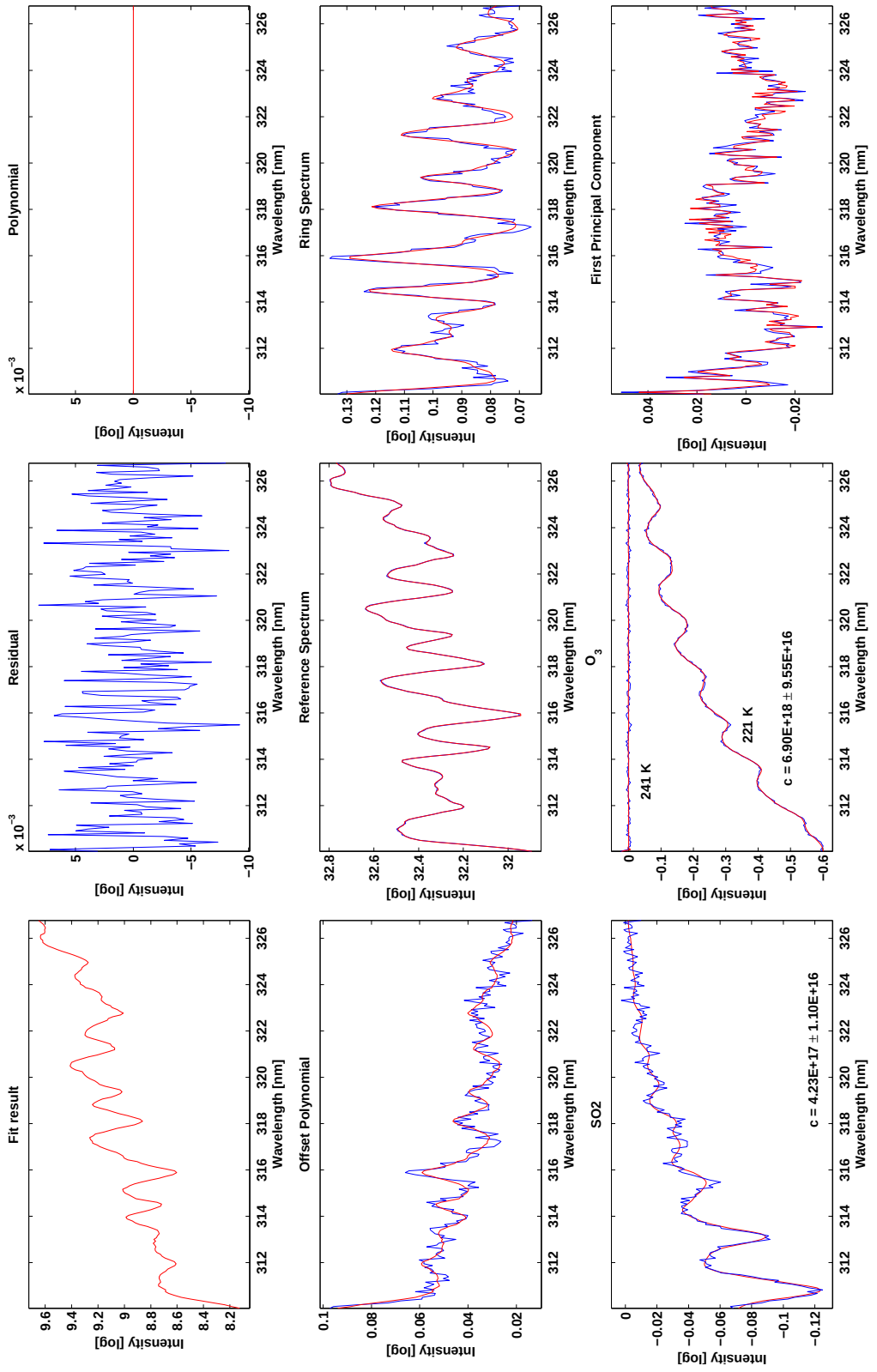

Figure 8.3.: Example of a DOAS retrieval using the Solar Atlas as a Fraunhofer Reference spectrum. The first principal component of the residual is included as a pseudo-absorber. The two O_3 results are shown together in one window.

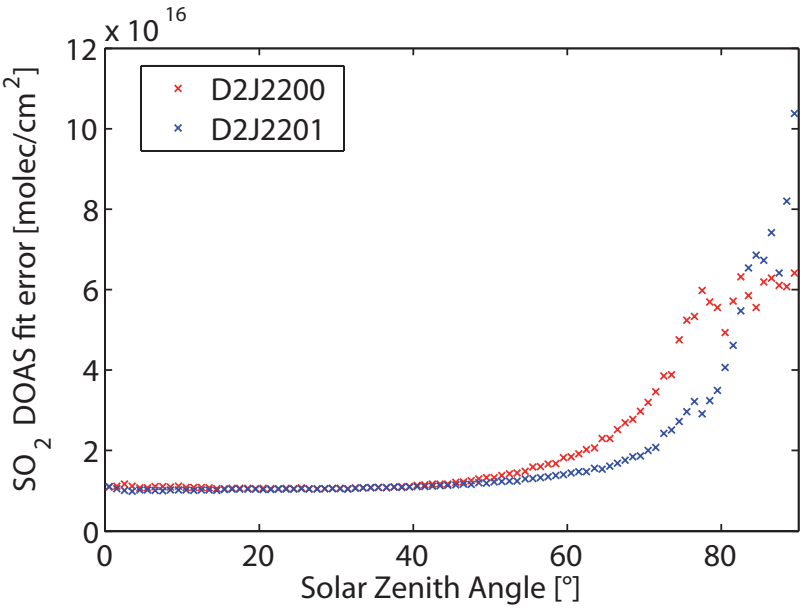

Figure 8.4.: Average SO_2 retrieval error as a function of the Solar Zenith Angle. Data from instrument D2J2200 and D2J2201 in 2011 was used for this plot.

observe that the SO_2 fit error increases with larger SZAs. At a larger SZA the light path through the stratosphere is longer which can lead to problems with strong absorption of stratospheric absorbers. Additionally there is less radiation intensity available at large SZAs which results in longer exposure times and therefore a stronger influence of the dark current on spectra.

The instrument's temperature shows a diurnal variation at Nevado del Ruiz. The ambient temperature is usually around 0°C in the morning and increases up to 30°C during the day. When looking at the DOAS fit error plotted as a function of ambient temperature (Figure 8.7), one can see a clear dependency of the DOAS fit error on the ambient temperature. At temperatures between 5°C and 20°C the NOVAC reference resulted in smaller DOAS fit errors than the two other methods. One cause for this behaviour are variations of the instrument's calibration and ILF (see Figure 7.6) that both vary strongly at decreasing temperature. While the NOVAC FRS was recorded with the same calibration and ILF as the measurement spectra, the two other methods have references that were recorded at other temperatures. For the Solar Atlas method the mercury emission line used for the convolution of the Chance and Kurucz (2010) Solar Atlas was recorded at a room temperature of 25°C while the fixed Reference was recorded at an ambient temperature of 24°C. An FRS that was recorded with a different ILF (caused, for example, by a different temperature) can lead to a large increase of the DOAS fit error (see Section 7). Between 20°C and 33° all three methods show comparable, low SO_2 fit errors before there is a large increase at a temperature above 33°C. This increase is probably a combination of an increasing dark current at a higher instrument temperature

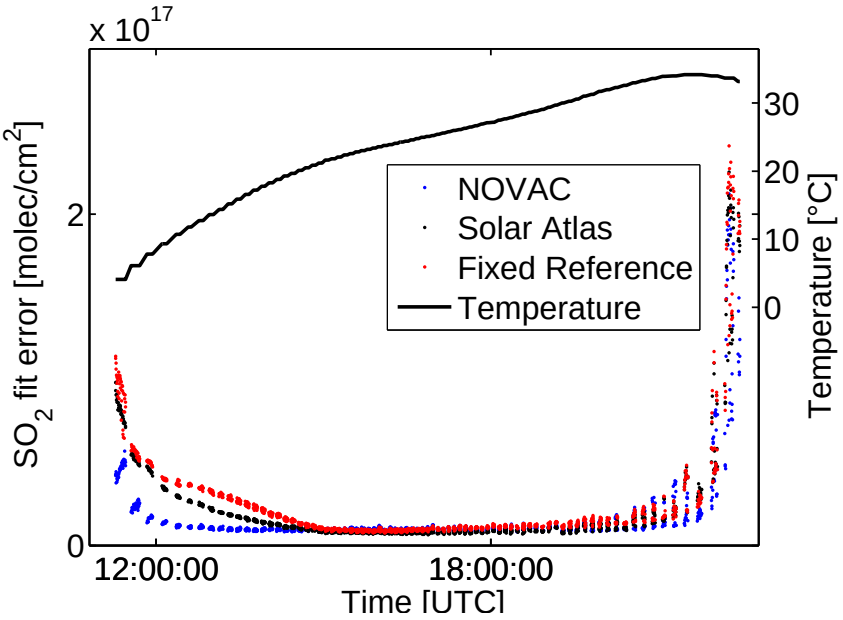

Figure 8.5.: SO_2 fit error of the DOAS fit for the three different methods described in the text as a function of time. Spectra shown here are from instrument D2J2200 on 1 January 2011. The black solid line shows the ambient temperature, the corresponding y-axis is on the right side.

and longer exposure times at high SZA values.

Comparison of the SO_2 column densities

To compare the results from the Solar Atlas evaluation with the NOVAC approach data from the years 2011 and 2012 was evaluated with both methods. As an additional validation, all data was also evaluated using a fixed, gas free FRS recorded with the same instrument. For this gas-free reference a zenith-looking spectrum with a minimal SZA was chosen. The fixed reference spectrum was selected after the two other methods identified it as SO_2 free.

An example of the retrieved SO_2 SCDs is shown in Figure 8.8. This day, 6 March, 2012, cannot be seen as exemplary for the entire data set, but was rather chosen as it nicely shows the main difference between the NOVAC approach and the two other methods. The plot shows the SO_2 SCDs for all spectra, e.g. different viewing directions are plotted subsequently. The Solar Atlas evaluation and the fixed reference show the excellent agreement throughout the complete day, the NOVAC approach shows much lower SO_2 SCDs, especially during the middle of the day. While the Solar Atlas and the fixed reference lead to SO_2 SCDs of up to 4.5×10^{18}molec/cm^2 the NOVAC approach yields much lower SO_2 SCDs ($< 1 \times 10^{18}$ molec/cm^2). On the other hand, when only looking at the variations within one scan (the different scans can be identified by the time gap between two scans) and not at the absolute SO_2 SCDs, one can see that the SO_2 SCDs for all three methods vary in a similar way.

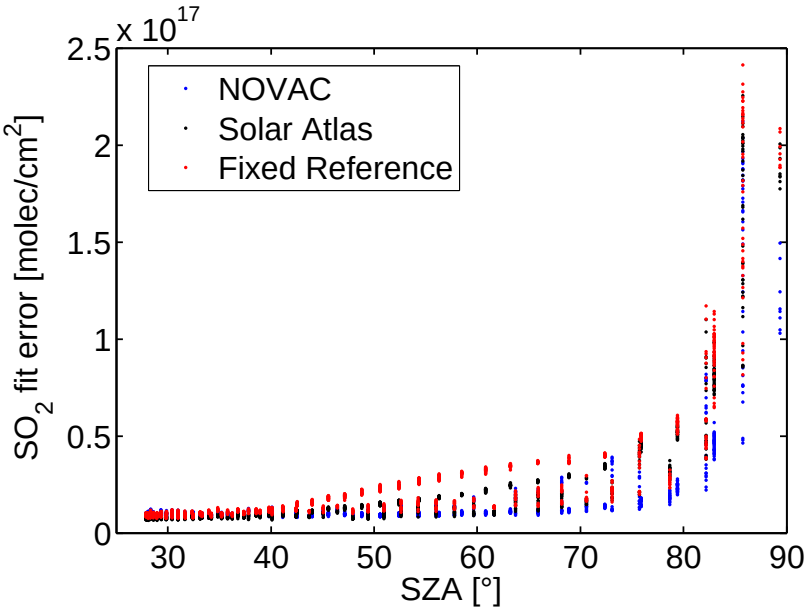

Figure 8.6.: SO_2 fit error of the DOAS fit as a function of solar zenith angle for all three evaluation methods.

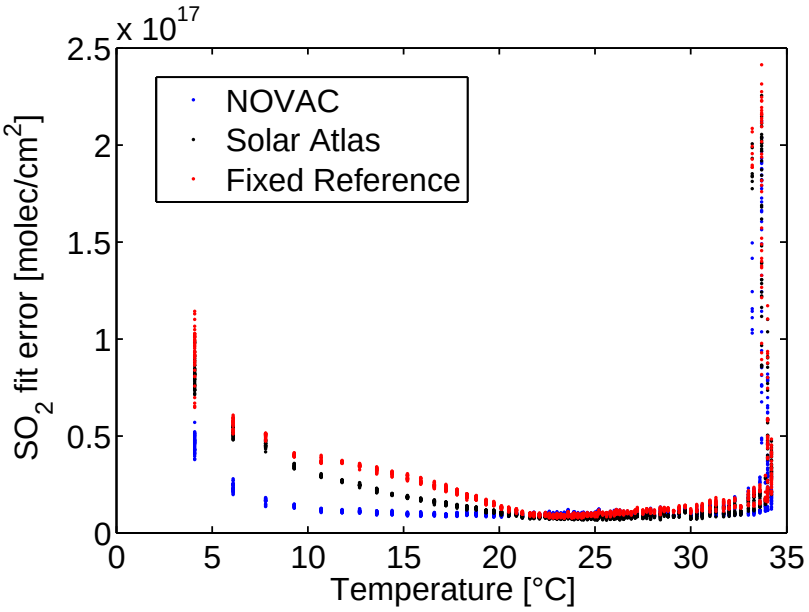

Figure 8.7.: SO_2 fit error of the DOAS fit as a function of ambient temperature for all three evaluation methods.

The explanation for this observation lies in the choice of FRS in the NOVAC evaluation. The NOVAC network uses a zenith-looking spectrum as an FRS. The dSCDs recorded from the NOVAC network are converted to SCDs by subtracting an SO_2 baseline value. The SO_2 baseline, e.g. the SO_2 dSCD for a spectrum that is assumed to be gas free, is found by averaging over the lowest 20% of the retrieved SO_2 dSCD's for each scan (see Chapter 5.2.1 and Galle et al., 2010). However, if volcanic SO_2 is apparent for all viewing directions, the baseline will only correspond to the lowest SO_2 dSCD, which is not gas free in this case. This suggests, that at least in the chosen example, gas was covering the complete surrounding of the instrument, leading to a strong underestimation of the true SO_2 SCD.

Figure 8.9 shows a colour coded histogram of the SO_2 SCDs evaluated with fixed reference (y-axis) plotted against the SCDs evaluated with the Solar Atlas spectrum (x-axis) for instrument D2J2200 (the plots for both instruments can be found in Appendix F). One can see a in general good agreement between the two methods, with only a few data points that deviate from a linear correlation. Most points that differ from a linear correlation between the two evaluation methods are from 2012 and usually at higher SO_2 SCDs. One possible explanation is ash and aerosol during the eruptive phases of Nevado del Ruiz, which negatively influenced the retrieval. As this kind of behaviour was observed for both instruments, investigating the cause for the deviations from a linear relation might help to recover additional information in the spectra in the future.

Looking at the same type of 2D histogram for the Solar Atlas and the NOVAC evaluation (Figure 8.9), one sees a more chaotic behaviour. The NOVAC evaluation never overestimate the SO_2 column density compared to the Solar Atlas evaluation, but leads to lower SO_2 SCDs in many cases. When looking at spectra that were all recorded within the same scan, one can see that the slope of all data is usually similar, but it is shifted towards higher SO_2 SCDs on the x-axis. This structure is caused by the shift of the zero-baseline in the NOVAC evaluation. The few negative SO_2 SCDs that occur in the NOVAC evaluation are caused by scans that sampled the edge of a volcanic plume. In this case the spectra with the lowest 20% SO_2 SCDs cover a large range of values, and the mean value leads to a few spectra with negative SO_2 SCDs.

These findings indicate that volcanic gas plumes, which cover the entire FOV of the NOVAC instruments can negatively influence the results. The next section investigates how frequent the problem of "contaminated" reference spectra is and under which circumstances it appears.

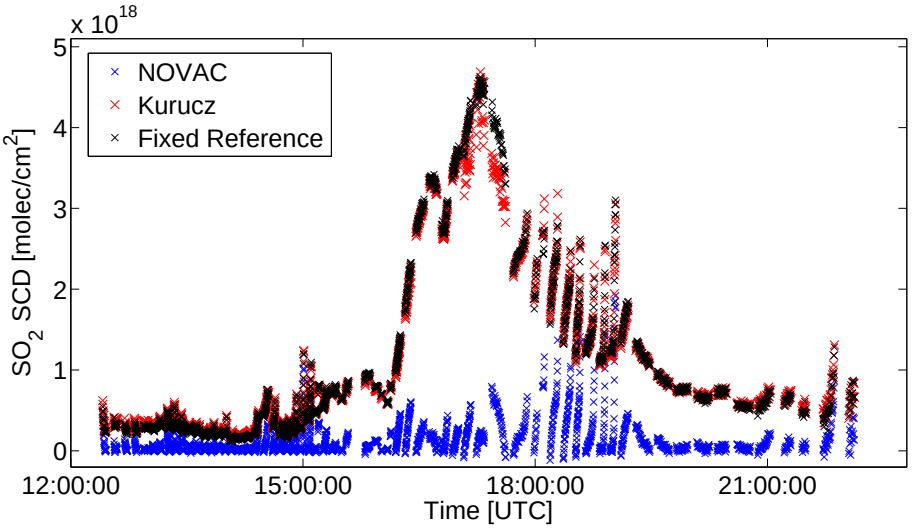

Figure 8.8.: Time series of the SO_2 SCD for instrument D2J2201 on 6 March, 2012. It can be clearly seen, that the NOVAC approach shows lower SO_2 SCDs in especially during the middle of the day, while the two other methods show largely the same SO_2 SCDs.

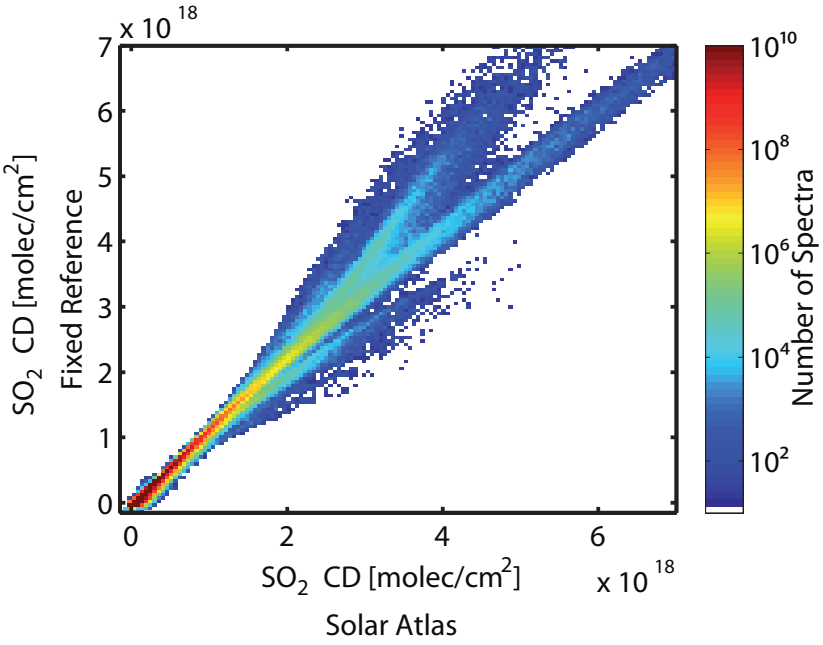

Figure 8.9.: 2D histogram of the SO_2 SCDs retrieved with the Solar Atlas vs. the SO_2 SCDs from a fixed reference spectrum for instrument D2J2200. The number of spectra in each interval is colour-coded with a logarithmic scale.

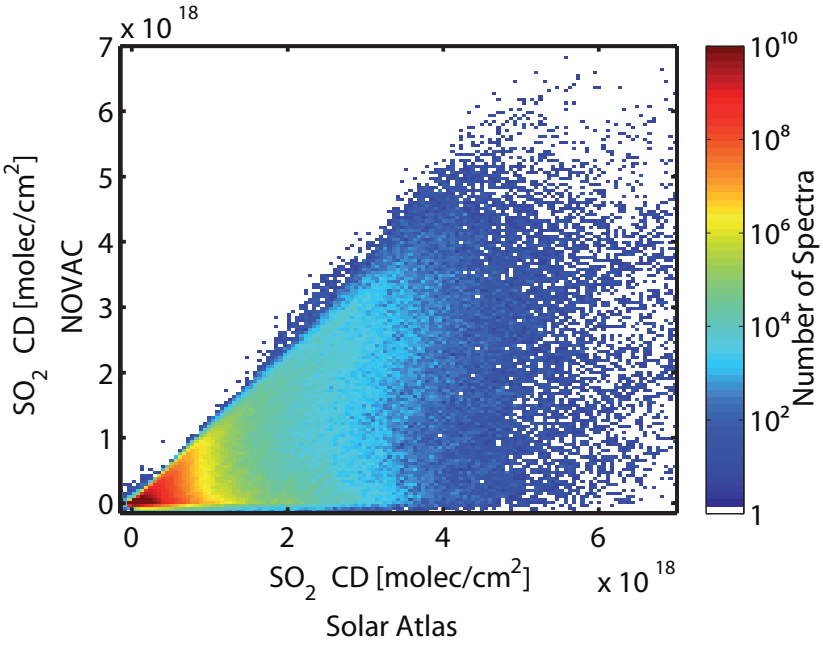

Figure 8.10.: 2D histogram of the SO_2 SCDs retrieved with the Solar Atlas vs. the SO_2 SCDs from the NOVAC approach for instrument D2J2200. The number of spectra in each interval is colour-coded with a logarithmic scale.

8.2.2 Underestimation of the SO_2 content

Underestimating the true SO_2 SCD, as described in Section 8.2, leads to significant problems. From a forecasting standpoint it is crucial to identify "contaminated" background spectra. If background spectra are more frequently contaminated during episodes of increased SO_2 emissions, variations of the volcanic activity can easily remain undetected. Contaminated reference spectra will also result in an underestimation of global SO_2 emissions. Recent comparisons between NOVAC instruments and measurements from satellites support this thesis (McCormick et al., 2013). These measurements showed larger SO_2 emission rates from satellites. For the BrO/SO_2 ratios a contaminated background spectrum leads to a reduction of the signal-to-noise ratio, but not necessarily to erroneous results. A contaminated background spectrum only leads to wrong results if the BrO/SO_2 ratio in the background spectrum differs from the measurement spectrum.

To investigate how often contaminated background spectra influence the measurements, the underestimation U of a scan was defined as:

$$U = \frac{\overline{S_{SO_2,Solar}} - \overline{dS_{SO_2,NOVAC}}}{\overline{S_{SO_2,Solar}}}, \tag{8.3}$$

where $\overline{S_{SO_2,Solar}}$ is the mean SO_2 SCD for all spectra from one scan for which the Solar Atlas evaluation leads to an SO_2 SCD above 5×10^{17} molec/cm^2.

$\overline{dS_{SO_2,NOVAC}}$ is the mean SO_2 dSCD from the NOVAC evaluation for the same spectra. An underestimation U of 1 means that the Solar Atlas evaluation finds significant amounts of SO_2, while the NOVAC evaluation does not find any SO_2. An underestimation of 0 means that both retrieval methods find the same amount of gas. To rule out problems with the Solar Atlas SO_2 retrieval, U was only investigated for scans with an SZA below 75° and a χ^2 below 0.02.

Several variables were checked, to find if U depends on them. No correlation between U and the viewing direction of the telescope, SZA and wind direction was found. The only clear dependency that was found, is that U depends on the wind speed. Figure 8.11 shows histograms of the underestimation for all scans, and for various wind speed intervals. Figure 8.11 **a** shows the histogram of U for all scans. While most of the scans are centred around an underestimation of 0 there are still $\approx 30\%$ of the scans that have an underestimation above 50%. **b** shows U for low wind speeds, below 5 m/s. There are almost as many scans not seeing any SO_2 as there are scans that measure the SO_2 content correctly. 44% of the spectra have an underestimation above 50%. **c** shows all scans with wind speeds between 5 and 10 m/s and **d** scans with wind speeds above 10 m/s. One can see, that higher wind speeds lead to a reduction of scans with a higher U. At wind speeds above 10 m/s there are only 10% of the spectra with $U > 0.5$.

One possible explanation for the observed behaviour are plumes that spread more at low wind speeds, while they are transported away from the mountain in a more concentrated manor, if the wind speed is high. While this explanation is in a way obvious, it is still unexpected how frequently these problems occur, especially when considering, that 5 m/s is still far away from very low wind speeds.

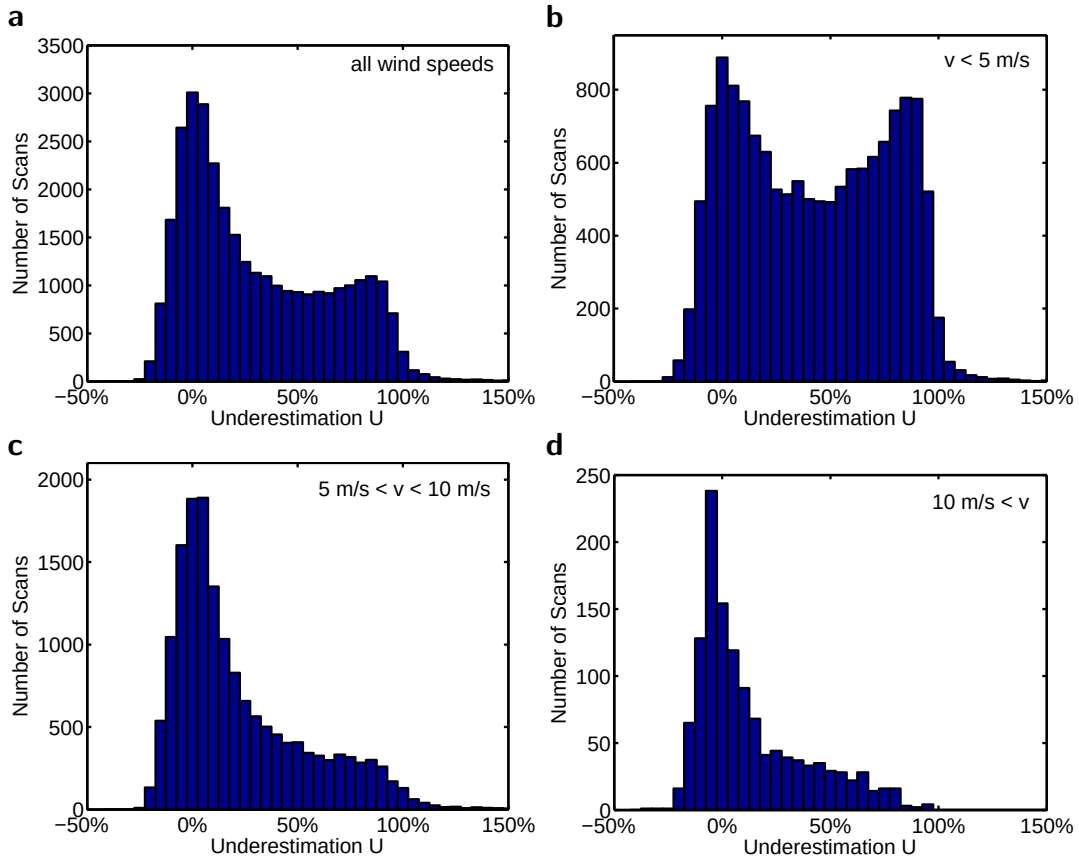

Figure 8.11.: Underestimation of the SO_2 column density when comparing the results from the Solar Atlas with the NOVAC approach. **a** All scans, **b** Scans with a wind speeds below $5\,\mathrm{m/s}$, **c** Scans with wind speeds between $5\,\mathrm{m/s}$ and $10\,\mathrm{m/s}$, **d** Scans with wind speeds above $10\,\mathrm{m/s}$.

Science never solves a problem
without creating ten more.

G.B. Shaw

9 Conclusions and Outlook

9.1 Conclusions

In this thesis, two techniques for the optical remote sensing of volcanic gas emissions were investigated. SO_2 camera measurements were performed in order to obtain high time-resolution SO_2 emission rates (frequency $\approx 1\,\mathrm{Hz}$). Using a co-aligned DOAS system greatly improved the calibration of the SO_2 camera. The frequency content of the SO_2 emission rates was examined with help of the wavelet analysis technique. On the other hand, spectra recorded by the Network for Observation of Volcanic and Atmospheric Change were evaluated for BrO/SO_2 ratios. An automatic evaluation algorithm was written to evaluate spectra from the NOVAC database for BrO and SO_2 column densities. A time series covering four years of interesting activity at Nevado del Ruiz was created and interpreted in a volcanological context. Several potential error sources were identified and their magnitude was estimated.

Conclusions related to the SO_2 camera

During the work on this thesis, two different calibration methods for the SO_2 camera, calibration cells and a co-aligned DOAS system, were critically compared using measurements at Popocatépetl, Mexico. Afterwards SO_2 emission rates were calculated for measurements at Popocatépetl and Stromboli, Italy. The frequency content of these SO_2 emission rates was further investigated by means of the wavelet analysis technqiue.

The most important results for the comparison of the two SO_2 camera calibration methods are listed below:

- The comparison of the two calibration methods exposed the major drawback of calibration cells. Calibration cells only show the influence of pure SO_2 on the apparent absorbance. However, in reality several other effects, like ash or plume condensation, can influence the SO_2 camera calibration. Under a favourable geometry and for an aerosol-free plume the difference between cell and DOAS calibration was only 6%. On a different day, a combination of plume aerosol conditions, illumination and viewing geometry led to deviations of up to 60% due to significant aerosol scattering and absorption effects. It should be noted, though, that even for the day with the largest deviations from calibration cells the plume was not opaque, indicating that even larger errors can occur. These effects are not taken into account when calibrating the SO_2 camera with calibration cells and can thus largely falsify the obtained SO_2 emission rate. Measurements at Stromboli, Italy, showed similar deviations between the two calibration methods.

- For the DOAS calibration it was shown in a sensitivity study that the SO_2 camera calibration is sensitive to the exact size, shape and position of the assumed DOAS FOV. These parameters should preferably be measured in the laboratory. But there are cases where the DOAS FOV is not known. For example, if it changed during transport to or from the volcano. It was shown that for these cases the spectrometer's FOV within the SO_2 camera image can be accurately determined by comparing a time series of the camera's AA with a time series of SO_2 column densities from the spectrometer. An IDOAS was used at Popocatépetl to verify that the calibration curve obtained from the co-aligned NFOV-DOAS system can be used for the complete FOV of the camera system.

- Several other potential problems (besides the one described above) were determined for calibration with calibration cells. Circular reflection structures were observed in calibration cell images that resulted from multiple reflections on the walls of the calibration cell. These reflections can influence the measured apparent absorbance and thus lead to an erroneous calibration curve.

The sensitivity of the SO_2 camera was long suspected to increase with increasing distance from the optical axis (e.g. Kern et al., 2010b). This effect is caused by a wavelength shift towards lower wavelengths when the band-pass interference filters used in the SO_2 camera are illuminated non-perpendicularly. During this work it was experimentally shown that the SO_2 camera used at Popocatépetl had an increase of sensitivity of up to 85% towards the corners of the detector. Images of calibration cells can be used to characterise and to correct for this issue.

SO_2 emission rates were calculated for the measurements at Popocatépetl and Stromboli. At Popocatépetl the mean SO_2 emission rates varied between 5.7 and 15 kg/s during the three days. Large variations of the SO_2 emission rates on short time scales were observed. At Stromboli a mean SO_2 emission rate of 1.1 kg/s was measured.

As a first step towards a volcanological interpretation of the high time-resolution SO_2 camera measurements, the frequency content of the signal was examined. The wavelet-analysis technique was applied to the SO_2 emission rates from Popocatépetl and Stromboli in order to find periodicities in the signal. Several different periodicities were found at Popocatépetl. At Stromboli two dominant periodicities of 2 – 3 minutes and 5 – 6 minutes were observed. These frequencies were compared to frequencies found in the sparse literature on this topic.

Conclusions related to the NOVAC BrO evaluation

This dissertation has shown that the spectra recorded by the Network for Observation of Volcanic and Atmospheric Change (NOVAC) can be evaluated for BrO, for which the instruments discussed here were not designed. An algorithm was developed to automatically evaluate spectra from the NOVAC database for BrO and SO_2. This algorithm is based on previous work by Vogel (2011). Spectra were pre-evaluated for SO_2 with a zenith-looking spectrum. Afterwards, a volcanic plume region and a gas-free reference region were identified and spectra from these regions were co-added. The resulting spectra have a higher signal-to-noise ratio and were evaluated for BrO and SO_2 using the DOAS method.

As a case study, data from Nevado del Ruiz, Colombia that was recorded by type 1 NOVAC instruments was evaluated for BrO and SO_2. The BrO fit error was further improved by co-adding spectra from different scans as well as from different viewing directions. The retrieval error decreased as expected by photon statistics; it decreased proportional to $1/\sqrt{N}$, where N is the number of scans, indicating that the BrO retrieval is still limited by insufficient radiation intensity. The average BrO fit error after co-adding spectra from four scans was $\approx 1.1 \times 10^{13}$ molec/cm^2 for both instruments. This is an excellent DOAS fit error for the simple instruments at Nevado del Ruiz.

A time series covering four years of interesting volcanic activity (November 2009 to June 2013) at Nevado del Ruiz was created. The BrO/SO_2 ratio is constant for almost one year during 2011 with BrO/SO_2 ratios of $\approx 4-5\times10^{-5}$. In the beginning of 2012, the BrO/SO_2 ratio exhibits a sharp drop to lower values of $1-2\times10^{-5}$ several months before an eruption on 30 June 2012. Assuming that bromine is less soluble than sulphur this decrease of the BrO/SO_2 ratio was interpreted as differential degassing during the magma's ascent. Additionally the data obtained at Nevado del Ruiz was used to investigate the BrO formation in the atmosphere. The BrO/SO_2 ratio was found to be constant between approximately 8 – 40 minutes after release into the atmosphere. This result shows a slower BrO formation than other studies at Etna and Pacaya, however, the BrO formation at Nevado del Ruiz is still faster than theoretical studies predict.

The influence of radiative transfer on the retrieved BrO/SO_2 ratios was investigated with several approaches.

- As a most simplistic approach, both trace gases were evaluated in different wavelength ranges. The choice of wavelength range did change the retrieved SO_2 and BrO column densities, but there was a linear relationship between the results obtained at different wavelengths. This means that variations of the BrO/SO_2 ratio were similar for all wavelength ranges, even though the absolute value did change.

- As a second approach to assess the influences of radiative transfer model calculations using the 3D RTM program McArtim were performed. For a cloudless atmosphere a volcanic plume was simulated and BrO and SO_2 column densities were simulated for lateral distances of up to 6 km between instrument and plume. An increasing distance between instrument and volcanic plume led to a small overestimation of less than 12% for the BrO/SO_2 ratio. Different cloud layers were simulated. Clouds with an optical density of 4 or 12 (for an upward looking instrument) were simulated above, below and at the same height as the volcanic plume. The results showed that the variations of the BrO/SO_2 ratio were below 8% if the SO_2 column density was simulated at 315.39 nm. These results indicate that the BrO/SO_2 ratio is extraordinarily robust against influences of radiative transfer.

- A third approach investigated whether existing methods to detect clouds from MAX-DOAS measurements can be applied to spectra from NOVAC. Three days with different cloud conditions were compared, and it was found that variations of the colour index and the radiation intensity can be used to identify clouds. Clouds led to an increase in radiation intensity and the colour index (radiation intensities at 329 nm/381 nm) had lower values when clouds were present. It was also found that the settings used when recording spectra in NOVAC currently prevent a successful O_4 retrieval.

Temperature-induced changes in the instrument line function (ILF) and the wavelength-pixel-mapping on the DOAS retrieval were investigated in Chapter 7. DOAS retrievals with synthetic spectra showed that the uncertainty of the BrO/SO_2 ratio due to variations of the ILF was below 15% if the same ILF was used for the measurement and Fraunhofer reference spectrum (FRS) (absorption cross sections were convolved with a different ILF). Using a different ILF for measurement and FRS led to a large increase of the residual structure and inhibited the BrO evaluation. These model studies also revealed that the wavelength range between 310 – 326.8 nm is more robust than other wavelength ranges for the SO_2 evaluation in case of an insufficiently well-known ILF.

The theoretical SO_2 results were verified experimentally by recording spectra with calibration cells covering the spectrometer's FOV. The instrument's temperature was adjusted in order to obtain variations of the ILF. The DOAS evaluation of these spectra also indicated that the wavelength range between 310 – 326.8 nm is ideal for the SO_2 DOAS evaluation if the ILF varies during measurements. It should be noted though, that the choice of the ideal wavelength range always depends on the specific situation. The wavelength range suggested by Vogel et al. (2011) has advantages regarding radiative transfer for an instrument with a controlled temperature.

Conclusions related to using a solar-atlas as an FRS

In Chapter 8, a DOAS retrieval using a high-resolution Solar Atlas (Chance and Kurucz, 2010) as an FRS was investigated. Due to the large optical density of SO_2 in volcanic plumes, the DOAS analysis was found to be possible without an FRS from the same instrument. The advantage of this method is that it assures that the FRS is free of volcanic absorbers. An almost constant (but wavelength-dependent) structure was found in most residuals. This structure was suspected to be an instrumental effect caused by the quantum efficiency of the spectrometer. It was included in the DOAS fit as a pseudo-absorber. After including this pseudo-absorber a very good fit quality was obtained for SZA's below 70°. The DOAS fit error was comparable to (in some cases even lower than) the DOAS fit error for an evaluation with a regular FRS. At larger SZA's problems with the instrument's temperature and with large column densities of stratospheric absorbers led to a lower fit quality and an increase of the DOAS fit error. When comparing the obtained SO_2 column densities from these two approaches, it was found that the Solar Atlas method showed similar SO_2 column densities as the NOVAC evaluation in some cases. However, in many cases the Solar Atlas method led to higher SO_2 column densities than the NOVAC evaluation. It was found that the NOVAC evaluation often underestimates the true SO_2 column densities when the complete instrument is surrounded by volcanic gas and thus the reference spectra are not free of volcanic absorbers. For 30% of the spectra that contained a significant amount of SO_2 according to

the Solar Atlas method, the NOVAC method underestimated the SO_2 content by more than 50%. Comparing the underestimation with different parameters revealed that this problem dominantly occurs at low wind speeds. At wind speeds below 5 m/s 44% of the spectra underestimated the SO_2 content by more than 50%. On the other hand, at wind speeds above 10 m/s only 10% of the spectra underestimated the SO_2 content by more than 50%.

9.2 Outlook

SO_2 camera outlook

In the future the SO_2 camera will hopefully mature from a technqiue that can be used during single measurement campaigns to a technique that allows operational monitoring. One of the first permanently installed SO_2 cameras was set up by our group at Popocatépetl, Mexico in 2011. In 2013 other groups installed SO_2 camera systems permanently at Stromboli and Kilauea, Hawaii (C.Kern, personal communication). It should be noted, though, that other techniques like the scanning DOAS networks NOVAC Galle et al. (2010) and FLAME (Burton et al., 2009) are better suited to monitor the magnitude of SO_2 emission rates. The DOAS technique is less vulnerable in terms of measurement geometry and radiative transfer issues.

Yet the SO_2 camera can be a valuable supplemental tool in a volcanologist's toolbox. Under suitable measurement conditions it produces high time-resolution measurements that can reveal the frequency content (currently up to 1 Hz) of the SO_2 emission rate. To use SO_2 cameras as an additional monitoring tool it is important to gather baseline values of typical frequencies involved in degassing processes. A larger data set can help answer the question of whether periodicities due to the degassing process change with volcanic activity. The available data from relatively short measurement campaigns can only be seen as a snapshot of the degassing signal.

A higher level of standardisation can help to establish this relatively new technique. The Imaging Volcanic Plume Workshop, held on Stromboli in June 2013, served as an important step towards this goal. Several groups performed simultaneous SO_2 camera measurements of the plume of Stromboli. These measurements will be used to compare different SO_2 camera systems and data evaluation procedures. A manuscript covering the results of the SO_2 camera comparison will be submitted soon (Kern et al., 2014, in preparation) in preparation). The advances on SO_2 camera calibration with a DOAS system made during this thesis will also help to accomplish this task. The DOAS calibration makes the SO_2 camera less vulnerable to influences of ash and aerosol and thus leads to more reliable SO_2 emission rates.

As the SO_2 camera technique is relatively new various technical improvements are currently being developed. Applying optical-flow models (see, for example Jähne, 2012) can improve the accuracy of the SO_2 emission rates and result in more reliable results in particular during explosive phases of activity. Using several SO_2 cameras that are distributed around a volcano allows for plume tomography. Initial attempts have been made with data from the Plume Imaging Workshop, which showed promising results. However, meaningful SO_2 camera tomography requires the presence of several cameras distributed

around the volcano. To make plume tomography feasible, SO_2 cameras have to be inexpensive. At this time most SO_2 cameras use expensive UV-sensitive CCD detectors, which prevent the installation of several SO_2 cameras at one volcano. One possible development towards achieving inexpensive SO_2 cameras is the use of luminous coatings. A luminous coating applied to a window or on the detector of a non-UV-sensitive, inexpensive camera system can convert incident UV radiation to visible light. This approach showed promising results for an inexpensive SO_2 camera system (Klein, 2012). Applying such a coating on Web cam detectors could result in even smaller, very inexpensive SO_2 cameras.

Another possibility would be to move the SO_2 camera technique from the UV to other spectral ranges, in particular the IR (Prata and Bernardo, 2014; Watson et al., 2004). Prata and Bernardo (2014) recently introduced an IR SO_2 imaging system and applied it at Stromboli and Etna. While IR cameras have different problems than UV systems (e.g. they need to be accurately temperature calibrated) they can solve parts of the radiative transfer influences that exist for UV SO_2 cameras. Additionally an IR SO_2 will be less influenced by clouds and could perform measurements during the day and at night, thus making it a good choice for monitoring applications.

The goal in employing all the above-mentioned technological and measurement technique related improvements is to obtain a better understanding of volcanic systems. Incorporating SO_2 cameras into other volcanological data sets is crucial to achieving this goal. Some initial steps to use SO_2 camera measurements to investigate processes in a volcano have been made by Holland et al. (2011); Nadeau et al. (2011); Pering et al. (2014); Tamburello et al. (2012, 2013). However, most of these studies used only qualitative arguments during interpretation. Besides comparing SO_2 camera measurements with other geophysical parameters, linking these measurements with theoretical models of volcanic processes can help to improve our understanding of processes occurring at depth.

NOVAC outlook

Although it has been shown in this thesis that data from NOVAC can be evaluated for BrO and SO_2, several technical tasks could further improve the quality of the BrO/SO_2 ratios. Some of these tasks were identified during this thesis.

- Variations in the instrument's temperature were found to produce errors of up to 15% on the BrO/SO_2 ratio. Different methods for finding the instrument slit function showed promising results. Implementing one of these methods to find the ILF could further improve the quality of the DOAS retrieval. This can be done by using a subset of the data (e.g. one year for each instrument) to determine the temperature dependency of the ILF and build a lookup table. Before convolving the trace gas cross sections the ILF corresponding to the instrument's temperature can be looked up and used for convolution.

- Chapter 8 showed that a significant amount of spectra suffers from a contaminated Fraunhofer reference spectrum. While this does not necessarily influence the retrieved BrO/SO_2 ratios it does certainly lead to a strong decrease in the signal-to-noise ratio. The Solar Atlas evaluation method that was introduced in Chapter 8 can be used to identify contaminated reference spectra. A database of plume-free reference spectra could be created and used to evaluate spectra with gas-free reference spectra. More research has to be conducted, however, into which parameters dominantly influence the DOAS retrieval. While it is certain that reference spectra should be recorded at the same instrument temperature, other effects (SZA, cloud cover) should be taken into account as well. Implementing this approach would result in a larger amount of data that can be evaluated and thus much better statistics for the variations in the BrO/SO_2 ratios.

- A more sophisticated plume-detection algorithm could further improve the quality of the NOVAC data. At this time, 10 adjacent spectra with low SO_2 content are defined as a reference region and 10 adjacent spectra with the highest average SO_2 content are chosen as the plume region. Using a more sophisticated routine to determine the plume and reference region has two advantages. Using more spectra for the plume and reference region increases the signal-to-noise ratio and thus leads to more reliable results. Additionally having a well-defined plume might make it possible to investigate chemistry effects like the increase of the BrO/SO_2 ratio towards the plume edges (as observed by Bobrowski et al., 2007; Louban et al., 2009). Of course this point should be combined with the Solar Atlas evaluation mentioned above.

In this thesis, data from Nevado del Ruiz were evaluated as one case study. However, the NOVAC database currently contains data from 26 different volcanoes. The algorithm used for data evaluation is largely automatic and can be used to evaluate data from other NOVAC volcanoes. This will allow for continuing research in two directions: 1) studies of atmospheric chemistry and 2) volcanology.

- BrO/SO_2 ratio in combination with SO_2 emission rates can be used to improve estimates of the global BrO emission rates from volcanoes into the atmosphere. The different volcanoes in NOVAC can be used to investigate the BrO formation (as shown in Chapter 5) in different geological and atmospheric conditions.

- The resulting BrO/SO_2 time series can be used to investigate the possibility of using BrO/SO_2 ratios as tracers of volcanic activity. Gas emission data (both BrO/SO_2 ratios and SO_2 emission rates) from NOVAC can be correlated with other geophysical parameters (e.g. deformation or seismic measurements) in order to find a volcanological interpretation of the observed BrO/SO_2 ratios. The DFG project "Analysis of spectroscopic long-term volcanic emissions of SO_2 and BrO data with respect to underlying geophysical processes" was recently funded and will begin in summer/autumn 2014. This project contains funding to visit the local observatories and thus allows the interpretation of BrO/SO_2 ratios in close collaboration with the local observatories.

Currently variations of the BrO/SO_2 ratio are interpreted empirically. The interpretation of BrO/SO_2 ratios can benefit from future research on the solubility of bromine in various melts. While the solubility of sulphur has been studied to some extent, only very sparse information exists for bromine. However, this information is crucial to overcome empirical interpretations and to obtain a true understanding of variations of the BrO/SO_2 ratio.

A

Appendix A

Radiative transfer correction for SO_2 emission rates from Popocatépetl

The SO_2 emission rate measurements at Popocatépetl (see Section 4.5) were performed at a distance L of 6–8 km from the volcanic plume. Therefore, the measured SO_2 column density is influenced by the light dilution effect (Kern et al., 2010a). A correction for this effect as suggested in Bluth et al. (2007) and Vogel et al. (2011) was applied to the column densities S such that:

$$S(L) = S_0 \cdot e^{-\epsilon \cdot \Delta L} \tag{A.1}$$

ϵ is an extinction coefficient and depends on the physical state of the atmosphere. We used a value of $\epsilon = 0.057\,\mathrm{km}^{-1}$ which was derived by Vogel et al. (2011) for a wavelength of 315.4 nm for measurements of the plume of Popocatépetl under comparable conditions. However, due to the difference in measurement set-ups between this study and that of Vogel et al. (2011) (especially regarding the altitude of the detector), this extinction coefficient represents a lower boundary for the influence of the light dilution effect. Solving Equation A.1 for S_0 therefore yields a conservative estimate of the SO_2 column density in the plume.

B

Appendix B

Supplements for the BrO formation in the atmosphere

Bromine is not released from the volcano in form of BrO but mainly as HBr. The formation of BrO after relase into the atmosphere was investigated in Section 5.3.4. To investigate the BrO formation at Nevado del Ruiz, the BrO/SO_2 ratios were sorted into different intervals depending on their time since release into the atmosphere. The number of BrO/SO_2 ratios in each interval is shown in Figure B.1. The intervals, the number of spectra per interval and the average BrO/SO_2 ratio are listed in Table B.1.

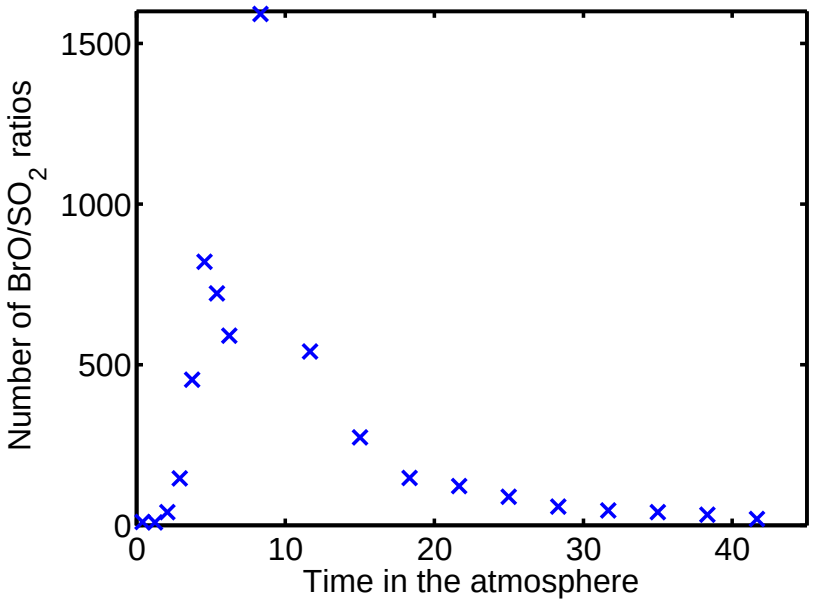

Figure B.1.: Number of scans for each interval in the investigation on the BrO formation in Section 5.3.4.

Time Inverval [s]	Number of Scans	BrO/SO_2 ratio $[10^{-5}]$
0 - 50	10	2.703
50 - 100	8	3.160
100 - 150	40	1.192
150 - 200	145	1.868
200 - 250	453	1.472
250 - 300	820	1.929
300 - 350	721	2.321
350 - 400	590	2.837
400 - 600	1592	3.080
600 - 800	540	3.150
800 - 1000	273	3.299
1000 - 1200	147	3.211
1200 - 1400	122	3.566
1400 - 1600	89	3.463
1600 - 1800	58	2.815
1800 - 2000	46	3.198
2000 - 2200	40	3.167
2200 - 2400	32	2.986
2400 - 2600	19	1.842

Table B.1.: Time intervalls used for the investigation of the time in the atmosphere of the volcanic plume, the number of scans per interval and the mean BrO/SO_2 ratio.

C

Appendix C

Results for the trace gas evaluation in different wavelength ranges

To investigate the influences of radiative transfer on the retrieved BrO/SO_2 ratios both trace gases were evaluated in different wavelength ranges (see Section 6.1). This appendix shows the results from the SO_2 and BrO evaluation in different wavelength ranges. Figures C.1 and C.2 show correlation plots for BrO and SO_2 evaluated in different wavelength ranges for the instruments D2J2200 and D2J2201, respectively. The resulting BrO/SO_2 time series for the possible combinations of evaluation ranges are shown in Figures C.3 and C.4.

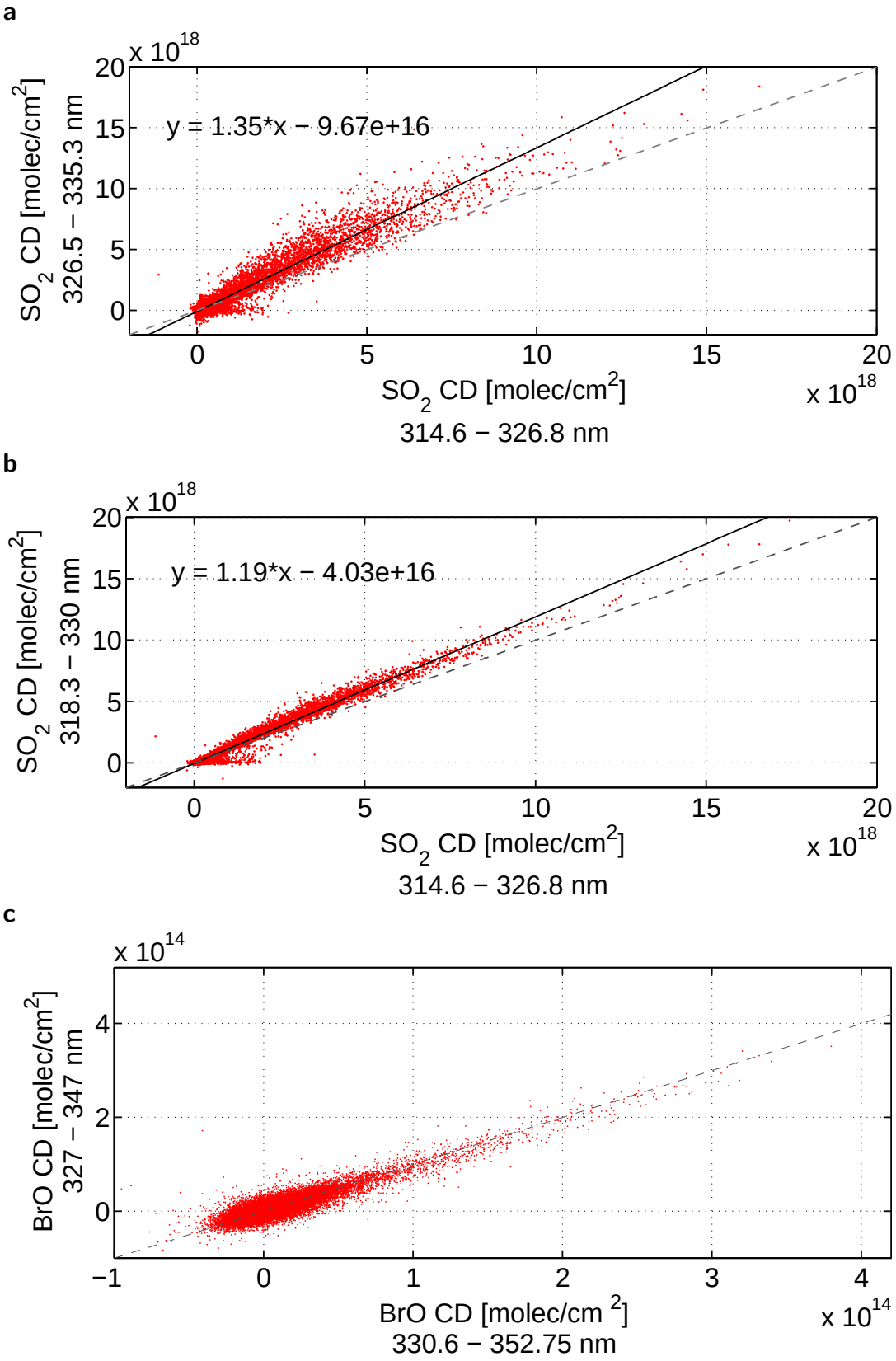

Figure C.1.: Correlation plot for different evaluation ranges for SO_2 and BrO for spectrometer D2J2200. Top: SO_2 314.6 - 326.8 nm vs. 326.5 - 353.5 nm, middle: SO_2 314.6 - 326.8 nm vs. 318.3 - 330.0 nm, bottom: BrO 330.6 - 325.75 nm - 327 - 347 nm. The grey-dashed line shows the identity function.

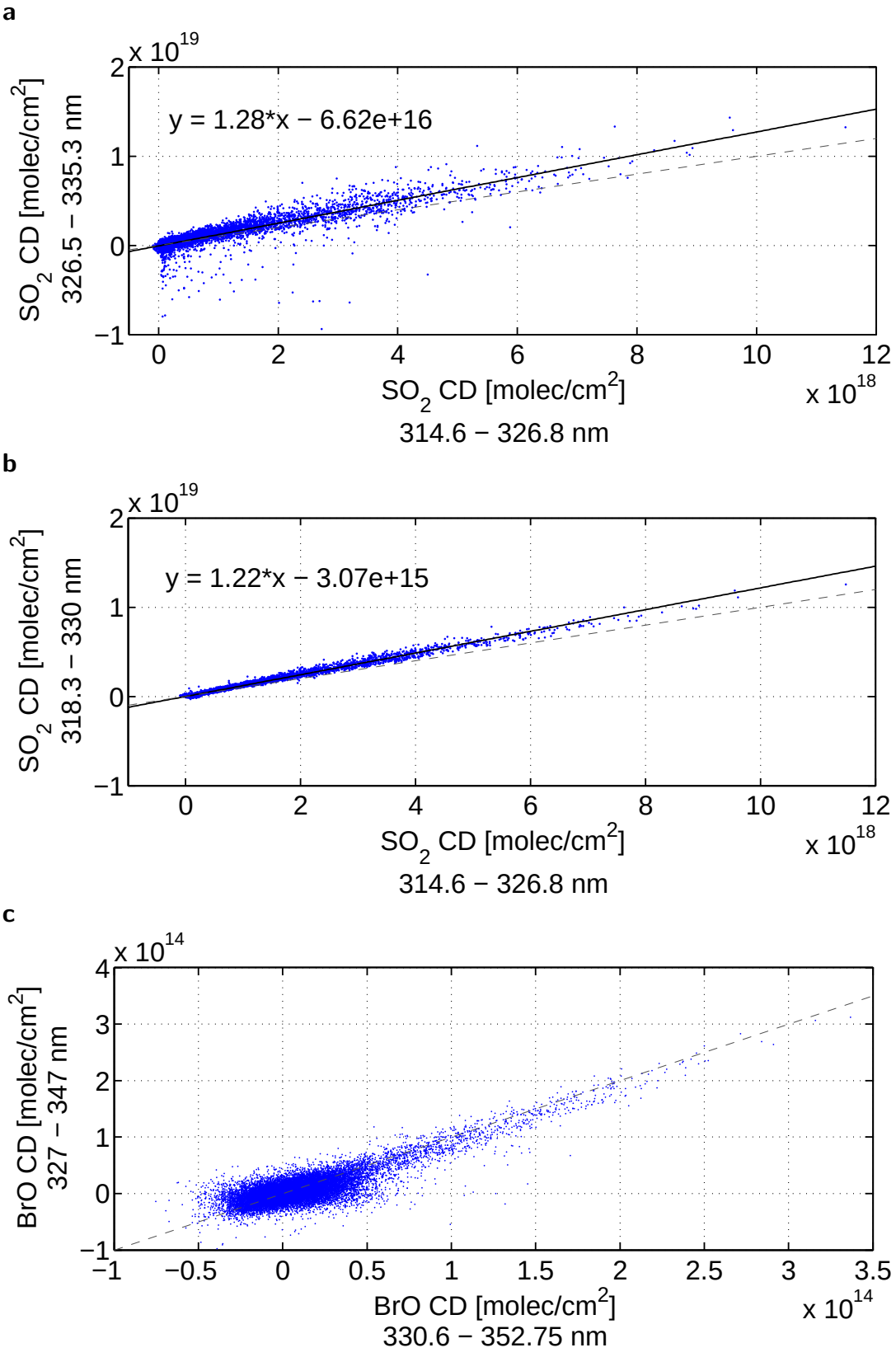

Figure C.2.: Correlation plot for different evaluation ranges for SO_2 and BrO for spectrometer D2J2201. Top: SO_2 314.6 - 326.8 nm vs. 326.5 - 353.5 nm, middle: SO_2 314.6 - 326.8 nm vs. 318.3 - 330.0 nm, bottom: BrO 330.6 - 325.75 nm - 327 - 347 nm. The grey-dashed line shows the identity function.

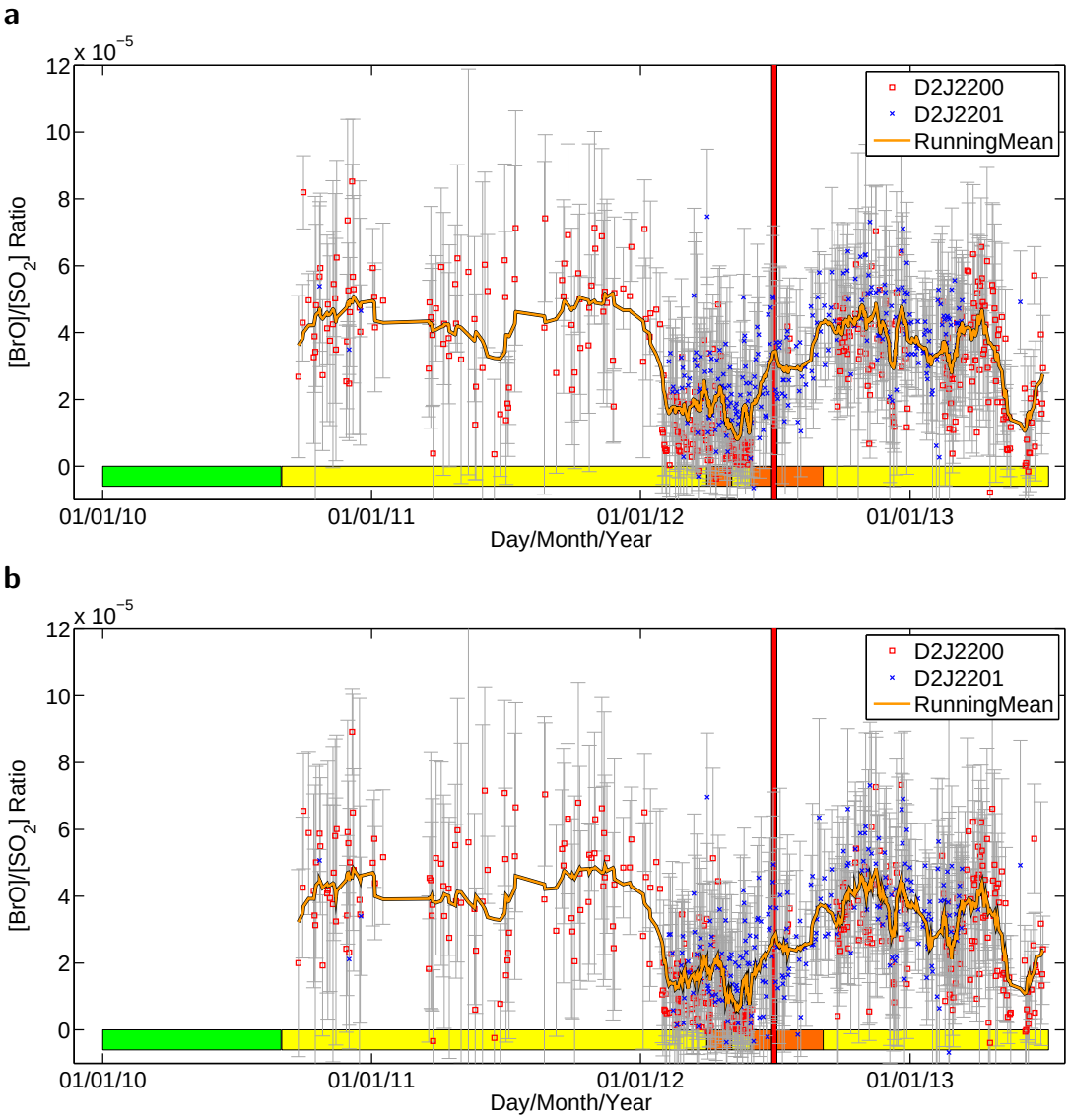

Figure C.3.: BrO/SO_2 ratio at Nevado del Ruiz for spectra evaluated in different wavelength ranges. **a** *Set 1* SO_2: 314.6 – 326.8 nm, BrO: 330.5 – 352.75 nm; this are the standard evaluation ranges used in the rest of this thesis **b** *Set 2* SO_2: 314.6 – 326.8 nm, BrO: 327 – 347 nm.

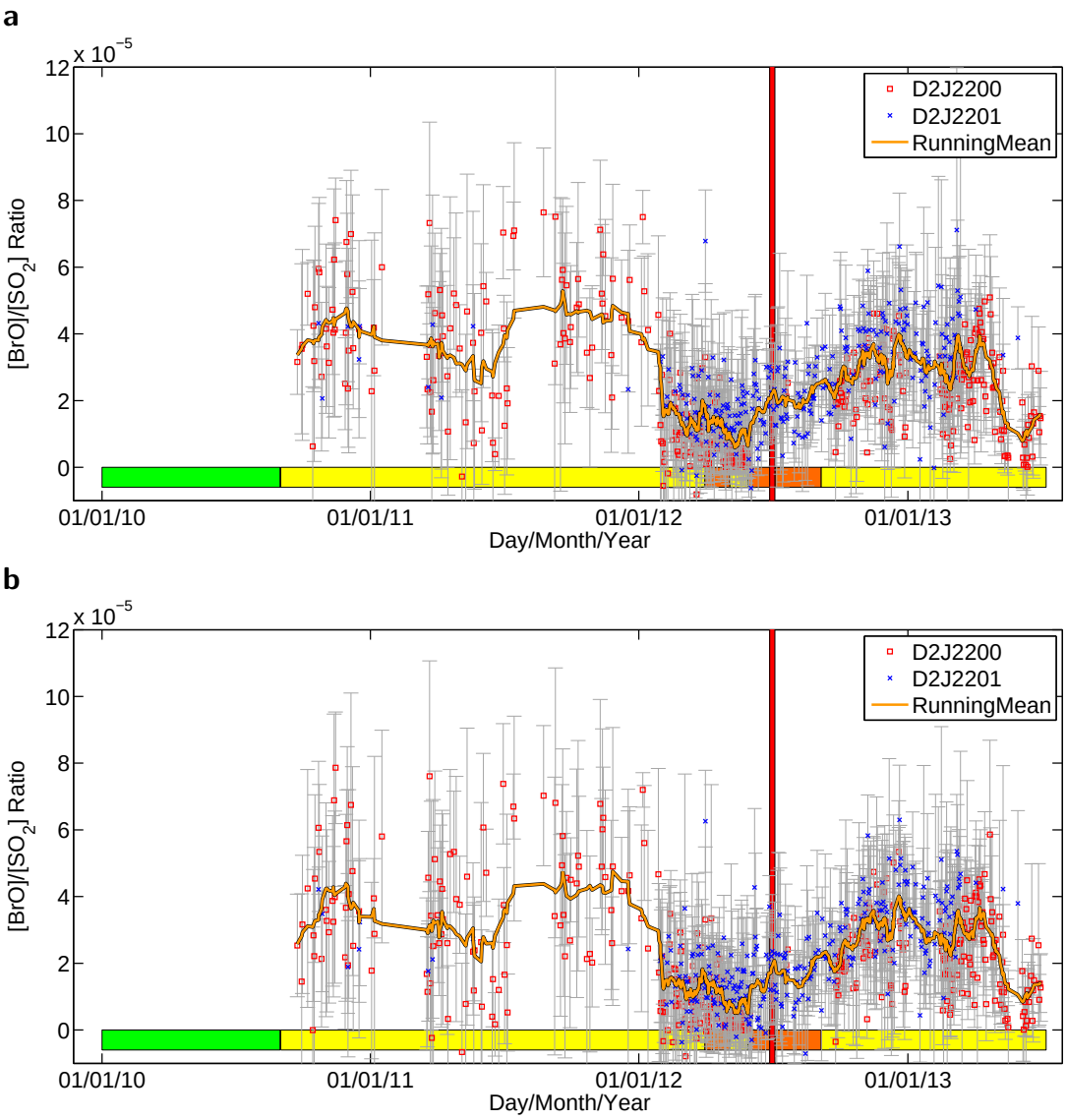

Figure C.4.: BrO/SO_2 ratio at Nevado del Ruiz for spectra evaluated in different wavelength ranges. **a** *Set 3* SO_2: 326.8 – 353.5 nm, BrO: 330.5 – 352.75 nm **b** *Set 4* SO_2: 326.8 – 353.5 nm, BrO: 327 – 347 nm

D

Appendix D

McArtim profiles used for the RTM calculations

In Section 6.2 radiative transfer calculations using the RTM program McArtim were used to assess the influences of an increasing distance between instrument and volcanic plume and clouds. Besides the volcanic absorbers SO_2 and BrO other atmospheric trace gases that can influence the radiative transfer in the wavelength range of interest were used in the McArtim simulations. The profiles for O_3, O_4, NO_2 and the temperature and pressure profiles, that were used in the simulations are shown in Figure D.1. These profiles were taken from the SCIATRAN database (Rozanov et al., 2005). The profiles for a latitude of 5 N in the month of April were chosen, as Nevado del Ruiz is located at this latitude.

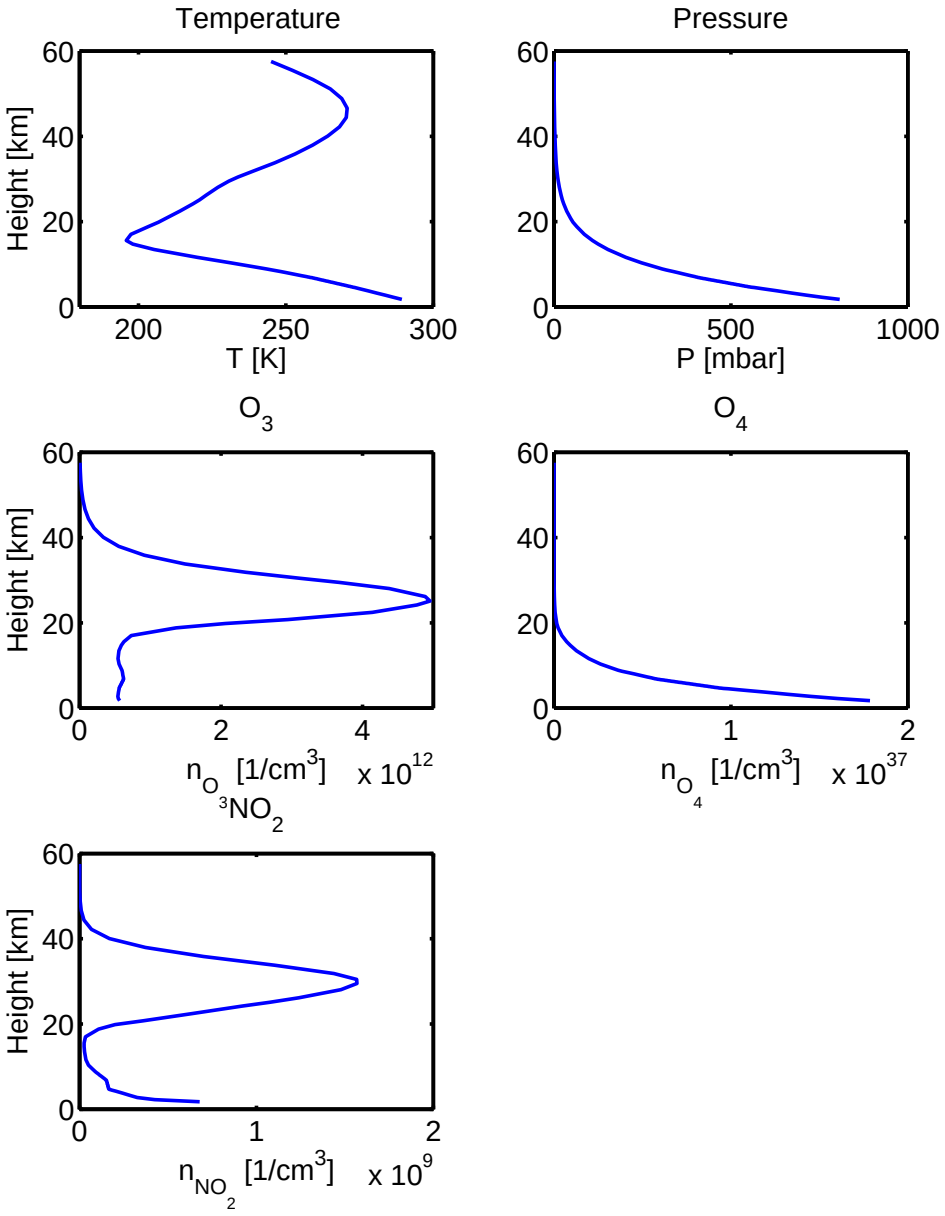

Figure D.1.: The temperature, pressure used and trace gas profiles used in the McArtim simulations in Chapter 6. The profiles (latitude of 5 N in April) were taken from the SCIATRAN database (Rozanov et al., 2005).

E

Appendix E

Satellite images used for cloud detection

Section 6.3 investigates the possibility to detect clouds from spectra recorded by the NOVAC instruments. The different cloud conditions were verified with help of Aqua MODIS satellite images. The cloud fraction and the optical density for 1 January 2011 is shown in Figure E.1. The same images for 2 February 2011 are shown in Figure E.2, for 5 May 2012 in Figure E.3.

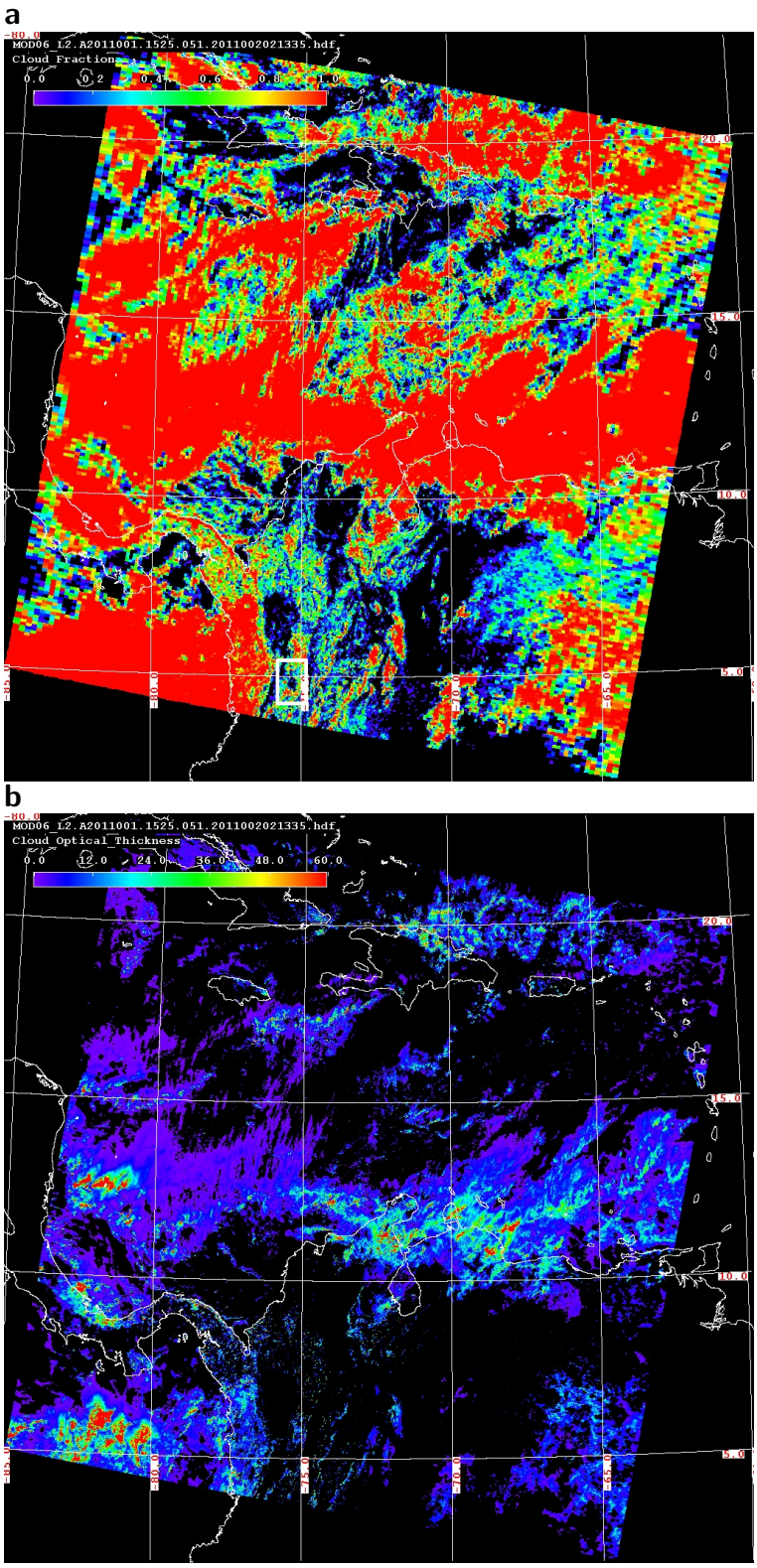

Figure E.1.: Aqua MODIS cloud fraction and cloud optical density images for 1 January, 2011. Nevado del Ruiz is located in the lower part of the image. An area of $\approx 1^\circ$ latitude and longitude around Nevado del Ruiz(4.883333°, -75.316667°) is shown by the white box at the bottom of the upper image. The data shown here were acquired as part of the NASA's Earth-Sun System Division and archived and distributed by the MODIS Adaptive Processing System (MODAPS).

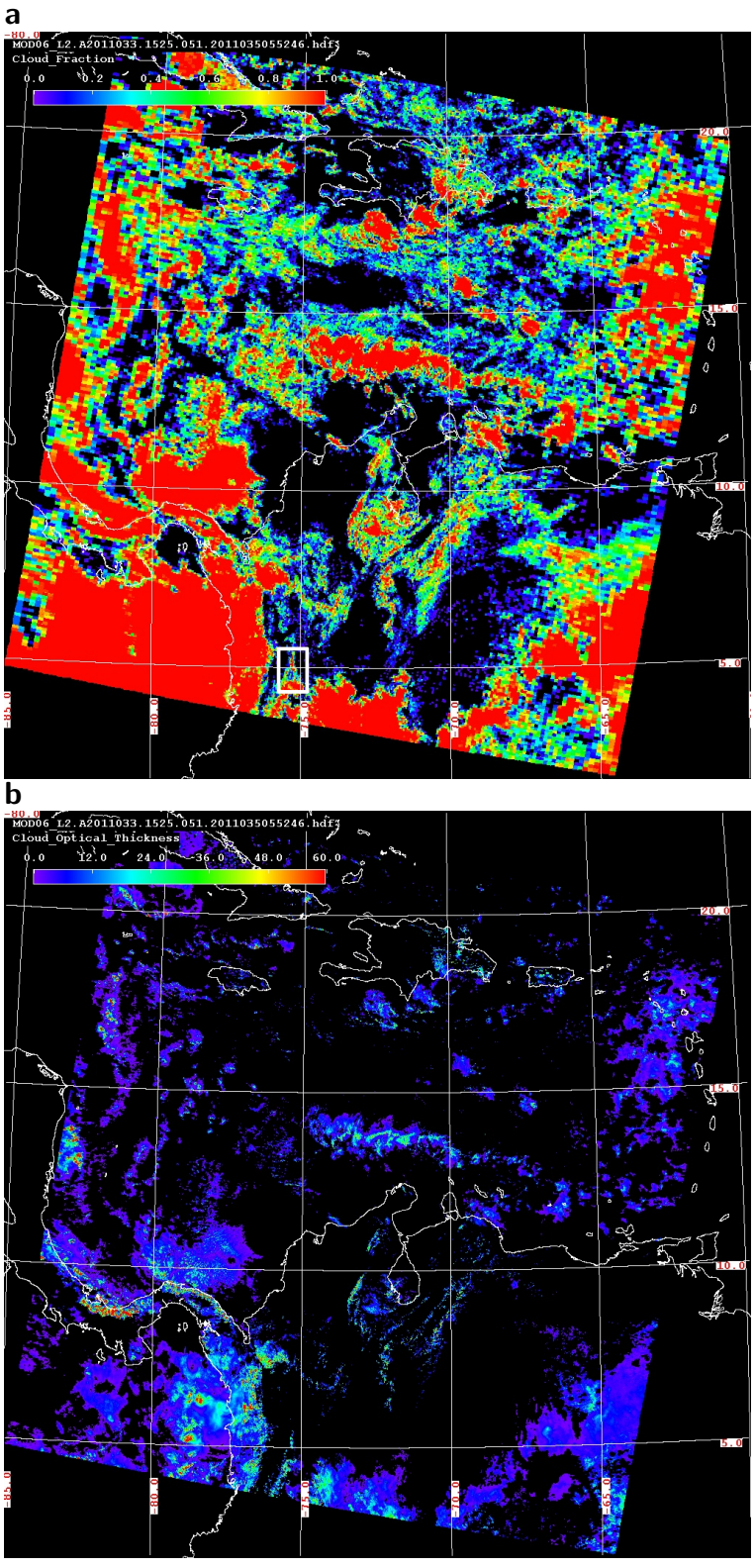

Figure E.2.: Aqua MODIS cloud fraction and cloud optical density images for 2 February, 2011. Nevado del Ruiz is located in the lower part of the image. An area of $\approx 1^\circ$ latitude and longitude around Nevado del Ruiz(4.883333°, -75.316667°) is shown by the white box at the bottom of the upper image. The data shown here were acquired as part of the NASA's Earth-Sun System Division and archived and distributed by the MODIS Adaptive Processing System (MODAPS).

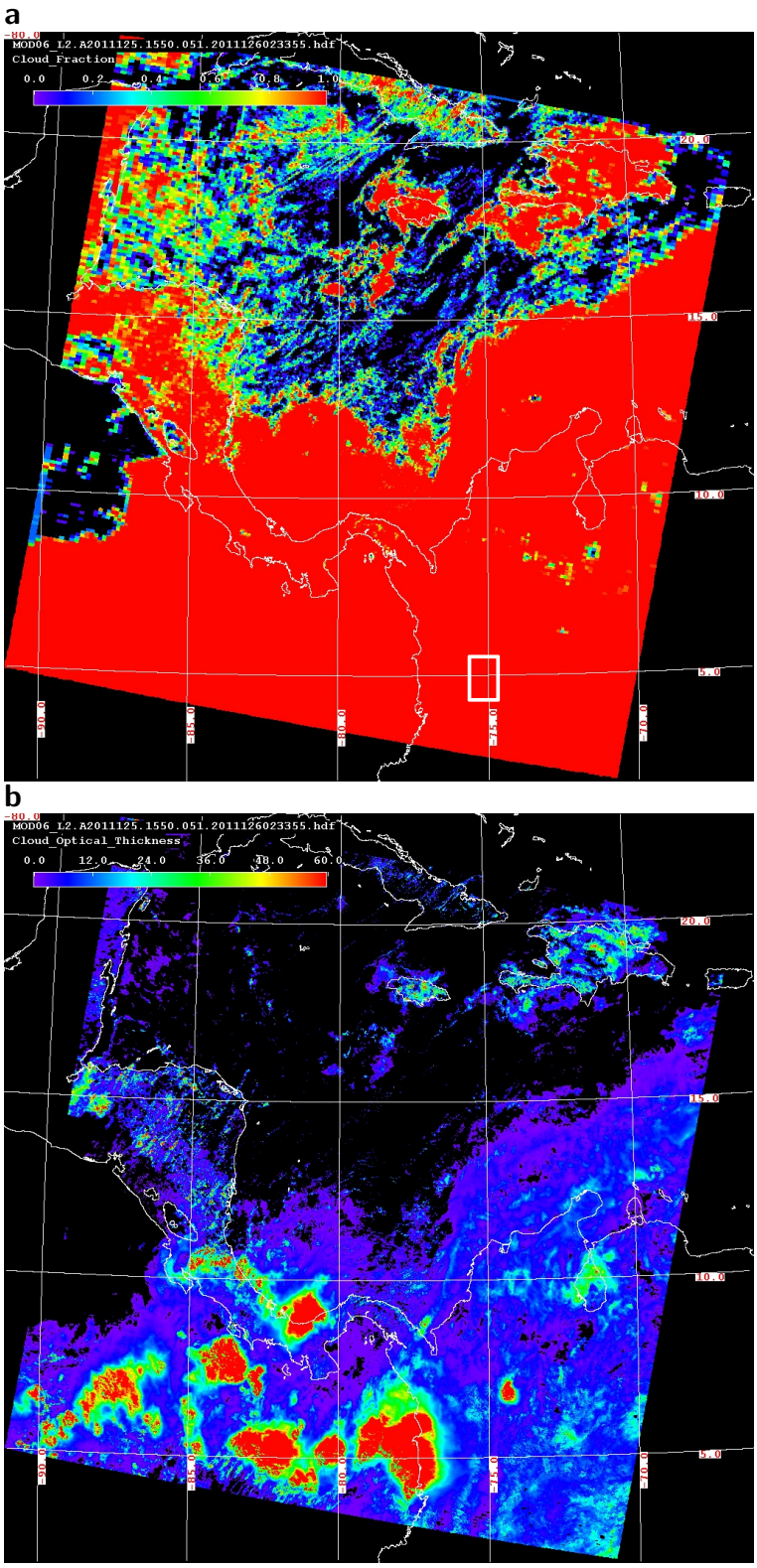

Figure E.3.: Aqua MODIS cloud fraction and cloud optical density images for 5 May, 2011. Nevado del Ruiz is located in the lower part of the image. An area of $\approx 1^\circ$ latitude and longitude around Nevado del Ruiz(4.883333°, -75.316667°) is shown by the white box at the bottom of the upper image. The data shown here were acquired as part of the NASA's Earth-Sun System Division and archived and distributed by the MODIS Adaptive Processing System (MODAPS).

F

Appendix F

Correlation plots for the Solar Atlas evaluation

In this appendix all results from the comparison of the Solar Atlas evaluation with the NOVAC evaluation and the fixed reference (see Chapter 8) are shown. The retrieved SO_2 column densities for the Solar Atlas evaluation and each of the two other methods are shown as colour-coded histogram for both instruments. Results for instrument D2J2200 are shown in Figure F.1 and for instrument D2J2201 in Figure F.2.

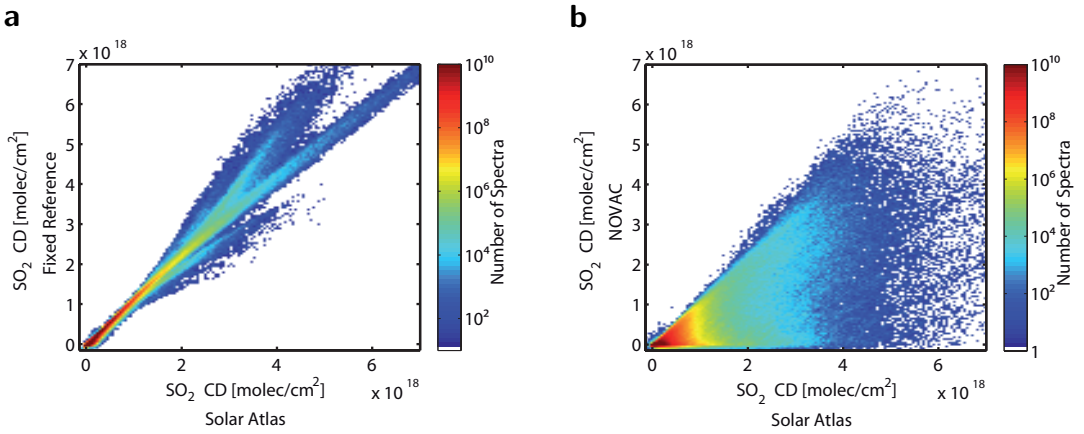

Figure F.1.: 2D histogram comparing the SO_2 SCDs using the Solar Atlas evaluation for instrument D2J2000 with: **a** A fixed reference spectrum, **b** the NOVAC evaluation.

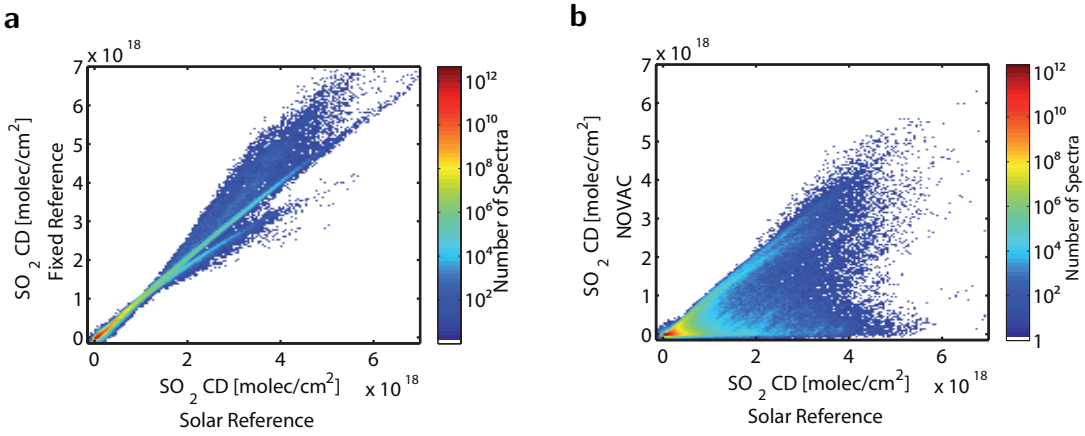

Figure F.2.: 2D histogram comparing the SO_2 SCDs using the Solar Atlas evaluation for instrument D2J2001 with: **a** A fixed reference spectrum, **b** the NOVAC evaluation.

Bibliography

Aiuppa, A., Franco, A., von Glasow, R., Allen, A. G., D'Alessandro, W., Mather, T. A., Pyle, D. M., and Valenza, M.: The tropospheric processing of acidic gases and hydrogen sulphide in volcanic gas plumes as inferred from field and model investigations, Atmospheric Chemistry and Physics, 7, 1441–1450, doi:10.5194/acp-7-1441-2007, URL http://www.atmos-chem-phys.net/7/1441/2007/, 2007.

Aiuppa, A., Baker, D., and Webster, J.: Halogens in volcanic systems - Halogens in Volcanic Systems and Their Environmental Impacts, Chemical Geology, 263, 1–18, doi:10.1016/j.chemgeo.2008.10.005, URL http://www.sciencedirect.com/science/article/pii/S0009254108004658, 2009.

Andres, R. J. and Kasgnoc, A. D.: A time-averaged inventory of subaerial volcanic sulfur emissions, Journal of Geophysical Research: Atmospheres, 103, 25 251–25 261, doi:10.1029/98JD02091, URL http://dx.doi.org/10.1029/98JD02091, 1998.

Ångströem, A.: On the Atmospheric Transmission of Sun Radiation and on Dust in the Air, Geografiska Annaler, 11, 156–166, URL http://www.jstor.org/stable/519399, 1929.

Ångströem, A.: Techniques of Determinig the Turbidity of the Atmosphere, Tellus A, 13, 214–223, doi:10.1111/j.2153-3490.1961.tb00078.x, URL http://dx.doi.org/10.1111/j.2153-3490.1961.tb00078.x, 1961.

Atkinson, R., Baulch, D. L., Cox, R. A., Crowley, J. N., Hampson, R. F., Hynes, R. G., Jenkin, M. E., Rossi, M. J., and Troe, J.: Evaluated kinetic and photochemical data for atmospheric chemistry: Volume I - gas phase reactions of O_x, HO_x, NO_x and SO_x species, Atmospheric Chemistry and Physics, 4, 1461–1738, doi:10.5194/acp-4-1461-2004, URL http://www.atmos-chem-phys.net/4/1461/2004/, 2004.

Barberi, F. and Carapezza, M.: The Problem of Volcanic Unrest: The Campi Flegrei Case History, in: Monitoring and Mitigation of Volcano Hazards, pp.

771–786, Springer Berlin Heidelberg, doi:10.1007/978-3-642-80087-0_23, URL http://dx.doi.org/10.1007/978-3-642-80087-0_23, 1996.

Beirle, S., Hörmann, C., Penning de Vries, M., Dörner, S., Kern, C., and Wagner, T.: Estimating the volcanic emission rate and atmospheric lifetime of SO_2 from space: a case study for Kīlauea volcano, Hawai'i, Atmospheric Chemistry and Physics Discussions, 13, 28 695–28 727, doi:10.5194/acpd-13-28695-2013, URL http://www.atmos-chem-phys-discuss.net/13/28695/2013/, 2013.

Bluth, G. J. S., Shannon, J. M., Watson, I. M., Prata, A. J., and Realmuto, V. J.: Development of an ultra-violet digital camera for volcanic SO_2 imaging, Journal of Volcanology and Geothermal Research, 161, 47–56, doi:10.1016/j.jvolgeores.2006.11.004, URL http://www.sciencedirect.com/science/article/pii/S0377027306003957, 2007.

Bobrowski, N. and Giuffrida, G.: Bromine monoxide / sulphur dioxide ratios in relation to volcanological observations at Mt. Etna 2006 – 2009, Solid Earth, 3, 433–445, doi:10.5194/se-3-433-2012, URL http://www.solid-earth.net/3/433/2012/, 2012.

Bobrowski, N. and Platt, U.: SO_2/BrO ratios studied in five volcanic plumes, Journal of Volcanology and Geothermal Research, 166, 147–160, doi:10.1016/j.jvolgeores.2007.07.003, URL http://www.sciencedirect.com/science/article/pii/S037702730700220X, 2007.

Bobrowski, N., Hönninger, G., Galle, B., and Platt, U.: Detection of bromine monoxide in a volcanic plume, Nature, 423, 273–276, doi:10.1038/nature01625, URL http://dx.doi.org/10.1038/nature01625, 2003.

Bobrowski, N., Hönninger, G., Lohberger, F., and Platt, U.: IDOAS: A new monitoring technique to study the 2D distribution of volcanic gas emissions, Journal of Volcanology and Geothermal Research, 150, 329–338, doi:10.1016/j.jvolgeores.2005.05.004, URL http://www.sciencedirect.com/science/article/pii/S0377027305001976, 2006.

Bobrowski, N., von Glasow, R., Aiuppa, A., Inguaggiato, S., Louban, I., Ibrahim, O. W., and Platt, U.: Reactive halogen chemistry in volcanic plumes, Journal of Geophysical Research: Atmospheres, 112, D06 311, doi:10.1029/2006JD007206, URL http://dx.doi.org/10.1029/2006JD007206, 2007.

Bobrowski, N., Kern, C., Platt, U., Hörmann, C., and Wagner, T.: Novel SO_2 spectral evaluation scheme using the 360–390 nm wavelength range, Atmospheric Measurement Techniques, 3, 879–891, doi:10.5194/amt-3-879-2010, URL http://www.atmos-meas-tech.net/3/879/2010/, 2010.

Bobrowski, N., von Glasow, R., Giuffrida, G., Tedesco, D., Aiuppa, A., Yalire, M., Arellano, S., M., J., and B., G.: Gas emission strength and evolution of

the molar ratio of BrO/SO_2 in the plume of Mt. Nyiragongo in comparison to Mt. Etna, Journal of Volcanology and Geothermal Research, submitted 2013, 2014.

Boichu, M., Oppenheimer, C., Tsanev, V., and Kyle, P. R.: High temporal resolution SO_2 flux measurements at Erebus volcano, Antarctica, Journal of Volcanology and Geothermal Research, 190, 325–336, doi:10.1016/j.jvolgeores.2009.11.020, URL http://www.sciencedirect.com/science/article/pii/S0377027309004569, 2010.

Briffa, K. R., Jones, P. D., Schweingruber, F. H., and Osborn, T. J.: Influence of volcanic eruptions on Northern Hemisphere summer temperature over the past 600 years, Nature, 393, 450–455, doi:10.1038/nature01625, 1998.

Bureau, H., Foy, E., Raepsaet, C., Somogyi, A., Munsch, P., Simon, G., and Kubsky, S.: Bromine cycle in subduction zones through in situ Br monitoring in diamond anvil cells, Geochimica et Cosmochimica Acta, 74, 3839–3850, doi:10.1016/j.gca.2010.04.001, URL http://www.sciencedirect.com/science/article/pii/S0016703710001754, 2010.

Burrows, J. P., Richter, A., Dehn, A., Deters, B., Himmelmann, S., Voigt, S., and Orphal, J.: ATMOSPHERIC REMOTE SENSING REFERENCE DATA FROM GOME2. TEMPERATURE DEPENDENT ABSORPTION CROSS SECTIONS OF O_3 IN THE 231-794 NM RANGE, Journal of Quantitative Spectroscopy and Radiative Transfer, 61, 509–517, doi:10.1016/S0022-4073(98)00037-5, URL http://www.sciencedirect.com/science/article/pii/S0022407398000375, 1999.

Burton, M. and Sawyer, G.: iFit and Light Dilution. Ultraviolet volcanic SO_2 measurements under the microscope, presentation at EGU General Assembly 2013, 2013.

Burton, M., Allard, P., Muré, F., and La Spina, A.: Magmatic Gas Composition Reveals the Source Depth of Slug-Driven Strombolian Explosive Activity, Science, 317, 227–230, doi:10.1126/science.1141900, URL http://www.sciencemag.org/content/317/5835/227.abstract, 2007.

Burton, M., Caltabiano, T., Murè, F., Salerno, G., and Randazzo, D.: SO_2 flux from Stromboli during the 2007 eruption: Results from the FLAME network and traverse measurements, Journal of Volcanology and Geothermal Research, 182, 214–220, doi:10.1016/j.jvolgeores.2008.11.025, URL http://www.sciencedirect.com/science/article/pii/S0377027308006240, 2009.

Bussemer, M.: Der Ring-Effekt: Ursachen und Einfluß auf die spektroskopische Messung stratosphärischer Spurenstoffe, Diplomarbeit, University of Heidelberg, 1993.

Casadevall, T., Rose, W., Gerlach, T., Greenland, L. P., Ewert, J., Wunderman, R., and Symonds, R.: Gas Emissions and the Eruptions of Mount St. Helens Through 1982, Science, 221, 1383–1385, doi:10.1126/science.221.4618.1383, URL http://www.sciencemag.org/content/221/4618/1383.abstract, 1983.

Chance, K. and Kurucz, R. L.: An improved high-resolution solar reference spectrum for earth's atmosphere measurements in the ultraviolet, visible, and near infrared, Journal of Quantitative Spectroscopy and Radiative Transfer, 111, 1289–1295, doi:10.1016/j.jqsrt.2010.01.036, URL http://www.sciencedirect.com/science/article/pii/S0022407310000610, 2010.

Chance, K. V. and Spurr, R. J. D.: Ring effect studies: Rayleigh scattering, including molecular parameters for rotational Raman scattering, and the Fraunhofer spectrum, Appl. Opt., 36, 5224–5230, doi:10.1364/AO.36.005224, URL http://ao.osa.org/abstract.cfm?URI=ao-36-21-5224, 1997.

Chester, D. K., Degg, M., Duncan, A. M., and Guest, J. E.: The increasing exposure of cities to the effects of volcanic eruptions: a global survey, Global Environmental Change Part B: Environmental Hazards, 2, 89–103, doi:10.1016/S1464-2867(01)00004-3, URL http://www.sciencedirect.com/science/article/pii/S1464286701000043, 2000.

Clarke, A.: Unsteady explosive activity: Vulcanian eruptions, in: Modelling Volcanic Processes, edited by S.A. Fagens, T.K.P. Gregg, R. L., chap. 7, pp. 129–152, Cambridge University Press, 2013.

Dalton, M. P., Watson, I. M., Nadeau, P. A., Werner, C., Morrow, W., and Shannon, J. M.: Assessment of the UV camera sulfur dioxide retrieval for point source plumes, Journal of Volcanology and Geothermal Research, 188, 358–366, doi:10.1016/j.jvolgeores.2009.09.013, URL http://www.sciencedirect.com/science/article/pii/S0377027309003655, 2009.

Dalton, M. P., Waite, G. P., Watson, I. M., and Nadeau, P. A.: Multiparameter quantification of gas release during weak Strombolian eruptions at Pacaya Volcano, Guatemala, Geophysical Research Letters, 37, n/a–n/a, doi:10.1029/2010GL042617, URL http://dx.doi.org/10.1029/2010GL042617, 2010.

Darrall, N. M.: The effect of air pollutants on physiological processes in plants, Plant, Cell & Environment, 12, 1–30, doi:10.1111/j.1365-3040.1989.tb01913.x, URL http://dx.doi.org/10.1111/j.1365-3040.1989.tb01913.x, 1989.

Delmelle, P., Stix, J., Baxter, P., Garcia-Alvarez, J., and Barquero, J.: Atmospheric dispersion, environmental effects and potential health hazard associated with the low-altitude gas plume of Masaya volcano, Nicaragua, Bulletin of Volcanology, 64, 423–434, doi:10.1007/s00445-002-0221-6, URL http://dx.doi.org/10.1007/s00445-002-0221-6, 2002.

Deutschmann, T., Beirle, S., Frieß, U., Grzegorski, M., Kern, C., Kritten, L., Platt, U., Prados-Román, C., Pukīte, J., Wagner, T., Werner, B., and Pfeilsticker, K.: The Monte Carlo atmospheric radiative transfer model McArtim: Introduction and validation of Jacobians and 3D features, Journal of Quantitative Spectroscopy and Radiative Transfer, 112, 1119–1137, doi:10.1016/j.jqsrt.2010.12.009, URL http://www.sciencedirect.com/science/article/pii/S0022407310004668, 2011.

Edmonds, M.: New geochemical insights into volcanic degassing, Philosophical Transactions of the Royal Society A: Mathematical, Physical and Engineering Sciences, 366, 4559–4579, doi:10.1098/rsta.2008.0185, URL http://rsta.royalsocietypublishing.org/content/366/1885/4559.abstract, 2008.

Edner, H., Ragnarson, P., Svanberg, S., Wallinder, E., Ferrara, R., Cioni, R., Raco, B., and Taddeucci, G.: Total fluxes of sulfur dioxide from the Italian volcanoes Etna, Stromboli, and Vulcano measured by differential absorption lidar and passive differential optical absorption spectroscopy, Journal of Geophysical Research: Atmospheres, 99, 18 827–18 838, doi:10.1029/94JD01515, URL http://dx.doi.org/10.1029/94JD01515, 1994.

Erle, F., Pfeilsticker, K., and Platt, U.: On the influence of tropospheric clouds on zenith-scattered-light measurements of stratospheric species, Geophysical Research Letters, 22, 2725–2728, doi:10.1029/95GL02789, URL http://dx.doi.org/10.1029/95GL02789, 1995.

Fickert, S., Adams, J. W., and Crowley, J. N.: Activation of Br_2 and BrCl via uptake of HOBr onto aqueous salt solutions, Journal of Geophysical Research: Atmospheres, 104, 23 719–23 727, doi:10.1029/1999JD900359, URL http://dx.doi.org/10.1029/1999JD900359, 1999.

Fleischmann, O. C., Hartmann, M., Burrows, J. P., and Orphal, J.: New ultraviolet absorption cross-sections of BrO at atmospheric temperatures measured by time-windowing Fourier transform spectroscopy, Journal of Photochemistry and Photobiology A: Chemistry, 168, 117–132, doi:10.1016/j.jphotochem.2004.03.026, URL http://www.sciencedirect.com/science/article/pii/S1010603004001522, 2004.

Francis, P. and Oppenheimer, C.: Volcanoes, Oxford University Press, Oxford, 2nd ed edn., 2004.

Francis, P., Maciejewski, A., Oppenheimer, C., Chaffin, C., and Caltabiano, T.: SO_2/HCl ratios in the plumes from Mt. Etna and Vulcano determined by Fourier Transform Spectroscopy, Geophysical Research Letters, 22, 1717–1720, doi:10.1029/95GL01657, URL http://dx.doi.org/10.1029/95GL01657, 1995.

Franklin, B.: Meteorological imaginations and conjectures, in: Manchester Literary and Philosophical Society Memoirs and Proceedings, vol. 2, pp. 373 – 377, 1784.

Frisch, W. and Meschede, M.: Plattentektonik, WBG (Wiss. Buchgesell.), Darmstadt, 5., unveränd. aufl. edn., 2013.

Galle, B., Oppenheimer, C., Geyer, A., McGonigle, A. J., Edmonds, M., and Horrocks, L.: A miniaturised ultraviolet spectrometer for remote sensing of SO_2 fluxes: a new tool for volcano surveillance, Journal of Volcanology and Geothermal Research, 119, 241–254, doi:10.1016/S0377-0273(02)00356-6, URL http://www.sciencedirect.com/science/article/pii/S0377027302003566, 2003.

Galle, B., Johansson, M., Rivera, C., Zhang, Y., Kihlman, M., Kern, C., Lehmann, T., Platt, U., Arellano, S., and Hidalgo, S.: Network for Observation of Volcanic and Atmospheric Change (NOVAC) - A global network for volcanic gas monitoring: Network layout and instrument description, Journal of Geophysical Research: Atmospheres, 115, n/a–n/a, doi:10.1029/2009JD011823, URL http://dx.doi.org/10.1029/2009JD011823, 2010.

Gerlach, T.: Volcanic versus anthropogenic carbon dioxide, Eos, Transactions American Geophysical Union, 92, 201–202, doi:10.1029/2011EO240001, URL http://dx.doi.org/10.1029/2011EO240001, 2011.

Gerlach, T. M.: Volcanic sources of tropospheric ozone depleting trace gases, Geochemistry, Geophysics, Geosystems, 5, Q09 007, doi:10.1029/2004GC000747, URL http://dx.doi.org/10.1029/2004GC000747, 2004.

Giggenbach, W.: Chemical Composition of Volcanic Gases, in: Monitoring and Mitigation of Volcano Hazards, pp. 221–256, Springer Berlin Heidelberg, 1996.

Gliß, J.: MAX-DOAS measurements of chlorine and bromine compounds in the volcanic plume of Mt. Etna, Master's thesis, University of Heidelberg, 2013.

Gorshelev, V., Serdyuchenko, A., Weber, M., Chehade, W., and Burrows, J. P.: High spectral resolution ozone absorption cross-sections - Part 1: Measurements, data analysis and comparison with previous measurements around 293 K, Atmospheric Measurement Techniques Discussions, 6, 6567–6611, doi:10.5194/amtd-6-6567-2013, URL http://www.atmos-meas-tech-discuss.net/6/6567/2013/, 2013.

Gorshkov, G.: On the depth of magmatic chamber of Kliuehevskiy Volcano C.R., Ac.Sc.USSR, 106, 703–705, (in Russian), 1956.

Gorshkov, G.: Prediction of volcanic eruptions and seismic methods of location of magma chambers - A review, Bulletin Volcanologique, 35, 198–211, doi:10.1007/BF02596817, URL http://dx.doi.org/10.1007/BF02596817, 1971.

Graf, H.-F., Feichter, J., and Langmann, B.: Volcanic sulfur emissions: Estimates of source strength and its contribution to the global sulfate distribution, Journal of Geophysical Research: Atmospheres, 102, 10 727–10 738, doi:10.1029/96JD03265, URL http://dx.doi.org/10.1029/96JD03265, 1997.

Grainger, J. and Ring, J.: Anomalous Fraunhofer Line Profiles, nature, 193, 762, 1962.

Gurlit, W., Bösch, H., Bovensmann, H., Burrows, J. P., Butz, A., Camy-Peyret, C., Dorf, M., Gerilowski, K., Lindner, A., Noël, S., Platt, U., Weidner, F., and Pfeilsticker, K.: The UV-A and visible solar irradiance spectrum: inter-comparison of absolutely calibrated, spectrally medium resolution solar irradiance spectra from balloon- and satellite-borne measurements, Atmospheric Chemistry and Physics, 5, 1879–1890, doi:10.5194/acp-5-1879-2005, URL http://www.atmos-chem-phys.net/5/1879/2005/, 2005.

Halmer, M., Schmincke, H.-U., and Graf, H.-F.: The annual volcanic gas input into the atmosphere, in particular into the stratosphere: a global data set for the past 100 years, Journal of Volcanology and Geothermal Research, 115, 511–528, doi:10.1016/S0377-0273(01)00318-3, URL http://www.sciencedirect.com/science/article/pii/S0377027301003183, 2002.

Harris, A. and Ripepe, M.: Temperature and dynamics of degassing at Stromboli, Journal of Geophysical Research: Solid Earth, 112, n/a–n/a, doi:10.1029/2006JB004393, URL http://dx.doi.org/10.1029/2006JB004393, 2007.

Heinzmann, B.: Frequenzanalyse von vulkanischen Schwefeldioxid-Emissionsraten, Staatsexamensarbeit, University of Heidelberg, 2013.

Heraeus: Spectrosil © 2000 Datasheet, HQS-SO Spectrosil, Online, URL http://optik.heraeus-quarzglas.de/media/webmedia_local/downloads/Spectrosilsyntheticfusedsilica.pdf, 2012.

Hermans, C., Vandaele, A., Fally, S., Carleer, M., Colin, R., Coquart, B., Jenouvrier, A., and Merienne, M.-F.: Absorption Cross-section of the Collision-Induced Bands of Oxygen from the UV to the NIR, in: Weakly Interacting Molecular Pairs: Unconventional Absorbers of Radiation in the Atmosphere, edited by Camy-Peyret, C. and Vigasin, A., vol. 27 of *NATO Science Series*, pp. 193–202, Springer Netherlands, doi:10.1007/978-94-010-0025-3_16, URL http://dx.doi.org/10.1007/978-94-010-0025-3_16, 2003.

Hernández-Andrés, J., Lee, R. L., and Romero, J.: Color and Luminance Asymmetries in the Clear Sky, Applied Optics, 42, 458–464, doi:10.1364/AO.42.000458, URL http://ao.osa.org/abstract.cfm?URI=ao-42-3-458, 2003.

Herrick, J.: Bulletin of the Global volcanism Network, URL http://www.volcano.si.edu/reports_bgvn.cfm, last accessed: 19.02.2014, 2012.

Heue, K.-P., Brenninkmeijer, C. A. M., Baker, A. K., Rauthe-Schöch, A., Walter, D., Wagner, T., Hörmann, C., Sihler, H., Dix, B., Frieß, U., Platt, U., Martinsson, B. G., van Velthoven, P. F. J., Zahn, A., and Ebinghaus, R.: SO_2 and BrO observation in the plume of the Eyjafjallajökull volcano 2010: CARIBIC and GOME-2 retrievals, Atmospheric Chemistry and Physics, 11, 2973–2989, doi:10.5194/acp-11-2973-2011, URL http://www.atmos-chem-phys.net/11/2973/2011/, 2011.

Holland, A. P., Watson, I. M., Phillips, J. C., Caricchi, L., and Dalton, M. P.: Degassing processes during lava dome growth: Insights from Santiaguito lava dome, Guatemala, Journal of Volcanology and Geothermal Research, 202, 153–166, doi:10.1016/j.jvolgeores.2011.02.004, URL http://www.sciencedirect.com/science/article/pii/S0377027311000515, 2011.

Hönninger, G. and Platt, U.: Observations of BrO and its vertical distribution during surface ozone depletion at Alert, Atmospheric Environment, 36, 2481–2489, doi:10.1016/S1352-2310(02)00104-8, URL http://www.sciencedirect.com/science/article/pii/S1352231002001048, 2002.

Hörmann, C., Sihler, H., Bobrowski, N., Beirle, S., Penning de Vries, M., Platt, U., and Wagner, T.: Systematic investigation of bromine monoxide in volcanic plumes from space by using the GOME-2 instrument, Atmospheric Chemistry and Physics, 13, 4749–4781, doi:10.5194/acp-13-4749-2013, URL http://www.atmos-chem-phys.net/13/4749/2013/, 2013.

Huwe, M.: Remote sensing of SO_2 Fluxes: further development and upgrading the SO_2 camera, Master's thesis, University of Heidelberg, 2013.

Illing, S.: Entwicklung und Erprobung eines kostengünstigen SO_2-Kamera Prototyps zur Messung von vulkanischen Gasemissionen, Diplomarbeit, University of Heidelberg, 2011.

IPCC: Intergovernmental Panel on Climate Change: Climate Change 2013: The Physical Science Basis. Contribution of Working Group I to the Fifth Assessment Report of the Intergovernmental Panel on Climate Change, Cambridge University Press, United Kingdom and New York, NY, USA, stocker, T.F. and Qin, D. and Plattner, G.-K. and Tignor, M. and Allen, S.K. and Boschung, J. and Nauels, A. and Xia, Y. and Bex V. and Midgley P.M. (eds), 2013.

Jaeschke, W., Berresheim, H., and Georgii, H.-W.: Sulfur emissions from Mt. Etna, Journal of Geophysical Research: Oceans, 87, 7253–7261, doi:10.1029/JC087iC09p07253, URL http://dx.doi.org/10.1029/JC087iC09p07253, 1982.

Jähne, B.: Digitale Bildverarbeitung, Springer Vieweg, Berlin ; Heidelberg, 7., neu bearb. aufl. edn., 2012.

Johansson, M.: Application of Passive DOAS for Studies of Megacity Air Pollution and Volcanic Gas Emissions, Ph.D. thesis, Chalmers University of Technology, 2009.

Johansson, M., Galle, B., Zhang, Y., Rivera, C., Chen, D., and Wyser, K.: The dual-beam mini-DOAS technique—measurements of volcanic gas emission, plume height and plume speed with a single instrument, Bulletin of Volcanology, 71, 747–751, doi:10.1007/s00445-008-0260-8, URL http://dx.doi.org/10.1007/s00445-008-0260-8, 2009.

Kantzas, E. P., McGonigle, A., Tamburello, G., Aiuppa, A., and Bryant, R. G.: Protocols for UV camera volcanic SO_2 measurements, Journal of Volcanology and Geothermal Research, 194, 55–60, doi:10.1016/j.jvolgeores.2010.05.003, URL http://www.sciencedirect.com/science/article/pii/S0377027310001447, 2010.

Kazahaya, K., Shinohara, H., and Saito, G.: Excessive degassing of Izu-Oshima volcano: magma convection in a conduit, Bulletin of Volcanology, 56, 207–216, doi:10.1007/BF00279605, URL http://dx.doi.org/10.1007/BF00279605, 1994.

Kelly, P. J., Kern, C., Roberts, T. J., Lopez, T., Werner, C., and Aiuppa, A.: Rapid chemical evolution of tropospheric volcanic emissions from Redoubt Volcano, Alaska, based on observations of ozone and halogen-containing gases, Journal of Volcanology and Geothermal Research, 259, 317–333, doi:10.1016/j.jvolgeores.2012.04.023, URL http://www.sciencedirect.com/science/article/pii/S0377027312001230, 2013.

Kern, C.: Spectroscopic measurements of volcanic gas emissions in the ultra-violet wavelength region, Ph.D. thesis, University of Heidelberg, URL http://archiv.ub.uni-heidelberg.de/volltextserver/volltexte/2009/9574, 2009.

Kern, C., Sihler, H., Vogel, L., Rivera, C., Herrera, M., and Platt, U.: Halogen oxide measurements at Masaya Volcano, Nicaragua using active long path differential optical absorption spectroscopy, Bulletin of Volcanology, 71, 659–670, doi:10.1007/s00445-008-0252-8, URL http://dx.doi.org/10.1007/s00445-008-0252-8, 2009.

Kern, C., Deutschmann, T., Vogel, L., Wöhrbach, M., Wagner, T., and Platt, U.: Radiative transfer corrections for accurate spectroscopic measurements of volcanic gas emissions, Bulletin of Volcanology, 72, 233–247, doi:10.1007/s00445-009-0313-7, URL http://dx.doi.org/10.1007/s00445-009-0313-7, 2010a.

Kern, C., Kick, F., Lübcke, P., Vogel, L., Wöhrbach, M., and Platt, U.: Theoretical description of functionality, applications, and limitations of SO_2 cameras for the remote sensing of volcanic plumes, Atmospheric Measurement Techniques, 3, 733–749, doi:10.5194/amt-3-733-2010, URL http://www.atmos-meas-tech.net/3/733/2010/, 2010b.

Kern, C., Deutschmann, T., Werner, C., Sutton, A. J., Elias, T., and Kelly, P. J.: Improving the accuracy of SO_2 column densities and emission rates obtained from upward-looking UV-spectroscopic measurements of volcanic plumes by taking realistic radiative transfer into account, Journal of Geophysical Research: Atmospheres, 117, n/a–n/a, doi:10.1029/2012JD017936, URL http://dx.doi.org/10.1029/2012JD017936, 2012.

Kern, C., Werner, C., Elias, T., Sutton, A. J., and Lübcke, P.: Applying UV cameras for SO_2 detection to distant or optically thick volcanic plumes, Journal of Volcanology and Geothermal Research, 262, 80–89, doi:10.1016/j.jvolgeores.2013.06.009, URL http://www.sciencedirect.com/science/article/pii/S0377027313001832, 2013.

Kern, C., Lübcke, P., Bobrowski, N., Campion, R., Mori, T., Smekens, J.-F., Stebel, K., Tamburello, G., Burton, M., Platt, U., and Prata, A. J.: Intercomparison of SO_2 camera systems for imaging volcanic gas plumes, Journal of Volcanology and Geothermal Research, XX, XX, in preparation, 2014.

Kick, F.: Eine UV-Kamera zur Bestimmung atmosphärischer Spurengasverteilungen, Staatsexamensarbeit, University of Heidelberg, 2008.

Klein, A.: Entwicklung einer SO_2 Kamera mit einem Fluoreszenzschirm, Bachelor's thesis, University of Heidelberg, 2012.

Kraus, S. G.: DOASIS - A Framework Design for DOAS, Ph.D. thesis, University of Mannheim, 2006.

Lampel, J.: Ship-borne MAX-DOAS Measurements of Tropospheric Halogen Oxides on Atlantic Transects, Diplomarbeit, University of Heidelberg, 2010.

Lampel, J.: TBD, Ph.D. thesis, University of Heidelberg, 2014.

Lau, K.-M. and Weng, H.: Climate Signal Detection Using Wavelet Transform: How to Make a Time Series Sing, Bulletin of the American Meteorological Society, 76, 2391–2402, doi:10.1175/1520-0477(1995)076<2391:CSDUWT>2.0.CO;2, URL http://dx.doi.org/10.1175/1520-0477(1995)076<2391:CSDUWT>2.0.CO;2, 1995.

Lehmann, T.: Improving the sensitivity of spectroscopic measurements of atmospheric trace gases by modern signal processing algorithms, in preparataion, Phd thesis, University of Heidelberg, 2014.

Lehrer, E., Wagenbach, D., and Platt, U.: Aerosol chemical composition during tropospheric ozone depletion at Ny Ålesund/Svalbard, Tellus B, 49, 486–495, doi:10.1034/j.1600-0889.49.issue5.5.x, URL http://dx.doi.org/10.1034/j.1600-0889.49.issue5.5.x, 1997.

Lissberger, P.: Properties of All-Dielectric Interference Filters. I. A New Method of Calculation, Journal of the Optical Society of America, 49, 121–122, URL http://www.opticsinfobase.org/abstract.cfm?URI=josa-49-2-121, 1959.

Lissberger, P. and Wilcock, W.: Properties of All-Dielectric Interference Filters. II. Filters in Parallel Beams of Light Incident Obliquely and in Convergent Beams, Journal of the Optical Society of America, 49, 126–128, URL http://www.opticsinfobase.org/abstract.cfm?URI=josa-49-2-126, 1959.

Lohberger, F., Hönninger, G., and Platt, U.: Ground-Based Imaging Differential Optical Absorption Spectroscopy of Atmospheric Gases, Appl. Opt., 43, 4711–4717, doi:10.1364/AO.43.004711, URL http://ao.osa.org/abstract.cfm?URI=ao-43-24-4711, 2004.

Longo, B. M., Grunder, A., Chuan, R., and Rossignol, A.: SO2 and fine aerosol dispersion from the Kilauea plume, Kau district, Hawaii, USA, Geology, 33, 217–220, doi:10.1130/G21167.1, URL http://geology.gsapubs.org/content/33/3/217.abstract, 2005.

Louban, I., Bobrowski, N., Rouwet, D., Inguaggiato, S., and Platt, U.: Imaging DOAS for volcanological applications, Bulletin of Volcanology, 71, 753–765, doi:10.1007/s00445-008-0262-6, URL http://dx.doi.org/10.1007/s00445-008-0262-6, 2009.

Lübcke, P.: Development of a new SO_2 camera for volcanic gas flux measurements, Diplomarbeit, University of Heidelberg, 2010.

Lübcke, P., Bobrowski, N., Arellano, S., Galle, B., Garzón, G., Vogel, L., and Platt, U.: BrO/SO_2 molar ratios from scanning DOAS measurements in the NOVAC network, Solid Earth Discussions, 5, 1845–1870, doi:10.5194/sed-5-1845-2013, URL http://www.solid-earth-discuss.net/5/1845/2013/, 2013a.

Lübcke, P., Bobrowski, N., Illing, S., Kern, C., Alvarez Nieves, J. M., Vogel, L., Zielcke, J., Delgado Granados, H., and Platt, U.: On the absolute calibration of SO_2 cameras, Atmospheric Measurement Techniques, 6, 677–696, doi:10.5194/amt-6-677-2013, URL http://www.atmos-meas-tech.net/6/677/2013/, 2013b.

Martin, R. S., Mather, T. A., and Pyle, D. M.: High-temperature mixtures of magmatic and atmospheric gases, Geochemistry, Geophysics, Geosystems,

7, n/a–n/a, doi:10.1029/2005GC001186, URL http://dx.doi.org/10.1029/2005GC001186, 2006.

Martini, M.: Chemical Characters of the Gaseous Phase in Different Stages of Volcanism: Precursors and Volcanic Activity, in: Monitoring and Mitigation of Volcano Hazards, pp. 199–219, Springer Berlin Heidelberg, doi:10.1007/978-3-642-80087-0_6, URL http://dx.doi.org/10.1007/978-3-642-80087-0_6, 1996.

McCormick, B., Herzog, M., Yang, J., Edmonds, M., Mather, T., Carn, S., Hidalgo, S., and Langmann, B.: An integrated study of SO_2 degassing from Tungurahua volcano, Ecuador, presentation at EGU General Assembly 2013, 2013.

McGonigle, A. J. S., Delmelle, P., Oppenheimer, C., Tsanev, V. I., Delfosse, T., Williams-Jones, G., Horton, K., and Mather, T. A.: SO_2 depletion in tropospheric volcanic plumes, Geophysical Research Letters, 31, n/a–n/a, doi:10.1029/2004GL019990, URL http://dx.doi.org/10.1029/2004GL019990, 2004.

McGonigle, A. J. S., Inguaggiato, S., Aiuppa, A., Hayes, A. R., and Oppenheimer, C.: Accurate measurement of volcanic SO_2 flux: Determination of plume transport speed and integrated SO_2 concentration with a single device, Geochemistry, Geophysics, Geosystems, 6, n/a–n/a, doi:10.1029/2004GC000845, URL http://dx.doi.org/10.1029/2004GC000845, 2005.

Meller, R. and Moortgat, G. K.: Temperature dependence of the absorption cross sections of formaldehyde between 223 and 323 K in the wavelength range 225-375 nm, Journal of Geophysical Research: Atmospheres, 105, 7089–7101, doi:10.1029/1999JD901074, URL http://dx.doi.org/10.1029/1999JD901074, 2000.

Millan, M. M.: Remote sensing of air pollutants. A study of some atmospheric scattering effects, Atmospheric Environment, 14, 1241–1253, doi:10.1016/0004-6981(80)90226-7, URL http://www.sciencedirect.com/science/article/pii/0004698180902267, 1980.

Moffat, A. J. and Millan, M. M.: The applications of optical correlation techniques to the remote sensing of SO_2 plumes using sky light, Atmospheric Environment, 5, 677–690, doi:10.1016/0004-6981(71)90125-9, URL http://www.sciencedirect.com/science/article/pii/0004698171901259, 1971.

Mogi, K.: Relations between the eruptions of various volcanoes and the deformations of the ground surfaces around them, Bulletin of the Earthquake Research Institute, 1958.

Möller, D.: Kinetic model of atmospheric SO_2 oxidation based on published data, Atmospheric Environment, 14, 1067–1076, doi:10.1016/0004-6981(80)90037-2, URL http://www.sciencedirect.com/science/article/pii/0004698180900372, 1980.

Mori, T. and Burton, M.: The SO_2 camera: A simple, fast and cheap method for ground-based imaging of SO_2 in volcanic plumes, Geophysical Research Letters, 33, n/a–n/a, doi:10.1029/2006GL027916, URL http://dx.doi.org/10.1029/2006GL027916, 2006.

Mori, T., Notsu, K., Tohjima, Y., and Wakita, H.: Remote detection of HCl and SO_2 in volcanic gas from Unzen Volcano, Japan, Geophysical Research Letters, 20, 1355–1358, doi:10.1029/93GL01065, URL http://dx.doi.org/10.1029/93GL01065, 1993.

Mori, T., Mori, T., Kazahaya, K., Ohwada, M., Hirabayashi, J., and Yoshikawa, S.: Effect of UV scattering on SO_2 emission rate measurements, Geophysical Research Letters, 33, n/a–n/a, doi:10.1029/2006GL026285, URL http://dx.doi.org/10.1029/2006GL026285, 2006.

Morlet, J.: Sampling Theory and Wave Propagation, in: Issues in Acoustic Signal — Image Processing and Recognition, edited by Chen, C., vol. 1 of *NATO ASI Series*, pp. 233–261, Springer Berlin Heidelberg, doi:10.1007/978-3-642-82002-1_12, URL http://dx.doi.org/10.1007/978-3-642-82002-1_12, 1983.

Nadeau, P. A., Palma, J. L., and Waite, G. P.: Linking volcanic tremor, degassing, and eruption dynamics via SO_2 imaging, Geophysical Research Letters, 38, n/a–n/a, doi:10.1029/2010GL045820, URL http://dx.doi.org/10.1029/2010GL045820, 2011.

Noguchi, K. and Kamiya, H.: Prediction of volcanic eruption by measuring the chemical composition and amounts of gases, Bulletin Volcanologique, 26, 367–378, doi:10.1007/BF02597298, URL http://dx.doi.org/10.1007/BF02597298, 1963.

Olmos, R., Barrancos, J., Rivera, C., Barahona, F., López, D., Henriquez, B., Hernández, A., Benitez, E., Hernández, P., Pérez, N., and Galle, B.: Anomalous Emissions of SO_2 During the Recent Eruption of Santa Ana Volcano, El Salvador, Central America, Pure and Applied Geophysics, 164, 2489–2506, doi:10.1007/s00024-007-0276-6, URL http://dx.doi.org/10.1007/s00024-007-0276-6, 2007.

Oppenheimer, C.: Volcanic degassing, Treatise on geochemistry, 3, 123–166, 2003a.

Oppenheimer, C.: Climatic, environmental and human consequences of the largest known historic eruption: Tambora volcano (Indonesia) 1815, Progress in Physical Geography, 27, 230–259, doi:10.1191/0309133303pp379ra, URL http://ppg.sagepub.com/content/27/2/230.abstract, 2003b.

Oppenheimer, C., Francis, P., and Stix, J.: Depletion rates of sulfur dioxide in tropospheric volcanic plumes, Geophysical Research Letters, 25, 2671–2674, doi:10.1029/98GL01988, URL http://dx.doi.org/10.1029/98GL01988, 1998.

Oppenheimer, C., Tsanev, V. I., Braban, C. F., Cox, R. A., Adams, J. W., Aiuppa, A., Bobrowski, N., Delmelle, P., Barclay, J., and McGonigle, A. J.: BrO formation in volcanic plumes, Geochimica et Cosmochimica Acta, 70, 2935–2941, doi:10.1016/j.gca.2006.04.001, URL http://www.sciencedirect.com/science/article/pii/S0016703706001669, 2006.

Oppenheimer, C., Scaillet, B., and Martin, R. S.: Sulfur Degassing From Volcanoes: Source Conditions, Surveillance, Plume Chemistry and Earth System Impacts, Reviews in Mineralogy and Geochemistry, 73, 363–421, doi:10.2138/rmg.2011.73.13, URL http://rimg.geoscienceworld.org/content/73/1/363.short, 2011.

Oppenheimer, C., Fischer, T., and Scaillet, B.: Volcanic Degassing: Process and Impact, in: Treatise on Geochemistry (Second Edition), edited by Holland, H. D. and Turekian, K. K., pp. 111–179, Elsevier, Oxford, second edition edn., doi:http://dx.doi.org/10.1016/B978-0-08-095975-7.00304-1, URL http://www.sciencedirect.com/science/article/pii/B9780080959757003041, 2014.

Oxford English Dictionary: "volcano, n.", Oxford University Press, URL http://www.oed.com/view/Entry/224428?rskey=zC8Ho8&result=1&isAdvanced=false, 2013.

Parfitt, E. A.: A discussion of the mechanisms of explosive basaltic eruptions, Journal of Volcanology and Geothermal Research, 134, 77–107, doi:10.1016/j.jvolgeores.2004.01.002, URL http://www.sciencedirect.com/science/article/pii/S0377027304000137, 2004.

Pearson, K.: LIII. On lines and planes of closest fit to systems of points in space, The London, Edinburgh, and Dublin Philosophical Magazine and Journal of Science, 2, 559–572, 1901.

Pennisi, M. and Le Cloarec, M.-F.: Variations of Cl, F, and S in Mount Etna's plume, Italy, between 1992 and 1995, Journal of Geophysical Research: Solid Earth, 103, 5061–5066, doi:10.1029/97JB03011, URL http://dx.doi.org/10.1029/97JB03011, 1998.

Pering, T., Tamburello, G., McGonigle, A., Aiuppa, A., Cannata, A., Giudice, G., and Patan, D.: High time resolution fluctuations in volcanic carbon dioxide

degassing from Mount Etna, Journal of Volcanology and Geothermal Research, 270, 115–121, doi:10.1016/j.jvolgeores.2013.11.014, URL http://www.sciencedirect.com/science/article/pii/S0377027313003508, 2014.

Perner, D. and Platt, U.: Detection of nitrous acid in the atmosphere by differential optical absorption, Geophysical Research Letters, 6, 917–920, doi:10.1029/GL006i012p00917, URL http://dx.doi.org/10.1029/GL006i012p00917, 1979.

Pfeilsticker, K., Erle, F., Funk, O., Marquard, L., Wagner, T., and Platt, U.: Optical path modifications due to tropospheric clouds: Implications for zenith sky measurements of stratospheric gases, Journal of Geophysical Research: Atmospheres, 103, 25 323–25 335, doi:10.1029/98JD01803, URL http://dx.doi.org/10.1029/98JD01803, 1998.

Pinardi, G., Roozendael, M. V., and Fayt, C.: The influence of spectrometer temperature variability on the data retrieval of SO_2., In NOVAC second annual activity report, pp 44–48, NOVAC consortium, 2007.

Platt, U. and Stutz, J.: Differential Optical Absorption Spectroscopy - Principles and Applications, Physics of Earth and Space Environments, Springer Berlin Heidelberg, 2008.

Platt, U., Marquard, L., Wagner, T., and Perner, D.: Corrections for zenith scattered light DOAS, Geophysical Research Letters, 24, 1759–1762, doi:10.1029/97GL01693, URL http://dx.doi.org/10.1029/97GL01693, 1997.

Pöhler, D.: Fast and durable electromechanical shutter for imaging spectrometers, Review of Scientific Instruments, 80, 036104, doi:10.1063/1.3103628, URL http://scitation.aip.org/content/aip/journal/rsi/80/3/10.1063/1.3103628, 2009.

Prata, A. J. and Bernardo, C.: Retrieval of sulphur dioxide from a ground-based thermal infrared imaging camera, Atmospheric Measurement Techniques Discussions, 7, 1153–1211, doi:10.5194/amtd-7-1153-2014, URL http://www.atmos-meas-tech-discuss.net/7/1153/2014/, 2014.

Roberts, T., Braban, C., Martin, R., Oppenheimer, C., Adams, J., Cox, R., Jones, R., and Griffiths, P.: Modelling reactive halogen formation and ozone depletion in volcanic plumes, Chemical Geology, 263, 151 – 163, doi:10.1016/j.chemgeo.2008.11.012, URL http://www.sciencedirect.com/science/article/pii/S0009254108005366, 2009.

Roberts, T. J., Martin, R. S., and Jourdain, L.: Reactive bromine chemistry in Mt. Etna's volcanic plume: the influence of total Br, high temperature processing, aerosol loading and plume-air mixing, Atmospheric Chemistry

and Physics Discussions, 14, 5445–5494, doi:10.5194/acpd-14-5445-2014, URL http://www.atmos-chem-phys-discuss.net/14/5445/2014/, 2014.

Robock, A.: Volcanic eruptions and climate, Reviews of Geophysics, 38, 191–219, doi:10.1029/1998RG000054, URL http://dx.doi.org/10.1029/1998RG000054, 2000.

Rodríguez, L. A., Watson, I. M., Edmonds, M., Ryan, G., Hards, V., Oppenheimer, C. M., and Bluth, G. J.: SO_2 loss rates in the plume emitted by Soufriere Hills volcano, Montserrat, Journal of Volcanology and Geothermal Research, 173, 135–147, doi:10.1016/j.jvolgeores.2008.01.003, URL http://www.sciencedirect.com/science/article/pii/S0377027308000188, 2008.

Rose, W. I., Palma, J. L., Delgado Granados, H., and Varley, N.: Open-vent volcanism and related hazards: Overview, Geological Society of America Special Papers, 498, vii–xiii, doi:10.1130/2013.2498(00), URL http://specialpapers.gsapubs.org/content/498/vii.abstract, 2013.

Rossini, E. G. and Krenzinger, A.: Maps of sky relative radiance and luminance distributions acquired with a monochromatic CCD camera, Solar Energy, 81, 1323–1332, doi:10.1016/j.solener.2007.06.013, URL http://www.sciencedirect.com/science/article/pii/S0038092X07001508, 2007.

Rozanov, A., Rozanov, V., Buchwitz, M., Kokhanovsky, A., and Burrows, J.: SCIATRAN 2.0–A new radiative transfer model for geophysical applications in the 175–2400nm spectral region, Advances in Space Research, 36, 1015–1019, 2005.

Salerno, G., Burton, M., Oppenheimer, C., Caltabiano, T., Tsanev, V., and Bruno, N.: Novel retrieval of volcanic SO_2 abundance from ultraviolet spectra, Journal of Volcanology and Geothermal Research, 181, 141–153, doi:10.1016/j.jvolgeores.2009.01.009, URL http://www.sciencedirect.com/science/article/pii/S0377027309000158, 2009.

Scarpa, R. and Gasparini, P.: A Review of Volcano Geophysics and Volcano-Monitoring Methods, in: Monitoring and Mitigation of Volcano Hazards, pp. 3–22, Springer Berlin Heidelberg, doi:10.1007/978-3-642-80087-0_1, URL http://dx.doi.org/10.1007/978-3-642-80087-0_1, 1996.

Schmincke, H.-U.: Volcanism, Springer, Berlin, URL http://www.loc.gov/catdir/enhancements/fy0816/2003056723-d.html, 2003.

Seinfeld, J. H. and Pandis, S. N.: Atmospheric chemistry and physics, Wiley, Hoboken, NJ, 2. ed. edn., previous ed.: 1998, 2006.

Serdyuchenko, A., Gorshelev, V., Weber, M., Chehade, W., and Burrows, J. P.: High spectral resolution ozone absorption cross-section - Part

2: Temperature dependence, Atmospheric Measurement Techniques Discussions, 6, 6613–6643, doi:10.5194/amtd-6-6613-2013, URL http://www.atmos-meas-tech-discuss.net/6/6613/2013/, 2013.

Shinohara, H.: Excess degassing from volcanoes and its role on eruptive and intrusive activity, Reviews of Geophysics, 46, n/a–n/a, doi:10.1029/2007RG000244, URL http://dx.doi.org/10.1029/2007RG000244, 2008.

Smith, L. I.: A tutorial on principal components analysis, Cornell University, USA, 51, 52, 2002.

Smithsonian Global Volcanism Program: Weekly Activity Report, 27 June-3 July 2012, URL http://volcano.si.edu/volcano.cfm?vn=351020&tab=2#June2012, 2012.

Solomon, S., Schmeltekopf, A. L., and Sanders, R. W.: On the interpretation of zenith sky absorption measurements, Journal of Geophysical Research: Atmospheres, 92, 8311–8319, doi:10.1029/JD092iD07p08311, URL http://dx.doi.org/10.1029/JD092iD07p08311, 1987.

Spampinato, L., Oppenheimer, C., Cannata, A., Montalto, P., Salerno, G., and Calvari, S.: On the time-scale of thermal cycles associated with open-vent degassing, Bulletin of Volcanology, 74, 1281–1292, doi:10.1007/s00445-012-0592-2, URL http://dx.doi.org/10.1007/s00445-012-0592-2, 2012.

Sparks, R.: Forecasting volcanic eruptions, Earth and Planetary Science Letters, 210, 1–15, doi:10.1016/S0012-821X(03)00124-9, URL http://www.sciencedirect.com/science/article/pii/S0012821X03001249, 2003a.

Sparks, R.: Dynamics of magma degassing, in: Volcanic Degassing, Special Publications, pp. 5–22, Geological Society, London, 2003b.

Spinetti, C. and Buongiorno, M.: Volcanic aerosol optical characteristics of Mt. Etna tropospheric plume retrieved by means of airborne multispectral images, Journal of Atmospheric and Solar-Terrestrial Physics, 69, 981–994, doi:10.1016/j.jastp.2007.03.014, URL http://www.sciencedirect.com/science/article/pii/S1364682607000855, 2007.

Stevenson, D. S. and Blake, S.: Modelling the dynamics and thermodynamics of volcanic degassing, Bulletin of Volcanology, 60, 307–317, doi:10.1007/s004450050234, URL http://dx.doi.org/10.1007/s004450050234, 1998.

Stix, J., Layne, G., and Williams, S.: Mechanisms of degassing at Nevado del Ruiz volcano, Colombia, Journal of the Geological Society, 160, 507–521, doi:10.1144/0016-764902-028, URL http://jgs.lyellcollection.org/content/160/4/507.abstract, 2003.

Stoiber, R. E. and Rose, W. I.: The Geochemistry of Central American Volcanic Gas Condensates, Geological Society of America Bulletin, 81, 2891–2912, doi:10.1130/0016-7606(1970)81[2891:TGOCAV]2.0.CO;2, URL http://gsabulletin.gsapubs.org/content/81/10/2891.abstract, 1970.

Stoiber, R. E., Malinconico, L. L., and Williams, S.: Use of the correlation spectrometer at volcanoes, in: Forecasting volcanic events, edited by Tazieff, H. and Sabroux, J.-C., pp. 424–444, Elsevier Science Pub. Co., Inc., New York, NY, 1983.

Stothers, R. B.: The Great Tambora Eruption in 1815 and Its Aftermath, Science, 224, 1191–1198, doi:10.1126/science.224.4654.1191, URL http://www.sciencemag.org/content/224/4654/1191.abstract, 1984.

Stutz, J. and Platt, U.: Problems in using diode arrays for open path DOAS measurements of atmospheric species, Proc. SPIE, 1715, 329–340, doi:10.1117/12.140192, URL http://dx.doi.org/10.1117/12.140192, 1993.

Tamburello, G., Aiuppa, A., Kantzas, E., McGonigle, A., and Ripepe, M.: Passive vs. active degassing modes at an open-vent volcano (Stromboli, Italy), Earth and Planetary Science Letters, 359–360, 106–116, doi:10.1016/j.epsl.2012.09.050, URL http://www.sciencedirect.com/science/article/pii/S0012821X12005468, 2012.

Tamburello, G., Aiuppa, A., McGonigle, A. J. S., Allard, P., Cannata, A., Giudice, G., Kantzas, E. P., and Pering, T. D.: Periodic volcanic degassing behavior: The Mount Etna example, Geophysical Research Letters, 40, 4818–4822, doi:10.1002/grl.50924, URL http://dx.doi.org/10.1002/grl.50924, 2013.

Teolis, A.: Computational signal processing with wavelets, Birkhäuser, Boston, 1998.

Textor, C., Graf, H.-F., Timmreck, C., and Robock, A.: Emissions from Volancoes, in: Emissions of atmospheric trace compounds, edited by Granier, C., Netto, P. E. A., and Reeves, C. E., pp. 269–303, Springer, 2004.

Theys, N., Van Roozendael, M., Dils, B., Hendrick, F., Hao, N., and De Mazière, M.: First satellite detection of volcanic bromine monoxide emission after the Kasatochi eruption, Geophysical Research Letters, 36, n/a–n/a, doi:10.1029/2008GL036552, URL http://dx.doi.org/10.1029/2008GL036552, 2009.

Thuillier, G., Floyd, L., Woods, T., Cebula, R., Hilsenrath, E., Hersé, M., and Labs, D.: Solar irradiance reference spectra for two solar active levels, Advances in Space Research, 34, 256–261, doi:10.1016/j.asr.2002.12.004, URL http://

www.sciencedirect.com/science/article/pii/S0273117704002388, solar Variability and Climate Change, 2004.

Tilling, R.: The critical role of volcano monitoring in risk reduction, Advances in Geosciences, 14, 3–11, 2008.

Tilling, R. I. and Lipman, P. W.: Lessons in reducing volcano risk, Nature, 364, 277–280, 1993.

Torrence, C. and Compo, G. P.: A Practical Guide to Wavelet Analysis, Bulletin of the American Meteorological Society., 79, 61–78, doi:10.1175/1520-0477(1998)079<0061:APGTWA>2.0.CO;2, URL http://dx.doi.org/10.1175/1520-0477(1998)079<0061:APGTWA>2.0.CO;2, 1998.

Twomey, S.: Pollution and the planetary albedo, Atmospheric Environment (1967), 8, 1251–1256, doi:10.1016/0004-6981(74)90004-3, URL http://www.sciencedirect.com/science/article/pii/0004698174900043, 1974.

van Rozendael, M.: UV-Vis DOAS Group, QDOAS Homepage, URL http://uv-vis.aeronomie.be/software/, 2013.

Vandaele, A., Hermans, C., Simon, P., Carleer, M., Colin, R., Fally, S., Merienne, M., Jenouvrier, A., and Coquart, B.: Measurements of the NO_2 absorption cross-section from 42 000 cm^{-1} to 10 000 cm^{-1} (238 - 1000 nm) at 220 K and 294 K, Journal of Quantitative Spectroscopy and Radiative Transfer, 59, 171–184, doi:10.1016/S0022-4073(97)00168-4, URL http://www.sciencedirect.com/science/article/pii/S0022407397001684, 1998.

Vandaele, A., Hermans, C., and Fally, S.: Fourier transform measurements of SO_2 absorption cross sections: II.: Temperature dependence in the 29000 - 44000 cm^{-1} (227-345 nm) region, Journal of Quantitative Spectroscopy and Radiative Transfer, 110, 2115–2126, doi:10.1016/j.jqsrt.2009.05.006, URL http://www.sciencedirect.com/science/article/pii/S0022407309001800, 2009.

Vergniolle, S.: Bubble size distribution in magma chambers and dynamics of basaltic eruptions, Earth and Planetary Science Letters, 140, 269–279, doi:10.1016/0012-821X(96)00042-8, URL http://www.sciencedirect.com/science/article/pii/0012821X96000428, 1996.

Vogel, L.: Volcanic plumes: Evaluation of spectroscopic measurements, early detection, and bromine chemistry, Ph.D. thesis, University of Heidelberg, URL http://archiv.ub.uni-heidelberg.de/volltextserver/volltexte/2012/13219, 2011.

Vogel, L., Galle, B., Kern, C., Delgado Granados, H., Conde, V., Norman, P., Arellano, S., Landgren, O., Lübcke, P., Alvarez Nieves, J. M., Cárdenas Gonzáles, L., and Platt, U.: Early in-flight detection of SO_2 via Dif-

ferential Optical Absorption Spectroscopy: a feasible aviation safety measure to prevent potential encounters with volcanic plumes, Atmospheric Measurement Techniques, 4, 1785–1804, doi:10.5194/amt-4-1785-2011, URL http://www.atmos-meas-tech.net/4/1785/2011/, 2011.

Voight, B.: The 1985 Nevado del Ruiz volcano catastrophe: anatomy and retrospection, Journal of Volcanology and Geothermal Research, 44, 349–386, doi:10.1016/0377-0273(90)90027-D, URL http://www.sciencedirect.com/science/article/pii/037702739090027D, 1990.

von Glasow, R.: Atmospheric chemistry in volcanic plumes, Proceedings of the National Academy of Sciences, 107, 6594–6599, doi:10.1073/pnas.0913164107, URL http://www.pnas.org/content/107/15/6594.abstract, 2010.

von Glasow, R., Bobrowski, N., and Kern, C.: The effects of volcanic eruptions on atmospheric chemistry, Chemical Geology, 263, 131–142, doi:10.1016/j.chemgeo.2008.08.020, URL http://www.sciencedirect.com/science/article/pii/S0009254108003756, 2009.

Wagner, T., Beirle, S., and Deutschmann, T.: Three-dimensional simulation of the Ring effect in observations of scattered sun light using Monte Carlo radiative transfer models, Atmospheric Measurement Techniques, 2, 113–124, doi:10.5194/amt-2-113-2009, URL http://www.atmos-meas-tech.net/2/113/2009/, 2009.

Wagner, T., Beirle, S., Dörner, S., Friess, U., Remmers, J., and Shaiganfar, R.: Cloud detection and classification based on MAX-DOAS observations, Atmospheric Measurement Techniques Discussions, 6, 10 297–10 360, doi:10.5194/amtd-6-10297-2013, URL http://www.atmos-meas-tech-discuss.net/6/10297/2013/, 2013.

Watson, I., Realmuto, V., Rose, W., Prata, A., Bluth, G., Gu, Y., Bader, C., and Yu, T.: Thermal infrared remote sensing of volcanic emissions using the moderate resolution imaging spectroradiometer, Journal of Volcanology and Geothermal Research, 135, 75–89, doi:10.1016/j.jvolgeores.2003.12.017, URL http://www.sciencedirect.com/science/article/pii/S0377027304000307, 2004.

Wennberg, P.: Atmospheric chemistry: Bromine explosion, Nature, 397, 299–301, 1999.

Wöhrbach, M.: Weiterentwicklung und Erprobung einer UV-Kamera zur Bestimmung atmosphärischer Spurengasverteilungen, Master's thesis, University of Heidelberg, 2008.

Zehner, C. E., ed.: Monitoring Volcanic Ash from Space. Proceedings of the ESA-EUMETSAT workshop on the 14 April to 23 May 2010 eruption at the Eyjafjoll

volcano, South Iceland, ESA-Publication STM-280, doi:10.5270/atmch-10-01, frascati, Italy, 26-27 May 2010, 2010.

List of Figures

List of Tables

Acknowledgements

Many people provided me with invaluable support and assistance over the past three years, and without them this thesis would never have been completed.

I would like to start out by thanking Prof. Dr. Platt for introducing me to this interesting field and not only giving me the opportunity to complete my thesis in his group but also supporting my research by offering me helpful ideas and advice.

Prof. Dr. Thomas Wagner also deserves mention for agreeing to serve as a referee on this thesis.

I would also like to thank the volcano group in Heidelberg. Huge thanks are due to my advisor, Nicole Bobrowski, who always found time to discuss my ideas despite having a lot on her plate. Leif Vogel and Christoph Kern both deserve special thanks for advising me during my diploma thesis and, even after they moved on to bigger things, helped me through my PhD as well. Thanks also to all the volcanology people in Heidelberg I have worked and travelled with and who made the campaigns in Mexico and Italy more fun: Johannes Zielcke, Christoph Hörmann, Julian, Sebastian and Marco.

I also am extremely grateful to all the people who read through the many drafts of this dissertation that I sent their way: in particular Nicole, Christoph, Johannes L. and Johannes Z., Katja G., Julian, Bodo, Katja B., Jonas G., Holger, Jonas K. and Angelika. I hope that I can return the favour for some of you!

The rest of our work group also deserves mention for keeping me motivated with valuable discussions at work or during lunch, a fun work atmosphere and occasional soccer games. In random order: Martin, Stefan, Stephan, Tobias, Denis, Klaus-Peter, Jens, Udo, Selami, Robert, Jan-Marcus, Lara, Tim, Tilman and Thomas L..

For listening to my occasional rants about work (or the Deutsche Bahn), I want to thank Daniel, Christine, Simon, Ugo, Florian, Bodo, Johannes, Johannes

and Martin.

I would also like to thank Tim Deutschmann for providing McArtim and helpful tips for using the software as well as Thomas Lehmann for his work to improve DOASIS.

I also would like to mention the people from other institutes who I met during various campaigns and workshops and with whom I had inspiring discussions about the remote sensing of volcanic gases: specifically Vladimir, Santiago, Patrick, Oscar, Bo, Matthias, Francisco, Jean-Francois, Andrew, Mike, Giancarlo, Fred, Kerstin, Hugo and José Manuel. And I can't forget all the great people I met during the Field Methods in Volcanology course in Hawaii.

Some non-physicists were also invaluable to this work: The mechanical workshop in our institute built some of the technically impressive instruments that conducted the measurements used in this thesis, and have my deepest gratitude for their skilled work. I'd also like to thank our administrative staff, especially Frau Clos, Frau Thomas and Frau Weirich, for their support in the face of a customs crisis, travel organisation and multiple forms and signatures.

Last but not least, I would like to thank my family, especially my parents, sister and brother for their support during my whole life. And I would not be able to conclude this section without expressing my gratitude to Abby for adapting so many of her plans so that I could complete my PhD and still supporting me the whole way.